Development of High Purity Lithium Bis(oxalate)borate, $LiB(C_2O_4)_2$ (LiBOB) and Its Effect on the Stability of Standard and New Generation Electrode Materials

by

Yaprak Subaşı

A Dissertation Submitted to the
Graduate School of Sciences and Engineering
in Partial Fulfillment of the Requirements for
the Degree of

Doctor of Philosophy

in

Materials Science and Engineering

KOÇ ÜNİVERSİTESİ

April, 2022

Development of High Purity Lithium Bis(oxalate)borate, $LiB(C_2O_4)_2$ (LiBOB) and Its Effect on the Stability of Standard and New Generation Electrode Materials

Koç University

Graduate School of Sciences and Engineering

This is to certify that I have examined this copy of a doctoral dissertation by

Yaprak Subaşı

and have found that it is complete and satisfactory in all respects, and that any and all revisions required by the final examining committee have been made.

Committee Members:

Prof. Dr. Mehmet S. Somer (Advisor)

Assist. Prof. Dr. Semih Afyon [Co-Advisor]

Assist. Prof. Dr. Umut Aydemir

Assoc. Prof. Dr. Uğur Ünal

Assist. Prof. Dr. Yılmaz Şimşek

Assoc. Prof. Dr. Mustafa Kemal Bayazıt

Date: 05.04.2022

Dedicated to my beloved family, Levent Subaşı and Prof. Dr. Feryal Subaşı… and to my beloved one…

ABSTRACT

Development of High Purity Lithium Bis(oxalate)borate, $LiB(C_2O_4)_2$ (LiBOB) and Its Effect on the Stability of Standard and New Generation Electrode Materials

Yaprak Subaşı

Doctor of Philosophy in Materials Science and Engineering

April 2022

Among other battery technologies, lithium-ion batteries have been extensively used in portable electronics, hybrid/electric vehicles (HEVs/EVs) and energy storage devices because of their high energy density, high capacity, long lifetime, low self-discharge rate, and design flexibility. Over the past decades, many attempts have been made to develop new battery materials towards higher energy density, longer life, safety, environmental friendliness, and sustainability. Currently, most commercial lithium-ion batteries have been used graphite as an anode, $LiCoO_2$ as a cathode and $LiPF_6$ in ethyl carbonate (EC) – dimethyl carbonate (DMC) as an electrolyte solution. However, graphite anode may suffer from its limited capacity and the dendrite formation, whereas $LiPF_6$ salt is susceptible to decompose into dangerous byproducts resulting in safety issues and poor electrochemical performances at high operating voltages. Therefore, various electrolyte additives have been introduced to prevent electrolyte degradation, structural changes, HF attack and impedance rise at the electrode surface by developing a solid electrolyte interface (SEI). Among alternative electrolyte additives, lithium bis(oxalate)borate, $LiB(C_2O_4)_2$ (LiBOB) has received significant interest owing to its high thermal stability, good solubility, high conductivity, low cost, and safety in a wide potential window.

In this thesis, high purity LiBOB was developed as an electrolyte additive to enhance the electrochemical performances of standard and new generation electrode materials. First,

LiBOB was synthesized using low-cost starting chemicals and fewer processing steps under a protective atmosphere. The detrimental effects of humidity and remaining impurities of LiBOB were evaluated through physical and chemical characterizations. Secondly, a practical recrystallization process was carried out to eliminate lithium oxalate ($Li_2C_2O_4$) impurity, which is susceptible to precipitate in the electrolyte solution resulting in high cell impedance and poor cycling stability. After obtaining a high purity product, the desired amount of LiBOB was dissolved in the base electrolyte to increase the stability of $LiCoO_2$ cathode at high potential. Thus, $LiCoO_2$ showed superior cycling stability, rate capability, and high energy density related to the enhanced interfacial stability by LiBOB originated SEI layer.

As a new generation anode material, surface modified TiO_2 / reduced graphite oxide (RGO) nanocomposite was fabricated due to its promising features like structural stability, cycling stability, environmental friendliness, safety, and low cost. First, anatase TiO_2 nanoparticles with an average crystallite size below 20 nm was synthesized by a sol-gel method. Coating with RGO as a conductive network and a surface modification process were applied to enhance overall electrochemical performance related to the better dispersion of nanoparticles and mechanical stability. Consequently, the surface modified TiO_2/RGO anode showed high capacity, superior cycling stability, high coulombic efficiency (> 99 %) and outstanding rate capability compared to the pristine composite and TiO_2 anodes.

Finally, the effects of LiBOB on the stability of surface modified TiO_2/RGO anode was studied via galvanostatic cycling tests and various post-mortem analyses. It was found that the applied current rate has a large impact on the correct formation of a SEI layer to ensure cycling stability. With the addition of LiBOB, surface modified TiO_2/RGO anode showed improved capacity retention and high coulombic efficiency at lower current density. Ex-situ scanning electron microscopy (SEM) images and X-ray photoelectron spectroscopy (XPS) evaluated the development of a chemically and mechanically stable SEI on the anode surface. However,

after first discharging, the huge irreversible capacity loss was occurred due to the preferential oxidation of LiBOB that could not be avoided even at low current densities.

The promising results given in this study for the high voltage $LiCoO_2$ cathodes and TiO_2/RGO anodes with high purity LiBOB could open new pathways for other high voltage cathodes and new generation anodes resulting in higher energy densities, cycling stability and safety for state-of-the-art lithium-ion batteries.

ÖZETÇE

Yüksek Saflıkta Lityum Bis(oksalat)borat, $LiB(C_2O_4)_2$ (LiBOB)

Geliştirilmesi ve Standart ve Yeni Nesil Elektrot Malzemelerinin Kararlılığına Etkisi

Yaprak Subaşı

Malzeme Bilimi ve Mühendisliği Doktora Tezi

Nisan 2022

Diğer pil teknolojileri arasında, lityum-iyon piller daha yüksek enerji yoğunluğu, kapasite, uzun ömür, düşük özboşalım oranı, ve tasarım esnekliği gibi üstün özellikleri sayesinde taşınabilir elektroniklerde, hibrit/elektrikli arabalarda ve enerji depoloma teknolojilerinde yaygın olarak kullanılmaktadırlar. Son yıllarda, daha yüksek enerji yoğunluğu, daha uzun ömür, güvenlik, çevre dostu ve sürdürülebilirliğe yönelik yeni pil malzemeleri geliştirmek için birçok çaba gösterilmektedir. Günümüzde, çoğu ticari lityum-iyon pillerde anot olarak grafit, katot olarak $LiCoO_2$ ve elektrolit çözeltisi olarak $LiPF_6$ esaslı etil karbonat (EC) – dimetil karbonat (DMC) kullanılmaktadır. Buna rağmen, grafit anot düşük kapasitesi ve dendrit oluşumundan sorun yaşarken, $LiPF_6$ tuzu tehlikeli yan ürünlere parçalanmaya eğilimli olması nedeniyle yüksek çalışma voltajlarında güvenlik sorunu ve düşük elektrokimyasal performans teşkil etmektedir. Bu nedenle, elektrolit parçalanması, yapısal değişim, HF saldırısı ve empedans artışını önlemek amacıyla katı elektrolit arayüzü (SEI) oluşturan çeşitli elektrolit katkıları kullanılmaktadır. Alternatif elektrolit katkıları arasında lityum bis(oksalat)borat (LiBOB) yüksek termal kararlılık, iyi çözünebilirlik, yüksek iletkenlik, düşük maliyet ve geniş voltaj aralığında güvenli olması nedeniyle yoğun ilgi görmektedir.

Bu tezde, standart ve yeni nesil elektrot malzemelerinin elektrokimyasal performanslarını iyileştirmek amacıyla elektrolit katkısı olarak yüksek saflıkta LiBOB geliştirilmiştir. İlk olarak LiBOB koruyucu atmosfer altında düşük başlangıç kimyasalları ve daha az proses aşamaları

kullanılarak sentezlenmiştir. Nem ve empüritenin LiBOB üzerindeki yıkıcı etkileri fiziksel ve kimyasal karakterizasyonlar ile değerlendirilmiştir. İkinci olarak, hücrede empedans artışına ve zayıf elektrokimyasal performansa neden olan elektrolit çözeltisinde çökelmeye eğilimli lityum oksalat ($Li_2C_2O_4$) empüritesini gidermek için pratik bir rekristalizasyon prosesi uygulanmıştır. Yüksek saflıkta ürün elde edildikten sonra, $LiCoO_2$ katotun yüksek voltajda karalılığını arttırmak amacıyla istenen oranda LiBOB referans elektrolit içerisinde çözündürülmüştür. Böylece, $LiCoO_2$ LiBOB esaslı SEI tabakası sayesinde arayüzeysel kararlılığın arttırılmasına bağlı olarak üstün çevrim karalılığı, hız kabiliyeti, ve yüksek enerji yoğunluğu göstermiştir.

Yeni nesil anot malzemesi olarak, yapısal kararlı, çevrimsel kararlı, çevre dostu, güvenli ve düşük maliyetli olması nedeniyle yüzeyi modifiye edilmiş TiO_2 / indirgenmiş grafit oksit (RGO) nanokompoziti üretilmiştir. Öncelikle anataz TiO_2 nanoparçacıkları sol-jel yöntemiyle ortalama kristalit boyutu 20 nm altında olarak elde edilmiştir. Elektrokimyasal performansı tamamen arttırmak için iletken ortam olarak RGO ile kaplama ve nanoparçacıkların daha iyi dağılmasını ve mekanik kararlılığı sağlamak için ise yüzey modifikasyonu uygulanmıştır. Sonuç olarak yüzeyi modifiye edilmiş TiO_2/RGO anot, standart kompozit ve TiO_2 naoparçacıklarına kıyasla daha yüksek kapasite, üstün çevrim kararlılığı, yüksek kulombik verimlilik (> %99), ve mükemmel hız kabiliyeti göstermiştir.

Son olarak, LiBOB'un yüzeyi modifiye edilmiş TiO_2/RGO anotun kararlılığına etkileri galvanostatik çevrim testleri ve çeşitli postmortem analizlerle incelenmiştir. Çevrim kararlılığını sağlamak için uygulanan akım oranının düzgün SEI oluşumu üzerinde önemli bir etkisi olduğu anlaşılmıştır. Yüzeyi modifiye edilmiş TiO_2/RGO anot, LiBOB ilavesi ile düşük akım yoğunluğunda iyileştirilmiş kapasite korunumu ve yüksek kulombik verimlilik göstermiştir. Anot yüzeyinde kimyasal ve mekanik olarak kararlı bir SEI oluşumu, doğal yeri dışında taramalı electron mikroskobu (SEM) görüntüleri ve X-ray fotoelektron spektroskopisi

(XPS) ile tayin edilmiştir. Fakat, düşük akım yoğunluğundaki ilk deşarjdan sonra bile LiBOB'un tercihi oksidasyonuna bağlı olarak yüksek olan tersinmez kapasite kaybı önlenememiştir.

Bu çalışmada yüksek voltaj $LiCoO_2$ katotların ve TiO_2/RGO anotların yüksek saflıkta LiBOB ile verilen gelecek vaadeden sonuçları, en gelişmiş lityum iyon piller için yüksek enerji yoğunluğu, çevrim karalılığı ve güvenlik unsurlarını beraberinde getirerek diğer yüksek voltaj katotlar ve yeni nesil anotlar için yeni yollar açabilmektedir.

ACKNOWLEDGMENTS

First, my sincere gratitude goes to Prof. Dr. Mehmet S. Somer for being not only my thesis advisor but also a caring father in all aspects. His outstanding knowledge, great support, understanding, patience, friendliness, limitless motivation, and encouragement inspired me to be more successful along with strengthening my personality. I will never forget our scientific discussions as well as the laughs we had together. He has been I learned so much from him and it will always be my great honor to be his last PhD student.

I would like to express my sincere gratitude to my co-advisor, mentor and friend, Asst. Prof. Dr. Semih Afyon for his great scientific attitude, belief in me and continuous motivation to pursue my goals. His guidance provided me to push my limits and extend my vision. He taught me to work under pressure and helped me to become a better version of myself. I learned so much from him and I feel lucky for working with him.

I would like to sincerely thank Asst. Prof. Dr. Umut Aydemir for his full support and significant scientific contributions. I am grateful for all opportunities that he has provided me to conduct my research. He always encouraged and gave valuable recommendations during my thesis.

My appreciation goes to Dr. Annamaria Miko for her kind support, understanding and friendliness. It has been a great pleasure for me to be her teaching assistant for four years. She is the kindest and funniest person that I have met at Koç University. I would like to thank Dr. Durat Haciu for her outstanding help and support during this study.

I would like to thank Dr. Barış Yağcı for his patience and support during SEM and XPS measurements, Dr. Gülsu Şimşek for FTIR and Dr. Amir Motallebzadef for AFM analysis at Koç University Surface Science and Technology Center (KUYTAM).

Special thanks must go to all members of Koç University Boron and Advanced Materials Application and Research Center (KUBAM) for their kind support and friendship. I could never forget our group events and memories within these years.

I would like to deeply thank my beloved family for their endless support, love, friendship, motivation, and belief in me throughout my whole life. I am grateful to be their daughter and I could never have achieved all these without them. Special thanks to my beloved one Salih Çavuş for being my soulmate since high school. He also pushed me harder to be more successful. I may not be the person who I am today. He made all these years much easier with love and fun.

Finally, I would like to acknowledge the generous financial support from the Scientific and Technological Research Council of Turkey (TÜBITAK, 2211C Domestic Priority Doctoral Fellowship Program).

TABLE OF CONTENTS

LIST OF TABLES

LIST OF FIGURES

ABBREVIATIONS

AFM	Atomic Force Microscopy
ATR	Attenuated Total Reflectance
BOB	Bis(oxalate) Borate
CCP	Cubic Close Packed
CE	Coulombic Efficiency
CNTs	Carbon Nanotubes
CV	Cyclic Voltammetry
CVD	Chemical Vapor Deposition
DEC	Diethyl Carbonate
DFT	Density Functional Theory
DMC	Dimethyl Carbonate
DTA	Differential Thermal Analysis
DTMSO	Di(trimethylsilyl) Oxalate
EC	Ethylene Carbonate
EDX	Energy-dispersive X-ray
EIS	Electrochemical Impedance Spectroscopy
EMC	Ethyl Methyl Carbonate
EVs	Electrical Vehicles
FEC	Fluoroethylene Carbonate
FTIR	Fourier Transform Infrared
FWHM	Full Width at Half Maximum
GBL	γ-Butyrolactone
GO	Graphene Oxide
GO	Graphite Oxide
HCP	Hexagonal Close Packed

HF	Hydrofluoric Acid
HW	Halder Wagner
ICSD	Inorganic Crystal Structure Database
LCO	$LiCoO_2$
LiBOB	Lithium Bis(oxalate) Borate
LiFAP	Lithium tris(pentafluoroethyl)trifluorophosphate
LiTFSI	Lithium bis(trifluoromethanesulfonyl)imide
LIB	Lithium-ion Battery
LIBs	Lithium-ion Batteries
LMNO	$LiNi_{0.5}Mn_{1.5}O_4$
LMO	$LiMn_2O_4$
LNFMO	$Li_{1-x}Ni_{0.42}Fe_{0.08}Mn_{1.5}O_4$
MCMB	Mesoporous Crystalline Microbeads
NCM	$Li(Ni_{1/3}Co_{1/3}Mn_{1/3})O_2$
NMO	$LiNi_{0.5}Mn_{0.5}O_2$
NMR	Nuclear Magnetic Resonance
NPs	Nanoparticles
OCP	Open Circuit Potential
PC	Propylene Carbonate
PVDF	Polyvinylidene Fluoride
RGO	Reduced Graphene Oxide
RGO	Reduced Graphite Oxide
RIR	Reference Intensity Ratio
RT	Room Temperature
SEI	Solid Electrolyte Interphase
SEM	Scanning Electron Microscopy
SHE	Standard Hydrogen Electrode
SUN	Suberonitrile
TBOT	Titanium (IV) n-butoxide
TGA	Thermogravimetric Analysis
THF	Tetrahydrofuran

TMP	Trimethylboroxine
VC	Vinylene Carbonate
VEC	Vinyl Ethylene Carbonate
XPS	X-ray Photoelectron Spectroscopy
XRD	X-ray Diffraction
XRPD	X-ray Powder Diffraction

Chapter 1:
INTRODUCTION

1.1 Lithium-Ion Batteries

Lithium-ion batteries (LIBs) have been regarded as an alternative renewable energy source instead of using fossil-fuels, thereby offering sustainability [1]. Lithium (Li) was highly appropriate for the design of energy storage systems with high energy density because of its high oxidation potential (-3.04 V vs. SHE), low weight (6.94 g mol^{-1}) and low density (0.53 g cm^{-3}) [2]. In 1976, M. Stanley Whittingham presented a lithium-based battery cell consisting of metallic Li as anode, titanium disulfide (TiS_2) as cathode and $LiPF_6$ in propylene carbonate as electrolyte in collaboration with Exxon [3, 4]. However, reactive metallic Li is susceptible to the dendrite formation at the metal surface during cycling resulting in a short circuit and potential fire hazard (**Figure 1.1**) [5].

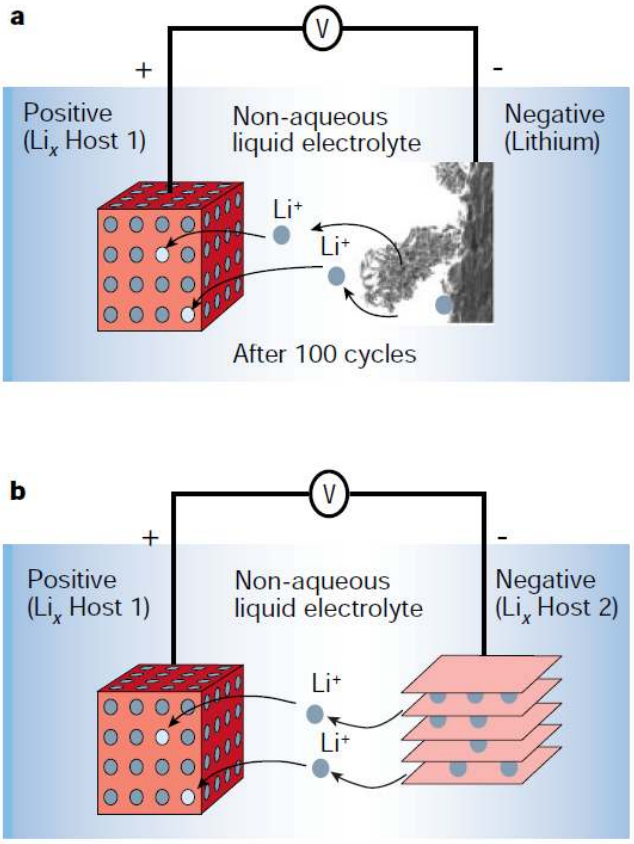

Figure 1.1: Schematic representation of (a) rechargeable Li-metal, (b) Li-ion battery [2].

In 1980, John B. Goodenough discovered that lithium cobalt oxide (Li_xCoO_2) gives higher cell voltage than TiS_2. Additionally, Li_xMO_2 (M: Co, Ni, Mn) was proposed as the positive electrode containing lithium for the first time [6, 7]. Finally, in 1985, Akira Yoshino revealed that petroleum coke is stable under required electrochemical conditions compared to metallic Li anode. Therefore, Goodenough's Li_xCoO_2 was used as a cathode material and Yoshino's graphite was used as an intercalation anode material in the first developed lithium-ion battery (LIB) cell (**Figure 1.2**) [8]. These developments led to the release of the first commercial LIB in 1991. This battery was consisted of petroleum coke as an anode, $LiCoO_2$ as a cathode, and a water-free electrolyte composed of $LiPF_6$ in propylene carbonate [9].

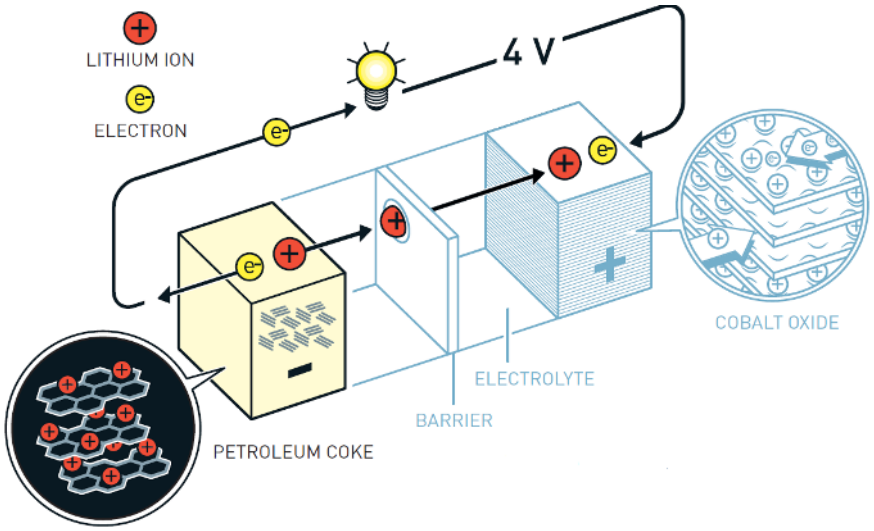

Figure 1.2: Ion transfer cell configuration [10].

Since the commercialization of lithium-ion batteries by Yoshino and Sony Corporation in the 1990s, LIBs have been widely used for portable electronic devices, energy storage systems and electric vehicles (EVs) with regard to their superior properties such as high energy density, high capacity, long life-time, low self-discharge rate, no memory effect and design flexibility compared to lead acid, nickel-cadmium and nickel-metal hydride batteries [11-15] (**Figure 1.3**). The global EV market is estimated to increase more than 151.6 billion by 2024 and the unit sales are likely to reach 97 million by 2025 [16].

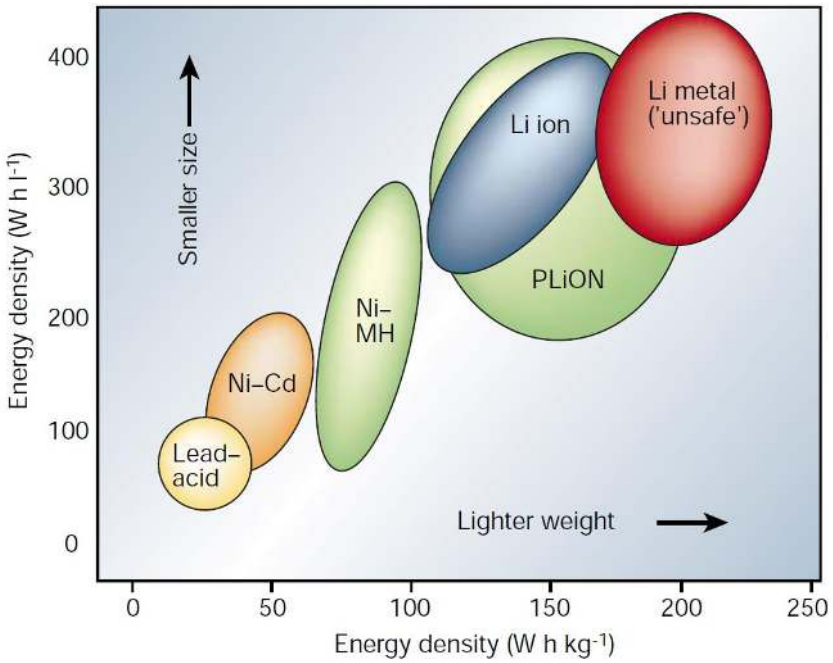

Figure 1.3: Comparison of the different battery technologies in terms of volumetric and gravimetric energy density [2].

Today, lithium transition metal oxides such as $LiCoO_2$ [6, 17, 18], $LiMn_2O_4$ [19, 20] and $LiFePO_4$ [21-23] are the most commercially used cathode materials for LIBs. Graphite is used as an anode because of its high conductivity with a theoretical capacity of 372 mA h g^{-1} [24], whereas $LiPF_6$ in ethyl carbonate (EC) - dimethyl carbonate (DMC) solution is the most commonly used electrolyte. However, $LiPF_6$ is prone to hazardous degradation reactions, which leads to undesirable side effects and safety issues [25]. As shown in **Figure 1.4**, during discharge process, Li ions move from the negative electrode (anode) to the layered positive electrode (cathode) with oxidation while the reverse reaction takes place for charging with a reduction [26]. The chemical reactions that occurred at the cathode (M: Co, Ni, Mn) and anode (graphite) are given as:

Their chemical reactions are described as below [27]:

Cathode: $LiMO_2 \leftrightarrow Li_{1-x}MO_2 + xLi^+ + xe^-$ **(1.1)**

Anode: $6C + xLi^+ + xe^- \leftrightarrow Li_xC_6$ **(1.2)**

Overall: $Li_{1-x}MO_2 + Li_xC_6 \leftrightarrow LiMO_2 + 6C$ **(1.3)**

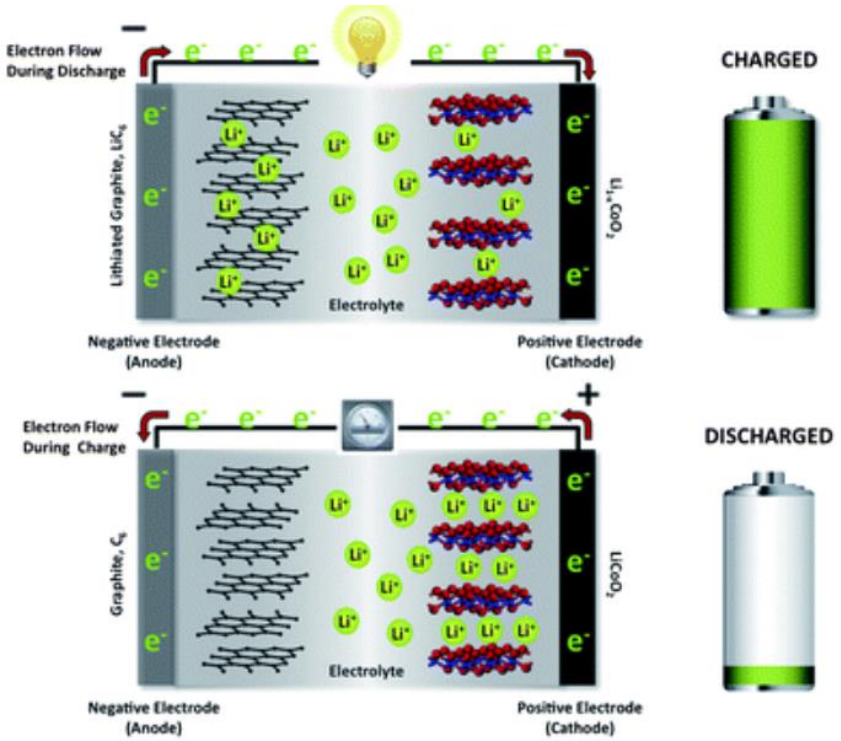

Figure 1.4: Schematic illustration of the working principles of a $Li_xC_6/Li_{1-x}CoO_2$ lithium-ion cell [26].

The desired LIB performances can be listed as high safety, long life-time and high energy density/power density that are related to battery components including anode, cathode, electrolyte and separator as well as operating conditions (**Figure 1.5**) [28].

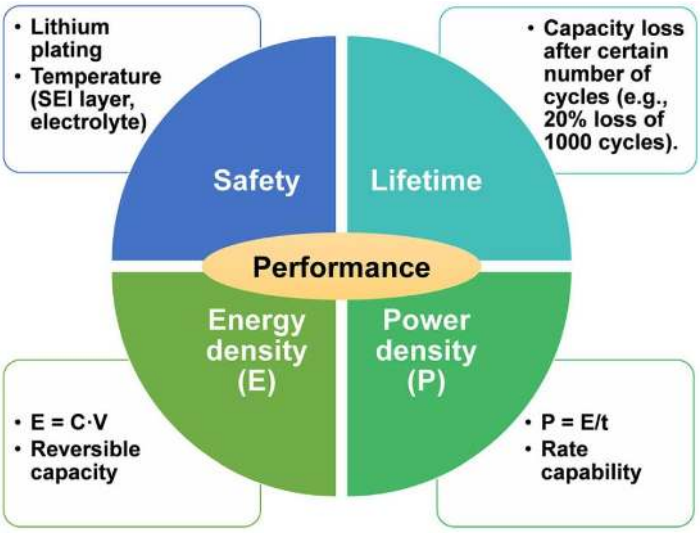

Figure 1.5: Schematic representation of the key requirements for high performance LIBs [28].

1.2 Cathode Materials

The improvement of enhanced LIB performance is determined by the development of suitable cathodes. Microstructure, morphology and electrochemical properties are the key factors for high performance, since the intercalation-deintercalation of Li ions takes place at the solid electrolyte interface (SEI) and the crystallinity has an influence on the electrode performance [29]. High energy density can be obtained for a cathode with high voltage and high capacity. Many efforts have been made to increase the cut-off voltage of current cathode materials to meet higher energy and power density requirements [30, 31].

In the 1980s, three classes of cathodes were discovered by Goodenough's group, Koichi Mizushima, Michael Thackeray and Arumugam Manthiram. These are layered oxides ($LiCoO_2$), spinel oxides ($LiMn_2O_4$) and polyanion oxides ($LiMPO_4$, M: Fe, Ni, Co, Mn), providing fundamentals for future investigations (**Figure 1.6**, **Figure 1.7**) [1].

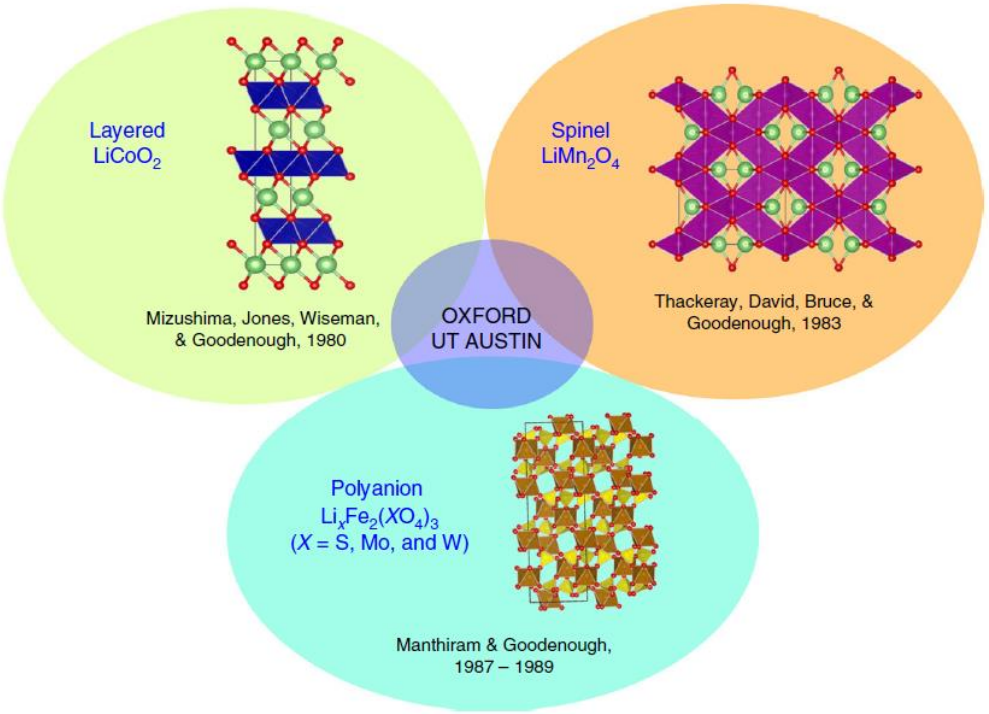

Figure 1.6: Discovery of cathodes in 1980s [1].

An efficient cathode material must:

- include a transition metal for the reduction/oxidation reaction
- react reversibly with Li very quickly during insertion-extraction with a high free energy
- high capacity
- high voltage (~ 4 V)
- high energy storage
- high electronic conductivity
- easy exchange of electrons

- minimum use of inactive conductive solvents
- structurally stable
- low cost and environmentally friendly [30].

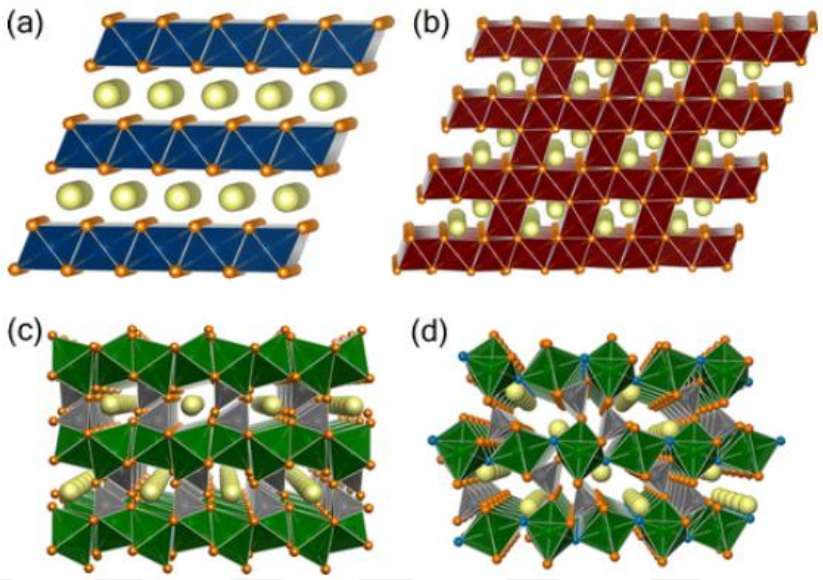

Figure 1.7: Illustration of the crystal structures of the most used cathodes (a) $LiCoO_2$, (b) $LiMn_2O_4$, (c) $LiFePO_4$, and (d) the tavorite-phase of $LiFeSO_4F$. Li atoms in yellow, transition metals in orange, Co, Mn, Fe in blue, red, and green, respectively [32].

Today, oxides have been used as cathode materials in commercial EVs/PHEVs that BMW uses $LiNi_{0.33}Mn_{0.33}Co_{0.33}O_2$ (NMC) whereas Tesla uses $LiNi_{0.8}Co_{0.15}Al_{0.05}O_2$ (NCA) due to their long cycle life, high energy density and low cost [16, 33].

1.2.1 Layered oxides

Layered oxides (Li_xMO_2, M: Co, Ni, Mn) have a rock salt structure with a cubic close-packed (ccp) oxygen array. The crystallographic space group symmetry varies in terms of atomic and electronic configurations (monoclinic, *C2/m* for Li_2MnO_3, $LiMnO_2$, trigonal, *R-3m* for $LiCoO_2$ and $LiNiO_2$) [34-36]. Triangular compositional phase diagrams are shown in **Figure 1.8**.

From the $LiCo^{3+}O_2$–$LiNi^{3+}O_2$–$LiMn^{3+}O_2$–$Li(Li_{1/3}Mn^{4+}{}_{2/3})O_2$ diagram (**Figure 1.8a**), the number of cations are same with the number of anions, whereas for the phase diagram of $LiCoO_2$–$LiNiO_2$–$LiMnO_2$ (**Figure 1.8b**), isosceles triangle contains the $Li(Li_{1/3}Mn_{2/3})O_2$ vertex of the tetrahedron. According to **Figure 1.8c**, In Li-excess layered structure Mn oxides, Li is contained within the metal layer at the expense of cations [37].

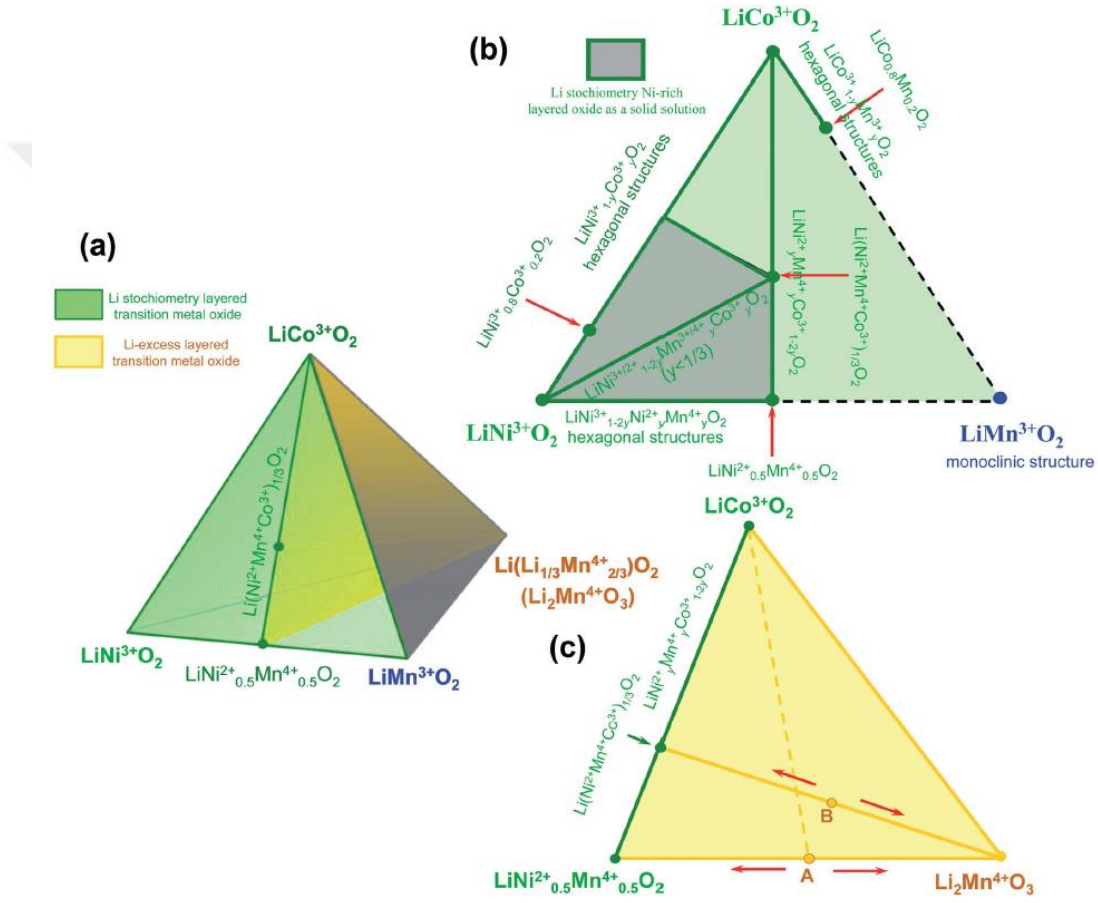

Figure 1.8: Compositional phase diagrams of (a) layered lithium transition metal oxide tetrahedron $LiCo^{3+}O_2$–$LiNi^{3+}O_2$–$LiMn^{3+}O_2$–$Li(Li_{1/3}Mn^{4+}{}_{2/3})O_2$, (b) lithium-stoichiometric layered transition metal oxide $LiCo^{3+}O_2$–$LiNi^{3+}O_2$–$LiMn^{3+}O_2$, (c) lithium-excess Mn-based layered oxide: $LiCo^{3+}O_2$–$LiNi^{3+}1/2Mn^{4+}$ $1/2O_2$–$Li_2Mn_{4+}O_3$ [37].

In 1958, the crystal structure of $LiCoO_2$ was first reported as α-$NaFeO_2$-type by

Johnston's group [38]. In which, Li^+ and Co^{3+} ions are ordered on alternating (1 1 1) planes of *R-3m* space group with cell parameters of a = 2.816(2) Å, c= 14.08(1) Å [39]. Additionally, the large charge and size difference between Li^+ and Co^{3+} ions result in fast Li-ion diffusion and conduction [1]. Nevertheless, at low-temperature synthesis conditions (~ 400 °C), the rock salt structure of $LiCoO_2$ transforms to spinel structure (*Fd3-m*), causing poor cycling performance compared to the $LiCoO_2$ (900 °C) [40]. The electrochemical properties of $LiCoO_2$ were further described by using $LiBF_4$ in propylene carbonate as the electrolyte solution by Goodenough in 1980 [6]. The irreversible hexagonal close-packing of oxygen is occurred during the removal of Li ions from $LiCoO_2$ because of the rearrangement of oxygen layers for a distorted ccp oxygen array. Thus, a large anisotropic expansion-contraction takes place due to the continuous phase transition [41]. $LiCoO_2$ has received great attention because of its high theoretical capacity, high compacted density (4.1-4.2 g cm^{-3}), high Li mobility, good cycling stability, excellent rate capability, and high safety [42-46]. $LiCoO_2$ and Co_3O_4 are the thermal decomposition products of delithiated $Li_{1-x}CoO_2$ ($0.4<x<0.6$, $x=0.5$) [47]. However, the practical capacity of $LiCoO_2$ is limited to 130-140 mA h g^{-1} in a potential window of 3.0 - 4.2 V vs. Li^+/Li for 0.5 Li^+ exchange even though its theoretical capacity of 274 mA h g^{-1} [41, 48-50]. In addition, $LiCoO_2$ cathodes may suffer from capacity fade at higher potentials due to the cobalt dissolution, structural changes, electrolyte degradation, hydrofluoric acid (HF) attack, and impedance increase at the surface leading to performance decay [51-54]. Therefore, there are various strategies to avoid electrolyte decomposition, which leads to a higher electrochemical performance of $LiCoO_2$ cathodes. Surface modification with metal oxide particles such as Al_2O_3, ZrO_2, SnO_2 and ZnO have been used to protect cathode from structural destruction. Nevertheless, it seems difficult to adapt to large-scale applications because of the high cost and complicated production

process [55-60]. Cho et al. used a thin-film coating of high fracture-toughness oxides like ZrO_2, Al_2O_3, TiO_2, and B_2O_3 in order to avoid lattice-constant change and phase transitions during cycling above 4.4 V, resulting in improved capacity retention [61]. Nevertheless, it seems hard and unpractical to adapt in large-scale application because of the high cost and complicated production process [62]. On the other hand, several electrolyte additives have been extensively employed for the development of a stable and protective SEI for the high voltage cycling performance of $LiCoO_2$ cathodes [41, 43] which will be explained in detail in the following sections.

$LiNiO_2$ possess a rhombohedral structure with a trigonal symmetry (space group: *R-3m*) in which Li^+ and Ni^{3+} ions are located along the (1 1 1) plane of a α-$NaFeO_2$ structure with a cell parameter of (a_h=2.9 Å, c_h=14.2 Å) [63]. $LiNiO_2$ has a higher capacity of above 160 mA h g^{-1}, higher energy density with a suitable cycling performance since the amount of Li extraction is ~ 0.55 whereas 0.5 for $LiCoO_2$ [64, 65]. It has similar theoretical capacity of 275 mA h g^{-1} with LCO. However, its synthesis method is quite difficult to fill all Li sites that can be deviate from the regular stoichiometry [66-68]. Furthermore, $LiNiO_2$ undergoes irreversible phase transition, thermal instability, and safety issues even though its low cost and high capacity [29].

$LiMnO_2$ can be synthesized in two forms of layered zigzag-type orthorhombic $LiMnO_2$ with *Pmnm* symmetry and monoclinic $LiMnO_2$ with *C2/m* symmetry that they are both electrochemically active with a theoretical capacity of 285 mA h g^{-1}. It can be prepared by the ion-exchange process and hydrothermal method [37, 69-71]. During charge-discharge cycling between 2.0 - 4.2 V, a transformation into the spinel structure takes place due to its unstable structure [72, 73]. Armstrong and Bruce reported that layered $LiMnO_2$ achieved higher charge capacity (270 mA h g^{-1}), good cycling stability as well as lower cost in comparison with $LiCoO_2$ and $LiMn_2O_4$ [71]. Ceder et al. used Al, Co, Cr,

V, Ti, Mo, Mg, Nb, Zn and Pd as dopants to stabilize the orthorhombic structure of $LiMnO_2$, but still, it showed poor cycling performance [74].

$LiNi_{0.5}Mn_{0.5}O_2$ (NMO) was first reported as an alternative to $LiCoO_2$ owing to its outstanding properties like high theoretical capacity (280 mA h g^{-1}), availability, chemical stability, environmental friendliness, and low cost [75-77]. NMO delivers a reversible capacity of 200 mA h g^{-1} within a voltage range of 2.5 - 4.5 V [37]. NMO cathode shows each benefit of $LiCoO_2$ with a low cost because of the Co-free composition. However, during charging Ni^{2+} oxidizes to Ni^{4+} which is very unstable and reacts with the electrolyte resulting in the capacity decay [78]. Thus, it may still suffer from poor rate capability and cycling performance due to the similar sizes of Li^+ (r = 0.076 nm) and Ni^{2+} (r= 0.069 nm) and mixing of these cations [79, 80]. Many efforts have been made to increase rate capability of NMO cathodes, such as optimizing calcination temperature [81], partial substitution of transition metals [82], surface coating [83, 84] and doping with Li_2TiO_3 [85]. Dahn et al. also reported that the capacity of $Li/Li_xMn_yNi_{1-y}O_2$ cells increased with a decrease of Mn concentration [86].

In 2001, $Li(Ni_{1/3}Co_{1/3}Mn_{1/3})O_2$ (NCM_{111}) was described as a more promising cathode material than $LiCoO_2$, $LiNiO_2$ and $LiMnO_2$ [87]. It has a layered hexagonal structure with *R3m* symmetry showing a practical capacity of 200 mA h g^{-1} in a potential window of 2.5 – 4.6 V [88]. Bruce et al. synthesized $Li(Ni_{1/3}Co_{1/3}Mn_{1/3})O_2$ via a more practical method than the hydroxide and carbonate process achieving high capacity (195 mA h g^{-1} at 1 C rate), superior diffusion may be hindered due to the Li^+ (0.76 Å) and Ni^{2+} (0.69 Å) between the layers which cause irreversible side reactions of highly reactive Ni^{4+} with electrolyte and LIB performance decay at high rates [89, 90]. Therefore, various strategies like nanosizing and surface modifications have been conducted to increase the structural and thermal stability of NCM cathodes [91-94].

1.2.2 Spinel oxides

The crystal structure of spinel LiM_2O_4 (M= Mn, Ti, V) in a ccp array of oxygen anions is given in **Figure 1.9** [1, 29, 95]. $LiMn_2O_4$ (LMO) is a spinel structure with a space group of *Fd3-m* symmetry in which Li^+ occupies the tetrahedral 8a sites, Mn^{4+} fills octahedral 16d sites and O^{2-} locates 32e sites. It was proposed as a cathode material for the first time by Thackeray et al. related to its high energy density, abundance, safety, low cost and environmental friendliness [96-98].

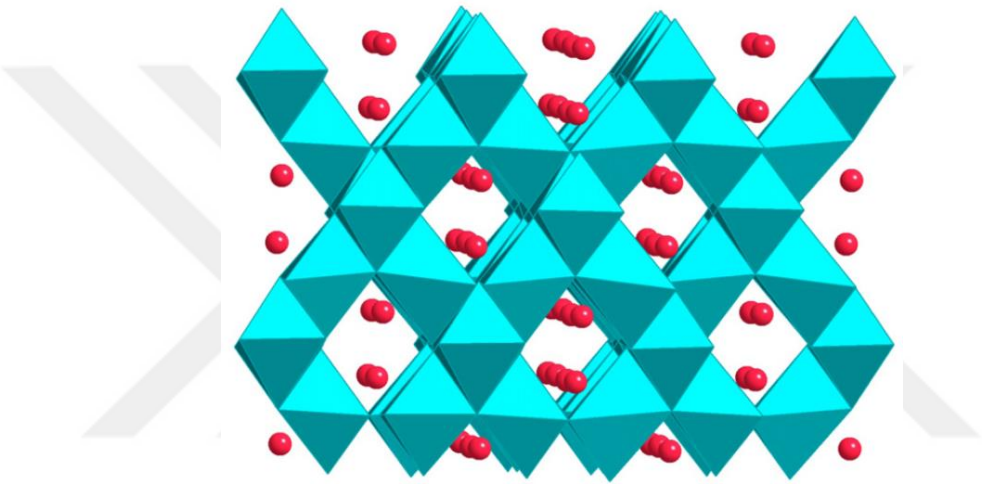

Figure 1.9: Crystal structure of spinel LiM_2O_4 (blue: transition metal ions; red: Li ions) [99].

Nevertheless, LMO cathode suffers from serious capacity fading at high temperature because of the Mn^{2+} dissolution into the electrolyte [100-102] and the irreversible phase transition to distorted tetragonal $Li_2Mn_2O_4$ upon cycling [103, 104]. Substitution with other 3d transition metals ($LiM_xMn_{2-x}O_4$, M=Ti, Cr, Fe, Co, Ni, Cu, Zn) has been carried out to stabilize the spinel crystal structure of LMO, which leads to better electrochemical performance [105-108].

Among other doped spinel oxides $LiM_xMn_{2-x}O_4$, $LiNi_{0.5}Mn_{1.5}O_4$ (LNMO) has received great interest due to its high capacity at a higher voltage plateau ~ 4.7 V with superior cycling stability compared to other cathodes [109]. LNMO spinel crystallizes in two

different structures of stoichiometric ordered with $P4_332$ ($LiNi_{0.5}Mn_{1.5}O_4$) and the non-stoichiometric disordered structure with space group *Fd-3m* ($LiNi_{0.5}Mn_{1.5}O_{4-\delta}$) [110]. $LiNi_{0.5}Mn_{1.5}O_{4-\delta}$ has a face-centered cubic (fcc) structure exhibiting superior capacity retention and rate capability compared to the ordered structure due to the random distribution of Ni/Mn ions in 16d sites [111, 112]. Kim et al. synthesized these two structures of LNMO via a molten-salt process. It was found that $LiNi_{0.5}Mn_{1.5}O_{4-\delta}$ (*Fd-3m*) showed good structural reversibility and excellent electrochemical performance at a high rate [113]. The structure of $LiNi_{0.5}Mn_{1.5}O_{4-\delta}$ showing the diffusion path, is given in **Figure 1.10** [114].

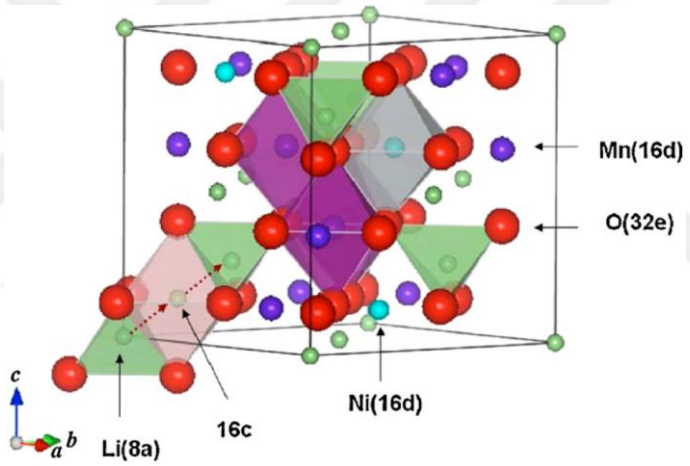

Figure 1.10: The structure of non-stoichiometric spinel $LiNi_{0.5}Mn_{1.5}O_{4-\delta}$ (*Fd-3m*) [114].

LNMO cathode can be produced by ball-milling [115, 116], sol-gel method [117-119], and molten-salt method [120, 121]. Among these methods, ball-milling has several disadvantages such as agglomeration, uncontrollable particle growth and inhomogeneous distribution, whilst the sol-gel process ensures narrow particle size distribution, homogeneity, and good crystallization with smaller particle size and lower synthesis temperature. On the other hand, the molten-salt method is considered as facile to synthesis complex compositions but not practical because of its high calcination temperature and

high energy consumption [122-124]. LNMO cathode delivers a higher energy density of 686 W h kg^{-1} with a high working voltage around 4.7 V and a theoretical capacity of ~ 135 mA h g^{-1} than $LiCoO_2$ (518 W h kg^{-1}), $LiNiO_2$ (630 W h kg^{-1}), $LiMn_2O_4$ (440 W h kg^{-1}), $LiFePO_4$ (495 W h kg^{-1}) and $Li(Ni_{1/3}Co_{1/3}Mn_{1/3})O_2$ (576 W h kg^{-1}) [112, 125, 126]. Nevertheless, there are still some drawbacks, including the dissolution of Mn^{3+} and Ni^{2+} ions, irreversible phase transitions, undesirable side reactions with electrolyte and Jahn-Teller distortion that cause capacity deterioration [127-130]. Thus, various parameters in terms of morphology, cation ordering, doping, surface modification and electrolyte additives have been adjusted to obtain higher capacity retention and rate capability for LNMO cathode [126]. Surface modifications with metal oxides (Al_2O_3, ZnO, MgO, ZrO_2) [131-134] and phosphates (Li_3PO_4, $AlPO_4$, $FePO_4$) [135-137] have been extensively studied to overcome electrolyte oxidation and dissolution of transition metals at high temperatures (~ 55 °C) [138].

1.2.3 Polyanion oxides

Large polyanions ($(XO_4)^{3-}$, X = S, P, As, Mo, W) have been received great interest due to their high redox potential, structural stability and thermal stability, which are also related to the strong covalent bond of oxygen [68, 139]. In olivine structure (*Pnma*) $LiMPO_4$, P occupies tetrahedral sites, whereas M occupies octahedral sites [29]. In 1997, Padhi and Goodenough reported the electrochemical properties of the most used type of $LiFePO_4$ which delithiates to $FePO_4$ [140, 141]. It has a high theoretical capacity of ~ 170 mA h g^{-1} and an appropriate theoretical energy density 580 W h kg^{-1} at 3.45 V vs. Li/Li^+ with a lot of advantages like thermal stability, low cost, safety and low toxicity. Nevertheless, its low electric and ionic conductivity limit its applications in real systems [142-144]. The crystal structure of $LiMPO_4$ compounds is shown in **Figure 1.11**. According to the structure, ½ of the octahedral sites are occupied by M and 1/8 are filled with Li while

oxygen atoms form distorted hexagonal-close packing (hcp) structure [99].

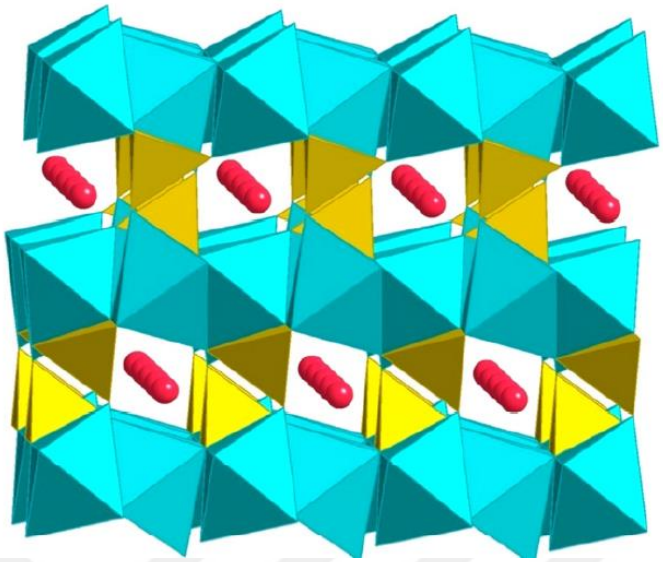

Figure 1.11: Crystal structure of olivine $LiMPO_4$ (blue: M, yellow: P, red: Li) [99].

Polyanions can be prepared by various procedures like solid-state reaction [145-147], sol-gel method [147, 148], solution precipitation [149] and hydrothermal/solvothermal process [147, 150]. Sol-gel synthesis is considered as a most practical route to obtain controllable particle size and uniform distribution with high purity compounds [139]. To solve low conductivity issue of $LiFePO_4$, various approaches have been conducted such as nanosizing [151-153], formation of a conductive layer by conductive carbon [154-156], improving electron transport in the bulk form [157, 158].

$LiMnPO_4$ olivine structure has higher redox potential (4.1 V vs. Li/Li^+) and specific energy density (684 W h kg^{-1}) but lower conductivity and lower rate capability than $LiFePO_4$ related to the Jahn-Teller deformations of Mn^{3+} [159, 160]. In addition, 9.5% volume change of $LiMnPO_4$ takes place during cycling, which is larger compared to $LiFePO_4$ (6.81%) [139]. On the other hand, $LiCoPO_4$ possesses a high operating voltage around 4.8 V vs. Li/Li^+ with a high energy density at 800 W h kg^{-1} which is quite higher

compared to $LiMnPO_4$ [161]. **Figure 1.12** compares the first specific discharge capacity/voltage curves of different olivine compounds [159]. However, during delithiation, thermally unstable phases of Li_zCoPO_4 (z = 0.6) and $CoPO_4$ are formed that may be susceptible to decompose above 100 °C [162]. Therefore, the structural deterioration of $LiCoPO_4$ and oxidation of electrolyte limits its use for the commercial purpose [159].

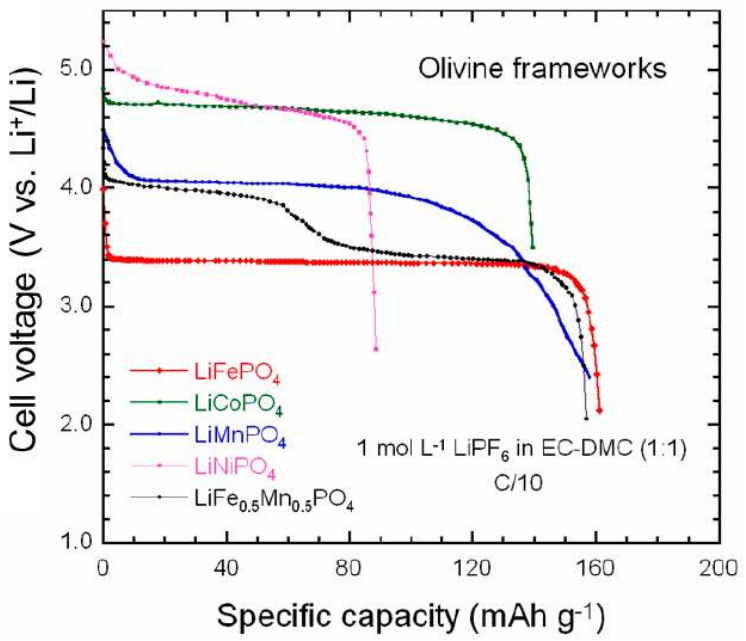

Figure 1.12: First discharge curves of $LiMPO_4$ and $LiFe_{0.5}Mn_{0.4}PO_4$ cathode [159].

Consequently, **Table 1.1** compares both specific and volumetric capacity as well as average voltages of three type of cathode compounds.

Table 1.1: Summary of electrochemical performances for layered, spinel and olivine cathodes [68].

Crystal structure	Compound	Specific capacity (theo./exp.) $mAhg^{-1}$	Volumetric capacity (theo./exp.) $mAhcm^{-3}$	Average voltage (V)	Level of development
Layered	$LiCoO_2$	274/148	1363/550	3.8	Commercial
	$LiNiO_2$	275/150	1280	3.8	Research
	$LiMnO_2$	285/140	1148	3.3	Research
	$LiNi_{0.33}Mn_{0.33}Co_{0.33}O_2$	280/160	1333/600	3.7	Commercial
	$LiNi_{0.8}Co_{0.15}Al_{0.05}O_2$	279/199	1284/700	3.7	Commercial
Spinel	$LiMn_2O_4$	148/120	596	4.1	Commercial
	$LiCo_2O_4$	142/84	704	4.0	Research
Olivine	$LiFePO_4$	170/165	589	3.4	Commercial
	$LiMnPO_4$	171/168	567	3.8	Research
	$LiCoPO_4$	167/129	510	4.2	Research

1.3 Anode Materials

Lithium metal was the best choice as anode material due to its high theoretical capacity (3860 mA h g^{-1}, 2061 mA h cm^{-3}), low density (0.59 g cm^{-3}) and the most negative reduction potential (−3.04 V vs. SHE). However, dendritic growth of lithium upon cycles, low coulombic efficiency (CE) and potential fire hazard have limited the real application of lithium metal anode [163, 164]. Therefore, a "locking-chair" concept has been developed in which ions are spontaneously discharged from the intercalation structure and the reverse reaction takes place for charging [165]. Graphite has been commercially

used anode since the deposition of Li and the dendritic growth are avoided due to the layered structure of graphite. [166, 167]. **Figure 1.13** compares lithium metal and graphite as anodes for LIBs.

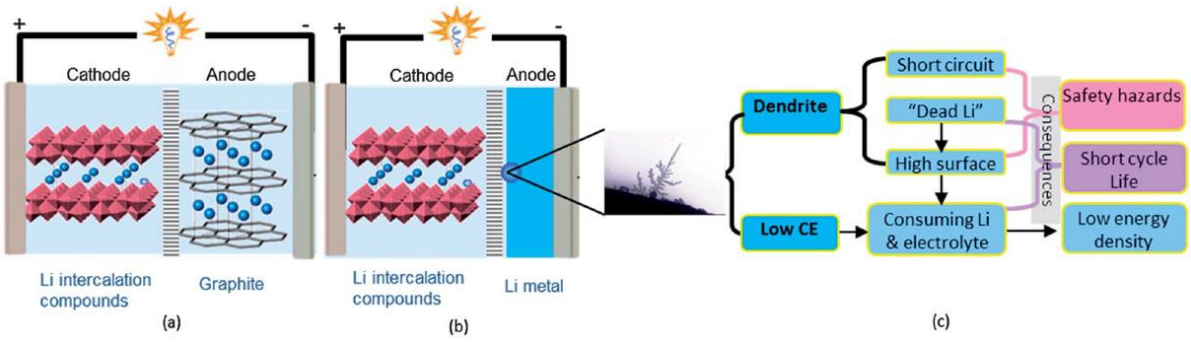

Figure 1.13: Schematic diagram of (a) LIB, (b) Li metal batteries, (c) main problems related to dendrites and low Coulombic efficiency [163].

Graphite suffers from its low power density because each six carbon atoms can take just one Li atom with the formation of LiC_6, which results in a low lithium-ion diffusion rate (10^{-12} – 10^{-6} cm^2 s^{-1}) [168]. Various types of anode materials like carbonaceous, alloys, transition metal oxides, silicon-based, tin-based and titanium-based compounds have been investigated because of the demand for high power and energy density [169-171]. **Table 1.2** shows the advantages and disadvantages of anode types.

Table 1.2: Advantages and disadvantages of anode types [169, 172].

Material	Advantages	Disadvantages
Carbon based	High electronic conductivity Good hierarchical structure Abundant and low-cost	Low specific capacity High irreversible capacity Low rate capability Safety problem
Alloys	High specific capacity (400-2300 mA h g^{-1}) High energy density Safety	Low electronic conductivity Large volume change (100%)
Transition metal oxides (CuO, NiO, Fe_3O_4 etc.)	High specific capacity (600-1000 mA h g^{-1}) Good stability	Low coulombic efficiency Large potential hysteresis Unstable SEI Poor cycling
Silicon	Highest specific capacity (3579 mA h g^{-1}) Rich, low-cost, clean	High irreversible capacity Poor cycling Large volume change (300%)
Tin	Good electronic conductivity High specific capacity (990 mA h g^{-1}) Safety, low-cost	Poor cycling

Therefore, an efficient anode material must:

- contain elements with low atomic weight
- high specific surface area to diffuse high amount of Li ion
- large pore size
- low volume change upon cycling
- deliver stable cycling performance with high capacity
- display a voltage close to the lithium metal for high voltage operations
- not chemically react with the electrolyte
- cheap, environmentally benign, safe
- have good electrical and ionic conductivity [173, 174].

Figure 1.14 gives an overview of anode materials with their redox potentials vs. Li/Li^+ and specific capacity required to improve energy density.

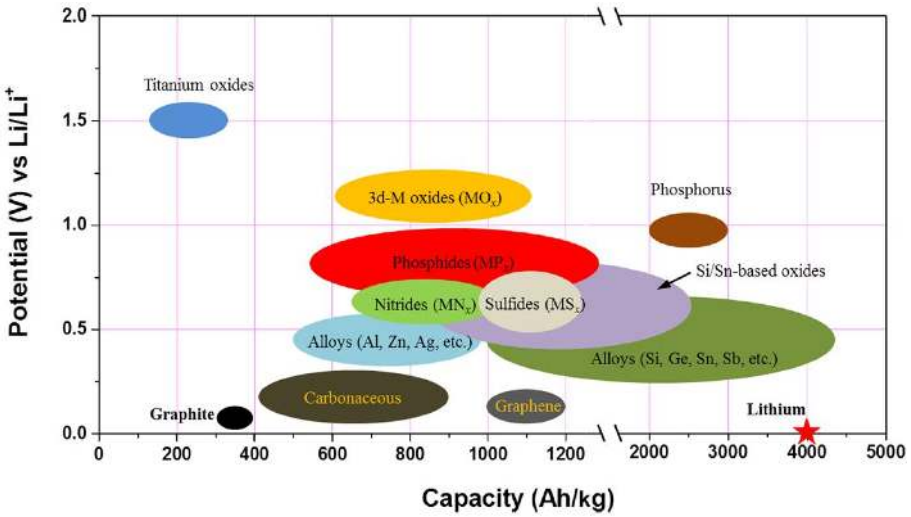

Figure 1.14: Different anode materials for high energy density LIBs [175].

1.3.1 Carbon-based

Carbon-based materials have been commercially used as anodes because of their dimensional stability, high capacity and more electronegative potentials, low cost and availability than most metal oxides, chalcogenides and polymers [46]. The reversible reaction that occurred between Li-C during the intercalation is given as:

$$Li_xC_n \leftrightarrow xLi^+ + xe^- + C_n\,(n=6) \qquad \textbf{(1.4)}$$

Carbonaceous materials can be categorized into two types as graphitic carbon (soft carbon) and non-graphitic carbon (hard carbon). Graphitic carbon can deliver a theoretical capacity of 372 mA h g^{-1} with the formation of Li_xC_6, whereas the non-graphitic one can adsorb less Li [169, 176]. Dahn et al. investigated Li-ion intercalation mechanism for carbonaceous materials for the first time [177]. The strong sp^2 bonds of carbon atoms are the reason for the large surface area, high charge mobility, high electrochemical, mechanical properties of graphene (**Figure 1.15**). The Li-ion storage capacity could be enhanced because of the multiple layers of graphene via ameliorating the infiltration of

electrolyte and shortening the Li-ion diffusion distance [175, 178].

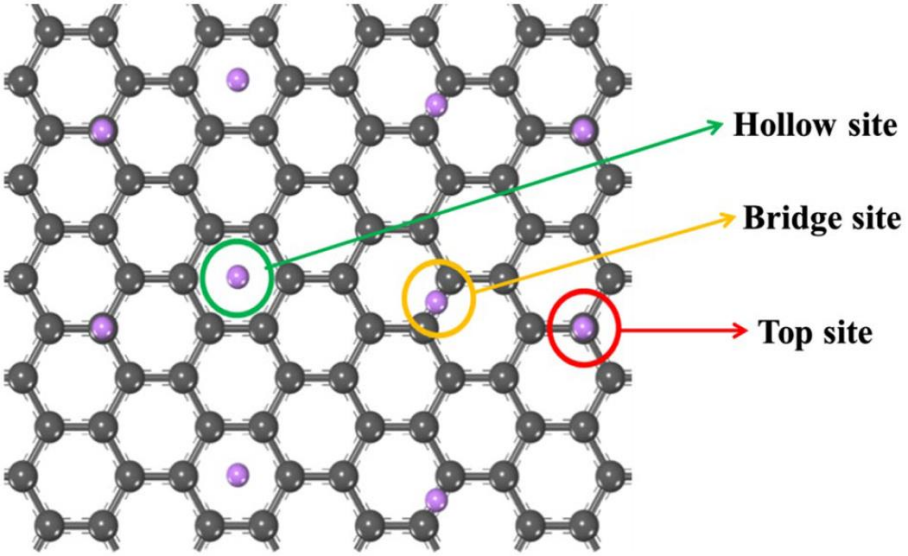

Figure 1.15: Schematic illustration of a graphene structure and the potential sites for Li storage [175].

Amorphous soft carbon can be produced by performing a pyrolysis of petroleum pitch around 1500 °C which leads to weak crosslinking between the layers, whilst hard carbon can be prepared by a pyrolysis of chars or glassy carbon at 2500-3000 °C resulting in high mechanical strength. Therefore, hard carbon possesses a high specific capacity around 200-600 mA h g^{-1} related to the value of x=1.2-5 in Li_xC_6. The crystal structure and the defects of carbon-based material determine the diffusion of Li-ion [176, 179]. Various carbon nanomaterials like carbon nanotubes (CNTs) (1D) [180], carbon nanofibers (1D) [181], graphene nanosheets (2D) [182] and porous carbon sphere (3D) [183] have been studied as anodes to achieve superior properties by increasing the surface to volume ratio [176].

CNTs have been received great attention for their high electrical conductivity (10^2 to 10^6 S cm^{-1}), thermal conductivity (6000 W m^{-1} K^{-1}) with a negligible thermal expansion,

mechanical properties due to the presence of sp^2 carbon-carbon bonds. Lithium ions can accommodate into stable sites on the nanotube surface, inside nanotubes, as well as in the interstitial sites of bundles [184, 185]. CNTs anodes show three times the higher specific capacity (~1116 mA h g^{-1}) compared to the conventional graphite anode. In addition, the specific energy density could be enhanced by over 50 % [180]. CNTs have been used as a conductive additive instead of carbon black and graphite because of their high aspect ratio [186-188]. Unfortunately, the high production cost and complicated purification process limit their commercial use [189].

Graphene has very high mechanical strength, high electrical conductivity and thermal conductivity (~3000 W m^{-1} K^{-1}) and high electron mobility (2.5×10^5 cm^2 V^{-1} s^{-1}) and thereby, ensures more electrochemical reaction due to its high specific surface area than CNTs. The synthesis method for graphene is simpler to restack together compared to CNTs [190]. Yoo et al. reported that the specific capacity of graphene nanosheets was found 540 mA h g^{-1}. Additionally, this value was further increased above 730 mA h g^{-1} by the addition of CNTs and fullerene (C_{60}) within the graphene nanosheets due to the layer spacing between graphene sheets [191]. The incorporation of metal oxides like TiO_2 [192-194], SnO_2 [195-197], Fe_3O_4 [198-200], Mn_3O_4 [201, 202], CuO [203]and NiO [204, 205] into graphene nanosheets have been employed to eliminate the irreversible capacity loss during cycling by using their synergistic effects [176]. Zhou et al. evaluated that graphene nanosheets has various benefits that can diminish the volume change and agglomeration of magnetite particles, provide a large surface area for the dispersion of particles and act as a conductive agent to improve electron transport. Therefore, Fe_3O_4/graphene nanosheet composite anode achieved high reversible capacity, good cycling stability and superior rate capability [200]. Nevertheless, there are several challenges that require to be solved, such as low density and restacking of graphene sheets

leading low volumetric density. In addition, controlling the growth of defects and achieving high conductivity with a large surface at the same time have been considered very problematic [169].

Porous carbon structures show lower irreversible capacity loss compared to CNTs and graphene nanosheets. They can be synthesized by template-assisted synthetic routes or pyrolysis of bulk materials. There is three types of porous structures depending on the pore size as microporous (< 2 nm), mesoporous (2-50 nm) and microporous (> 50 nm) [176]. Zhou et al. synthesized ordered mesoporous carbon from silica template and achieved the highest reversible capacity around 800-1100 mA h g^{-1} with a good cycling performance for the first time [206]. In another study, Zeng et al. combined synergistic effects of silica and ordered mesoporous carbon. It was found that as-fabricated Si/SiO_2-ordered mesoporous carbon delivered a high reversible capacity of 958 mA h g^{-1} at 0.2 A g^{-1} after 100 cycles and remained its capacity of 459 mA h g^{-1} at 2 A g^{-1} after 1000 cycle owing to a uniform size and the large volume of pores [207].

1.3.2 Transition metal oxides

Transition metal oxides have been considered as promising anode materials because of their high specific capacity. However, there are several drawbacks such as low electronic conductivity, agglomeration of particles, large volume change upon charge/discharge, which causes severe capacity fading and poor rate capability performance [208]. The conversion mechanism takes place as follows:

$$MO + xLi^+ + xe^- \leftrightarrow Li_2O + M \text{ (M= Fe, Co, Ni, Cu)} \quad \textbf{(1.5)}$$

The forward reaction is thermodynamically stable, resulting in a high theoretical capacity, whereas the formation of Li^+ from Li_2O is unstable that can be accelerated by the formed metal nanoparticles during the first discharge process. Additionally, there are other

disadvantages like low electronic conductivity and low Li-ion diffusion coefficient that need to be resolved by developing appropriate nanostructures or using different combinations [176, 209]. Tarascon's group used Fe_3O_4, NiO, Co_3O_4 nanoparticles as anode materials for the first time and they reported that the occurred reaction was different from the regular insertion/extraction mechanism by the formation and decomposition of Li_2O and the redox of nanoparticles (**Figure 1.16**) [175, 210].

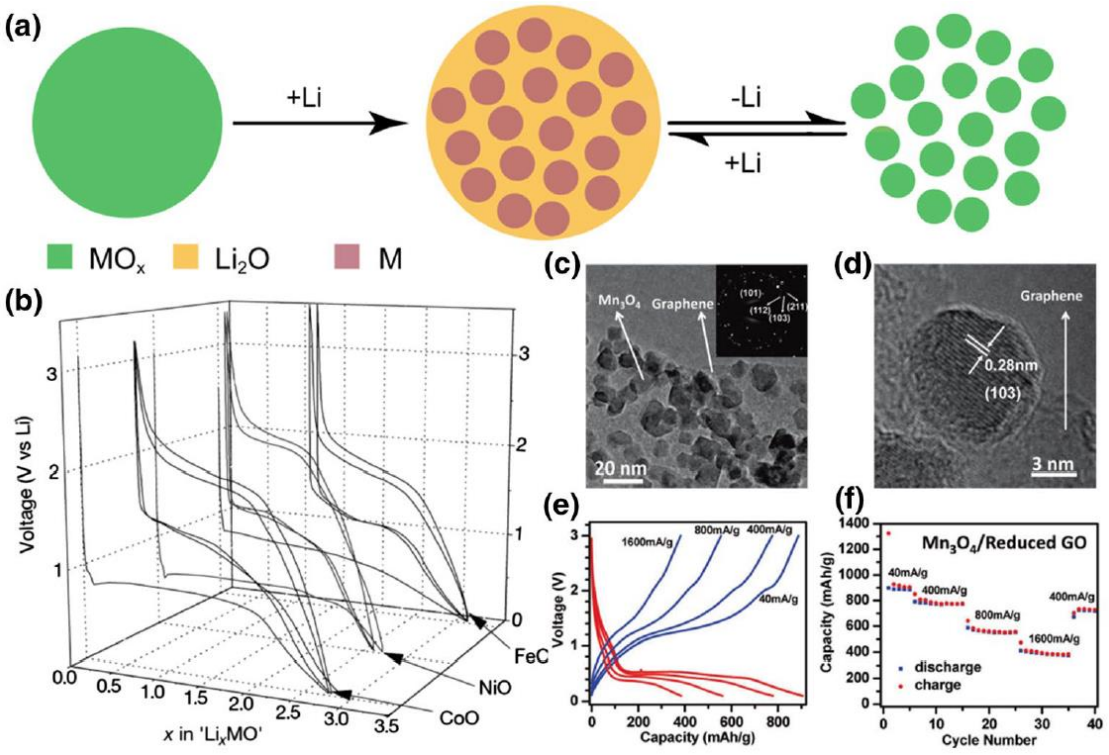

Figure 1.16: (a) Conversion MO anodes, (b) voltage composition profile for various MO/Li cells cycled between 0.01 and 3 V at a rate of C/5, (c) TEM image of Mn_3O_4/reduced graphene oxide (RGO), (d) TEM image of an individual Mn_3O_4 nanoparticle on RGO, (e, f) charge/discharge curves, (e) capacity retention (f) of Mn_3O_4/RGO at various current densities [175].

Mn_3O_4 anode exhibits a high theoretical capacity of 936 mA h g^{-1} but very a low capacity around 400 mA h g^{-1} even with Co doping because of its extremely low electrical

conductivity (~10^{-7}–10^{-8} S cm^{-1}). Additionally, it suffers from fast capacity fading and low-rate capability due to the large volume change during Li insertion/extraction [211-213]. Therefore, RGO has been extensively used as a conductive agent to improve the electrical conductivity and electrochemical performance of Mn_3O_4 anode with regard to its high electrical conductivity, mechanical flexibility, chemical stability and high specific surface area (~2360 m^2 g^{-1}) [208, 214-217]. Wang et al. fabricated Mn_3O_4/RGO nanocomposite, which achieved a high specific capacity of 900 mA h g^{-1} with good rate capability and cycling stability, as shown in **Figure 1.16 (e, f)** [214].

Co_3O_4 can theoretically deliver a capacity of ~890 mA h g^{-1} due to its good chemical and physical properties [218]. Similarly, Co_3O_4/RGO composite anodes have been fabricated to avoid large volume expansion during charge/discharge process [217, 219, 220]. Wu et al. synthesized Co_3O_4 nanoparticles in the range of 10-30 nm and homogenously anchored them on graphene sheets. It was found that Co_3O_4/graphene nanocomposite showed a high reversible capacity of ~ 935 mA h g^{-1} after 30 cycles, good cycling stability, high coulombic efficiency and good rate capability [221].

Iron oxides such as hematite (α-Fe_2O_3) and magnetite (Fe_3O_4) have been used as anode materials due to their low cost, environmentally friendliness, abundance high corrosion resistance and high theoretical capacity of 1007 and 926 mA h g^{-1}, respectively [168, 222]. α-Fe_2O_3 is the most thermodynamically stable one because of its electroactivity and biocompatibility. It can be prepared in a variety of nanostructures like nanocrystals, nanocubes, nanowires, nanorods, nanotubes, nanodisc and hollow via a hydrothermal process [223-225]. A reversible conversion mechanism between Li ions and iron oxide takes place with the dispersion of Fe nanoclusters in a Li_2O matrix as follows:

$$Fe_2O_3 + 6Li^+ + 6e^- \leftrightarrow 3Li_2O + 2Fe \quad \textbf{(1.6)}$$

The forward reaction is thermodynamically stable, whereas the reverse one is considered as unfeasible because of the extraction of Li^+ from Li_2O matrix [226]. Furthermore, many efforts have been tried to overcome low conductivity, low Li-ion diffusion rate and large volume change issues to improve the cycling performance of iron oxide-based anodes [227, 228]. Kim et al. obtained α-Fe_2O_3 nanocapsules with a uniform diameter of 14 nm, length of 65 nm and shell thickness of 5 nm using a wrap-bake-peel process. A first specific capacity of 888 mA h g^{-1} with a capacity retention of 84% after 30 cycles was achieved owing to the hollow nanostructure. They also revealed that the thin shell led to the elimination of the large volume change and the reduction of the Li-ion diffusion path [229]. Similarly, Narsimulu et al. synthesized 3D multi-channeled spindle-like α-Fe_2O_3 nanostructures with controlled porosity via solvothermal technique. They reported that the novel hematite nanostructure anode fabricated at 180 °C showed a high discharge capacity (965 mA h g^{-1}) after 150 cycles at a rate of 500 mA g^{-1} and good rate capability due to its porous structure [230]. In another study, their group further deposited α-Fe_2O_3 nanostructured onto carbon cloth (CC) to obtain a binder-free anode. It was found that the flexible Fe_2O_3/CC anode delivered a high reversible capacity of 1350 mA h g^{-1} at a current density of 1000 mA g^{-1} after 100 cycles with outstanding durability owing to the high mass loading on CC [231]. A pioneer work of Zhu et al. was carried out to integrate Fe_2O_3 with graphene-based materials. RGO/Fe_2O_3 nanocomposite anode was synthesized by a two-step process of homogenous precipitation and subsequent reduction of graphite oxide (GO) with hydrazine under microwave irradiation. More importantly, they suggested that the developed synthesis method could be used for large-scale fabrication of all metal oxide/RGO nanocomposite anodes leading to high-performance LIBs [232].

Magnetite (Fe_3O_4) contained both Fe^{2+} and Fe^{3+} was reported by Tarascon et al. as an anode material for the first time [233]. Nanostructured materials are susceptible to

agglomerate and to pulverize again after long cycles, which results in a deterioration of electrochemical performance [234]. Therefore, carbonaceous materials have been effectively used to prevent volume-induced stresses by using 3D porous structures. Kopuklu et al. developed a 3D partially reduced graphite oxide aerogel supported Fe_3O_4 anode to improve the number of reachable active sites and Li^+ ion diffusion pathway. The reversible capacity was found 2151 mA h g^{-1} over 100 cycles at a rate of 0.5 A g^{-1}. After 600 cycles, the novel anode still achieved long cycle life because of the confinement of Fe_3O_4 nanoparticles (**Figure 1.17**) [235].

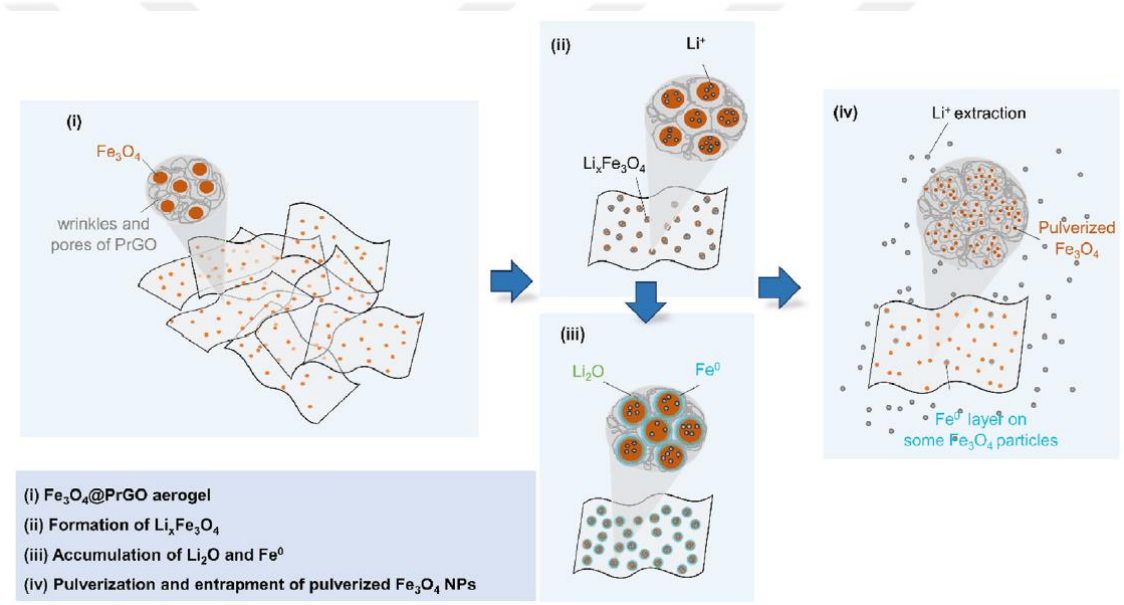

Figure 1.17: Long-term performance enhancement mechanism of the Fe_3O_4@PrGO anode [235].

1.3.3 Tin-based

Since the first development in 1997 by Fuji Photo film corporation, tin oxide (SnO_2) has been received great interest as a promising anode material due to its high theoretical capacity of 790 mA h g^{-1} and low working potential around 0.6 V vs. Li/Li^+ [236-238]. The electrochemical reaction mechanism in SnO_2/Li half-cells occurs as: [239]

$$SnO_2 + 4Li^+ + 4e^- \rightarrow Sn + 2Li_2O \quad \textbf{(1.7)}$$

$$Sn + xLi^+ + xe^- \leftrightarrow Li_xSn\ (0 \leq x \leq 4.4) \quad \textbf{(1.8)}$$

However, above 200% volume expansion/contraction takes place during cycling, which causes degradation of electrodes, loss of contact with the current collector, inhibition of Li-ion transport, as well as high initial capacity loss [168, 240, 241]. Thus, considerable efforts have been focused on preventing volume change which leads to poor cycling performance and high irreversible capacity loss [242, 243]. **Table 1.3** compares tin-based materials with graphite in terms of LIB characteristics [244].

Table 1.3: Comparison of Sn-based anodes with graphite [16, 244].

Material	Potential (V vs. Li/Li^+)	Active phase	Space group	Gravimetric capacity (mA h g-1)	Volumetric Capacity (mA h mL^{-1})	Volume change (%)
Graphite	0.05	LiC_6	-	372	804	10
Sn	0.4	$Li_{4.4}Sn$	F_{23}	993	2562	258
SnO_2	0.6	$Li_{4.4}Sn$	F_{23}	782	5438	252
SnS	0.6	$Li_{4.4}Sn$	F_{23}	782	4083	-
SnS_2	0.6	$Li_{4.4}Sn$	F_{23}	645	2902	-

To address these issues, the dispersion of Sn-based nanostructures (nanofibers, thin films, hollow) onto flexible and conductive matrix like amorphous porous carbon, ordered mesoporous carbon, CNTs and graphene have been carried out by increasing electrical conductivity (**Figure 1.18**) [209, 245-249]. Tian et al. prepared 2D hollow SnO_2 nanocomposite via the ultrathin 2D temple-assisted hydrothermal method and subsequent carbonization process. It was found that the as-synthesized composite anode exhibited

specific capacities of 707.8 and 483.2 mA h g^{-1} after 100 cycles at current densities of 200 and 1000 mA g^{-1}, respectively achieving superior cycling performance and rate capability [250]. In another study, Yao et al. synthesized 2D carbon-coated sandwich-like mesoporous SnO_2/graphene/mesoporous SnO_2 nanosheets to accelerate Li^+ diffusion, to avoid large volume changes as well as to increase electrical conductivity by using both carbon coating and graphene. The novel anode showed outstanding reversibility, high rate capability and long cycling performance [246].

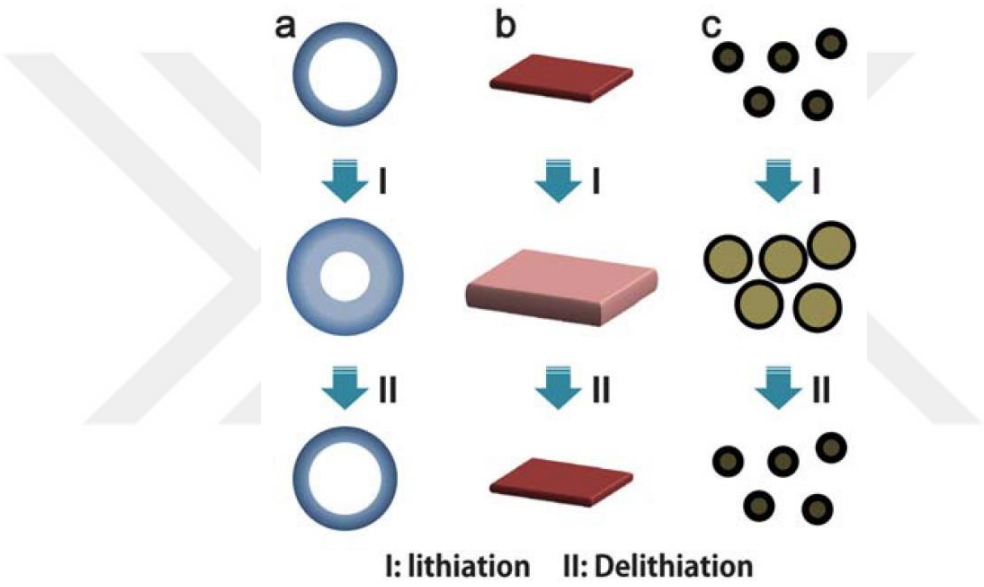

Figure 1.18: Schematic illustration of several strategies to avoid the pulverization issue of SnO_2 anode (a) hollow structure, (b) 2D nanosheet, (c) amorphous carbon coating [209].

Tin sulfide (SnS_2) possesses a layered CdI_2 structure in which Sn atoms are sandwiched between two layers with hcp array of S atoms. Luo and coworkers fabricated 2D porous graphene/SnS_2 nanocomposite through a solution approach followed by a chemical vapor deposition (CVD) method. The as-synthesized anode delivered its first discharge capacity of 650 mA h g^{-1} and superior rate capability (30 mA h g^{-1} at 6400 mA g^{-1}) [251]. In a later study, SnS_2/graphene nanocomposite was prepared by a simple one-pot approach at

moderate conditions that could be adapted to large-scale production for high performance LIBs [252].

The electrochemical performance of Sn anodes can be enhanced by obtaining nanoparticles below 10 nm with uniform particle size distribution for longer cycling stability [253]. Additionally, Sn nanoparticles should be embedded or encapsulated homogenously in a carbon-based material to ensure mechanical stability of the composite anode. Therefore, Xu et al. synthesized nano-Sn/C composite by a simple aerosol spray pyrolysis method. The outstanding performance was achieved due to the uniform dispersion of Sn nanoparticles within the carbon matrix as mechanical support by preventing agglomeration and ensuring continuous Li^+ diffusion length. They also indicated that the aerosol spray pyrolysis technique could be easily adapted to the real applications for LIBs [254]. Also, Qin et al. developed a simple and scalable in-situ CVD method to produce 3D porous graphene networks anchored with Sn nanoparticles. The new anode showed the best rate capability and the longest cycling performance even at higher rates compared to other reported Sn-based anodes [255]. On the other hand, Sn/CNTs rooted in graphene was proposed as an effective approach eliminating graphene agglomeration which resulted in high electrical conductivity, mechanical integrity, high Li^+ diffusion pathway through the buffering effect of both CNT and graphene nanosheets [256].

Another approach to hinder huge volume change of Sn-based compounds can be given as integration with electrochemically inert materials like Li_2O and SiO_2. SnO_2/SiO_2 composites can be fabricated by various methods, including sol-gel, hydrothermal, aqueous solutions or electrostatic spray deposition. Alloying with inert materials could cause capacity decay even though the cycling stability would be improved [244].

In 2005, Sony introduced a nanostructured Sn-Co-C based anode with high volumetric capacity than conventional cells. However, their anode could not be commercialized because of the high cost and toxicity of Co. After that various Sn-Fe-C composites were developed with regard to their lower price and superior capacity retention and rate capability. Nevertheless, Sn-Fe-C anodes suffered from large irreversible capacity loss and low coulombic efficiency due to the side reactions. To overcome these issues, fluoroethylene carbonate (FEC) was introduced into the commercial $LiPF_6$ electrolyte to improve cycling stability [16].

1.3.4 Titanium-based

Among other transition metal oxides, titanium (Ti) -based materials have drawn great interest as an anode due to their exceptional features such as low cost, low toxicity, safety, chemical stability, small volume change (< 4%) during repeated discharge/charge, long cycle life, and high power density. Additionally, their operation voltage is above 0.8 V vs. Li^+/Li where a stable SEI is not necessary [28, 257-259]. However, there are some drawbacks like low intrinsic electrical conductivity (10^{-12} - 10^{-7} S cm^{-1}), low Li^+ diffusion coefficient (10^{-15} – 10^{-9} cm^2 s), low theoretical capacity (175-330 mA h g^{-1}) and poor rate capability due to the large polarization at high rates [260-264].

Titanium dioxide (TiO_2) is the most common form of Ti-based materials, including various polymorphs like anatase, rutile, brookite and TiO_2-(B) bronze (**Figure 1.19**) [265]. Among them, the electrochemical performance of brookite has limited due to its complicated synthesis process [266].

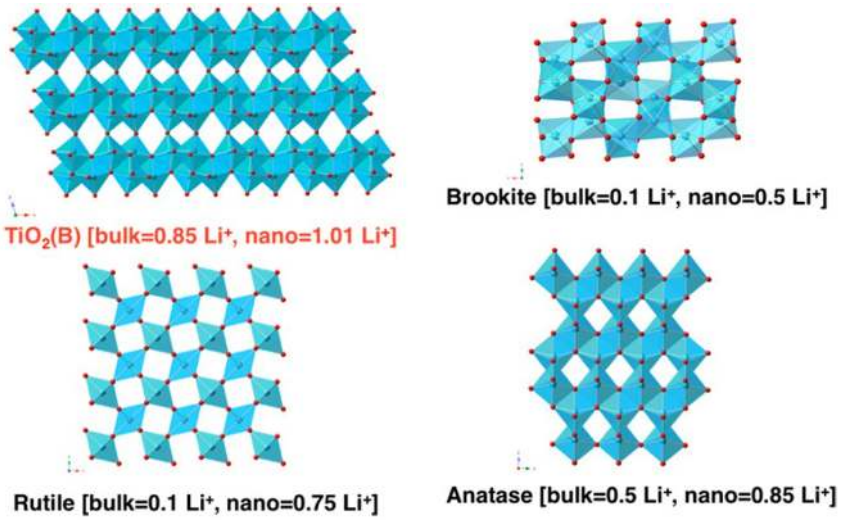

Figure 1.19: Polymorphs of TiO_2 [265].

The reversible Li-ion redox reaction of TiO_2 compounds occurs as follows [267]:

$$TiO_2 + xLi^+ + xe^- \leftrightarrow Li_xTiO_2 \quad \textbf{(1.9)}$$

in which x depends on the polymorph type, morphology and crystallographic orientation [172]. As shown in **Figure 1.19**, rutile TiO_2 is the most thermodynamically stable at the bulk form, which has tetragonal symmetry with a space group of $P4_2/mnm$ [268]. Wang et al. reported that mesoporous rutile could accommodate > 0.7 Li^+ with an initial specific capacity of 235 mA h g^{-1} at a current density of C/5 in 1.0-3.0 V, delivering a reversible capacity of 185 mA h g^{-1} with the transport of 0.55 Li^+ [269]. The capacity can be kinetically restricted, that higher temperatures are required for full Li^+ loading [209]. As given in **Figure 1.20**, during the first lithium insertion, for $0 < x < 0.5$ the structure of rutile TiO_2 transforms from tetragonal to monoclinic symmetry which is very similar to the first structure. On the other hand, for the Li concentration of $0.5 < x < 0.85$, the monoclinic phase transforms to the layered monoclinic structure with *P2/m* symmetry that may increase the irreversible capacity loss [270].

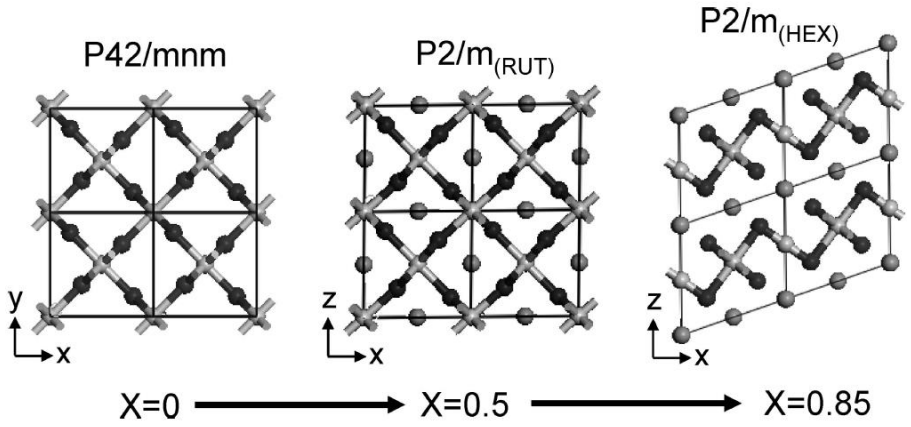

Figure 1.20: Structural transformation of nanoneedle rutile TiO_2 upon lithiation (Li_xTiO_2) [270].

Hollow nanostructures have been focused on to shorten the ionic/electronic diffusion pathway and to provide an extra free space for good structural integrity. Therefore, Jiao et al. synthesized Sn-doped rutile TiO_2 hollow nanocrystals via a temple-free hydrothermal route to improve capacity retention and rate capability. Tin was chosen as a dopant because of its much high theoretical capacity of SnO_2 (~790 mA h g^{-1}) than the rutile TiO_2 [271].

Anatase TiO_2 (tetragonal, $I4_1/mnm$) is the most studied form in the literature because of its high electroactivity that the diffusion of lithium ions takes place between octahedral interstitial sites [272]. During lithium insertion, the structure of anatase TiO_2 undergoes phase transformation into the mixture of tetragonal $Li_{0.01}TiO_2$ and orthorhombic $Li_{0.6}TiO_2$ form with a volume expansion of ~4% [273]. In addition, it can deliver a higher specific capacity even in the bulk form compared to the rutile phase [28]. However, its structure transforms irreversibly to the rutile phase above 600 °C [274]. Faster lithium insertion/extraction occurs when the surface density of (001) exposed facets increases. Therefore, Chen et al. synthesized hierarchical spheres self-assembled from ultrathin anatase TiO_2 to obtain 100% exposed (001) facets which provide a short Li-ion diffusion

pathway [275]. Nanostructuring has been extensively employed to improve both ionic and electrical conductivity by shortening the diffusion length. The reversible capacity of 200 mA h g^{-1} can be achieved by using nanoparticles below 100 nm due to the improved lithium ion reactivity [260, 276].

TiO_2(B) has a monoclinic *C2/m* structure containing an open channel in which 8 Ti sites and 10 Li^+ sites are filled [265]. Zukalova et al. evaluated that the open structure of TiO_2(B) results in a fast Li^+ transport through pseudocapacitive process [277]. Therefore, it delivers two times higher theoretical specific capacity around 335 mA h g^{-1} (1.01 Li^+ per Ti) than rutile, anatase and lithium titanate ($Li_4Ti_5O_{12}$). However, its low intrinsic electronic conductivity has limited the pseudocapacitive behaviour of TiO_2(B) [278]. Armstrong et al. synthesized TiO_2(B) nanowires (20-40 nm) through a simple hydrothermal reaction between sodium hydroxide, NaOH and anatase TiO_2. They achieved an outstanding specific capacity of 305 mA h g^{-1} (at 1.6 V vs. Li^+/Li), superior capacity retention and rate capability [279, 280]. In a later study, they constructed a LIB cell consisting of a TiO_2(B) nanowire as an anode, $LiFePO_4$ or $LiNi_{0.5}Mn_{1.5}O_4$ as cathodes using a gel polymer electrolyte. It was found that the average cell voltages of ~ 1 and 3 V were acquired with excellent cycling stability, rate capability and capacity retention of 80% [281].

TiO_2 can be synthesized by various processes like sol-gel [282, 283], hydrothermal [284, 285], solvothermal [275, 286], temple-assisted [287] and anodic oxidation methods [288]. Among them, sol-gel is one of the most utilized ones with the formation of various phases [289, 290]. For the synthesis of TiO_2-B nanostructures, hydrothermal method has been preferred to obtain various morphologies (nanotubes, nanowires, nanofibers) because of the determination of parameters like temperature, time, base solution and subsequent heat treatment [291-293].

Nanostructuring is considered as an effective strategy to reduce Li^+ diffusion length, providing more efficient interaction with lithium ions. Nevertheless, the formation of a conductive network using carbonaceous materials (CNTs, mesoporous carbon, graphene) have been widely used to decrease the charge transfer resistance, to improve Li^+ ion diffusion and electron transport, to reduce huge volume change upon cycling as well as pulverization of active materials [172, 272]. Chen et al. prepared carbon supported hierarchical structures from ultrathin anatase TiO_2 nanosheets via a modified solvothermal process. Consequently, they achieved a high reversible specific capacity of 110 mA h g^{-1} at high current rate and good cycling stability owing to the improved structural stability [294]. In another study, Chen et al. synthesized graphene-wrapped TiO_2 hollow structures through electrostatic interaction followed by a thermal treatment that the hybrid anode exhibited improved LIB performance compared to the pure TiO_2 [295]. CNTs are beneficial to provide electrons by forming Ti-C bond, thereby facilitating Li^+ ion transfer [296]. Wang et al. prepared a mesoporous CNT/anataseTiO_2-C nanocables below 8 nm by a simple and green one-pot hydrothermal technique. The novel nanostructured anode showed superior cycling stability, extraordinary rate capability with a capacity retention of 87% after 2000 cycle at 50 C-rate owing to the small particle size, improved electronic conductivity, mesoporous structure and high specific surface area [297].

The lithium insertion/extraction behaviour of amorphous TiO_2 was investigated for the first time by Wagemaker and coworkers. They revealed that the highly disordered structure resulted in an exceptional initial discharge capacity (819 mA h g^{-1}) and very high reversible capacity even at high rates (10C) [298]. Therefore, Li et al. used nitrogen-doped graphene (N-G) as conductive support to further enhance pseudocapacitance behaviour due to the defective surface of N-G (**Figure 1.21**). The as-prepared amorphous

TiO_2/N-G showed high reversible capacity at 182.7 mA h g^{-1} after 100 cycles at 10 C [299].

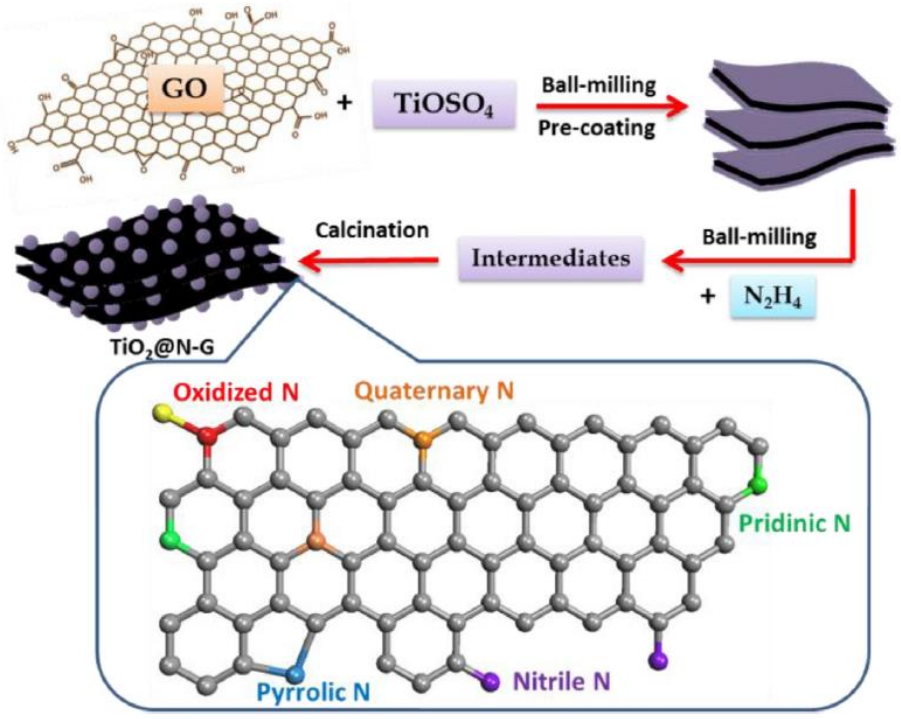

Figure 1.21: Schematic diagram of the preparation process of the TiO_2/N-G [299].

Spinel lithium titanate ($Li_4Ti_5O_{12}$) has been extensively investigated as an alternative anode material because of its safety and long lifetime. It shows a higher lithium insertion potential (1.55 V vs. Li^+/Li) compared to graphite delivering a theoretical capacity of ~175 mA h g^{-1} with a small volume change (~ 0.2-0.3%) upon cycling [300-302]. In addition, $Li_4Ti_5O_{12}$ has been regarded as a zero-strain insertion material that the 1/6 replacement of Ti with Li results in similar lattice parameters. Consequently, outstanding reversibility toward lithium insertion/extraction occurs [303, 304]. As shown in **Figure 1.22**, $Li_4Ti_5O_{12}$ has a spinel cubic structure (fcc) with the *Fd3-m* space group in which lithium ions accommodate in tetrahedral 8a sites and 1/6 octahedral 16d sites with a ratio of Li/Ti=1.5. Tetravalent Ti^{4+} ions occupy the octahedral 16d sites, whereas O^{2-} ions are located at 32e sites [305]. The phase transition from spinel to rock-salt takes place during

the electrochemical reaction as [306]:

$$\text{(Spinel) } Li_4Ti_5O_{12} + 3Li^+ + 3e^- \leftrightarrow 2Li_7Ti_5O_{12} \text{ (rock-salt)} \quad \textbf{(1.10)}$$

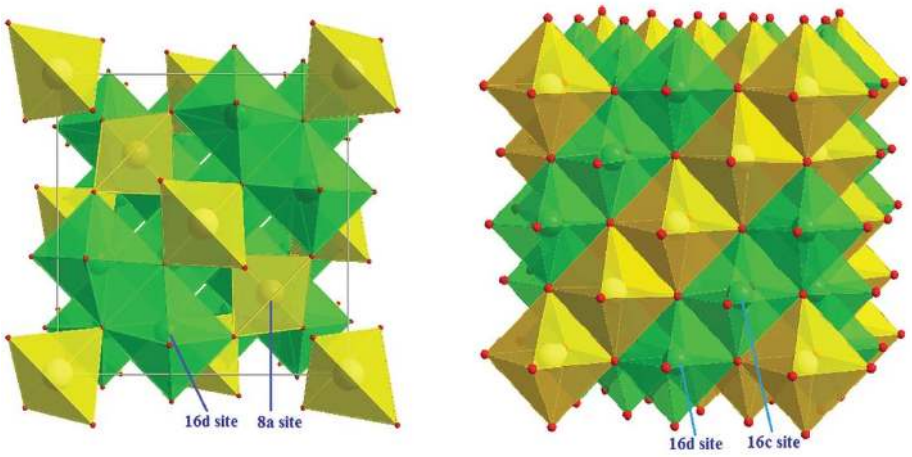

Figure 1.22: (a) Spinel- and (b) rock-salt $Li_4Ti_5O_{12}$ structures. Yellow tetrahedra represent Li^+, and green octahedra represent disordered Li^+ and Ti^{4+} [306].

The low electrical conductivity (~10^{-13} S cm^{-1}) and low lithium-ion diffusion coefficient (~10^{-9}-10^{-13} cm^2 s^{-1}) hinder its high rate capability [307, 308]. Thus, many strategies, including nanostructuring, ion doping and surface modification with carbonaceous materials, have been carried out to improve rate performance [306]. Zhou et al. reported a simple and economical process by using a filter paper as reaction matrix to synthesize carbon-coated $Li_4Ti_5O_{12}$ porous fiber that achieved excellent rate capability with a specific capacity of 165 mA h g^{-1} at 0.2 C and 141 mA h g^{-1} at 20 C related to the improved electrolyte wetting by porous structure, short Li^+ diffusion length by nanosizing and enhanced electron conductivity by carbon coating [309]. Recently, Zeng et al. investigated the effects of different coatings like mesoporous crystalline microbeads (MCMB) and amorphous carbon on the electrical conductivity of $Li_4Ti_5O_{12}$ anode. It was found that 3 wt.% MCMB-coated $Li_4Ti_5O_{12}$ anodes showed the highest reversible capacity at all current rates and the lowest total resistance owing to the crystallinity of

MCMB, prevention of agglomeration and small sized nanoparticles (~100 nm) [310].

Wang et al. employed an approach of using rutile TiO_2 coating to improve rate capability, tap density and mechanical stability of $Li_4Ti_5O_{12}$ nanosheets anode. 2D structure of nanosheets leads to a large contact surface area with the electrolyte reducing the diffusion pathway. They revealed that the nanocoating with rutile TiO_2 could give higher surface stability and longer cycling performance compared to the carbon coatings [311]. In another study, Rahman and coworkers synthesized a nanocrystalline duplex phase of $Li_4Ti_5O_{12}$-TiO_2 via a facile molten salt method using a eutectic mixture of $LiNO_3$–LiOH–Li_2O_2 at 400–500 °C. The sample prepared at 400 °C for 3 h yielded the best rate capability and cycling stability performance due to the small particle size (< 10-20 nm) [312].

Wang et al. integrated nitrogen, sulphur co-doped porous graphene with $Li_4Ti_5O_{12}$ by using one-step calcination and activation process for the first time. According to the density functional theory (DFT) calculation, co-doped porous graphene showed higher adsorption energy and lower Li^+ ion diffusion activation energy that enhanced both Li^+ storage and transfer. The final composite anode exhibited a high specific capacity at a very high rate (100 C) and superior cycling performance after 4000 cycles [313].

To sum up, $Li_4Ti_5O_{12}$ has been considered as an ideal anode material for practical applications because of its high safety and long lifetime. However, the lithiated $Li_{4+x}Ti_5O_{12}$ is susceptible to react with non-aqueous electrolyte forming an intrinsic gassing issue at high temperatures that limit its large scale application [259].

1.4 Electrolytes

The electrolyte plays a significant role in determining the battery performance, safety and cycling stability. The electrolyte serves as a charge transfer medium in which ions move

between cathode and anode (**Figure 1.23**) [314, 315]. The requirements for an electrolyte are listed below:

- Wide potential window (0-5 V) to avoid electrolyte decomposition
- Compatibility with both anode and cathode
- Chemically inertness with all cell components like separator, current collectors etc. upon cycling
- High ionic conductivity, low viscosity for high Li^+ ion mobility, high dielectric constant for a good lithium salt dissociation
- High thermal stability, high boiling point for safety
- Robust against electrical, mechanical, thermal conditions
- Environmentally friendliness, non-toxicity, low cost [316-318].

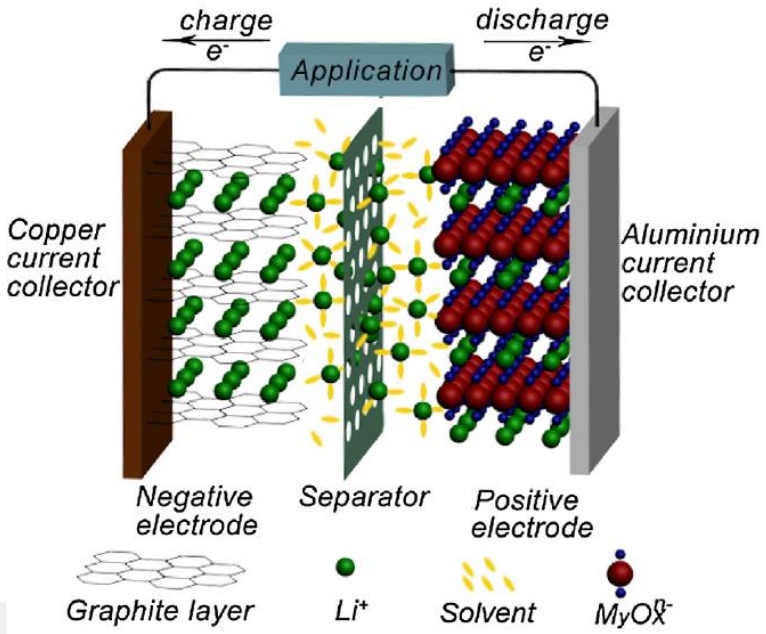

Figure 1.23: Operating principle of LIBs [314].

The most used commercial electrolytes for LIB are principally composed of lithium salts including, lithium hexafluorophosphate ($LiPF_6$), lithium tris(pentafluoroethyl)trifluorophosphate (LiFAP), lithium tetrafluoroborate ($LiBF_4$), lithium hexafluoroarsenate ($LiAsF_6$), lithium perchlorate ($LiClO_4$), and lithium bis(trifluoromethanesulfonyl)imide (LiTFSI) dissolved in a solvent. Their properties are given in **Table 1.4** [318]. Among them, $LiPF_6$ has been widely used lithium salt whereas propylene carbonate (PC), ethylene carbonate (EC), ethyl methyl carbonate (EMC), diethyl carbonate (DEC), dimethyl carbonate (DMC) and their mixtures have been the most commonly used solvents. In order to improve ionic conductivity and low temperature rate capability of LIBs, moderate dielectric constant and low viscosity are required. Therefore, a mixture of cyclic carbonates and linear carbonates have been used due to the synergistic effects of the high dielectric constant of cyclic carbonates and low viscosity of linear carbonates [314]. Additionally, fire-induced toxicity and the formation of gaseous compounds can be eliminated by using electrolyte mixtures [319]. **Table 1.5**

compares properties of organic carbonates [318].

Table 1.4: Properties of Lithium salts [318, 320, 321].

Properties	**$LiPF_6$**	**LiFAP**	**$LiBF_4$**	**$LiAsF_6$**	**$LiClO_4$**	**LiTFSI**
Ionic conductivity	high	high	medium	high	high	high
Electrochemical stability	high	medium	medium	high	high	high
Thermal stability	low (≥50°C)	medium (≥60°C	medium (293°C)	high (240°C)	low (>236°C)	high (430°C)
Stability towards moisture	low	medium	medium	medium	medium	High
Passivation of Al current collector	high	high	high	high	medium	low
Nontoxicity	low	low	low	low	low	low
Safety	low	low	medium	low	low	high

Table 1.5: Properties of organic carbonate solvents [316, 318].

Properties	**EC**	**PC**	**DMC**	**DEC**	**EMC**
Structure	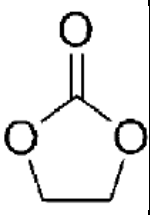	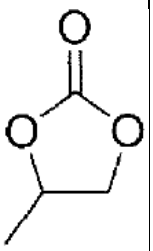	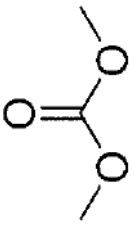	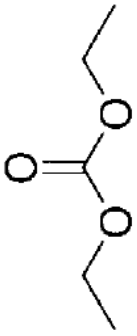	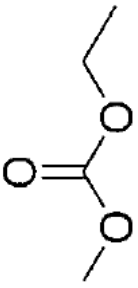
Dielectric constant	high (89.78)	high (64.92)	low (3.107)	low (2.805)	low (2.958)
Viscosity	high (1.90 cP)	high (2.53 cP)	low (0.59 cP)	low (0.75 cP)	low (0.65 cP)

Melting temperature	high (36.4°C)	low (-48.8°C)	medium (4.6°C)	low (-74.3°C)	low (-53°C)
Boiling temperature	high (248°C)	high (242°C)	high (91°C)	high (126°C)	medium (110°C)
Flash point	high	high	low	low	low
Volatility	low	low	high	high	high
Contribution to SEI	high	low	low	low	low
Anodic stability	high	medium	medium	medium	medium
Safety	high	medium	low	low	low

The electrolyte solvent must have a high dielectric constant to dissolve enough amount of salt, must have a low viscosity to maintain ionic transportation, must be chemically inert to all cell components, must have a low melting temperature and a high boiling temperature to conserve its liquid phase. Additionally, it should have a high flash point to ensure safety [316]. Most of the commercial used electrolyte solutions are composed of EC with EMC or DMC mixtures because of the high melting temperature issue of EC. The final melting point should be below -20 °C with lower viscosity [322]. Furthermore, the ionic conductivity of an electrolyte solution should be in the range of $5 – 10 \times 10^{-3}$ S cm^{-1} in order to operate temperatures of -30 – 60 °C [320].

1.4.1 Lithium salts

An electrolyte salt should meet the following requirements:

- High ionic conductivity
- High lithium salt solubility

- Chemically inertness to solvents
- Robust towards all cell components
- Passivation of Al current collector to avoid corrosion at high potentials (>3.6 V vs. Li/Li^+)
- Formation of SEI to maintain cycling stability and safety
- Hydrolysis stability to prevent HF formation at high temperatures and high voltages (>4.8 V vs. Li/Li^+) [323].

1.4.1.1 Lithium hexafluorophosphate ($LiPF_6$)

Lithium hexafluorophosphate ($LiPF_6$) is the most practically used salt due to its good solubility in various carbonate-based organic solvents, high ionic conductivity, good electrochemical stability, passivation of Al current collector against corrosion at high potentials and ability to form a stable SEI with carbon-based anodes. However, there are some drawbacks that limits its high temperature applications [324, 325]. $LiPF_6$ is unstable at high temperatures that decompose to LiF and PF_5 due to the absorption of moisture **(Eqs. (1.11)** and **(1.12)**. At high temperatures above 55 °C, the strong Lewis acid PF_5 is susceptible to undergo hydrolysis, generating dangerous byproducts like HF and PF_3O **(Eqs (1.13)** and **(1.14)**, which react with all cell components resulting in the deterioration of LIB performance in terms of capacity fading and low coulombic efficiency [21, 25, 326-328]. PF_5 can accelerate the ring-opening polymerization of cyclic carbonates resulting in electrolyte decomposition [329].

$$LiPF_6 + H_2O_{\text{(moisture)}} \leftrightarrow LiF + PF_5 \quad \textbf{(1.11)}$$

$$PF_6^- + 2e^- + 3Li^+ \rightarrow 3LiF + PF_3 \quad \textbf{(1.12)}$$

$LiPF_6 + H_2O \rightarrow POF_3 + LiF + 2HF$ **(1.13)**

$PF_5 + H_2O \rightarrow POF_3 + 2HF$ **(1.14)**

Furthermore, $LiPF_6$ has lower conductivity in EC/DMC compared to $LiAsF_6$, lower dissociation constant than LiTFSI, lower ionic mobility than $LiBF_4$ and lower thermal stability than $LiAsF_6$ and $LiClO_4$.

- Dissociation constant: LiBOB > LiTFSI > $LiAsF_6$ > $LiPF_6$ > $LiClO_4$ > $LiBF_4$ > LiTf
- Ion mobility: $LiBF_4$ > $LiClO_4$ > $LiPF_6$ > $LiAsF_6$ > LiTf > LiTFSI
- Solubility: LiTFSI > $LiPF_6$ > $LiAsF_6$ > $LiBF_4$ > LiTf
- Thermal stability: LiTFSI > LiTf > $LiAsF_6$ > $LiBF_4$ > $LiPF_6$
- Chemically inertness: LiTf > LiTFSI > $LiAsF_6$ > $LiBF_4$ > $LiPF_6$

Therefore, these limitations have triggered to investigate other lithium salts [324, 330].

1.4.1.2 Lithium tris(pentafluoroethyl)trifluorophosphate (LiFAP)

Lithium tris(pentafluoroethyl)trifluorophosphate $LiPF_3(CF_2CF_3)_3$ (LiFAP) has been proposed by Merck as an alternative salt to overcome the hydrolysis issue of $LiPF_6$. The steric shielding of phosphorous through the perfluorinated alkyl groups leads to stability against hydrolysis. Besides, its conductivity is comparable to $LiPF_6$ because of its strong electron-withdrawing properties. Thus, the thermal stability with a combination of flame-retardancy is improved by the stabilization of P-F bonds [321, 331, 332]. Granaraj et al. investigated the thermal stabilities of LiFAP, $LiPF_6$, $LiClO_4$ and LiBETI solutions in EC/DEC/DMC solution in the temperature range 40–350 °C by accelerating rate

calorimetry (ARC) and differential scanning calorimetry (DSC). It was found that the thermal decomposition of LiFAP was in the range of 210-290 °C, which is higher than $LiPF_6$ [333]. In another study, they compared the capacity retention of LiFAP and $LiPF_6$ electrolyte solutions in EC/DMC/DEC mixture. As shown in **Figure 1.24**, the irreversible capacity loss of the graphite electrode cycled with LiFAP was lower than $LiPF_6$ at 30 °C, whilst a double-salt solution of LiFAP and $LiPF_6$ showed superior cycling stability at 80 °C due to their synergistic effects [334].

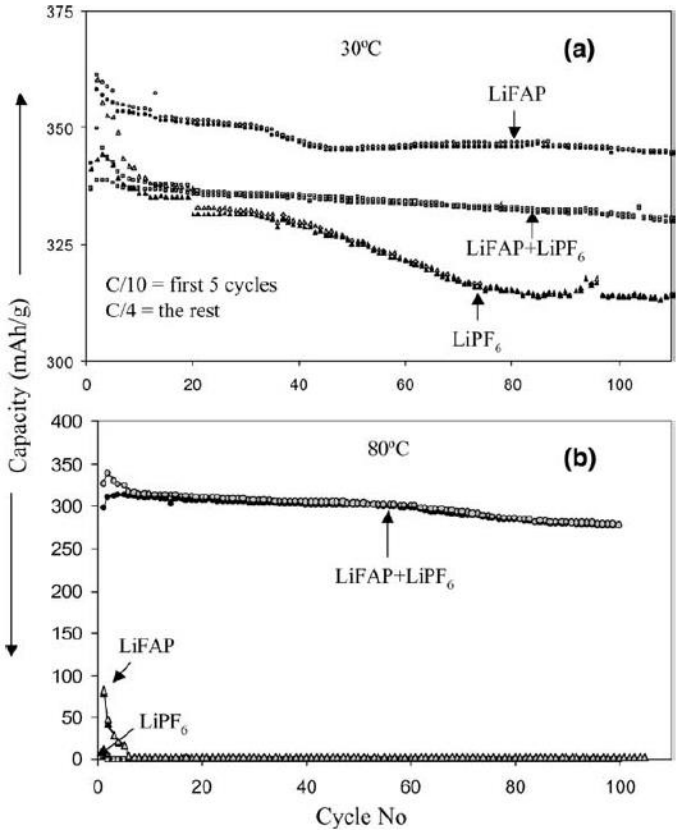

Figure 1.24: Capacity vs. cycle number of graphite electrodes during galvanostatic lithiation–delithiation, C/4 rates in LiFAP, $LiPF_6$ (1 M) and LiFAP–$LiPF_6$ (0.5 each) solutions in EC–DEC–DMC 2:1:2 at 30 and 80 °C, as indicated. The electrodes were cycled in the 0.005–1.6 V domain (vs. Li ref. electrodes). The irreversible capacities at

30 °C were usually around 30% for the solutions containing $LiPF_6$ and around 20–25% for the LiFAP solution [334].

Similarly, Arbizanni et al. investigated the electrochemical performance of high voltage $LiNi_{0.4}Mn_{1.6}O_4$ cathode and graphite anode with LiFAP, $LiPF_6$ as well as with SEI additives. It was found that the capacity retention of 1 M LiFAP in EC/DMC with the use of additives reached from 70% to 87% with regard to their beneficial effects [335].

1.4.1.3 Lithium tetrafluoroborate ($LiBF_4$)

$LiPF_6$ containing moisture-free electrolytes could perform in a temperature range (-20 – 60 °C). In the early 2000s, lithium tetrafluoroborate ($LiBF_4$) has received great interest as an alternative to $LiPF_6$ because of its high temperature (above 60 °C) and low temperature (below -20 °C) electrochemical performance [336, 337]. $LiBF_4$ possess less toxicity than $LiAsF_6$, higher safety than $LiClO_4$, high thermal stability, less moisture sensitivity, better passivation of Al current collector at high voltages compared to $LiPF_6$ [316, 338]. However, the main disadvantage is its low ionic conductivity which leads to a dissociation in organic solvents (PC/EMC, PC/DME) [339]. Besides, its low anodic oxidation potential and electrochemical potential window (3.5 V vs. Li/Li^+) limit its high voltage applications [314]. More importantly, $LiBF_4$ based electrolytes have poor ability to form a protective SEI on the surface of graphite anode due to their low solubility in solvents. Therefore, Zhang et al. used LiBOB as an additive in $LiBF_4$-PC electrolyte to improve SEI formation as well as low temperature performance. They also reported that the presence of lithium oxalate (Li_2CO_3) as an impurity of LiBOB resulted in a reduction of the expected performance of graphite/$LiNiO_2$ cells [340]. Similarly, lithium difluoro (oxalate) borate (LiODFB) has been used as an electrolyte additive in order to improve low temperature performance [341] and cycling stability in a wide temperature range [342] because of its superior formation of SEI, passivation of Al current collector and

thermal stability. As shown in **Figure 1.25**, a mixture of LiODFB/$LiBF_4$ (4:1) in EC-DMC-EMC electrolyte showed a major progress in the high-rate cycling performance of high voltage LNMO cathode for different temperatures [342].

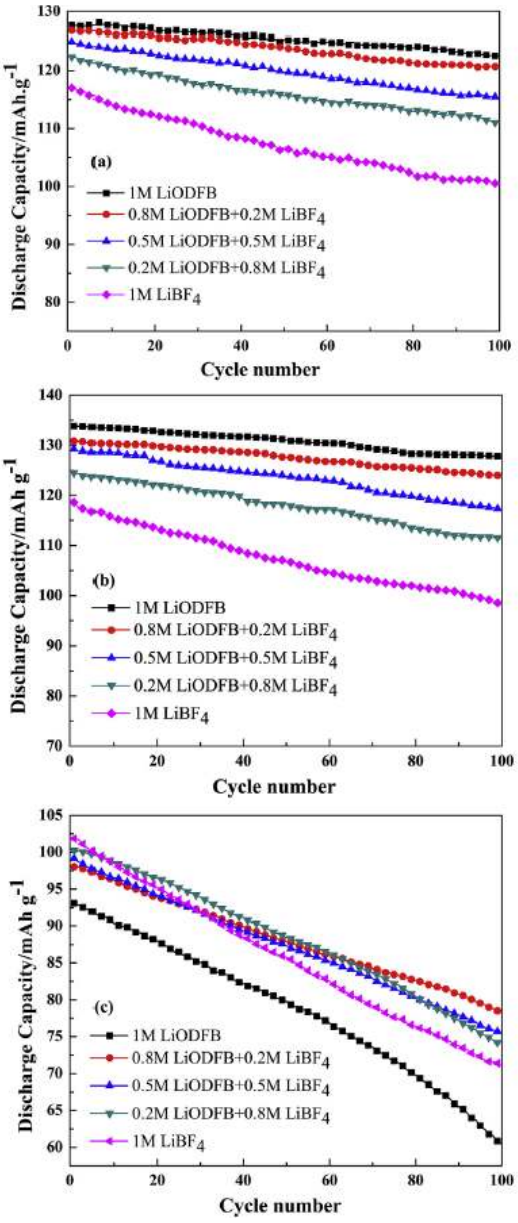

Figure 1.25: Cycling curves of the $LiNi_{0.5}Mn_{1.5}O_4$/graphite cells with different electrolyte systems at different temperature. (a) 25 °C, (b) 60 °C and (c) -20 °C [342].

1.4.1.4 Lithium hexafluoroarsenate ($LiAsF_6$)

In the late 1970s, lithium hexafluoroarsenate ($LiAsF_6$) was proposed as an alternative salt

for $LiClO_4$ owing to its high ionic conductivity, good solubility in aprotic solvents (DEC, DMC etc.), high thermal and electrochemical stability, favorable passivation of Al current collector and the formation of SEI [323]. As shown in **Figure 1.26**, $LiAsF_6$ has a high solubility in EC:PC and superior conductivity compared to $LiPF_6$ [343].

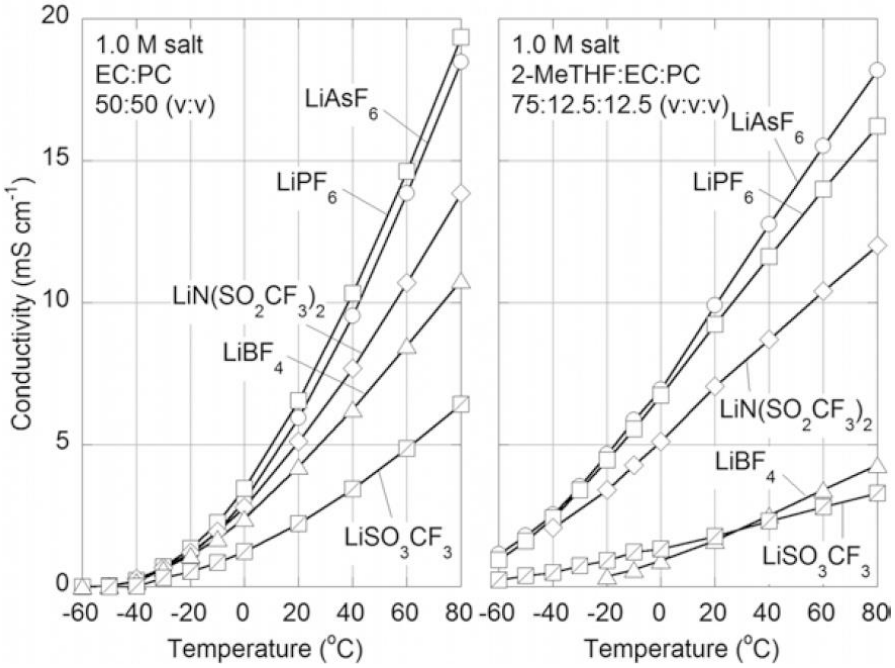

Figure 1.26: Ionic conductivity of EC:PC (50:50 v:v) and 2-MeTHF:EC:PC (75:12.5:12.5 v:v:v) mixtures with the indicated lithium salts (1 M) [323].

Nevertheless, the toxicity of As^{III} and As^0 states limits its commercial use [323]. Additionally, $LiAsF_6$ is likely to undergo hydrolysis forming dangerous by-products like HF, AsF_5 or AsF_3 (**Eqs. (1.15)**, **(1.16)** and **(1.17)**) which can also cause degradation of SEI [327].

$$LiAsF_6 + H_2O_{(moisture)} \rightarrow HF + AsF_5 + LiOH \quad \textbf{(1.15)}$$

$$LiAsF_6 + 2e^- + 2Li^+ \rightarrow AsF_3 + 3LiF \quad \textbf{(1.16)}$$

$$AsF_3 + 2ne^- + 2nLi^+ \rightarrow Li_nAsF_{3-n} + nLi^+ \quad \textbf{(1.17)}$$

1.4.1.5 Lithium perchlorate ($LiClO_4$)

A fluorine-free salt lithium perchlorate ($LiClO_4$) exhibits high ionic conductivity (~9.0 mS cm^{-1} in EC/DMC at 20 °C), high solubility in aprotic solvents, good thermal stability, high electrochemical stability, appropriate passivation of Al current collector and stability towards hydrolysis without the formation of HF [318, 344]. Nevertheless, $LiClO_4$ could not be practically used because the strong oxidant ClO_4^- reacts easily with organic compounds at elevated temperatures and high current densities, which may result in the explosion [314, 327]. However, it has been widely utilized by various researchers due to its low cost and handling [316].

1.3.1.6 Lithium bis(trifluoromethanesulfonyl)imide (LiTFSI)

In 1984, Lithium bis(trifluoromethanesulfonyl)imide $LiN(SO_2CF_3)_2$ (LiTFSI) was reported as a lithium imide by Foropoulos and Desmarteau [345]. In the early 1990s, 3M Corporation commercialized LiTFSI as LIB conducting salts owing to its high electrochemical stability, good ionic conductivity, low sensitivity towards moisture, thermal stability up to 360 °C and safety [316]. Thus, the incorporation of LiTFSI with $LiPF_6$ ensures safety in a wide temperature range due to the stability of $TFSI^-$ anion [320]. However, the main drawback of LiTFSI is corrosion of Al current collector at a high voltage related to the acid-base nature and stereochemistry of anion. Therefore, other imide salts like LiFSI, LiBETI, LiFTNFSI have been investigated to suppress Al corrosion [318, 346-348].

1.4.1.7 Lithium bis(oxalate)borate (LiBOB)

Lithium bis(oxalate)borate $LiB(C_2O_4)_2$ (LiBOB) (**Figure 1.27**) has been regarded as a promising electrolyte salt due to its excellent physicochemical, electrochemical properties and thermal stability [314]. LiBOB was patented as a new candidate of Li-ion conducting salt by Lishka et al. in 1999 [349] and investigated by Angell et al. in 2001 for the first

time [350, 351]. Xu and Angell synthesized LiBOB by mixing stoichiometric amount of tetramethanolatoborate, $LiB(OCH_3)_4$ and di(trimethylsilyl) oxalate (DTMSO) in an excess amount of anhydrous acetonitrile followed by a recrystallization process using acetonitrile-toluene (1:1) mixture to achieve high ionic conductivity for elevated temperatures (~ 60 °C) [351].

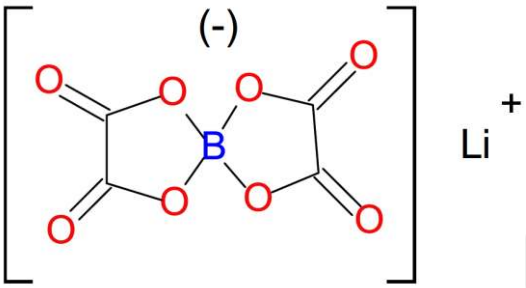

Figure 1.27: Molecular structure of LiBOB [352].

It has been reported that the oxalate borate anion group $B(C_2O_4)^{2-}$ of LiBOB shows the formation of a protective SEI on both graphite anode and cathodes [353]. Various advantages of LiBOB are given as:

- Higher crystallin stability than $LiPF_6$
- No formation of a dangerous by-products like HF, PF_5, LiF due to its fluorine-free structure
- Formation of a stable SEI protecting Al current collector from corrosion
- High electrochemical stability (>4.5 V vs. Li/Li^+)
- Good solubility in EC, DMC, DEC etc.
- High conductivity in various non-aqueous solvents

- Good cycling stability at high temperature
- Superior overcharge tolerance
- Environmentally friendliness, low cost
- Better thermal stability than $LiPF_6$ (~ 300 °C) [354].

Xu et al. prepared LiBOB through a solid-state reaction for the first time using oxalic acid dihydrate ($C_2H_2O_4.2H_2O$), lithium hydroxide (LiOH) and boric acid (H_3BO_3) followed by a purification step. It was found that the cell with LiBOB electrolyte showed much higher capacity retention compared to the one containing $LiPF_6$ at 55 °C as evaluated in **Figure 1.28** [355].

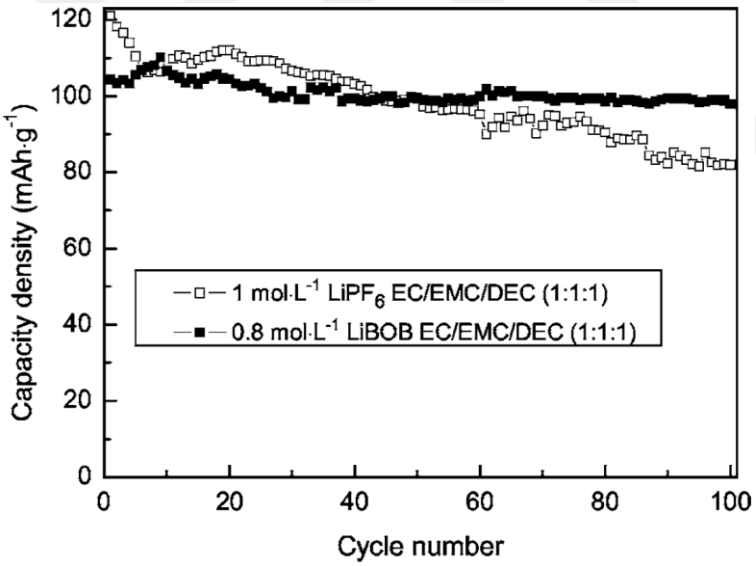

Figure 1.28: Cycling performances of $LiMn_2O_4$/Li cells in 3.3 - 4.35 V at 55 °C using $LiPF_6$ based and LiBOB based electrolytes at 70 mA h g^{-1} [355].

In another study, they investigated the cycling performance of $LiM_xFe_{1-x}PO_4$/Li cells with LiBOB- and $LiPF_6$-based electrolytes for various temperatures. At 65 °C, LiBOB showed a higher discharge capacity and improved cycling stability because of the

dissolution of $LiFePO_4$ in $LiPF_6$ electrolyte, which was three times higher than LiBOB [356]. LiBOB has high solubility and excellent conductivity in γ-butyrolactone (GBL) solvent. Therefore, LiBOB-GBL/DMS electrolyte system achieved a high oxidation potential above 5.3 V forming a lower impedance of the SEI than that of the cell with $LiPF_6$-EC/DMC electrolyte [357].

However, there are some limitations of LiBOB electrolytes, such as low solubility and unsatisfactory ionic conductivity, which may cause poor rate capability and low-temperature performance [358]. Thus, LiBOB has also been received huge interest as an electrolyte additive because of its outstanding features, including the inhibition of electrolyte decomposition and Mn/Ni dissolution as well as the development of stable SEI demonstrated in **Figure 1.29**.

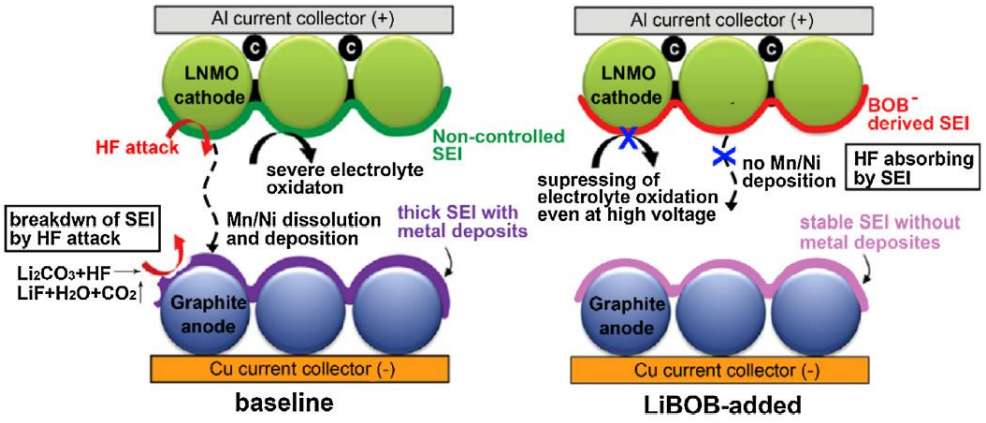

Figure 1.29: Schematic illustration of unique functions of LiBOB additive in a graphite/$LiNi_{0.5}Mn_{1.5}O_4$ cell [314].

2 wt.% LiBOB added $LiPF_6$ electrolyte could suppress the electrolyte oxidation, which results in exfoliation of graphite anode. Besides, the addition of LiBOB leads to improved cycling stability at high operation temperatures (> 60 °C) and high potentials because of its ability to trap PF_5 and HF from the degradation of $LiPF_6$ [314]. Similarly, Choi and

coworkers reported that at 60 °C, the capacity retention of $Li_{1.17}Ni_{0.17}Mn_{0.5}Co_{0.17}O_2$ cathode was improved from 28.6% to 77.6% with the addition of 1 wt.% LiBOB into the electrolyte after 100 cycles. In addition, rate capability was also improved owing to the elimination of oxidative decomposition of $LiPF_6$ electrolyte [359]. Aravindan et al. evaluated that the incorporation of 3 wt.% LiBOB in 1 M $LiPF_6$ EC:DEC (1:1) resulted in capacity retention of 74% after 25 cycles improving the cycling stability of $LiCoPO_4$ cathode at 5.2 V vs. Li/Li^+ [360].

The possible oxidative and reductive decomposition of LiBOB for the formation of SEI on the cathode surface is presented in **Figure 1.30&1.31**. An oxalatoborate radical is formed after the ring-opening of LiBOB related to the loss of two CO_2 from the high voltage cathode. After that polycarbonate like oligomers is generated because of the reaction between radical and EC. Additionally, LiBOB can also form a SEI with semi-carbonate like species on carbonaceous anodes [361].

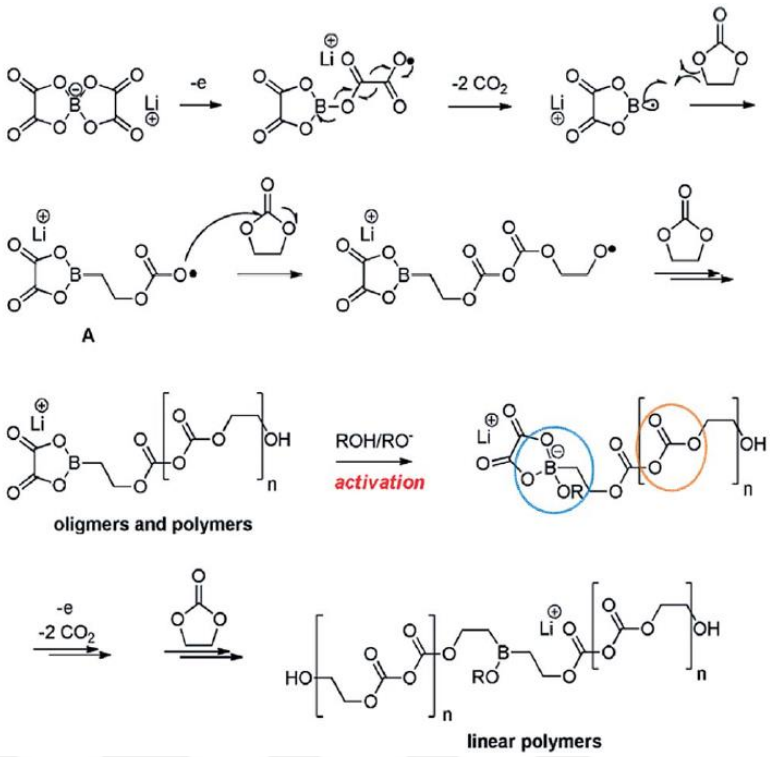

Figure 1.30: Possible mechanism for the LiBOB oxidative decomposition products [361].

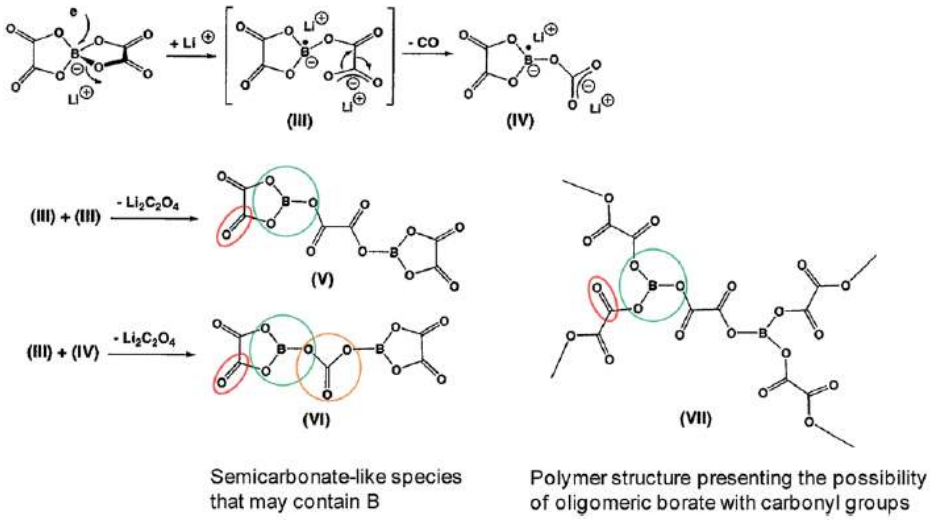

Figure 1.31: Possible mechanism for the LiBOB reductive decomposition products [361].

1.5 Aim of the Thesis

The desired battery performances are high safety, long lifetime, high energy density and high power density. The problem is current battery materials partially meet these requirements. Today, electric cars have a specific energy of 200-300 km, which needs to be increased by developing new generation batteries. $LiPF_6$ is the most commonly used electrolyte salt with several disadvantages such as poor thermal stability, low decomposition temperature and the formation of toxic and corrosive compounds like HF, causing safety issues. As an anode, metallic Li could cause dendrite formation on the metal surface during the charge-discharge process, which results in short circuit and potential fire hazard. So, there has been ongoing research efforts to develop alternative anode materials due to safety issues. The main motivation for this thesis is safety.

LiBOB could be used as an electrolyte additive in order to prevent structural change and electrolyte decomposition by developing a protective SEI on both graphitic anode and cathode surfaces. However, the use of LiBOB is limited due to the remaining impurities and hydrated phase, which results in an electrochemical performance decay related to higher full cell impedance.

Therefore, the first aim of this work is to obtain high purity anhydrous LiBOB using low cost starting chemicals and fewer processing steps compared to the reported other methods in the literature. Herein, LiBOB is synthesized through the mixing of lithium carbonate, boric acid and oxalic acid in an excess amount of water. After the evaporation of the water, a pellet of this precursor powder is covered with the same precursor and the reaction is carried out under protective atmosphere to obtain high purity product. And then, the desired amount of LiBOB additive is dissolved in the base electrolyte in order to study the influence of LiBOB on the cycling stability of electrodes. Therefore, better electrolyte and cell stability, stable SEI, thermal stability, safety and cycling stability will

be achieved.

The second aim is to fabricate surface modified TiO_2/reduced graphite oxide (RGO) nanocomposite anode as a next-generation anode material for LIBs. TiO_2 have been considered as a promising anode material with regard to its outstanding properties such as excellent structural stability, cycling stability, environmental friendliness, safety and low cost compared to other materials. But it has a few disadvantages like low capacity, low electrical conductivity and low Li-ion diffusion coefficient. These are under focus in this research. Therefore, nanosizing and using carbon composites have been considered as an efficient approach to increase the capacity of LIBs. By using nanosized materials, Li-ion diffusion pathway can be reduced with an increase in the surface area. Secondly, coating with carbon sources like graphene could be used to improve electrical conductivity. Graphene has received great attention owing to its superior properties, including high electron mobility, high electrical conductivity, large surface area, chemical stability, structural flexibility, and mechanical properties. Here, TiO_2 nanoparticles are synthesized with a sol-gel process. Graphite oxide (GO) is also integrated as a conductive additive by performing mechanical mixing and further reduced thermally. Finally, a surface modification process with hydrogen peroxide solution is applied to obtain better surface interaction between TiO_2 NPs, more stable composite resulting in superior electrochemical performance.

The third aim is to investigate the effects of LiBOB on the electrochemical performance of high voltage $LiCoO_2$ cathodes. At high operating voltages above 4.2 V, LCO may suffer from irreversible structural change, capacity fade and poor cycling performance due to the electrolyte decomposition. Therefore, various electrolyte additives like Al_2O_3, Li_2CO_3, trimethylboroxine (TMB) have been used to improve the high-voltage application of LCO cathode by forming a stable SEI layer that decreases the interfacial

resistance. Here, a practical purification process is performed to further increase the purity of as-synthesized LiBOB above 99%. Then, LiBOB is added 1 wt.% in 1 M $LiPF_6$ in EC/DMC (1 : 1) electrolyte solution to improve the cycling stability of high voltage LCO cathode. As a result, superior cycling performance, rate capability, energy density and coulombic efficiency are obtained compared to the pristine electrolyte and the one containing unpurified LiBOB by eliminating the electrolyte decomposition and the formation of dangerous byproducts (LiF, PF_5, HF).

The fourth aim is to study the influences of high purity LiBOB on the cycling stability and surface chemistry of surface modified TiO_2/RGO anodes. Effects of LiBOB have been investigated in cycling performances of cathodes, but there is a lack of research in combination with next-generation anode materials. The addition of LiBOB within the base electrolyte leads to a huge irreversible capacity loss due to the decomposition products of LiBOB increasing the interphase resistance. However, cycling stability and coulombic efficiency can be enhanced with the formation of a proper SEI at a lower current density.

Chapter 2:
A Guide to Water Free Lithium Bis(oxalate) Borate (LiBOB)

2.1 Abstract

Lithium bis(oxalate)borate, $LiB(C_2O_4)_2$ (LiBOB), is one of the most important electrolyte additives for Li-ion batteries (LIBs) due to its numerous advantages such as thermal stability, good solubility in organic solvents, high conductivity, and low cost as well as providing safer operations with superior electrochemical performance compared to conventional electrolyte combinations. However, the use of LiBOB is limited due to slight instability issues under ambient conditions that might require extra purification steps and might result in poorer performances in real systems. Here, we address some of these issues and report the high purity water free LiBOB synthesized with fewer processing steps employing lithium carbonate, oxalic acid, and boric acid as low-cost starting materials, and via ceramic processing methods under protective atmosphere. The physical and chemical characterizations of both anhydrous and monohydrate phases are performed with X-ray powder diffraction (XRPD), Fourier-transform infra-red spectroscopy (FTIR), Raman spectroscopy and scanning electron microscopy (SEM) analyses to determine the degree of the purity and the formation of impurities like $LiBOB.H_2O$, HBO_2 and $Li_2C_2O_4$ as a result of the aging investigations where the as-synthesized salt was exposed to ambient conditions for different durations. Differential

thermal analysis (DTA) is applied to determine the optimum synthesis conditions for anhydrous LiBOB and to analyze the water loss and the decomposition of $LiBOB.H_2O$. Aging experiments with the water free LiBOB are carried out to evaluate the effect of humidity in the phase changes and resulting impurities under various conditions. The detrimental effect of even slightest humidity conditions is shown, and protective measures during and after the synthesis of LiBOB are discussed. Anhydrous LiBOB could be widely used as an electrolyte additive to improve the overall electrochemical performances for LIBs through development of a protective solid electrolyte interphase (SEI) on the surface of high voltage cathodes and bringing about superior electrochemical properties with increased cycling stability, rate capability and coulombic efficiency, if synthesized, purified, and handled properly before use in real electrochemical systems.

2.2 Introduction

Electrolyte salts and additives play a crucial role in increasing the cycle life, capacity and safety of batteries especially for high voltage applications [361-363]. Lithium bis(oxalate) borate, $LiB(C_2O_4)_2$ (LiBOB), is one of the most widely used electrolyte additives in Li-ion batteries and has a potential to be an alternative of the commercially used lithium hexafluorophosphate ($LiPF_6$) as an electrolyte salt when dissolved in suitable solvents. LiBOB provides electrochemical stability at high applied potentials and high thermal stability under different electrochemical conditions [364-366]. LiBOB also promotes the formation of a protective solid-electrolyte interphase (SEI) layer; thus increasing capacity and cycle life when used as an electrolyte additive [314, 354, 367-372].

LiBOB can address the need for stable electrolyte compositions for high voltage cathode materials and applications. In a mixed solvent system (γ-butyrolactone and dimethyl carbonate), it was shown that LiBOB provides oxidative stability up to 5.3 V in Li-ion

batteries [357, 361], whereas $LiPF_6$ can be only employed up to 4.5 V. The thermal stability of bulk $LiPF_6$ is 80 °C, and it is safe to use up to 50 °C in LIBs. Additionally, at higher temperatures, $LiPF_6$ is susceptible to decompose into LiF and PF_5 resulting in low electrochemical performances and safety issues [354, 373]. On the other hand, bulk LiBOB decomposes at 300 °C and it is stable up to 70 °C in LIBs [374]. There are several other reports where LiBOB enables a stable operation at voltages higher than 4.5 V [375-377]. Besides, LiBOB provides safer operation for Li-ion batteries not only due to its high thermal stability but also due to the protective SEI formation. SEI layer formation does not only play an active role only in the first cycle in the battery; yet, SEI keeps growing and changing with processes such as dissolution and precipitation [378, 379]. Thus, understanding the SEI chemistry and stabilizing the SEI are important challenges in the development of long-life and safe Li-ion batteries, as well.

Other common Li-ion battery salts such as $LiPF_6$, $LiAsF_6$, and $LiClO_4$ were shown to decompose to form corrosive and reactive chemicals [316]. The high oxidation state of Cl(VII) in $LiClO_4$ causes reactions with a range of organic solvents [380], and As(III) and As(0) that form during redox reactions involving $LiAsF_6$ are toxic [381], and LiTf based electrolytes are highly corrosive [316]. On the other hand, LiBOB has received great interest owing to its superior properties such as thermal stability, good solubility in organic solvents, improved cycling stability with high voltage cathodes, environmentally friendliness, and low cost [367, 369, 372, 382, 383]. LiBOB was also shown to protect graphite anodes from exfoliation in PC-based electrolytes and to develop a SEI on the graphitic anode surface [366]. Additionally, corrosive and dangerous by-products such as HF do not evolve upon cycling when LiBOB is used instead of $LiPF_6$. Unlike $LiPF_6$ and other salts such as $LiClO_4$, $LiAsF_6$ and LiTf, LiBOB directly forms a protective SEI independent of the carbonate electrolyte solvent employed. Additionally, other

potentially corrosive and dangerous by-products such as PF_5 and LiF do not evolve upon cycling when LiBOB is used [384-386]. If the applications of LiBOB as an additive are considered, Pieczonka et al. observed that the addition of 1 wt.% LiBOB in traditional electrolytes increases the cycling stability and coulombic efficiency for a high voltage spinel/graphite battery system, and the addition of 3 wt.% LiBOB eliminated the PF_5 decreasing the Mn dissolution from the $Li_{1-x}Ni_{0.42}Fe_{0.08}Mn_{1.5}O_4$ (LNFMO) cathode [376]. In another study, Lee and coworkers employed LiBOB as an electrolyte additive to develop a protective SEI for high potential $Li_{1.17}Ni_{0.17}Mn_{1.5}Co_{0.17}O_2$ cathodes improving the cycling stability and rate capability via eliminating the electrolyte decomposition [387].

Although LiBOB is a very promising electrolyte salt and additive for Li-ion batteries, up to date, there are only few reports [355, 388, 389] investigating different synthetic routes. Yu et al. employed a solid-state reaction for the first time using oxalic acid, lithium hydroxide and boric acid as starting materials followed by a thermal treatment in air and a recrystallization process to obtain LiBOB. They also reported that LiBOB decomposes into $Li_2C_2O_3$, B_2O_3, CO_2, and CO when the temperature is higher than 300 °C [355, 390]. In another study, Lestariningsih and coworkers utilized lithium carbonate instead of lithium hydroxide to eliminate the $LiBOB.H_2O$ phase. However, they improved the purity of anhydrous LiBOB only up to 59.1% using Li_2CO_3 instead of LiOH which yielded only 17.2% pure anhydrous product [389, 391]. Also, Lian and his group performed a rheological phase reaction using oxalic acid dihydrate, lithium hydroxide monohydrate and boric acid. They reported that LiBOB synthesized from a solid-state reaction may suffer from impurities requiring additionally recrystallization steps [388]. In addition, to the best of our knowledge, $LiBOB.H_2O$ is present as a by-product in all reported LiBOB synthesis methods in the literature. Depending on the reactants used in LiBOB synthesis,

impurities such as lithium oxalate and lithium carbonate were also detected in the final product. In addition, there is a lack of research focusing on the stability of this important electrolyte salt and additive under humidity during and after the synthesis, and under prolonged air exposure [392, 393]. Therefore, herein, we focus on these issues and report on the importance of new synthetic routes and humidity conditions to obtain a high purity water free LiBOB. We synthesize anhydrous and higher purity LiBOB using low cost starting materials and fewer processing steps compared to most prevalent synthesis methods in the literature. Avoiding moisture and impurities in LiBOB and such electrolyte salts are vital for the performance of LIBs. Thus, we also underline the importance of synthesizing and employing LiBOB under protective atmosphere to eliminate hydrous phase and impurity formation by investigating the aging results of the synthesized high purity salt under atmospheric conditions.

2.3 Experimental Procedure

2.3.1 Synthesis of anhydrous LiBOB

LiBOB is synthesized using lithium carbonate (Li_2CO_3, ≥ 99 %, Alfa Aesar), oxalic acid ($C_2H_2O_4$, ≥ 98 %, Alfa Aeasar), and boric acid (H_3BO_3, ≥ 99 %, Alfa Aesar) as starting materials. Stoichiometric amounts of the compounds (following the equation in **Figure 2.1d**) are mixed and ground in a mortar. Excess amount of deionized water is added to the powder mixture, and the mixture is stirred continuously at 80 °C under ambient conditions, in a fume hood exposed to air, until all water is evaporated. A pellet made from this powder precursor is placed in a glassy carbon boat and covered/protected with the same precursor powder. Then, the reaction boat is placed in a quartz tube within a horizontal tubular furnace, and the reaction is carried under protective atmosphere (Ar, N_2 or dry air) at 250 °C for 10-15 hours. The products are transferred into an Ar glovebox (O_2 and H_2O < 1 ppm) without exposure to ambient atmosphere. After the synthesis, the

protective powder is discarded, and the anhydrous LiBOB pellet is ground in a mortar in the glovebox. Aging of the anhydrous LiBOB powder is done under ambient conditions (at RT (~25 °C), and 70 % Average Relative Humidity). The main aim of aging experiments is to determine the effect of humidity on storing, handling and using LiBOB in air, and stress the importance of synthesized under protective conditions. 2-3 grams of LiBOB powder is placed in semi-closed autoclave bottles and left in fume hoods with ventilation for 5, 15, 30 minutes, and 2 days.

2.3.2 Characterization of LiBOB

The phase and purity of the samples are determined by X-ray powder diffraction (XRPD) method using a Bruker D8 Advance X-ray diffractometer, and Cu $K_{\alpha 1}$ radiation (operated at 40 mA, 40 kV). The purity of the as synthesized LiBOB and impurities forming upon aging are further characterized by vibrational spectroscopy analyses. Fourier-transform infra-red spectroscopy (FTIR) is performed on a Thermo Scientific Nicolet iS10 spectrometer with a single reflection diamond attenuated total reflectance (ATR) module, and Renishaw inVia Raman microscope equipped with a 532 nm laser as the excitation source is used to perform Raman spectroscopy. The morphology of the as synthesized and aged powders is investigated by scanning electron microscopy (SEM) analysis using a Zeiss Ultra Plus field emission GeminiSEM. Differential thermal analysis (DTA) is utilized to monitor the reaction and any exothermic and endothermic reactions in the selected temperature range using a Netzsch STA 449 thermal analysis system. For XRPD measurements, as synthesized anhydrous LiBOB samples are prepared in an Ar glovebox and the samples holders are covered with Kapton® tape to prevent exposure to air. No special precaution is taken for SEM, Raman and FTIR spectroscopy. Samples are put in a sealed protective container in an Ar glovebox and taken to the measurement stages of the instruments. For SEM, samples were directly transferred to the vacuum chamber of

SEM after being removed from the sealed container. For Raman and FTIR spectroscopies, the anhydrous samples were exposed to air briefly during the measurement after being removed from the sealed sample holders.

2.4 Results and Discussion

LiBOB is synthesized in high purity following the procedure depicted in **Figure 2.1a and 2.1b**. The phase and purity of as-synthesized LiBOB is investigated via XRPD analysis by comparing the experimental reflection pattern with the calculated reflection pattern of LiBOB (ICSD 281623) (**Figure 2.1c**). The XRPD pattern of the as-synthesized LiBOB match the theoretical pattern, and the reflections belong only to anhydrous LiBOB [394]. This finding shows that single phase anhydrous LiBOB could be obtained in a single synthetic step without the need of any extra recrystallization steps to eliminate LiBOB.H_2O. The lack of any other reflections belonging to possible impurity phases shows that they are under ~ 1 wt-%. Most importantly, LiBOB.H_2O which is the main impurity in the synthesis that could also cause parasitic reactions in LIBs is not observed. Key points in achieving high purity anhydrous LiBOB with the experimental design were conducting the reaction under inert atmosphere (under argon, nitrogen, and dry air) and protecting the pellet with the precursor powder following well-known ceramic processing methods (**Figure 2.1a, Figure 2.1c and Figure 2.2**).

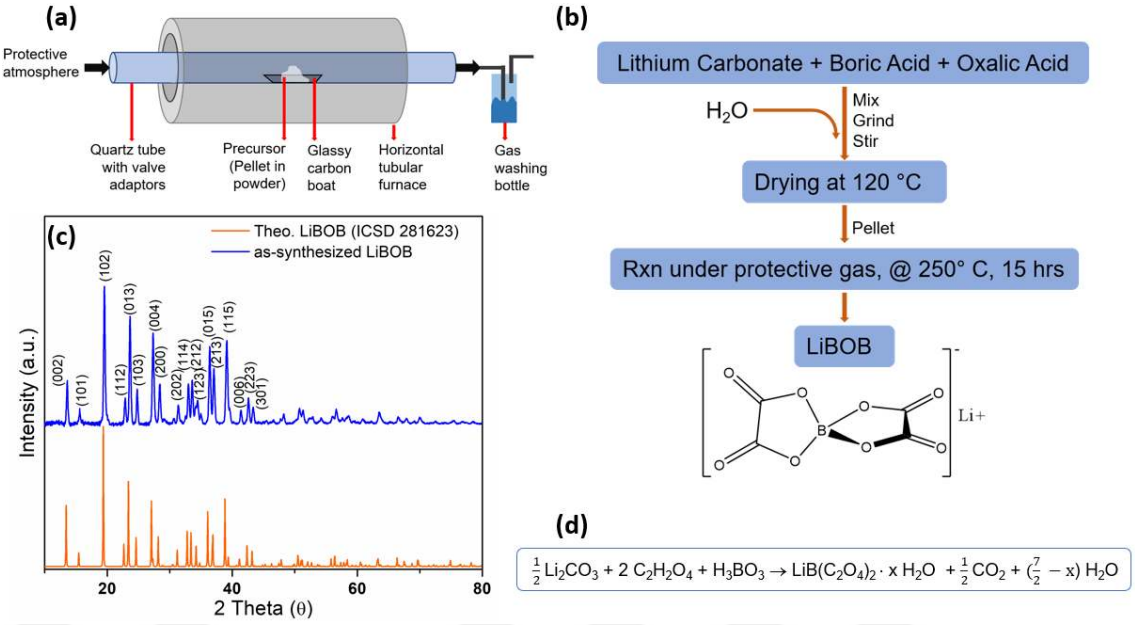

Figure 2.1: (a) A schematic representation of the experimental setup for high purity anhydrous LiBOB synthesis. Ar, N_2 and dry air are employed as protective gases. (b) Processing steps used in the synthesis of high purity anhydrous LiBOB. (c) XRPD patterns of theoretical LiBOB (ICSD 281623) [394] (orange) and as-synthesized LiBOB (blue). Reflections belonging only to LiBOB are observed in the XRPD pattern for the synthesized sample. d) The overall chemical equation for the LiBOB synthesis reaction.

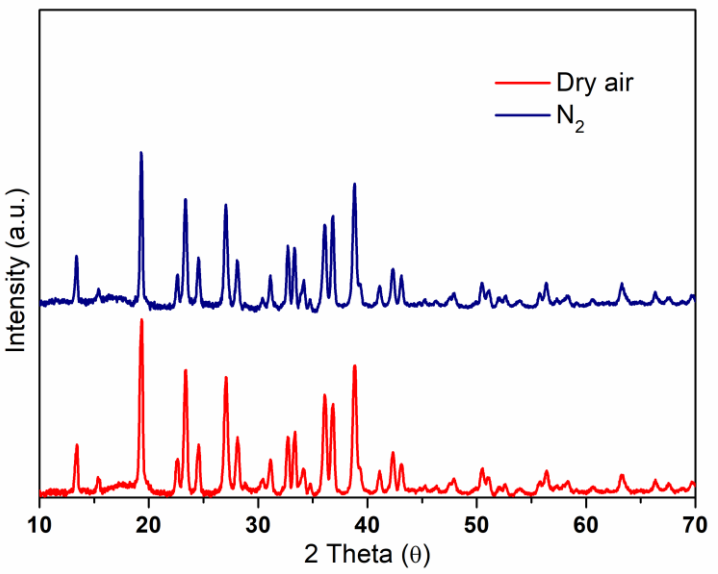

Figure 2.2: XPRD patterns of high purity anhydrous LiBOB synthesized using different protective gases *i.e.* under dry air and N_2 atmosphere.

The reaction of the precursor pellet was monitored via differential thermal analysis (DTA), and different synthesis conditions were also carried out at varied temperatures to determine the optimum temperature window for the high purity LiBOB synthesis (**Figure 2.3**). From the XRPD analysis and DTA data, 225 - 300 °C temperature range could be claimed to be the optimum range for this synthesis. The XRPD and DTA findings show that anhydrous LiBOB decompose into lithium oxalate ($Li_2C_2O_4$) and other amorphous phases at temperatures ca. > 315 °C and at temperatures below 250 °C either monohydrate phase is observed or the reaction is not complete (**Figure 2.3a & Figure 2.4**). According to the Reference intensity ratio (RIR) method [395-397], the percentage of anhydrous LiBOB for as-synthesized samples at 200 °C, and 250 °C was found ~ 95 wt-% and ~ 99.0 wt-%, respectively. Humidity and impurities in LiBOB have detrimental effects on the performance of Li-ion batteries [398], and although it was claimed that monohydrate of LiBOB is stable [399], we show that hydrated LiBOB could decompose into HBO_2, $Li_2C_2O_4$ when exposed to air (**Figure 2.5**). The presence of such impurities in electrolyte solution could cause capacity fading and safety problems under extensive cycling.

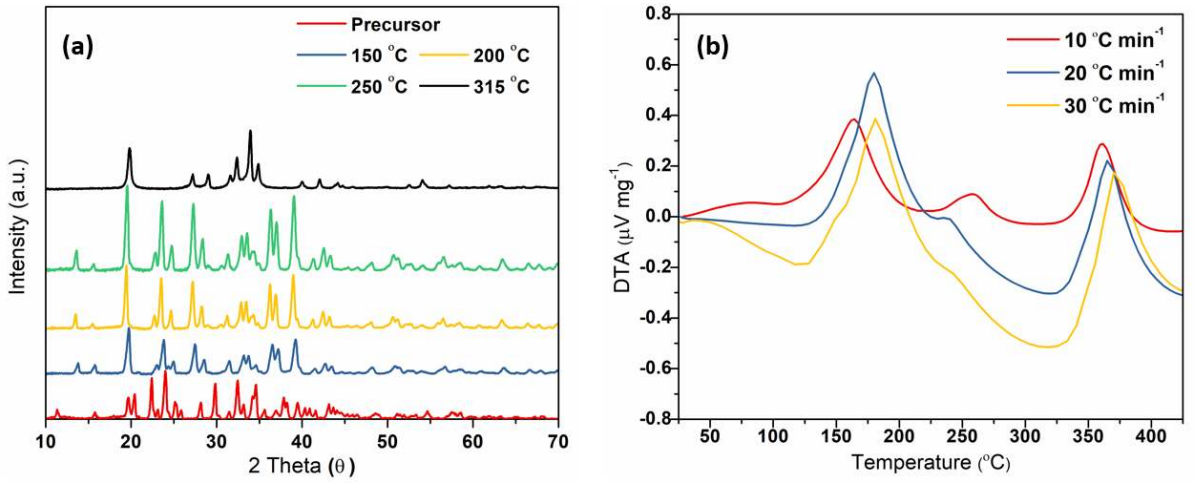

Figure 2.3: (a) XRPD patterns for the precursor and samples synthesized at 150 °C (blue), 200 °C (yellow), 250 °C (green) and 315 °C (black). (b) DTA data taken at different heating rates showing the reaction temperature for LiBOB synthesis and decomposition temperature of the synthesized LiBOB.

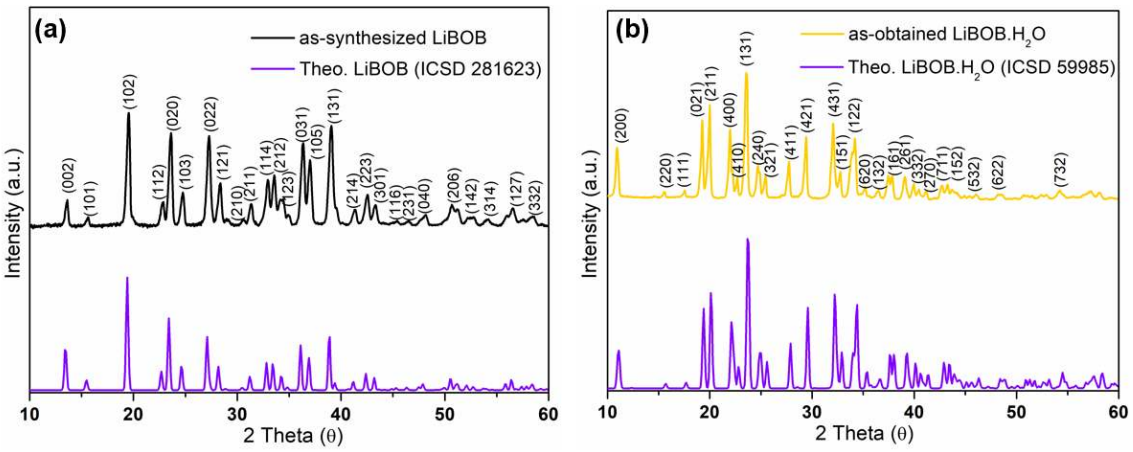

Figure 2.4: XRPD patterns of (a) theoretical anhydrous LiBOB (violet) and as-synthesized anhydrous LiBOB (black), (b) theoretical LiBOB.H_2O (violet) and as-obtained LiBOB.H_2O (30 mins air exposed sample) (yellow).

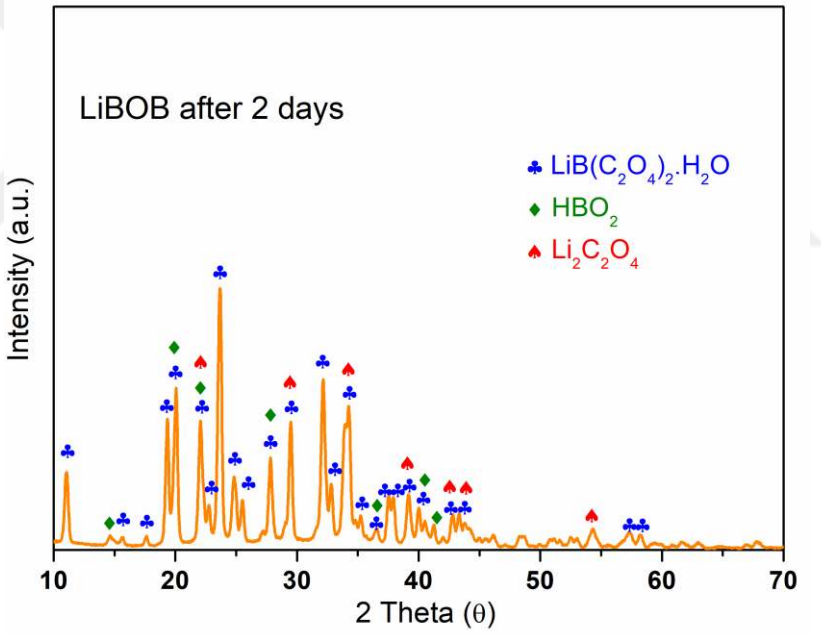

Figure 2.5: XRPD pattern showing crystalline water, HBO_2, and $Li_2C_2O_4$ formation after aging anhydrous LiBOB for 2 days under ambient conditions.

Scanning electron microscopy (SEM) was employed to further understand the particle morphologies and the effect of humidity on those. A homogeneous distribution of particles is observed in SEM images for the samples calcined at temperatures between 250 - 300 °C (**Figure 2.6a, c, d**). These anhydrous LiBOB particles are few microns in

size and prism shaped, whereas synthesis at lower temperatures (< 150 °C) and the product after prolonged air exposure yield rumbled morphologies without any well-defined structures. (**Figure 2.6b, Figure 2.7**). The detrimental effect of humidity on high purity LiBOB can be easily observed via SEM analysis, as well (**Figure 2.8**). The morphology of the anhydrous LiBOB particles start changing after ≤ 5-minute-long exposure to air, and curvatures and pores start to form on the surface of prisms (**Figure 2.8**).

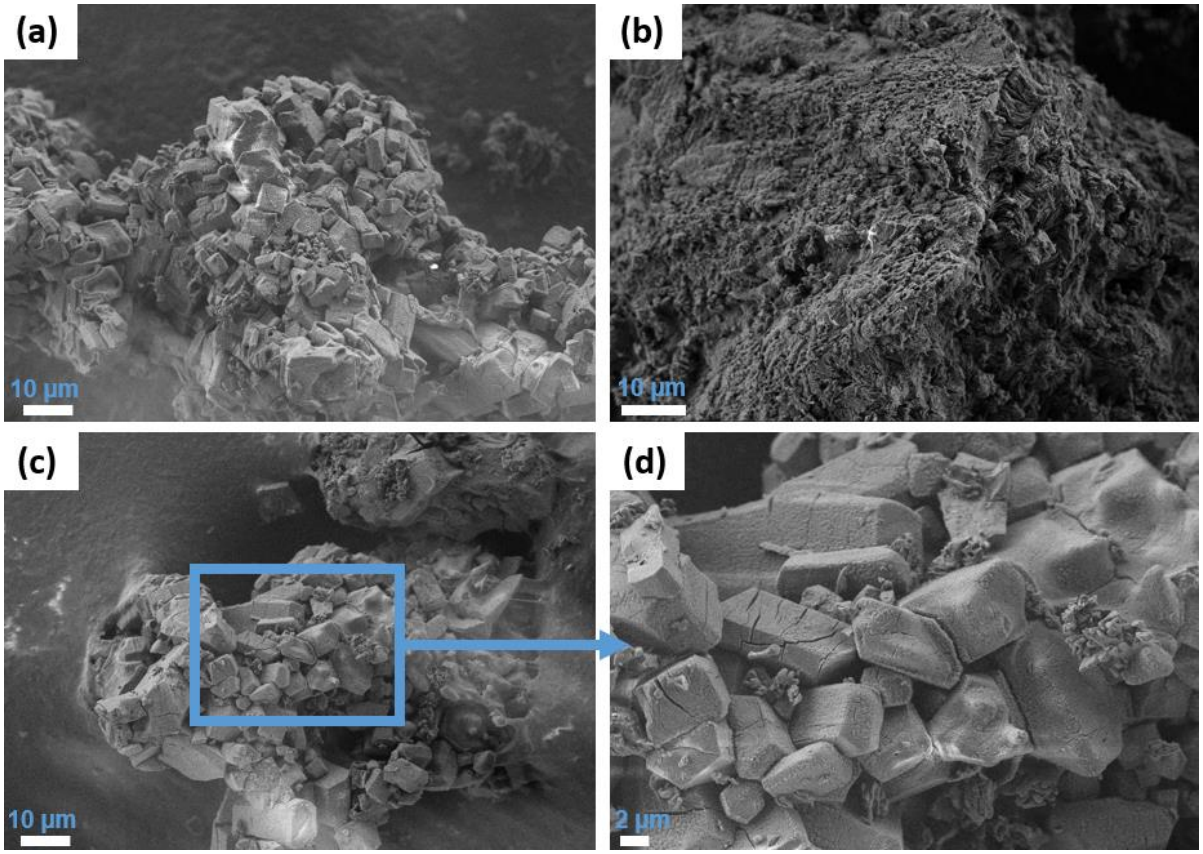

Figure 2.6: (a), (c) SEM micrographs showing the particle size and morphology of anhydrous LiBOB synthesized at 250 °C. (b) Morphology of the products synthesized at 150 °C. (d) Magnified region from c, displaying LiBOB crystals.

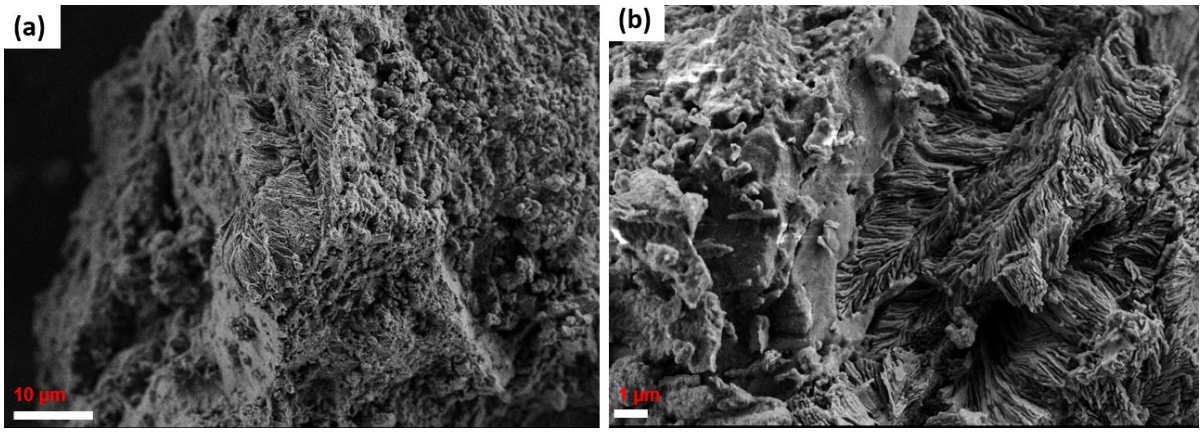

Figure 2.7: SEM micrographs showing the morphology of the products synthesized at 150-200 °C.

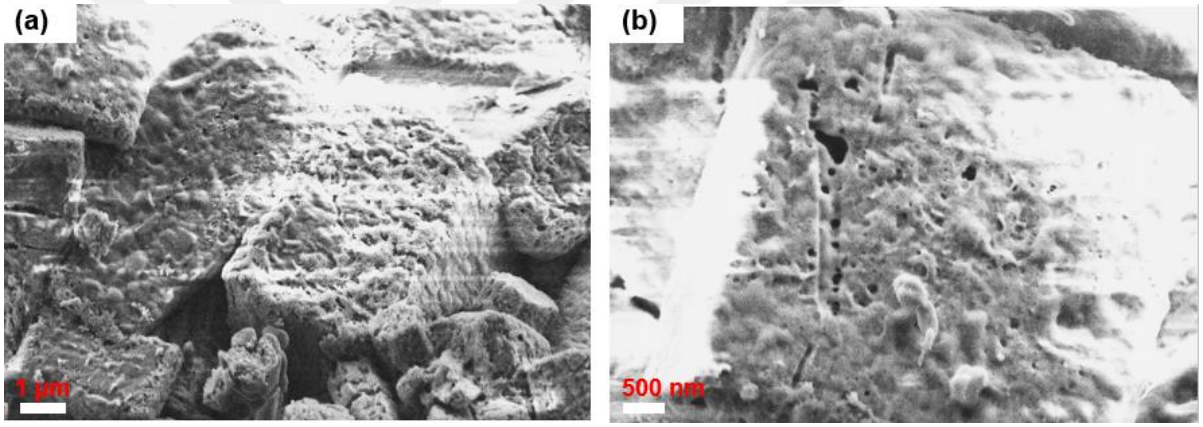

Figure 2.8: SEM micrographs for anhydrous LiBOB ages under ambient conditions showing changes in the prismatic morphology and formation of pores.

In order to analyze the effect of prolonged air exposure to this important electrolyte additive, and to further investigate the influence of humidity in phase changes, aging experiments were performed. Aging of the anhydrous LiBOB powder was done under ambient conditions (at RT (~ 25°C), and 70 % Average Relative Humidity) for 5, 15, 30 minutes and 2 days. The effect of humidity is first investigated through XRPD analysis. XRPD powder patterns in **Figure 2.9a** show that as-synthesized powder consists of only anhydrous LiBOB phase, and ~ 42 wt-% monohydrate phase (LiBOB.H_2O) forms after 5

minutes of aging under given conditions according to the RIR method. After only 15 minutes of exposure to air under given conditions, almost all of the anhydrous LiBOB turns into LiBOB.H_2O, and the complete hydration occurs after 30 minutes of aging (**Figure 2.9a, Figure 2.3 & Figure 2.9b**). The presence of water in the structure can be further confirmed by DTA analysis (**Figure 2.9c**). The structural water is given from the monohydrate phase at ~ 150 °C, and the phase decomposition into $Li_2C_2O_4$ and other amorphous phases start at ~ 315 °C. These findings signify the importance of synthesizing and preserving LiBOB under protective atmosphere. The thermogravimetric analysis (TGA) also corroborates these points and the lack of monohydrate phase if the synthesis and preservation are done under given conditions (**Figure 2.10**). Since purity of electrolyte salts and additives play a crucial role in the cycle life and safety of LIBs [400], the measures taken here in the synthesis of LiBOB can be considered as critical necessary steps.

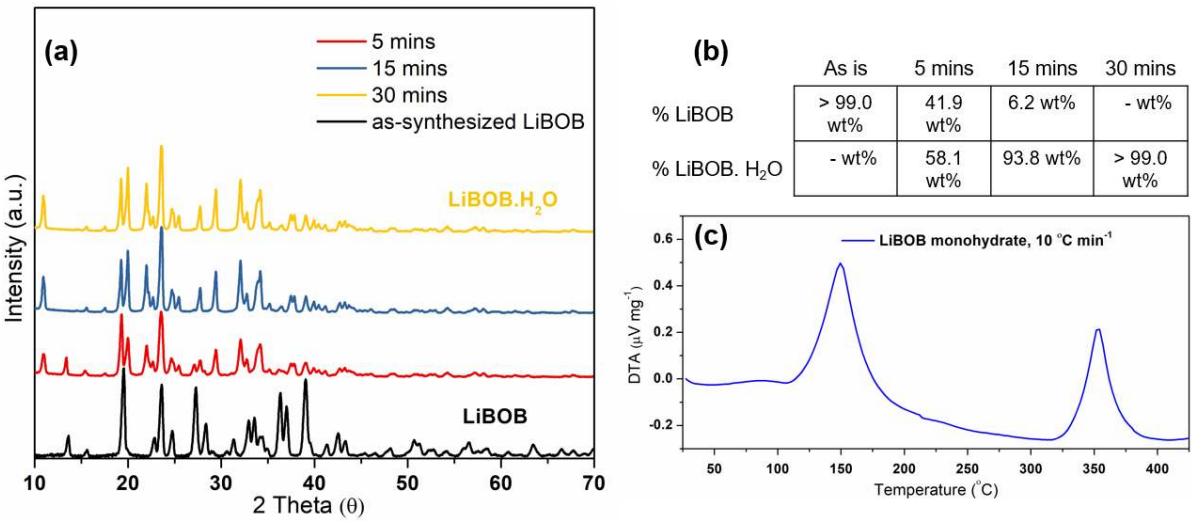

	As is	5 mins	15 mins	30 mins
% LiBOB	> 99.0 wt%	41.9 wt%	6.2 wt%	- wt%
% LiBOB. H_2O	- wt%	58.1 wt%	93.8 wt%	> 99.0 wt%

Figure 2.9: (a) XRPD patterns of the as-synthesized and aged (5, 15, and 30 minutes) LiBOB samples. (b) Phase composition of LiBOB and LiBOB.H_2O in as-synthesized and

aged samples calculated via reference intensity ratio (RIR) method. c) DTA analysis showing the water loss and decomposition of $LiBOB.H_2O$.

The vibrational spectroscopy analysis is in good agreement with XRPD and DTA analyses in terms of confirming the high purity LiBOB phase after the synthesis, and verifies the humidity effect after aging. Both Raman and FTIR spectra of the as-synthesized phase clearly show the high purity of the as-prepared LiBOB after the synthesis [368, 398, 401] and no major impurity phases are observed (**Figure 2.10a & Figure 2.10b**). In the FTIR spectrum (**Figure 2.10b**) of the LiBOB phase, the strong absorption peak at 1765-1825 cm^{-1} could be assigned to the stretching vibrations of C=O bond, whereas the region of 980-1370 cm^{-1} is attributed to the C-O and B-O stretching modes [355, 368]. To analyze the hydration of the anhydrous phase, the FTIR spectra from the aged LiBOB samples were also collected. The water absorption peak intensity at ca. 3500 cm^{-1} increases with the aging time, and several absorption peaks in the range of 1500-800 cm^{-1} shift-change due to the structural deterioration of LiBOB [398, 402]. It should be also noted that a very small water peak might be visible in the spectrum of the as-synthesized sample, since the measurement was not done in a protective atmosphere, so the sample was exposed to air for a minute. As the aging time increases, it is also evident that there is $Li_2C_2O_4$ formation in samples with the observation of small intensity peaks at 1658 and 778 cm^{-1} [398, 403]. These finding are also consistent with XRPD patterns of the aged LiBOB for two days and the decomposed LiBOB (**Figure 2.5, Figure 2.3a**-315 °C pattern). As shown in the **Figure 2.5**, in addition to the diffraction pattern of the $LiBOB.H_2O$, reflections at 20.08° and 27.88° could be attributed to the formation of

HBO_2, and reflections at 22.06° and 29.48° indicate the presence of $Li_2C_2O_4$, as similarly observed by other investigators [388, 404].

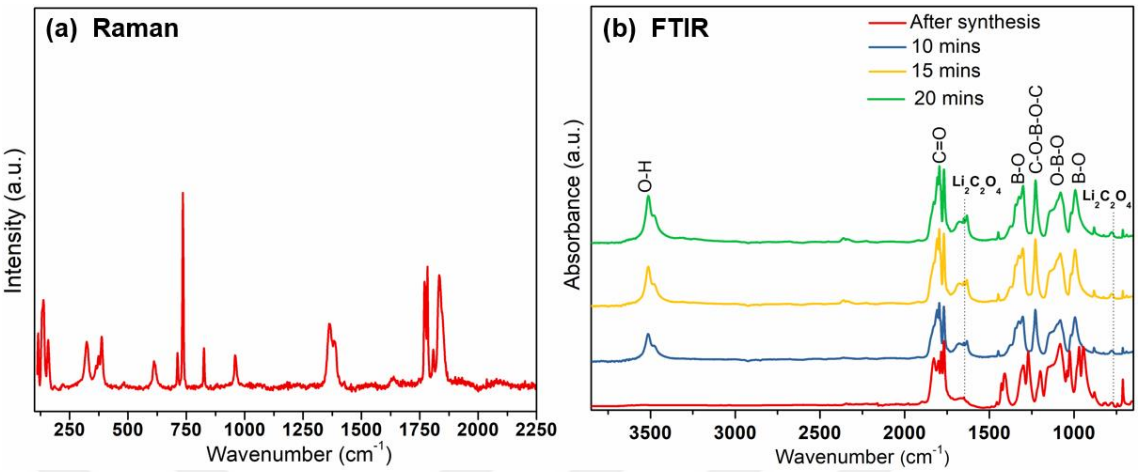

Figure 2.10: (a) Raman spectra of anhydrous LiBOB. (b) FTIR spectra of as synthesized and aged LiBOB showing the formation of monohydrate phase and secondary phases upon exposure to ambient conditions i.e. humidity in air.

To sum up, the detrimental effect of humidity during and after the synthesis of LiBOB is evident with the monohydrate phase formation that could further decompose mainly into $Li_2C_2O_4$ and amorphous other phases. These impurities could of course be eliminated through repeated recrystallization steps with polar aprotic organic solvents, but this would bring about additional complications, such as cost increases and environmental burden with the use of organic solvents. Therefore, high purity synthesis of anhydrous LiBOB with least possible steps is very important, and would decrease the number of recrystallization steps in case if they are needed. The employment and widespread application of LiBOB as an electrolyte additive in LIBs could be considered as limited in the current state-of-art. Yet, we think that this limitation is also present because of the unexpected or low quality results obtained due to the occurrence of impurities and hydrated phases [398-400, 405]. This occurrence and impurities may not even be realized by the unsuspecting, as they are very easy to form as we have shown here. Nevertheless,

with the proper use, LiBOB could be expected to bring superior electrochemical performances when it is used as an electrolyte additive for LIBs including cycling stability, rate capability, energy density and coulombic efficiency by preventing the electrolyte decomposition and the formation of dangerous byproducts [325, 387, 388, 406, 407]. Additionally, a protective LiBOB-derived SEI will develop on the electrode surface enhancing the interfacial stability for high temperature operations [372, 401].

2.5 Conclusion

LiBOB was synthesized under protective atmosphere using lithium carbonate, oxalic acid, and boric acid as low-cost starting materials by applying ceramic processing methods to achieve a high purity product. Aging investigations were also carried out to further evaluate the effect of humidity and the formation of $LiBOB.H_2O$ and impurities such as HBO_2, $Li_2C_2O_4$ that are undesirable in applications for high performance LIBs. According to the DTA results, the synthesis temperatures above 315 °C cause decomposition of anhydrous LiBOB into impurities and at temperatures below 200 °C the formation of the monohydrate phase may result in the capacity fade and poor cycling performance for LIBs. As shown from the XRPD data and FTIR and Raman spectra, the resulting salt is anhydrous and high purity over ~ 99 wt-%; thus, a higher purity is obtained with fewer and practical processing steps compared to some commercial products and LiBOB reported in the literature. XRPD analysis showed that ~ 42 wt-% monohydrate phase ($LiBOB.H_2O$) formed only after 5 minutes of aging at RT (~25 °C)-70 % relative humidity, and only after 30 minutes of exposure to air under given conditions, the complete hydration occurred. From the SEM micrographs, consistent with the findings from XRPD and FTIR, the structural deterioration of LiBOB can also be tracked. The longer exposures in the time scale of days further decomposed $LiBOB.H_2O$ into other impurity phases, mainly $Li_2C_2O_4$. Keeping the purity high and avoiding

exposure to humidity in all processing steps are crucial for stable performance of batteries using LiBOB either as an electrolyte salt or additive and towards widespread applications, especially high voltage LIBs.

Chapter 3:

Surface Modified TiO_2 / Reduced Graphite Oxide Nanocomposite Anodes for Lithium-Ion Batteries

3.1 Abstract

Anatase TiO_2 nanoparticles with an average crystallite size of ~ 20 nm are synthesized through a sol-gel method. A composite anode for Li-ion batteries is prepared with the synthesized TiO_2 nanoparticles and reduced graphite oxide (RGO) as the conductive carbon source. After the preparation of TiO_2/RGO nanocomposite, a novel surface modification is carried out by the employment of H_2O_2 to enhance the overall electrochemical performance of nanocomposite anode (TiO_2/RGO-P composite). The physical and chemical characterizations of the surface modified TiO_2/RGO-P composites are performed with X-ray powder diffraction (XRPD), X-ray Photoelectron Spectroscopy (XPS), scanning electron microscopy (SEM), and atomic force microscopy (AFM) analyses. The electrochemical performance of TiO_2/RGO-P composite electrodes is investigated via galvanostatic charge-discharge cycling tests in a potential window of 1.0 - 3.0 V. Compared to the plain TiO_2/RGO composite anode, the TiO_2/RGO-P composite anode has higher reversible capacities and better cycling performance due to the enhanced and stable formation of 3D channels of TiO_2 nanoparticles with RGO stemming from the surface modification with H_2O_2. The TiO_2/RGO-P composite anode delivers reversible discharge capacities around 291 mA h g^{-1} at a rate of 100 mA g^{-1}, whereas the value stays at 214 and 143 mA h g^{-1} for the plain TiO_2/RGO composite and TiO_2

nanoparticle without any RGO, respectively.

3.2 Introduction

Among the available battery technologies, Lithium-ion Batteries (LIBs) are one of the best performing power sources in portable electronics and hybrid/electric vehicles (EVs) due to their high energy density, high capacity, long cycle life, low self-discharge rate and little memory effect [11, 408, 409]. However, the currently existing electrode materials cannot meet the high energy density, safety, long lifespan and low-cost requirements for various energy storage applications. Since the introduction of LIBs into the market, there have been ongoing research efforts to develop alternative anode materials due to the dendrite formation and safety issues posed by metallic Li anodes [410].

Among alternatives, titanium dioxide has been extensively used as anode materials owing to their outstanding properties including high capacity, safety in comparison to graphite, silicon, and tin anodes [411]. In addition, TiO_2 has superior features such as high theoretical capacity of 335 mA h g^{-1}, low toxicity, low cost, chemical stability, and feasibility with various types of nanostructures. With the employment of nanoparticles, the Li-ion diffusion length can be reduced thereby improving the flux. In addition, TiO_2 exhibits a small volume change during Li-ion insertion/extraction (3 - 4 %), leading thus to long term cyclability [176, 412, 413]. There are various factors including particle size, surface area, and morphology which determine the Li-ion insertion/extraction process [168, 414]. Kasuga et al. [415, 416] synthesized TiO_2 nanotubes with a diameter of 8 nm and a length of 10 nm for the first time from the amorphous product by alkali treatment in order to improve their chemical, electric, and electromagnetic properties. Bruce et al. [279, 417, 418] first synthetized various types of nanostructured TiO_2, bronze (B) such as nanotubes and nanowires, and they investigated the effects on the performance of Li-ion batteries. It was revealed that TiO_2 (B) in the form of a nanowire, which has similar properties as $Li_4Ti_5O_{12}$ (175 mA h g^{-1}), shows two times higher

capacity [281]. Wagemaker et al. [276] investigated the effects of the particle size of anatase TiO_2 nanoparticles on the insertion reactions and it was found that the smaller particle size enhances electrochemical properties.

There are different phases of TiO_2 that are anatase (space group $I4_1/amd$), rutile ($P4_2/mnm$, thermodynamically more stable), brookite (*Pbca*), and TiO_2-B (bronze, C2/*m*) [419, 420]. Among these, the anatase form is considered the most electrochemically-active Li insertion host [421-423]. However, the low electrical conductivity (~10^{-13} S cm^{-1}) of TiO_2 and the low Li^+ ion diffusion coefficient limits its performance as an anode material [424-426]. Coating of TiO_2 with carbon, such as graphene, is used as a general method to improve its electrical conductivity [262, 294, 427-430]. Graphene has received great attention owing to its superior properties including high electron mobility (~15 000 $cm^2 V^{-1} s^{-1}$), high electrical conductivity (200 S m^{-1}), large specific surface area (2630 $m^2 g^{-1}$), chemical stability, structural flexibility, and mechanical properties in order to improve rate capability and cycling performance of TiO_2 as an anode material [420, 431-435]. Wang et al. [434] prepared a nanostructured TiO_2-graphene composite material by using an anionic surfactant to increase the hydrophilicity of graphene and to improve the compatibility between graphene and TiO_2 particles. They reported that the hybrid material showed a two times higher capacity compared to pure TiO_2 nanoparticles. Xin et al. [262] reported a scalable synthesis of TiO_2/graphene nanocomposite with a high specific capacity of 230 mA h g^{-1} at 0.1 C. Similarly, Li et al. [436] synthesized ultra-dispersed TiO_2/graphene composite with a high specific capacity of 94 mA h g^{-1} at 10 A g^{-1}. Additionally, Liu et al. [437] reported hybrid TiO_2 nanoparticles *in situ* grown on RGO nanosheets with a capacity of 186.6 mA h g^{-1} after 100 cycles at 0.1 A g^{-1}. Also, Wang et al. [431] synthesized a hydrogenated TiO_2-RGO nanocomposite through a hydrogenation treatment process. They found that hydrogenated-TiO_2 (H-TiO_2) nanoparticles were homogenously dispersed on the surface of RGO which is crucial for an efficient Li storage

and improved rate capability. Similarly, Zeng et al. [438] developed a hydrogenation strategy for adjusting the particle size of anatase TiO_2 nanoparticles by increasing the concentration of oxygen vacancies.

As summarized, though great progresses have been made for the use of TiO_2-based nanocomposites as anode materials for Li-ion batteries, there is still room for improvement especially in terms of practical surface modifications that can lead to higher capacities, long cycle life and enhanced rate capabilities. In line with this matter, herein, we demonstrate a simple surface modification via the employment of H_2O_2 for the TiO_2 nanoparticles / reduced graphite oxide (RGO) nanocomposite anodes. TiO_2 nanoparticles are synthesized by a sol-gel method in the range of 10-20 nm. Then, TiO_2/RGO (reduced graphite oxide) composites are fabricated as anode materials for Li-ion batteries, and a novel surface treatment method for TiO_2/RGO composite is applied by using H_2O_2 in order to improve the electrochemical performance and cycling stability. The surface treated TiO_2/RGO composite electrodes are investigated via galvanostatic charge-discharge cycling tests in a potential window of 1.0 - 3.0 V, and it is found to deliver higher reversible capacities and to be more stable compared to the TiO_2 nanoparticles and plain TiO_2/RGO composite electrodes.

3.3 Experimental Section

3.3.1 Synthesis

Anatase TiO_2 nanoparticles were synthesized by a sol-gel method using Titanium (IV) n-butoxide (TBOT) (Alfa Aesar) as a precursor. 6 mL (6 g) TBOT was mixed with 2-propanol, and this solution was added dropwise into a 50 mL nitric acid solution (48 mL water and 2 mL nitric acid) under vigorous stirring (pH=1.3). The suspension was continually stirred at 80 °C for 20 hours. After the formation of a white suspension, the latter was evaporated at 80 °C and rinsed with deionized water. The resulting white precipitates were dried at 60 °C overnight and calcined at 250 °C for 6 hours under argon flow, and the anatase TiO_2 nanoparticles were

obtained afterwards. For the preparation of the TiO_2/RGO composite electrode material, synthesized TiO_2 nanoparticles were thoroughly mixed with graphite oxide (GO) ~ 66.6 wt.% TiO_2 with ~ 33.3 wt.% GO in an agate mortar followed by a thermal treatment at 275 °C for 8 h under dry air flow to reduce the GO into the RGO. The final carbon content was ~18 wt.% in TiO_2/RGO composite after the reduction. For the surface treatment of anode material, 10 ml of hydrogen peroxide solution (30%, Merck) was mixed 50 mg TiO_2/RGO composite under constant stirring at 75 ºC for 6 hours. Finally, this surface modified TiO_2/RGO-P composite was dried at 70 °C for 24 hours. The final carbon content was ~17 wt.% for the TiO_2/RGO-P composite.

3.3.2 Material Characterization

XRPD characterization was done by using a Rigaku MiniFlex X-Ray diffractometer (operated at 15 mA, 40 kV). The carbon content measurements were carried out in a Thermo scientific flash 2000 CHNS-O analyzer. The distribution of the RGO content was confirmed by energy-dispersive X-ray spectroscopy (EDX) performed with Zeiss Ultra Plus Field Emission Detector Scanning Electron Microscopy equipped with 123 eV resolution Bruker XFlash® 5010 EDS detector under 13 kV EHT. The morphologies of the prepared composites were characterized by the same Scanning electron microscope. X-ray photoelectron spectroscopy (XPS) was carried on in a Thermo Scientific K-Alpha spectrometer using an Aluminum anode (Al Kα= 1468.3 eV) at an electron take-off angle of 90º (between the sample surface and the axis of the analyzer lens). The spectra were recorded using an Avantage 5.9 data system. The binding energy scale was calibrated by assigning the C1 s signal at 284.5 eV. Fourier transform infrared (FTIR) spectra of samples were recorded on a Thermo Scientific iS50 FT-IR. The surface roughness of anode materials was characterized by tapping mode of an atomic force microscope (AFM) (Bruker Dimension Icon AFM).

3.3.3 Electrochemical Tests

For the fabrication of TiO_2 based anode, synthesized anatase TiO_2 nanoparticles, (65 wt.%) active material, (25 wt.%) conductive carbon (Super P® Timcal) and (10 wt.%), polyvinylidene fluoride (PVDF) (Sigma-Aldrich) binder were mixed in an agate mortar. For the preparation of TiO_2/RGO composite electrode, (80 wt.%), (10 wt.%) conductive carbon (Super P® Timcal) and (10 wt.%) PVDF binder were mixed in an agate mortar. After that, a slurry of this powder was ultrasonicated in THF (≥99%, Merck) : toluene (≥99%, Merck) (4 : 1) solution. This slurry was cast on Titanium (Ti) current collectors and dried at 80 °C overnight. The loading of the active material on Ti current collectors was approximately ~ 4 mg / cm^2 after drying. Swagelok type cells were assembled in a argon filled glove-box using polypropylene (Celgard) and glass fiber membrane (Whatman®) separators, Li metal disks cut from Li rods serving as a counter and reference electrode, and 1 M $LiPF_6$ in ethylene carbonate (EC) and dimethyl carbonate (DMC) (1 : 1) solution as the electrolyte. The galvanostatic charge-discharge cycling tests were carried out using a Neware battery tester BTS3000 in a potential window of 1.0 - 3.0 V vs. Li/Li^+.

3.4 Results and Discussion

The synthesis scheme for anatase TiO_2 nanoparticles, TiO_2/RGO composite and surface modified TiO_2/RGO is shown in **Figure 3.1a**. TiO_2 nanoparticles are synthesized through the hydrolysis of titanium butoxide (**Eq. (3.1)**) and subsequent condensation (**Eq. (3.2)**) [439].

$$Ti(OC_4H_9)_4 + 4H_2O \rightarrow Ti(OH)_4 + 4C_4H_9OH \quad \textbf{(3.1)}$$

$$m Ti(OH)_4 \rightarrow (TiO_2)_m + 2mH_2O \quad \textbf{(3.2)}$$

Graphite oxide (GO) is integrated by mechanical mixing and is partially reduced afterwards in order to obtain a composite anode material with enhanced electrical conductivity and specific capacity. After thermal treatment at 275 °C, TiO_2/GO is transformed to TiO_2/RGO.

In order to further increase electrochemical performance and cycling properties of the composite anode material, a surface modification process is applied through the employment of H_2O_2 (**Figure 3.1a**).

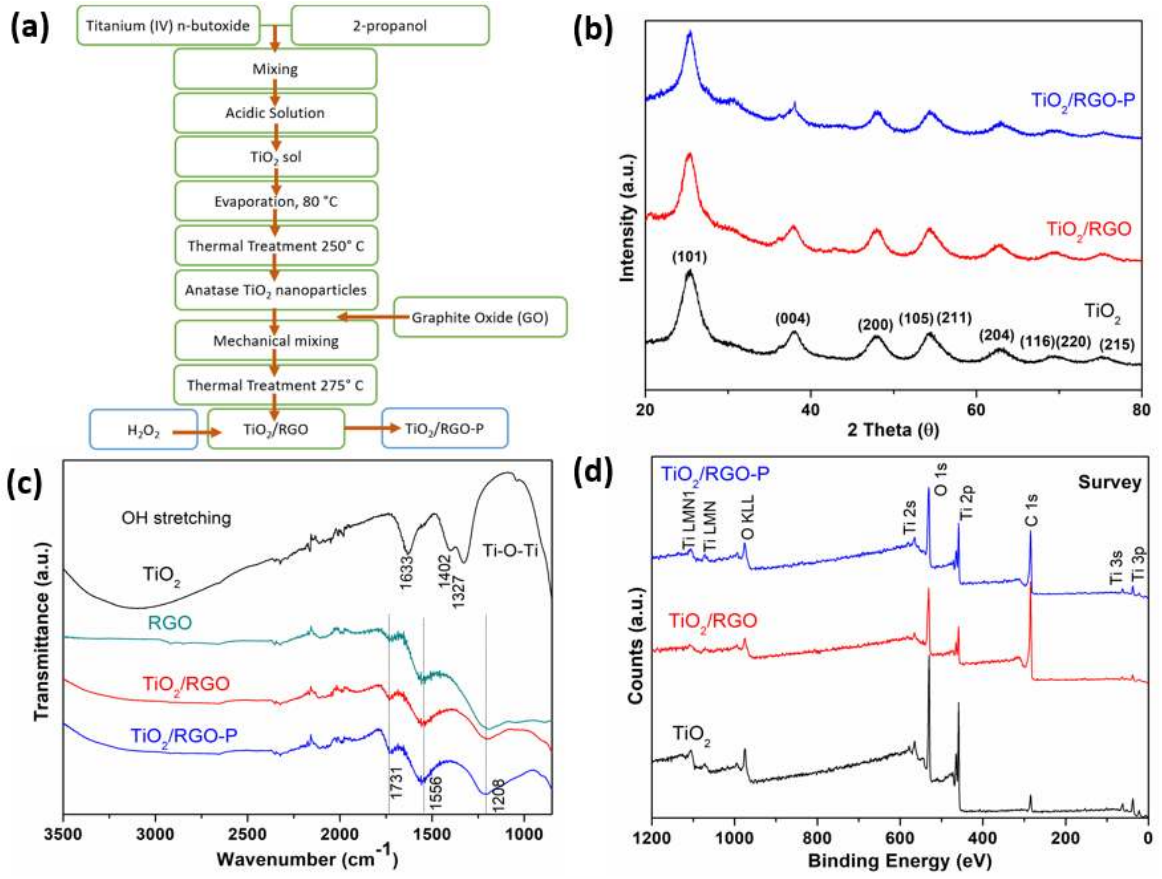

Figure 3.1: (a) Schematic illustration for the fabrication process of TiO_2 nanoparticles, TiO_2/RGO composite and surface modified TiO_2/RGO composite, (b) XRD patterns of TiO_2 nanoparticles, TiO_2/RGO composite, TiO_2/RGO-P composite, (c) FTIR spectra of TiO_2 nanoparticles, RGO, TiO_2/RGO composite, TiO_2/RGO-P composite, and (d) XPS survey spectra of TiO_2 nanoparticles, TiO_2/RGO composite, TiO_2/RGO-P composite.

XRD powder patterns of TiO_2, TiO_2/RGO, TiO_2/RGO-P are shown in **Figure 3.1b**. According to XRPD characterization, both TiO_2/RGO and surface modified TiO_2/RGO-P composite show similar diffractions corresponding to (101), (004), (200), (105) and (211) planes stemming from pure anatase TiO_2 nanoparticles (JCPDS 21-1272, space group: $I4_1/amd$, a =

3.7852 Å, c = 9.5139 Å) [275]. No reflections from RGO could be observed due to its low ratio in the composite and low diffraction intensity of few layered compound [440]. Additionally, this observation can be attributed to the homogenous dispersion RGO flakes among TiO_2 nanoparticles [441]. The mean crystallite size of TiO_2 was found to be app. 20 nm by using the Halder Wagner (HW) method [442] and Scherrer's equation: $\tau = (K\lambda)/(\beta \cos \theta)$, where τ is the mean size of the ordered (crystalline) domains, which may be smaller or equal to the grain size, K is the shape factor with a typical value of 0.9, λ is the X-ray wavelength, β is the line broadening full width at half maximum (FWHM) peak height in radians. The size of TiO_2 crystallites was found to increase from ~ 20 nm to ~ 25 nm after the heat treatment to form the TiO_2/RGO composite.

FTIR spectra of TiO_2, RGO, TiO_2/RGO, and TiO_2/RGO-P are depicted in **Figure 3.1c**. The broad peak in the range of 3000-3500 cm^{-1} indicates the O-H stretching vibrations of oxygen containing functional groups such as OH, -COOH groups that is diminished after the thermal treatment to obtain TiO_2/RGO composite [443]. Vibrational bands at ca. 1400-1600 cm^{-1} could be assigned to the Ti-O-C stretching modes indicating the interaction between TiO_2 and RGO, whereas the broad absorption below 1000 cm^{-1} is attributed to the bending modes of Ti-O-Ti [444, 445]. It can be speculated that the intensity of the broad peak at 3000-3500 cm^{-1} slightly increases for TiO_2/RGO-P in comparison to TiO_2/RGO after the H_2O_2 treatment, indicating thus the surface oxidation and an increase in the hydrophilic nature of the RGO in the composite. XPS characterization is done to further investigate the surface properties of the composites. According to the survey spectrum (**Figure 3.1d**), the peaks at 459.08, 531.08, and 285.08 correspond to Ti 2p, O 1s, and C 1s peaks, respectively; that is further discussed in **Figure 3.7** [445].

We turn to Scanning Electron Microscopy images to discuss the long-range arrangement and morphology of TiO_2, RGO, TiO_2/RGO, and TiO_2/RGO-P composites.

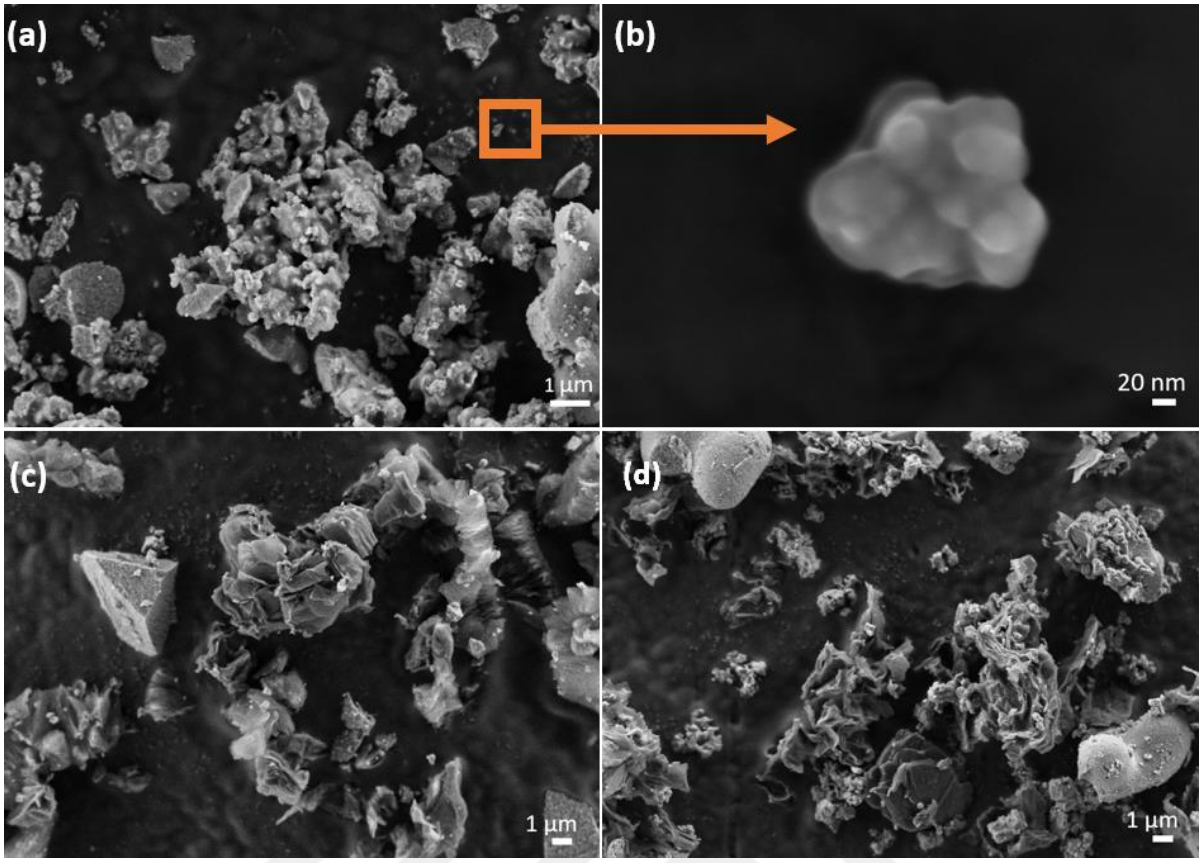

Figure 3.2: Scanning electron microscopy (SEM) images of (a) sol-gel synthesized anatase TiO_2 nanoparticles, (b) magnified region in (a) displaying TiO_2 crystallites, (c) TiO_2/RGO composite, and (d) TiO_2/RGO-P composite.

TiO_2 nanoparticles are sized in the range of ca. 15 - 25 nm forming larger agglomerates that is in line with the crystallite size determination from XRPD patterns (**Figure 3.2a & Figure 3.2b, Figure 3.3**). After the composite formation with RGO, (**Figure 3.2c**), TiO_2 particles and larger agglomerates were covered by RGO flakes that can act as a protective coating while improving the long and short range conductivity within the electrodes [446-448]. As shown in the **Figure 3.2d** and the AFM topography images (**Figure 3.4**) the surface modification with H_2O_2 changed the homogeneity of composites leading to a more uniform dispersion of TiO_2 nanoparticles within the RGO flakes, plausibly due to changes in the hydrophilicity, wetting and mechanical stability with surface oxidation [449, 450].

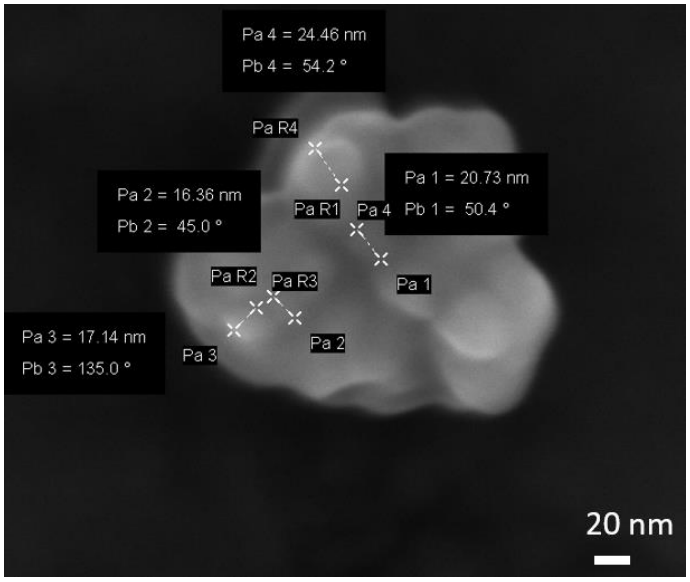

Figure 3.3: SEM image of the sol-gel synthesized anatase TiO_2 crystallites forming larger agglomerates.

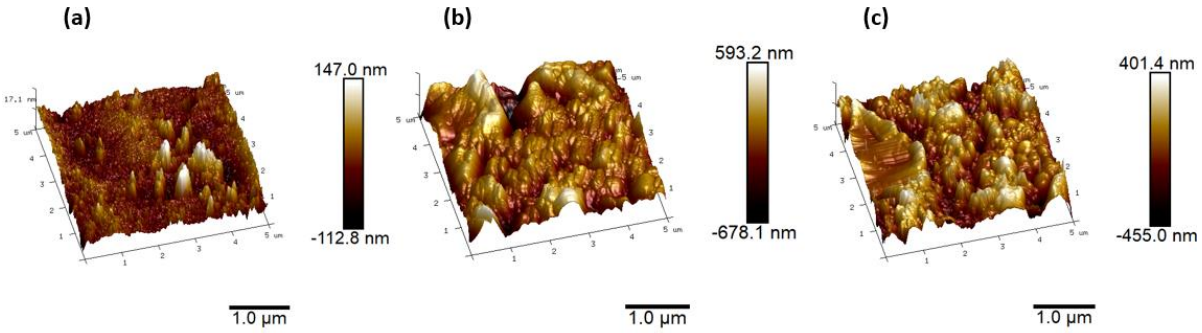

Figure 3.4: AFM topography images (5 × 5 µm) of (a) TiO_2 anode, (b) TiO_2/RGO anode, and (c) TiO_2/RGO-P anode.

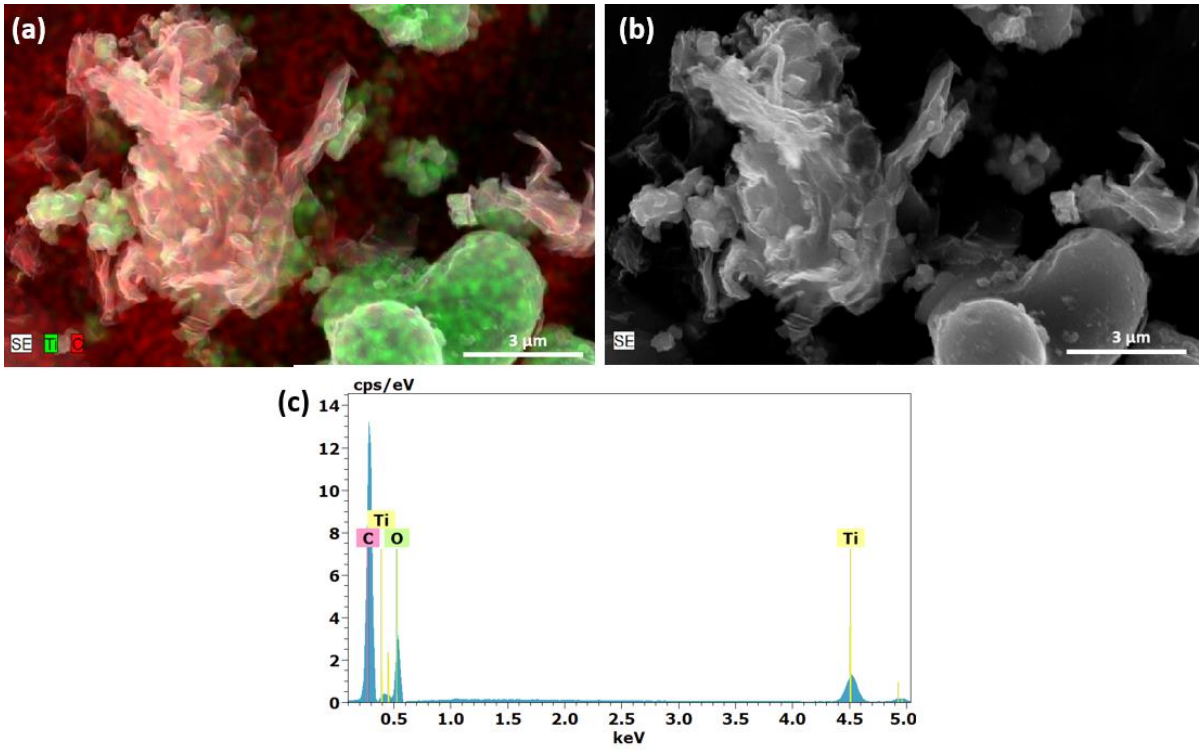

Figure 3.5: (a) Elemental map obtained by EDX (Ti and C) shown in green and red colors, respectively, (b) SEM micrograph of the mapped area, and (c) EDX analysis result showing the characteristic energies of K_α and L_α radiation of EDX detectable elements present in the active material for the TiO_2/RGO-P composite.

The SEM-EDX analysis also shows that the peroxide treated composite has an improved homogeneity. The RGO coverage and the integration of TiO_2 nanoparticles into the conducting carbon network is better compared to the plain TiO_2/RGO composite (**Figure 3.2d & Figure 3.5**), whereas RGO flakes have a more freestanding nature in the plain composite before the peroxide treatment (**Figure 3.6**). However, there are still large agglomerates in TiO_2/RGO-P composite that are not well integrated into the conductive carbon. These larger agglomerates are expected to be eliminated by further improving the surface modification process.

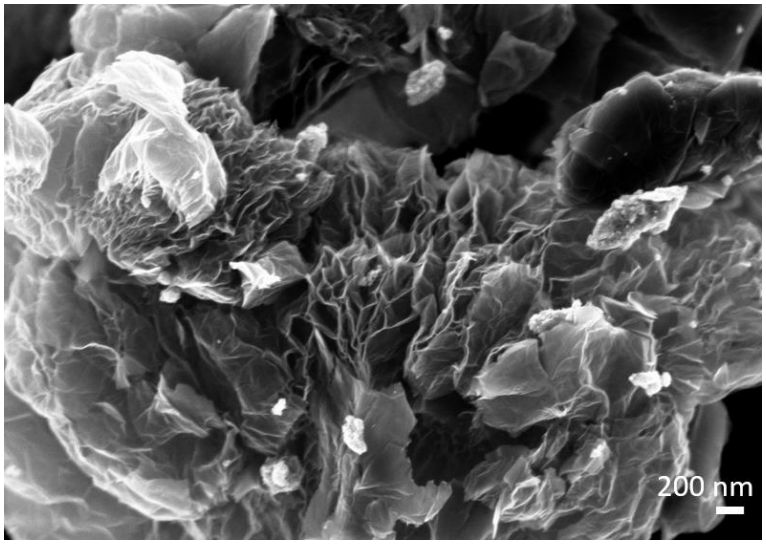

Figure 3.6: SEM image of the TiO_2/RGO composite.

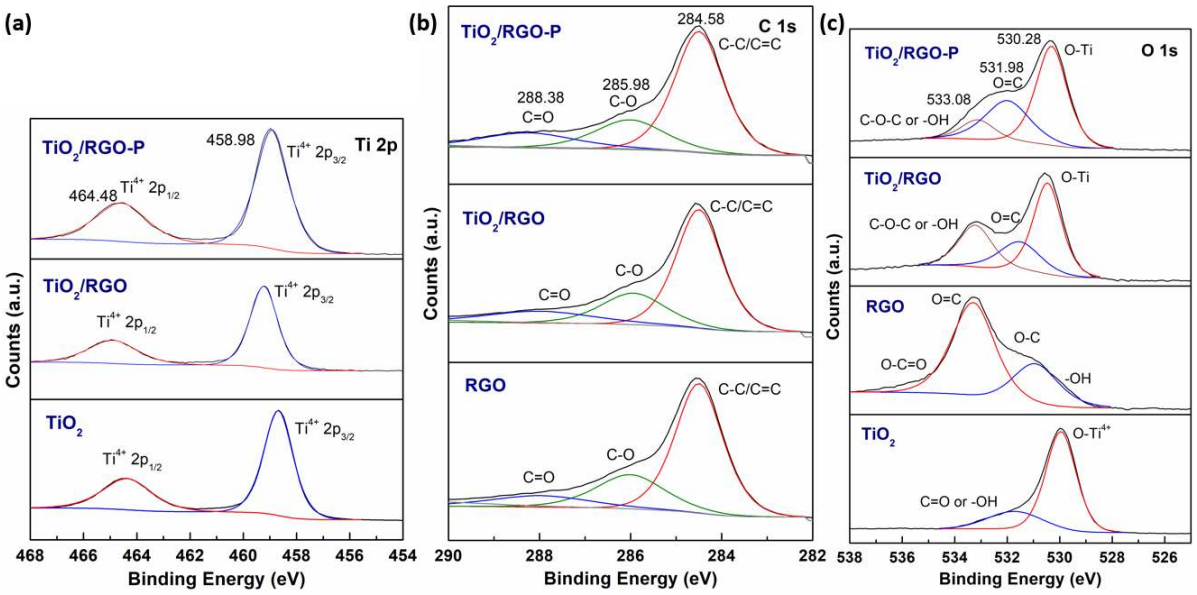

Figure 3.7: Typical high resolution XPS of (a) Ti 2p, (b) C 1s, and (c) O 1s for TiO_2, RGO, TiO_2/RGO, TiO_2/RGO-P composite.

Typical high resolution XPS analyses are depicted in **Figure 3.7**. From the high resolution Ti 2p scan (**Figure 3.7a**), the bands at 458.98, and 464.48 eV can be attributed to Ti $2p_{3/2}$ and Ti $2p_{1/2}$ spin-orbital splitting electrons in the Ti^{4+} state [420, 451]. As shown in the C 1s spectrum (**Figure 3.7b**), the peaks at the binding energies 284.58, 285.98, and 288.38 eV are assigned

to C-C, C-O, and C=O, respectively [452]. The O 1s spectrum (**Figure 3.7c**) can be divided into three peaks at 530.28, 531.98, and 533.08, corresponding to O-Ti, O=C, and C-O-C or -OH respectively [425]. By the treatment of TiO_2/RGO with hydrogen peroxide, surface oxidation is expected which improves the encapsulation of TiO_2 (**Figure 3.8**) that is in line with the intensity changes in O 1s spectra [449]. Additionally, it can be speculated that the hydrophilicity of graphene layers may improve the adhesion of different components within the composite anode due to the stability of the corresponding graphene-TiO_2 interface.

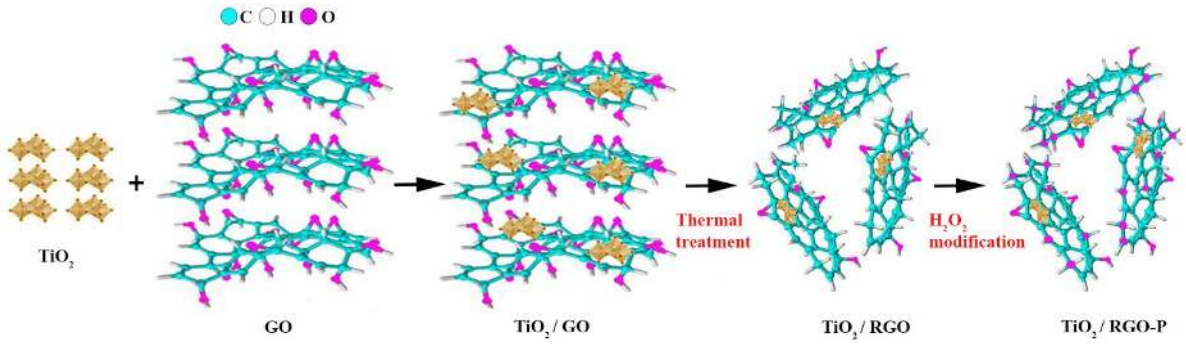

Figure 3.8: Schematic illustration of the fabrication process of surface modified TiO_2/RGO-P composite.

The lithium insertion/extraction properties of anode materials were evaluated by galvanostatic charge discharge measurements within a voltage window of 1.0 - 3.0 V. In general, for anatase TiO_2 anodes, lithium insertion and extraction can be tracked by the following reaction (**Eq. (3.3)**):

$$TiO_2 + xLi^+ + xe^- \leftrightarrow LixTiO_2\ (x \leq 1) \qquad \textbf{(3.3)}$$

The theoretical capacity of anatase TiO_2 is reported as ~ 168 mA h g^{-1} and 335 mA h g^{-1} for the fully reversible reaction if x=0.5 and x = 1.0, respectively [294, 453].

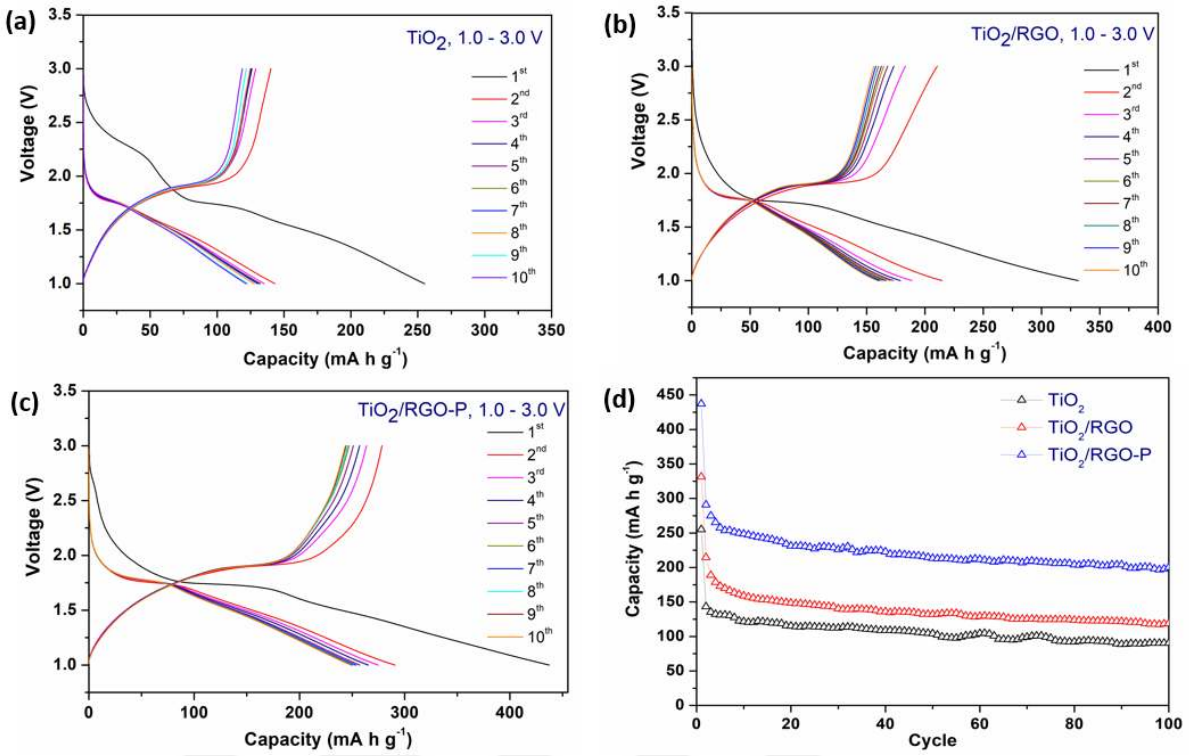

Figure 3.9: The first ten galvanostatic charge−discharge curves of the (a) TiO_2, (b) TiO_2/RGO, and (c) TiO_2/RGO-P cycled between 1.0 - 3.0 V at a current rate of 100 mA g^{-1}, and (d) cycling performances of TiO_2, TiO_2/RGO, and TiO_2/RGO-P at a current density of 100 mA g^{-1}.

Figure 3.9 shows the first ten galvanostatic charge−discharge curves of the TiO_2, TiO_2/RGO, and TiO_2/RGO-P cycled between 1.0 - 3.0 V at a rate of 100 mA g^{-1}. As shown in **Figure 3.9**, the reversible specific capacity for anatase TiO_2 nanoparticles is 143.2 mA h g^{-1} at the 2nd discharge cycle, while the capacity has increased to 214.5 mA h g^{-1} for the TiO_2/RGO composite anode. The electrochemical performance was further improved after H_2O_2 treatment, as the reversible capacity increases to 290.8 mA h g^{-1} at the 2nd discharge cycle for the TiO_2/RGO-P composite. The cycling stability was also enhanced in comparison to plain nanoparticles and composite, as discharge capacities of 200.3 and 155.7 mA h g^{-1} are still delivered at 100th and 300th cycles for the TiO_2/RGO-P composite with high coulombic efficiencies above 99 %. (**Figure 3.9d and Figure 3.10**) The average capacity loss per cycle

is only ~ 0.31 % for the TiO_2/RGO-P composite anode, while this value is 0.37 % and 0.44 % for TiO_2 nanoparticles and the plain TiO_2/RGO composite, respectively.

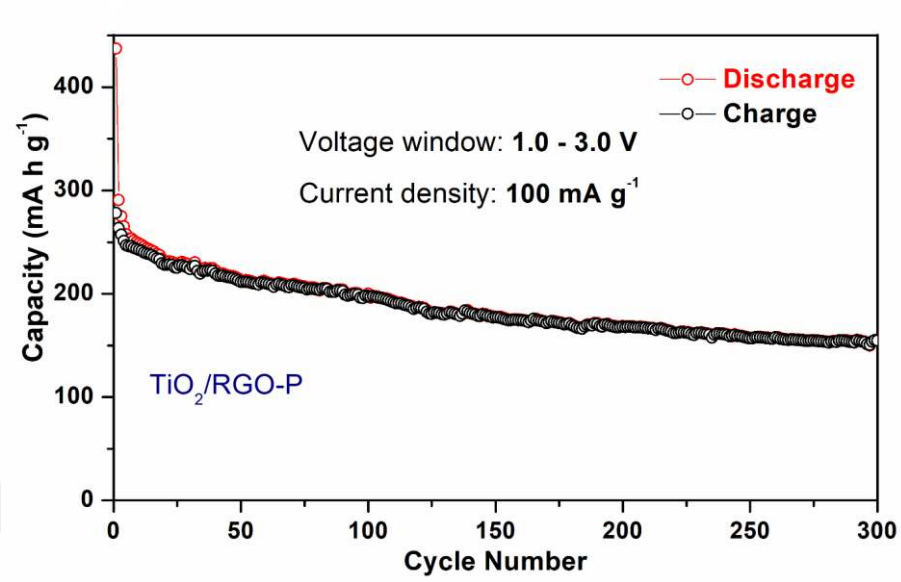

Figure 3.10: Cycling performance of the TiO_2/RGO-P composite (300 cycle).

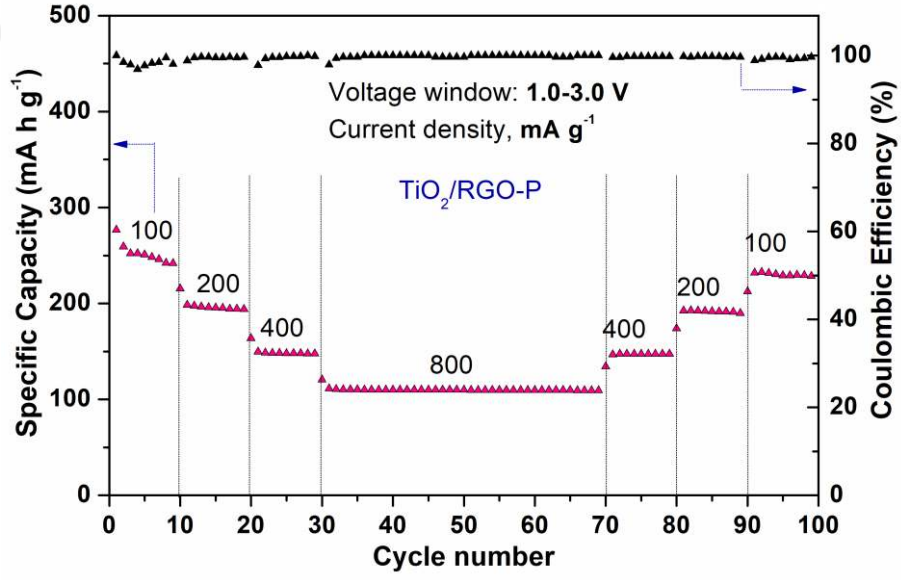

Figure 3.11: The rate capability of TiO_2/RGO-P composite within 3.0 – 1.0 V at 100, 200, 400, and 800 mA g^{-1} rate (at room temperature).

Figure 3.11 shows the rate capability test for the TiO_2/RGO-P composite anode within 3.0 – 1.0 V. The capacities in the range of 250, 195, 148 and 110 mA h g^{-1} are delivered at rates of 100, 200, 400, and 800 mA g^{-1}, respectively. When the rate is changed back to 100 mA g^{-1}, the discharge capacity recovers to 232 mA h g^{-1} at the 91st cycle confirming the favorable response of the electrochemical system at high charge/discharge during relatively extended use and cycles. The TiO_2/RGO-P composite shows better rate capability performance compared to the TiO_2 and pristine TiO_2/RGO anodes as shown in **Figure 3.12**.

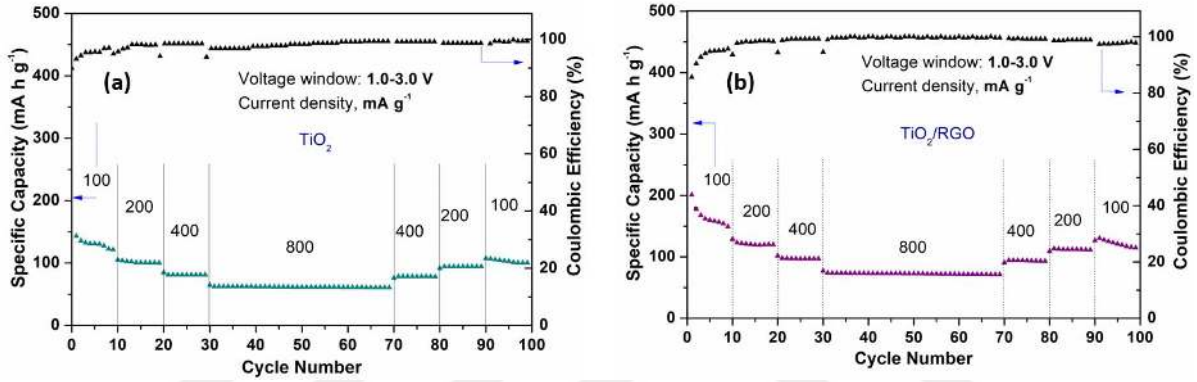

Figure 3.12: The rate capability of TiO_2, TiO_2/RGO composite electrode within 3.0 – 1.0 V at 100, 200, 400, and 800 mA g^{-1} rate (at room temperature).

The enhanced electrochemical properties for the TiO_2/RGO-P composite anode can be attributed to number of reasons. The surface oxidation and increase of oxygen groups, as shown by XPS and FTIR analyses, provide a better interaction between RGO and TiO_2 leading to a more homogenous and mechanically stable composite structure; thus, RGO network better facilitates Li^+ ion and electron transports within the electrode. The stable RGO layer also prevents contact losses under extensive cycling and acts as a protective layer against cycling by-products (e.g. HF, PF_5). The surface roughness increases after applying the surface oxidation process which results in better contact properties as seen from AFM images (**Figure 3.4**). By the treatment of TiO_2/RGO with hydrogen peroxide, surface oxidation is expected which improves the encapsulation of TiO_2 that is in line with the intensity changes in O 1s

spectra. The treatment of TiO_2 by hydrogen peroxide was also shown in previous investigations [449], and this encapsulation of active material TiO_2 is expected to protect the active anode material from detrimental cycling by products. The intimate embedding of TiO_2 into the RGO flakes seemingly improves short range conductivity as well as long range conductivity within the whole electrode as noticeably better kinetic properties are obtained in terms of a decreased polarization, cycling stability and a better rate capability for the TiO_2/RGO-P composite anode. The results obtained here for the surface modified composite TiO_2 based anodes are considered to be promising and may encourage further investigations on similar electrochemical systems with new and comparable surface modifications.

3.5 Conclusion

In summary, anatase TiO_2 nanoparticles with a crystallite size of ~ 20 nm were synthesized through a sol-gel method. RGO was used as a protective coating for TiO_2 nanoparticles to form composites with enhanced electrochemical properties such as improved conductivity, specific surface area, and mechanical and cycling stability. After the fabrication of the nanostructured TiO_2/RGO composite anode, a novel surface modification process was applied by using H_2O_2 in order to further improve electrochemical properties; mainly cycling stability and rate capability. The surface modification with H_2O_2 leads to more homogeneous dispersion of TiO_2 nanoparticles within the RGO flakes due to the improvement of hydrophilicity and mechanical stability with surface oxidation, as observed from SEM-EDX, FTIR and XPS investigations.

The galvanostatic charge-discharge cycling tests in a potential window of 1.0 - 3.0 V at various rates were performed to study the electrochemical performance of composite anodes. The surface modified TiO_2/RGO-P composite anode delivered a reversible discharge capacity around 291 mA h g^{-1} at a rate of 100 mA g^{-1}, while the value stayed at 214 and 143 mA h g^{-1} for the pristine TiO_2/RGO composite and TiO_2 nanoparticle anodes, respectively. The cycling

performance for TiO_2/RGO-P composite anode was also improved with a high coulombic efficiency above 99 % and with an average discharge capacity loss of ~ 0.31% per cycle for the first 100 cycles stemming from the more mechanically and chemically stable composite structure compared to the plain composite.

Chapter 4:

High Voltage $LiCoO_2$ Cathodes with Water Free Lithium Bis(oxalate) Borate (LiBOB) for Lithium-Ion Batteries

4.1 Abstract

Lithium bis(oxalate) borate, $LiB(C_2O_4)_2$ (LiBOB) could be used as an electrolyte additive to prevent structural change and electrolyte decomposition by developing a protective solid electrolyte interphase (SEI) on the cathode surface. However, impurities present in LiBOB results in significant electrochemical performance decays related to higher full cell impedance. We have previously reported the synthesis method of anhydrous LiBOB with various physical and chemical characterizations to investigate the impact of impurities and moisture for lithium-ion batteries (LIBs). Here, a novel purification technique is performed to remove these impurities within LiBOB that we further added 1 wt.% in 1 M $LiPF_6$ in EC:DMC (1:1) electrolyte to achieve more stable cycling performance of high voltage $LiCoO_2$ (LCO) cathode. The phase and purity of as-synthesized LiBOB and recrystallized LiBOB is determined by a combination of X-ray powder diffraction (XRPD), Fourier-transform infrared (FTIR) spectra and scanning electron microscopy (SEM) measurements. The LIB performance with the addition of high purity LiBOB as an electrolyte additive is investigated via galvanostatic charge-discharge cycling, rate capability and cyclic voltammetry (CV) measurements within a voltage range of 3.0 – 4.4 V. The cell containing 1 wt.% recrystallized LiBOB shows superior cycling performance, rate capability with higher energy density and

coulombic efficiency in comparison with the reference cell through the formation of a passivation layer on the LCO surface. Thus, for LiBOB added cell, the crystal structure of $LiCoO_2$ is well-maintained even at higher potential after 100 cycles according to the ex-situ XRPD and SEM analyses. Therefore, high purity LiBOB improves the interfacial stability of LCO cathode by inhibiting oxidative decomposition of electrolyte, undesirable structural changes and cobalt dissolution bringing about safer cycling at high operation voltages.

4.2 Introduction

Lithium-ion batteries (LIBs) have been extensively used in portable electronics, electric vehicles (EVs) and energy storage devices in terms of high energy density, high capacity, long cycle life, low self-discharge rate and little memory effect [11-14, 408, 409]. In order to meet higher energy and power density requirements, many efforts were made to increase the cut-off voltage of current cathode materials [30, 31]. However, at high voltages, capacity fade, poor cycling performance and safety issues can occur due to the oxidative decomposition of the electrolyte [454, 455]. The lithium transition metal oxides such as $LiCoO_2$ [6, 17, 18], NMC derivatives [456-458], $LiMn_2O_4$ [19, 20] and $LiFePO_4$ [21-23] are the most commercially used cathode materials for LIBs. Among these, $LiCoO_2$ (LCO) has received great attention because of its high theoretical capacity, high compacted density (4.1-4.2 g cm^{-3}), good cycling stability, excellent rate capability, and high safety [42-45]. However, LCO gives a moderate specific capacity of 130-140 mA h g^{-1} in a potential window of 3.0 - 4.2 V vs. Li^+/Li for 0.5 Li^+ exchange even though its theoretical capacity of 274 mA h g^{-1} for 1 Li^+ exchange [41, 48, 49, 459]. In addition, LCO cathodes may suffer from capacity fade at higher potentials due to the cobalt dissolution, structural changes, electrolyte degradation, HF attack, and impedance increase at the surface leading to performance degradation [51-54]. In order to solve this issue, there has been ongoing efforts including the formation of a protective solid electrolyte interphase (SEI) with various electrolyte additives [41, 431, 460, 461].

Presently, $LiPF_6$ in ethyl carbonate (EC)-dimethyl carbonate (DMC) solution is the most widely used electrolyte in LIBs. Nevertheless, $LiPF_6$ is prone to hazardous degradation reactions resulting in undesirable side effects and safety problems. It decomposes into LiF and PF_5 at high temperatures reacting with water to produce HF which deteriorates the cell performance [25, 327, 388, 462, 463]. After long term cycle at higher voltages above 4.6 V, the cell impedance is susceptible to increase due to the electrolyte oxidation at the cathode side [377, 464]. On the other hand, lithium bis(oxalate) borate, $LiB(C_2O_4)_2$ (LiBOB), has received great attention as an electrolyte additive improving the electrolyte and cell stability by eliminating impedance rise at the cathode surface [387, 406, 407, 465, 466]. Xu et al. synthesized and used LiBOB as an electrolyte salt for LIBs for the first time [350, 386, 467]. LiBOB exhibits various outstanding properties including its more stable crystalline state and better thermal stability up to 300 °C than $LiPF_6$ [374], good stability in a wide potential window, good solubility in organic solvents, high conductivity in non-aqueous solvents, good cycling behavior, overcharge tolerance, environmental friendliness and low cost. More importantly, LiBOB forms a SEI that contains borate and oxalate groups on the graphite and silicon anode [314, 327, 367, 368, 382, 388, 468] with an ability to stabilize aluminum current collector up to 5.0 V vs. Li^+/Li [25, 469]. However, oxalate and carboxylate impurities in LiBOB samples have detrimental effects on the cell performance forming gas pressure to vent the cell. Therefore, these impurities should be eliminated by applying recrystallization processes [399, 470]. Yang et al. studied the impacts of impurities and moisture of LiBOB on the cycling performance by performing nuclear magnetic resonance spectroscopy (NMR), Fourier transform infrared spectroscopy (FTIR), and thermogravimetric analysis (TGA) measurements. They identified that the presence of lithium oxalate ($Li_2C_2O_4$) impurity results in insolubility of LiBOB in 3EC:7EMC solvent causing higher cell impedance. Additionally, the formation of $B(C_2O_4)(OH)$ and $LiB(C_2O_4)(OH)_2$ could be related to the storage of LiBOB in high-moisture conditions which also inhibits the dissolution in carbonate solutions [398].

Xu et al. showed that using LiBOB as an additive as 1-5% molar could be an effective approach to form a stable SEI on the graphite anode in a wide temperature range [471]. In another study, Aravindan et al. used 3 wt.% LiBOB as an additive in 1M $LiPF_6$ ethylene carbonate (EC):diethyl carbonate (DEC) electrolyte solution in order to increase cycling performance of $LiCoPO_4$ electrode [360]. Additionally, LiBOB has been used to improve cycling stability of high voltage cathodes by generating a protective SEI [369, 406, 465, 472]. Ha et al. investigated effects of LiBOB on the cycling stability of $LiNi_{0.5}Mn_{1.5}O_4$ at 60 °C [375]. Also, Dalavi et al. revealed that the addition of LiBOB enhances the electrochemical performance by forming a cathode passivation layer as well as preventing the formation of HF or PF_5 from the electrolyte [472]. Similarly, Lee et al. utilized LiBOB to form protective layer on the surface of $Li_{1.17}Ni_{0.17}Mn_{1.5}Co_{0.17}O_2$ cathodes by eliminating the electrolyte decomposition. They achieved 77.6% of discharge capacity with employing LiBOB-added electrolyte after 100 cycle [387]. In another study, Pieczonka et al. found that LiBOB stabilizes the electrolyte via trapping PF_5 when it was used for $LiNi_{0.42}Fe_{0.08}Mn_{1.5}O_4$ electrodes [465]. For another cathode material, $Li_{1.16}(Mn_{0.75}Ni_{0.25})_{0.84}O_2$, Lian and coworkers reported that the addition of LiBOB increases the cycling stability of by the formation of a SEI preventing the surface degradation and enhancing the interfacial stability [388].

Herein, we focus on these proven properties of LiBOB and look into the high voltage applications of Li_xCoO_2 ($x > 0.5$) together with LiBOB to implement the aforementioned advantages. There are some investigations for high voltage applications of Li_xCoO_2 showing the irreversible structural change, capacity fade and poor cycling performance at high operating voltages (> 4.2 V) [473-475]. The effects of suberonitrile (SUN) and LiBOB as electrolyte additives on the electrochemical performance of high voltage $LiCoO_2$ cathode were already tried in an earlier study [461]. However, it was revealed that capacity decreases rapidly when only LiBOB is used as an additive [461]. It might be thought that the use of unpurified

LiBOB could cause performance decay related to the humidity and impurities [476]. Thus, the main focus of this study is to develop high voltage applications of $LiCoO_2$ electrode by performing a different purification process for LiBOB to overcome above issues. To the best of our knowledge there are few reports studying high voltage $LiCoO_2$ cathode by using LiBOB as an electrolyte additive. We synthesize LiBOB by the stoichiometric reaction of oxalic acid ($C_2H_2O_4$), boric acid (H_3BO_3) and lithium carbonate (Li_2CO_3) in water [476]. A novel purification processes performed to obtain a high purity LiBOB and circumvent the detrimental effects of impurities. Then, LiBOB is used as an additive in 1 M $LiPF_6$ in EC:DMC (1:1) electrolyte solution in order to improve the electrochemical performance and the cycling stability of $LiCoO_2$ (LCO) cathode at high voltages (~ 4.4 V). The effects of LiBOB on the cycling performance is investigated via galvanostatic charge-discharge cycling tests in a potential window of 3.0 - 4.4 V, and it is found that the recrystallized LiBOB added electrolyte cells achieved more stable cycling performance compared to the performances with the plain electrolyte and with unpurified LiBOB.

4.3 Experimental Section

4.3.1 Recrystallization of LiBOB

High purity water free LiBOB was previously synthesized by a novel wet-chemical method as reported in our recent study [476]. LiBOB was obtained here similarly and 0.3 g of LiBOB was placed in a Schlenk tube, and then 20 mL of acetonitrile (99.8%, Merck) was added to dissolve the sample. The mixture was stirred at 40 °C for 2 h under argon flow. After 2 h, argon gas was closed for 0.5 h in order to settle down impurities. The LiBOB + acetonitrile solution was then transferred into the flask contained a cartridge filter via cannula and 60 mL of cold toluene (Merck) was added to form solid precipitate of LiBOB. The resulting solution was kept at 0 °C overnight to enhance the settlement of precipitates. Afterwards, the solution was evaporated at 120 °C under argon flow. Finally, the resulting recrystallized product was ground followed by a thermal treatment in a tube furnace at 250 °C under argon flow for 15 h

to further eliminate residual solvents. The schematic illustration for the recrystallization process was shown in **Figure 4.1b**.

4.3.2 Material Characterization

X-ray powder diffraction (XRPD) characterization was performed to determine the phase and purity of the samples by using a Rigaku MiniFlex X-Ray diffractometer (operated at 15 mA, 40 kV). Fourier transform infrared (FTIR) spectra of samples were recorded on a Thermo Scientific iS10 FT-IR Scanning electron microscopy (SEM) analysis was performed with a Zeiss Ultra Plus field emission GeminiSEM. The cycled cells were disassembled in an Argon filled glovebox and the electrodes were washed with tetrahydrofuran (THF) to remove residual impurities after cycling.

4.3.3 Electrochemical Tests

For the fabrication of the positive electrode $LiCoO_2$ (LCO) (Strem Chemicals), (70 wt.%) active material, (7.5 wt.%) graphite (Merck), (15 wt.%) conductive carbon (Super P® Timcal) and (7.5 wt.%), polyvinylidene fluoride (PVDF) (Sigma-Aldrich) binder were mixed in an agate mortar. After that, a slurry of this powder was ultrasonicated in THF (≥99%, Merck) : toluene (≥99%, Merck) (4 : 1) solution. This slurry was cast on Titanium (Ti) current collectors and dried at 80 °C overnight. The loading of the active material on Ti current collectors was approximately ~ 4-6 mg / cm^2 after drying. Swagelok type cells were assembled in a argon filled glove-box using polypropylene (Celgard) and glass fiber membrane (Whatman®) separators, Li metal disks cut from Li rods as the counter and reference electrode, and 1 M $LiPF_6$ in ethylene carbonate (EC) and dimethyl carbonate (DMC) (1 : 1) (Sigma-Aldrich) solution as the base electrolyte. For the preparation of LiBOB added electrolyte, 1 wt.% LiBOB (0.07 mol L^{-1}) was dissolved in the base electrolyte overnight in an argon-filled glove-box. The galvanostatic charge-discharge cycling tests were carried out using a Neware battery tester BTS3000 in a potential window of 3.0–4.4 V vs. Li/Li^+ at the current density of 50 mA

g^{-1}. Cyclic voltammetry (CV) and electrochemical impedance spectroscopy (EIS) were carried out on an Autolab potentiostat/galvonastat workstation. The sweep rate of Li/$LiCoO_2$ half-cells was 0.1 mV s^{-1} and the voltage range was between 3.0 and 4.4 V vs. Li/Li^+. EIS measurements were conducted in a frequency ranging from 100 kHz to 0.1 Hz and with amplitude of 5 mV.

4.4 Results and Discussion

The phase and purity of as-synthesized LiBOB was investigated via XRPD analysis by comparing the experimental pattern with the theoretical pattern of LiBOB (ICSD 281623) (**Figure 4.1a**). The XRPD data of the as-synthesized LiBOB match the theoretical data, and the reflections belong only to anhydrous LiBOB [394]. This finding suggests that the amount of any possible impurity in as-synthesized LiBOB is less than ~ 1-2 wt. %. After obtaining the anhydrous product, a recrystallization process (**Figure 4.1d**) was performed to remove trace impurities as lithium oxalate ($Li_2C_2O_4$) which may be susceptible to precipitate in the electrolyte solution resulting in a capacity reduction, poor cycling performance and safety issues of LIBs [398]. XRPD patterns of LiBOB, recrystallized LiBOB and $Li_2C_2O_4$ as an impurity are shown in **Figure 4.1b**. Both LiBOB and recrystallized LiBOB shows diffraction peaks based on an orthorhombic crystal structure (space group: *Pnma*, no. 62, a= 6.3635 Å, b= 7.5998 Å, c=13.1715 Å) [477]. There are no reflections belonging to LiBOB.H_2O (JCPDS card no. 01-073-9447), HBO_2 (JCPDS card no. 22-1109) or $Li_2C_2O_4$ (JCPDS card no. 24-0646) impurity due to its purification process. The purity of the recrystallized product was found above 99% via the Reference Intensity Ratio (RIR) method [395, 396, 478, 479].

The elimination of impurities, mainly oxalates, was further confirmed by vibrational spectroscopy. FTIR spectra of LiBOB, recrystallized LiBOB and $Li_2C_2O_4$ as an impurity are given in **Figure 4.1c**. For the recrystallized LiBOB, strong absorption peaks of C=O stretching zones occurs in the range of 1740-1820 cm^{-1} whereas C-O and B-O stretching modes appear

in the range of 980-1370 cm^{-1}. After the purification, peaks of $Li_2C_2O_4$ at 1658 and 778 cm^{-1} can no longer be observed [398, 403]. Scanning electron microscopy (SEM) was performed to evaluate the morphology of the samples before and after the recrystallization procedure. Well-defined rectangular morphologies were observed in the as-synthesized samples, whereas needle-shaped crystals were obtained after the purification and recrystallization steps (**Figure 4.2**).

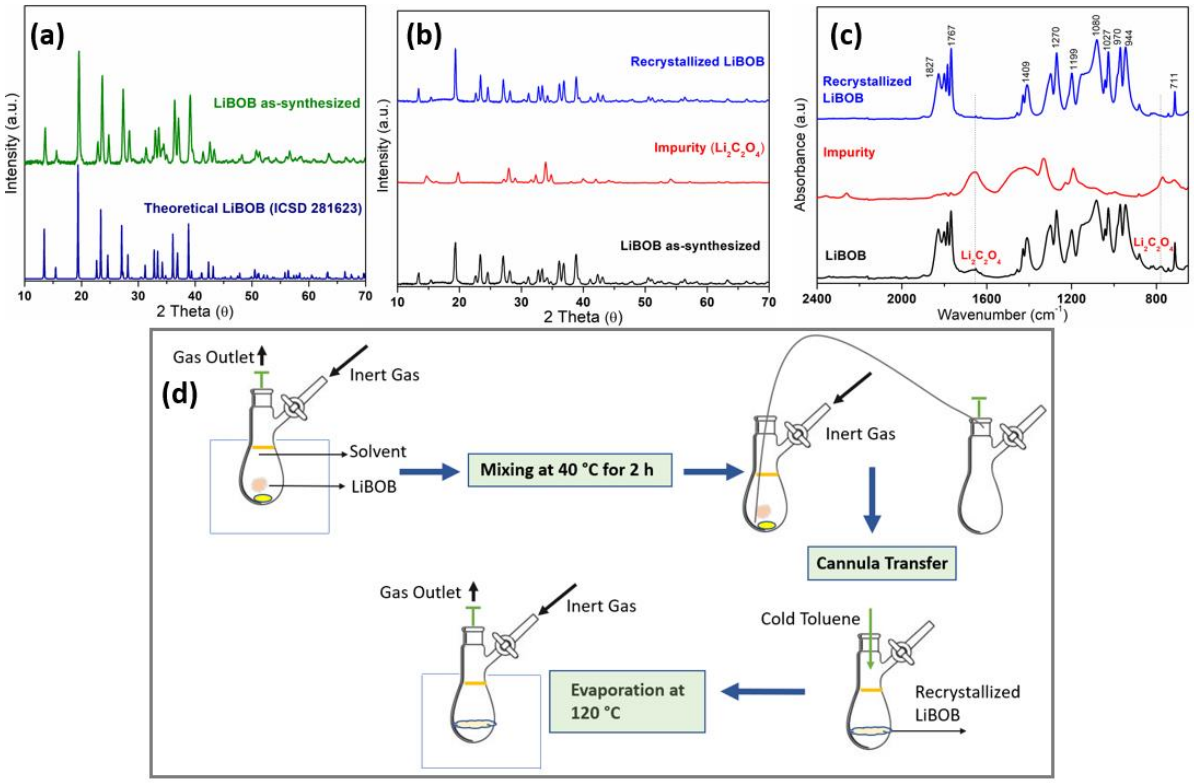

Figure 4.1: (a) XRD patterns of theoretical LiBOB (ICSD 281623) [394] (blue) and as-synthesized LiBOB (green). Reflections belonging only to LiBOB are observed in the XRD pattern for the synthesized sample. (b) XRD patterns of as-synthesized LiBOB (black), impurity (red), and recrystallized LiBOB (blue). (c) FTIR spectra of as-synthesized LiBOB (black), impurity (red), and recrystallized LiBOB (blue). (d) Schematic illustration for the recrystallization process of LiBOB via cannula transfer.

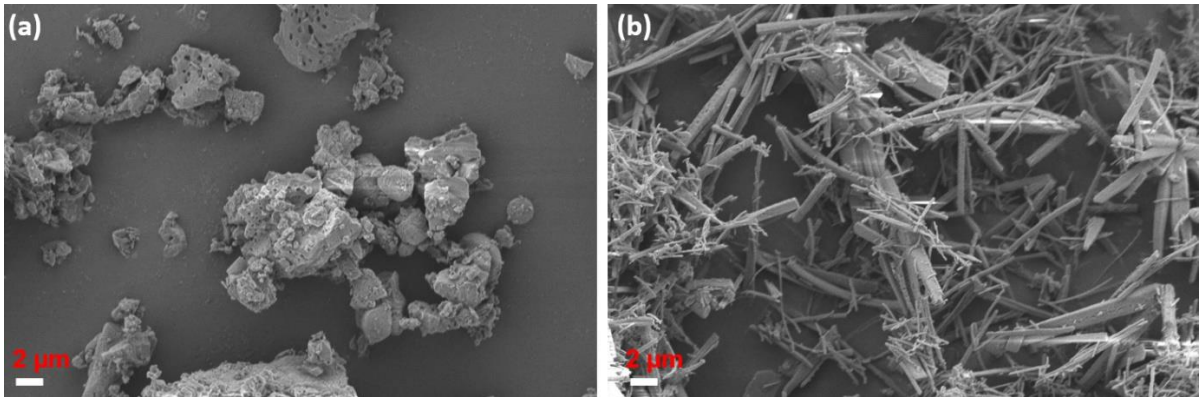

Figure 4.2: SEM images of (a) as-synthesized LiBOB and (b) recrystallized LiBOB.

The electrochemical performances of $LiCoO_2$ cathode in 1M $LiPF_6$ ethylene carbonate (EC) and dimethyl carbonate (DMC) electrolyte with and without LiBOB additive were evaluated by galvanostatic charge-discharge measurements in a voltage window of 3.0 – 4.4 V at a rate of 50 mA g^{-1}. The initial charge-discharge curves and the cycling performance are given in **Figure 4.3a**. According to the first charge-discharge curves, the lithium insertion/extraction behavior of $LiCoO_2$ did not change with the addition of LiBOB as an electrolyte additive. The voltage plateaus are observed at ~3.93 V and ~3.98 V for reference cell and 1 wt.% LiBOB added cell, respectively, which indicates the $Co^{3+/4+}$charge-discharge redox couple [480].

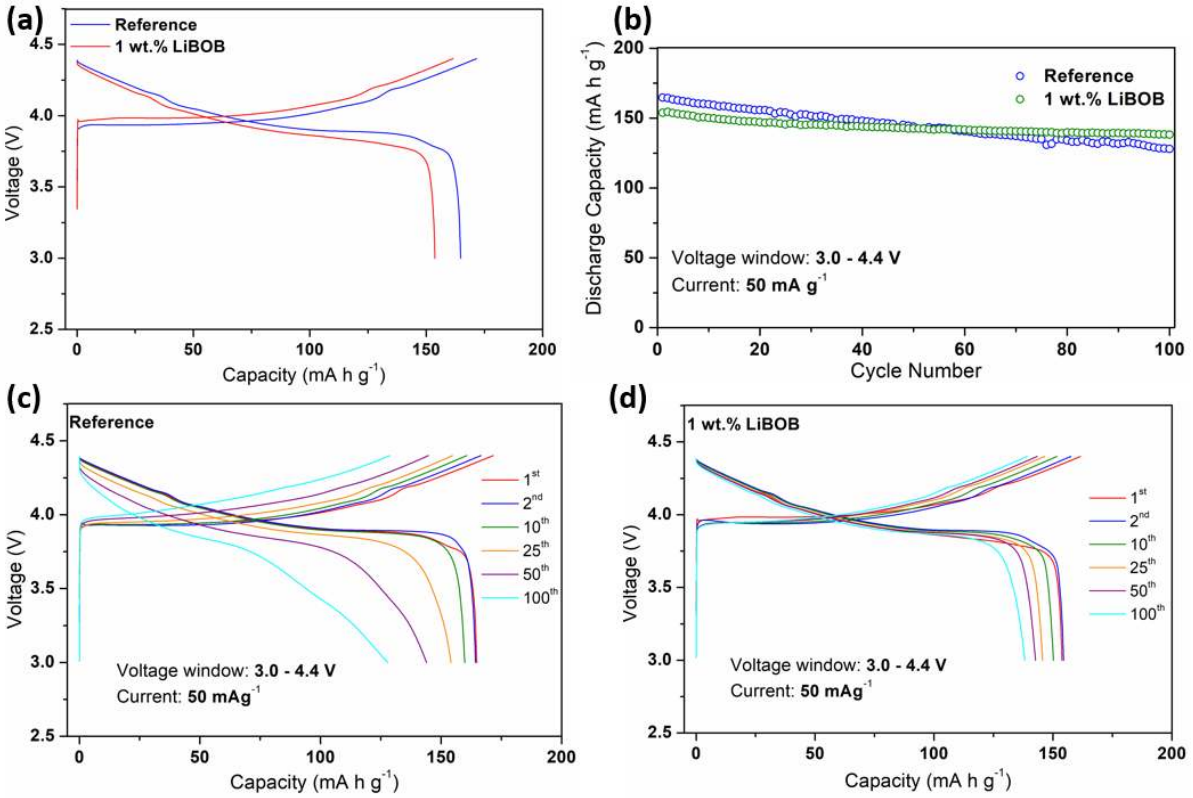

Figure 4.3: (a) The first charge/discharge curves of Li/$LiCoO_2$ half cells with and without LiBOB additive. (b) The comparison of their cycling performances. (c) The galvanostatic charge discharge curves of Li/$LiCoO_2$ half cells with reference electrolyte, and (d) with LiBOB.

The galvanostatic charge/discharge curves of $LiCoO_2$ cathodes within 3.0 – 4.4 V at a current density of 50 mA g^{-1} are shown in **Figure 4.3** and **Figure 4.4**. The initial charge-discharge capacity, irreversible capacity loss (C_{irr}) and coulombic efficiencies (CE) are listed in **Table 4.1**.

Table 4.1: The comparison of electrochemical performances between the reference electrolyte, containing as-synthesized and purified LiBOB.

Electrolyte	1st charge capacity (mA h g^{-1})	1st discharge capacity (mA h g^{-1})	C_{irr} (mA h g^{-1})	CE (%)	100th discharge (mA h g^{-1})	Capacity retention (%)	Capacity retention per cycle (medium in %)
Reference	171.5	164.7	6.8	96.0	128.0	77.7	99.5
1 wt.% as-synthesized LiBOB	163.8	155.9	7.9	95.1	121.9	78.2	99.7
1 wt.% LiBOB	161.4	153.8	7.6	95.3	138.2	89.8	99.8

The first charge/discharge capacities for the cell containing purified LiBOB was found lower with values of 161.4 mA h g^{-1} and 153.8 mA h g^{-1} than the reference cell (no LiBOB additive) with values of 171.5 mA h g^{-1} and 164.7 mA h g^{-1}. Additionally, for the cells cycled in electrolytes with 1 wt.% as-synthesized and purified LiBOB, the first C_{irr} are slightly higher than the pristine one. These results may be related to the development of SEI by LiBOB additive consuming Li ions and incomplete activation of $LiCoO_2$ phase in the initial cycle [364, 387].

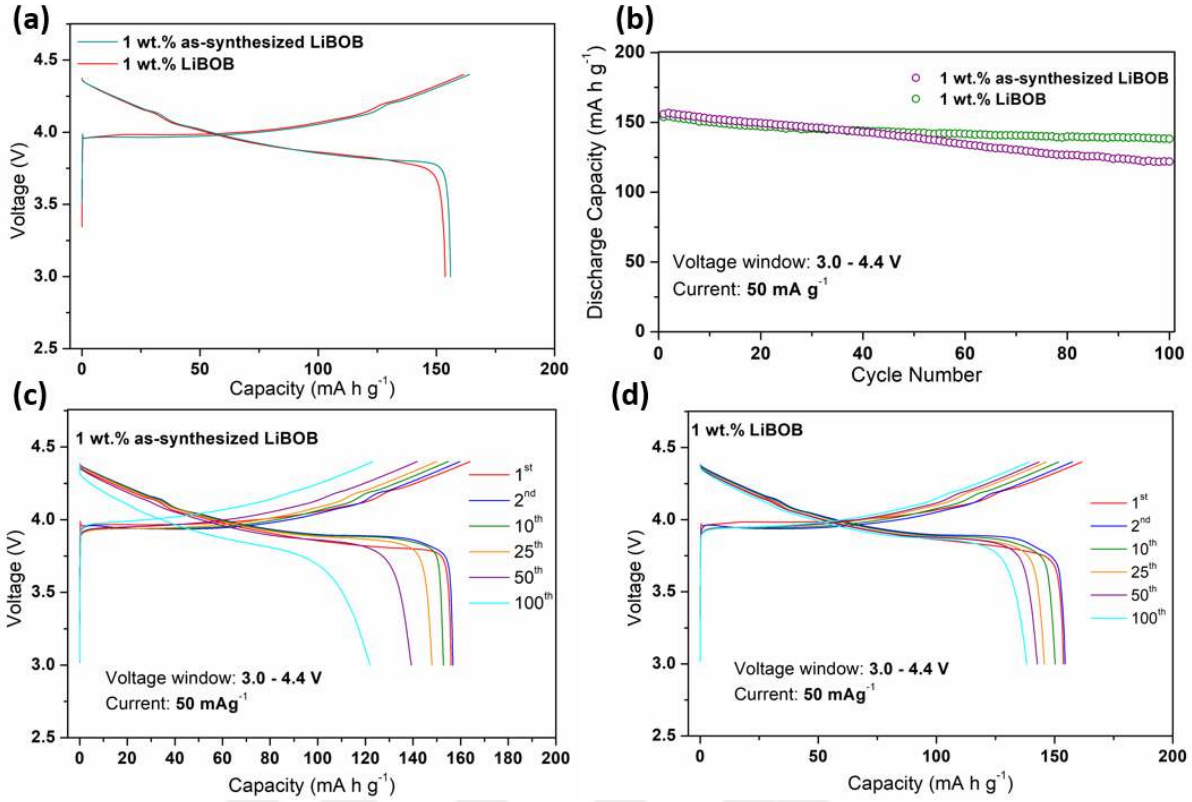

Figure 4.4: (a) The first charge/discharge curves of Li/$LiCoO_2$ half cells with as-synthesized LiBOB and recrystallized LiBOB additive. (b) The comparison of their cycling performances. (c) Galvanostatic charge discharge curves of Li/$LiCoO_2$ half cells with as-synthesized LiBOB, and (d) with LiBOB.

The discharge capacity of $LiCoO_2$/Li half-cell with the plain electrolyte suddenly reduces after 60^{th} cycle which can be related to the degradation of the bulk electrolyte and deterioration of the interphase layer at high operating voltages [463]. The oxidation of the electrolyte at the cathode surface also causes increase of the full cell impedance due to the highly extracted lithium ions from $LiCoO_2$ cathode above 4.2 V [481, 482]. For the cell with the reference electrolyte, the discharge capacity decreases to 128.0 mA h g^{-1} after 100^{th} cycle with a capacity retention of 77.7%, whereas 100^{th} discharge capacity of the cells with as-synthesized and purified LiBOB added electrolyte are 121.9 mA h g^{-1} and 138.2 mA h g^{-1} with a capacity retention of 78.2% and 89.8%, respectively (**Table 4.1**). Thus, the recrystallization process of LiBOB can be regarded as an efficient way to achieve superior cycling performance by

eliminating impurities, as improved electrochemical performances are observed for the cells with purified LiBOB additive in comparison to both reference cells with no LiBOB electrolyte additive and cells with as-synthesized LiBOB additives (**Figure 4.3** and **Figure 4.4**). Furthermore, after 100 cycle the average capacity retention per cycle is ~ 99.5% for the reference cell, ~ 99.7% for as-synthesized LiBOB and ~ 99.8% for recrystallized LiBOB. These findings can be attributed to the formation of LiBOB originated SEI layer on the cathode surface which suppresses the decomposition of electrolyte during cycling [375]. The first three cycles of the cells with 1 wt.% LiBOB additive give also more stable coulombic efficiencies at 95.3%, 98.1%, and 98.3% compared to the reference cell (**Figure 4.5**). The improved coulombic efficiency suggests that the SEI formed by the recrystallized LiBOB results in the passivation of the cathode surface which also inhibits the oxidation of the electrolyte [468].

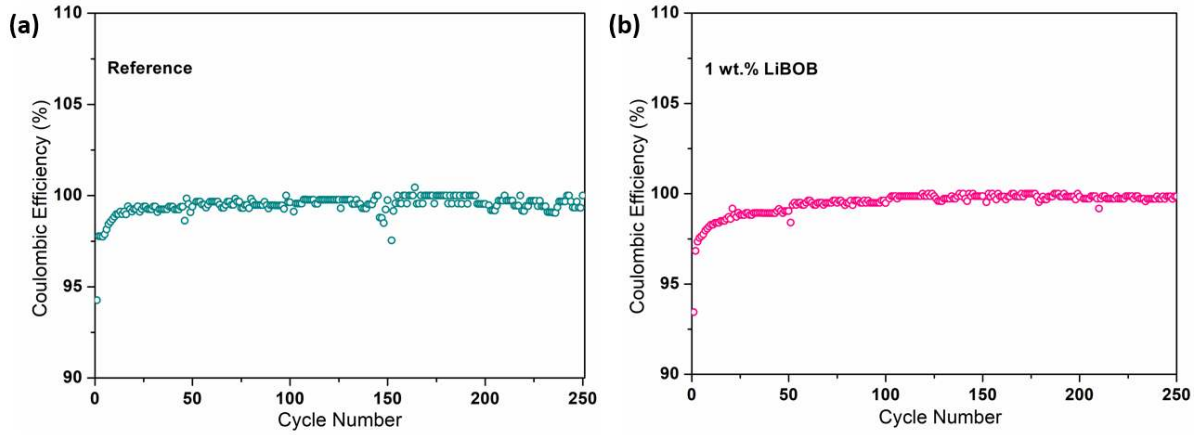

Figure 4.5: The comparison of coulombic efficiency values of reference cell vs. LiBOB added cell.

The comparison of midpoint discharge voltages and the energy densities are given in **Figure 4.6a&b**.

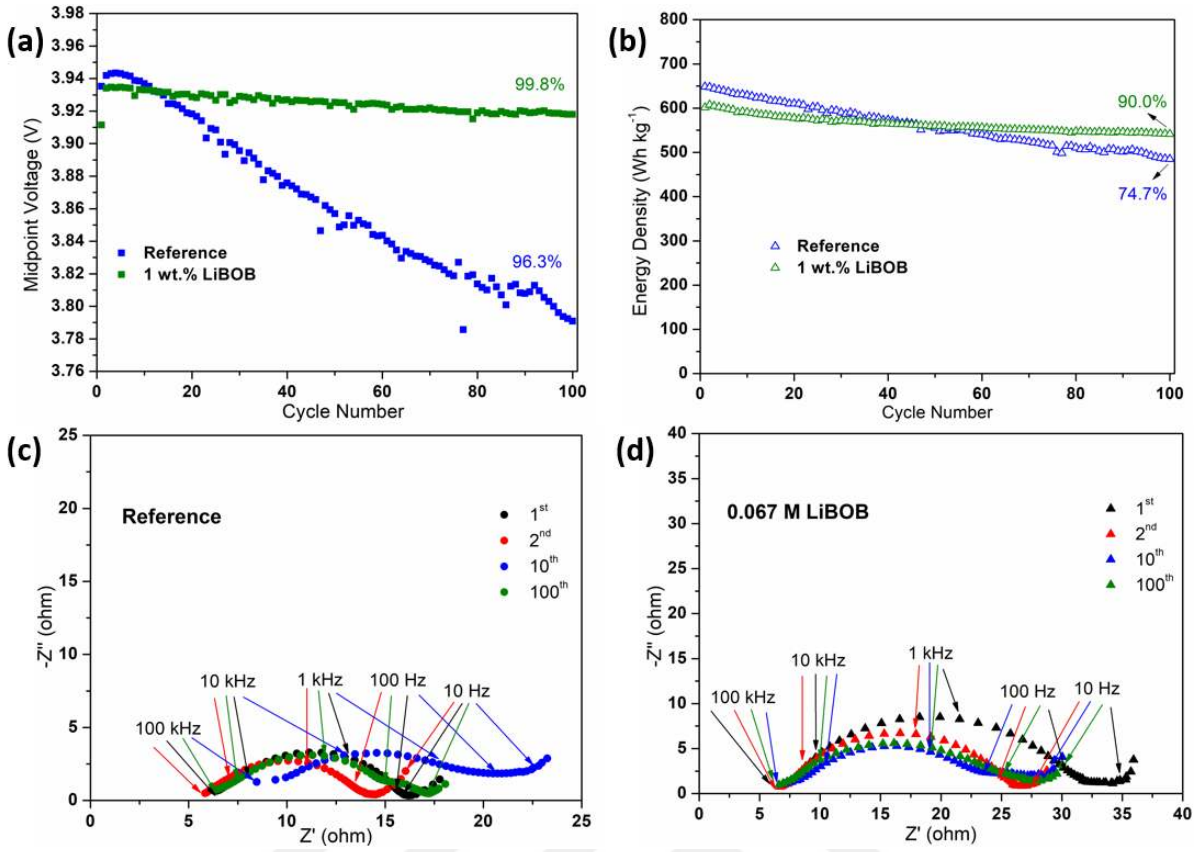

Figure 4.6: (a) Midpoint discharge voltages and (b) energy densities of Li/$LiCoO_2$ cells with and without LiBOB additive. (c) EIS spectra of Li/$LiCoO_2$ cells with reference electrolyte and (d) with LiBOB additive.

It can be clearly seen that midpoint discharge voltage of the cell containing pristine electrolyte decreases rapidly from 3.93 V to 3.79 V which reveals a continuous cell polarization in agreement with the cycling performance. Nevertheless, with the addition of LiBOB achieves more stable midpoint discharge voltage trend with a retention of 99.8% over 100 cycles showing a superior cycling stability compared to the reference cell. According to the **Figure 4.8b**, energy densities were determined by $C \times V$ where C is the discharge capacity and V is the median discharge voltage. After 60 cycles, the energy density of the cell with the plain electrolyte reduces quickly to 484.8 W h kg^{-1} retaining 74.7% of the initial energy density, whereas the value for the cell with the LiBOB additive decreases to 541.4 W h kg^{-1} with an energy density retention of 90.0%. These results suggest that high purity LiBOB additive plays

an effective role in the mitigation of voltage fade and energy degradation. Additionally, CV measurements were performed to further evaluate the effects of purified LiBOB on the reduction and oxidation behavior of LCO cathode at high voltages.

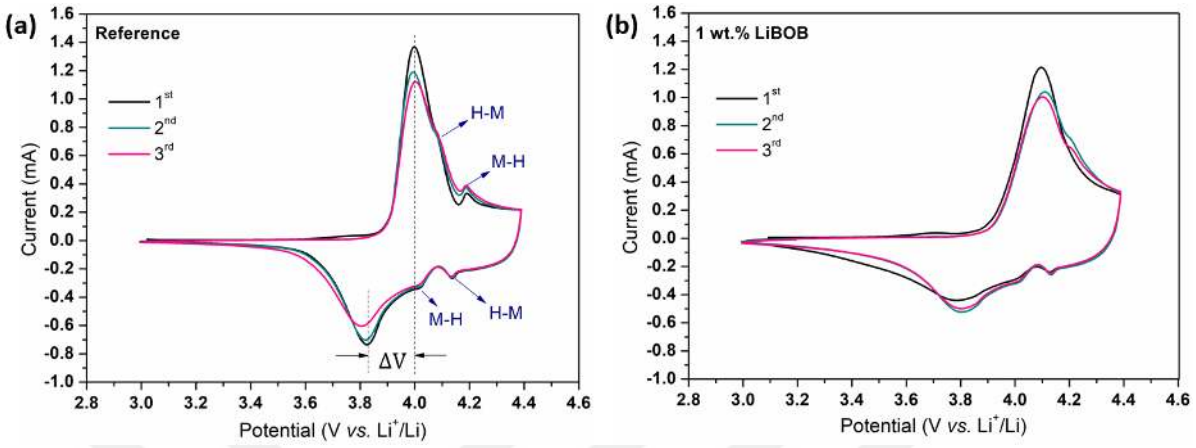

Figure 4.7: Cyclic voltammetry (CV) profiles of $LiCoO_2$ cathodes cycled with (a) reference electrolyte and (b) 1 wt.% LiBOB added electrolyte with a scan rate of 0.1 mV s^{-1} between 3.0 and 4.4 V.

As shown in **Figure 4.7,** the major anodic and cathodic peaks around at 4.0 V and 3.8 V are attributed to the Li^+ extraction/insertion process by the redox reaction of $Co^{3+/}Co^{4+}$ [483]. It can be seen that during the first cycle, the cell containing LiBOB possess higher redox peak current compared to the reference cell. This phenomenon can be due to the preferentially oxidation of electrolyte additives forming a robust SEI layer on the LCO cathode surface [484]. For the cell with LiBOB, the peak symmetry and peak currents are also more stable showing a higher reversibility for Li^+ extraction and better capacity retention that is in good agreement with the results obtained from charge/discharge tests.

Table 4.2: Potential differences (ΔV) between the major anodic and cathodic peaks in CV profiles.

Electrolyte	ΔV_1 (V)	ΔV_2 (V)	ΔV_3 (V)
Reference	0.1727	0.1743	0.1935
1 wt.% LiBOB	0.3488	0.3051	0.2981

Moreover, according to the **Table 4.2** the potential differences between major anodic and cathodic peaks (ΔV) of LiBOB added electrolyte continuously decreases suppressing the interfacial polarization whereas for the plain cell a larger polarization occurs related to the degradation of electrolyte at high voltages. The minor peaks at ~ 4.1 - 4.2 V are corresponded to the order-disorder transformation between hexagonal and monoclinic phases [485]. It can be clearly seen that the hexagonal-monoclinic-hexagonal (H-M-H) phase transitions of the cell incorporated LiBOB are significantly mitigated (**Figure 4.7**) in accordance with the ex-situ XRD results (**Figure 4.8**).

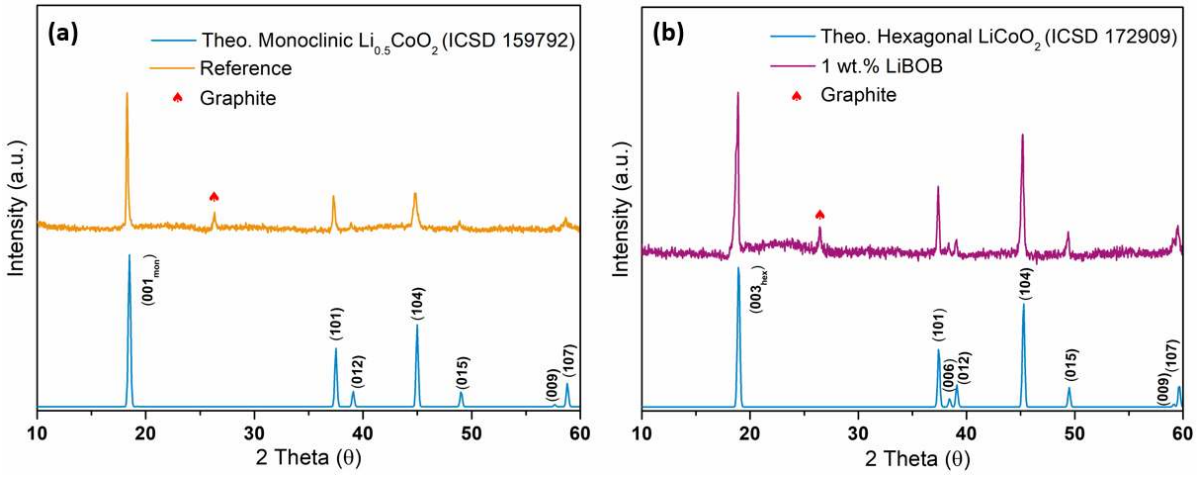

Figure 4.8: XRPD patterns of $LiCoO_2$ cathodes cycled with (a) reference electrolyte after 100th cycle (orange) and theoretical monoclinic $Li_{0.5}CoO_2$ (blue), (d) 1 wt.% LiBOB added electrolyte after 100th cycle (purple) and theoretical hexagonal $LiCoO_2$ (blue).

Ex-situ XRD measurements were performed to investigate the relationship between structural changes in $LiCoO_2$ cathode, SEI and LiBOB additive (**Figure 4.8**). All of the XRD patterns

reveal typical diffraction peaks of layered $LiCoO_2$. The reflection of (002) at 26° is observed due to the presence of graphite within the slurry. After 100 cycles, the diffraction peaks at (003) and (104) of $LiCoO_2$ cathode cycled in the reference electrolyte shift toward lower 2θ angles related to the lattice expansion in the c direction, cobalt dissolution accordingly structural deterioration in agreement with its poor cycling performance, as similarly observed in other investigations [480, 486-489]. However, $LiCoO_2$ cycled with the high purity LiBOB added electrolytes preserves its hexagonal crystal structure upon cycling. The structure of $LiCoO_2$ within the cell with plain electrolyte irreversibly changes to a monoclinic phase [474].

EIS measurements for different cycles were performed to investigate the progress of cell polarization [490]. The impedance spectra of Li/$LiCoO_2$ cells with and without LiBOB additive are shown for different cycles (1^{st}, 2^{nd}, 10^{th}, 100^{th}) in **Figure 4.6c&d**. After the initial cycle, the resistance of the cell with LiBOB was higher than the reference cell which may be related to the more stable LiBOB derived SEI at the cathode surface. It can be clearly seen that resistance values are more stable and slightly reduce for the cells with high purity LiBOB additive. However, cells containing the base electrolyte with no LiBOB additive show highly unstable resistance values as changes and increases after extensive cycling. Thus, it can be stated that the SEI formed by LiBOB prevent the electrolyte decomposition even at high voltage cycling of $LiCoO_2$ that results in a better resistive stability as well as cycling stability in line with other findings. Additionally, the interfacial resistance should decrease as cycling proceeds due to the LiBOB originated protective SEI layer possessing high ionic conductivity by eliminating the cell polarization and the voltage fade [62].

Figure 4.9 shows the rate capability tests at different current densities.

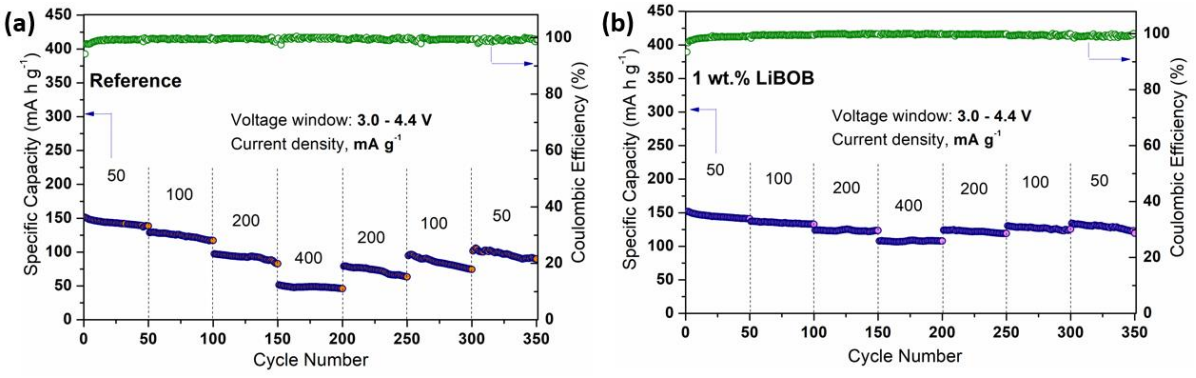

Figure 4.9: The rate capability test of $LiCoO_2$ cathodes at current densities of 50, 100, 200, 400 mA g^{-1} containing (a) reference electrolyte, (b) 1 wt.% LiBOB added electrolyte.

For the cells containing reference electrolyte, discharge capacities in the range of 138, 117, 83, and 46 mA h g^{-1} are delivered, whereas the cell with high purity LiBOB additive give capacities in the range of 140, 133, 123, and 108 mA h g^{-1} at rates of 50, 100, 200, and 400 mA g^{-1}, respectively. When the rate is changed back to 50 mA g^{-1}, the discharge capacity recovers to 134 mA h g^{-1} at the 301st cycle. These results suggest that the addition of high purity LiBOB as an electrolyte additive lead to better cycling stability and rate capability for the high voltage cycling of $LiCoO_2$.

SEM images of $LiCoO_2$ cathodes before cycling and after the 100th cycle for reference cell and 1 wt.% recrystallized LiBOB added cell are presented in **Figure 4.10**.

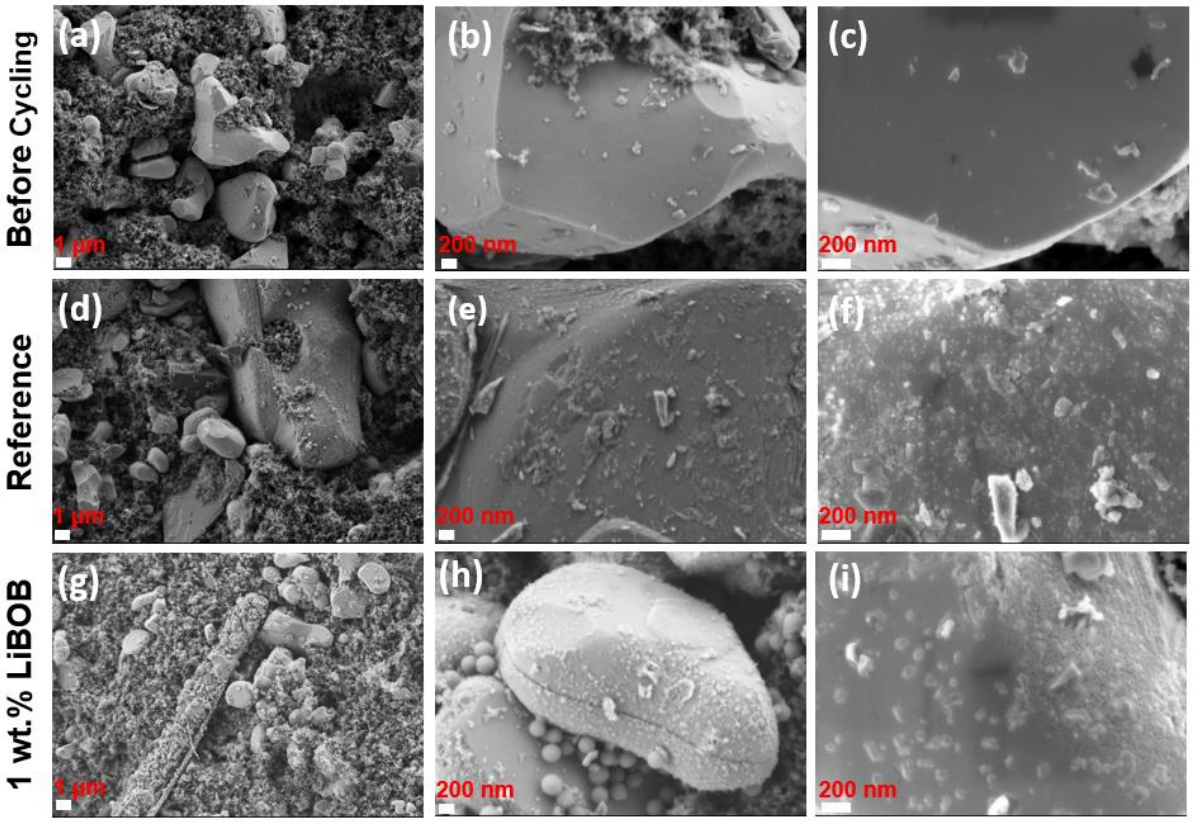

Figure 4.10: SEM images of $LiCoO_2$ cathodes from $LiCoO_2$/Li cells (a, b, c) before cycling; (d, e, f) after 100 cycles with reference electrolyte; (g, h, f) after 100 cycles with 1 wt.% recrystallized LiBOB added electrolyte.

The fresh cathode shows clean and smooth surface (**Figure 4.10a&b**) whereas for the one cycled in reference electrolyte, more heterogenous surface is occurred with the formation of holes and cracks after cycling at high voltages (**Figure 4.10d&e**). However, by adding 1 wt.% LiBOB, the morphology of the cycled cathode is well preserved after cycling. In addition, according to the (**Figure 4.10h&i)**, protective SEIs are seemingly formed on the surface of $LiCoO_2$ increasing the interfacial stability by eliminating electrolyte decomposition and Co dissolution [491]. These results are in line with the ex-situ XRD data (**Figure 4.8**) that LCO cathode without any additives is susceptible to the formation of structural damage above 4.4 V which also cause poor cycling stability for LIBs [492].

Higher energy densities could be achieved for Li_xCoO_2 ($x > 0.5$) by charging above 4.2 V

against Li. However, oxygen release, structural changes and the dissolution of cobalt ions may take place resulting the electrolyte decomposition which also cause performance decay together with the high interfacial impedance [493]. Therefore, various electrolyte additives have been used to improve high-voltage application of $LiCoO_2$ by forming a stable SEI layer that decreases the interfacial resistance. **Table 4.3** compares the electrochemical performance of the results obtained here with $LiCoO_2$ at high voltage cycling by using 1 wt.% recrystallized LiBOB added electrolyte with different additives investigated in the literature.

Table 4.3: Overview of electrochemical performances of high voltage $LiCoO_2$ cathode with various electrolyte additives.

Electrolyte composition	Voltage range (V *vs.* Li/Li^+)	Current density (mA g^{-1})	1st discharge capacity (mA h g^{-1})	Capacity retention (%)	Coulombic efficiency (%)	Ref.
Nano Al_2O_3 in 1 M $LiPF_6$ EC-DMC	3.3-4.5	0.15 mA cm^{-2}	192	85 (100^{th})	-	[494]
Li_2CO_3 in 1 M $LiPF_6$ EC-PC-DMC	2.8-4.5	0.1 C	190	94 (120^{th})	88	[482]
BMP in 1 M $LiPF_6$ EC-DMC	2.75-4.5	0.2 C	181	96 (50^{th})	97	[83]
TMB in 1 M $LiPF_6$ EC-EMC-DEC	3.0-4.5	1 C (185 mA g^{-1})	180	86 (300^{th})	-	[495]
SUN-LiBOB in 1 M $LiPF_6$ EC-DMC	3.0-4.5	14	187	62 (500^{th})	94	[461]
EEEP in 1 M $LiPF_6$ EC-DMC	3.0-4.4	40	166	91 (100^{th})	-	[62]
PFPN in 1 M $LiPF_6$ EC-DMC	3.0-4.5	14	185	90 (300^{th})	88	[53]
DMSE in 1 M $LiPF_6$ EC-DMC-EMC	3.0-4.5	0.5 C	175	85 (200^{th})	-	[493]
LiBOB in 1 M $LiPF_6$ EC-DMC	3.0-4.4	50	154	90 (100^{th})	95	This work

For higher potentials, some inorganic additives such as nano-Al_2O_3 [494] and Li_2CO_3 [482] were combined with the commercial electrolyte leading to enhanced energy density and cycling performance of LCO electrode for the first time. The presence of Li_2CO_3 results in quite high capacity retention of 94% after 120 cycle whereas the coulombic efficiency value

remains at only 88% [482]. However, there are only few reports boron-containing additives [461] and no studies with only LiBOB to the best of our knowledge for LCO. Trimethyboroxine (TMB) was incorporated as an additive for improving the overall electrochemical performance under 4.5 V achieving a capacity retention of 86% at 300th cycle [495]. In another study, Ji et al. combined LiBOB with suberonitrile (SUN) and showed that after 500 cycle, the capacity retention increased from 25% to 62% with a first coulombic efficiency value of 94% [461]. LiBOB has been considered as an effective additive for inhibiting electrolyte decomposition by trapping PF_5 that suppresses oxidation because of the formation of SEI containing borates [369, 465, 496]. In comparison with these previous studies, similar improved electrochemical performances are obtained with the use of a single additive in a minimal amount (~ 1 wt-%) with high-capacity retention of 90% after 100 cycles, as well as high coulombic efficiency of 95%. Furthermore, a high energy density (**Figure 4.6b**) is achieved without any phase transition of $LiCoO_2$ after cycling. The improved performance of $LiCoO_2$ at high voltage cycling reported here can be mainly attributed to the use of high purity LiBOB obtained with a new practical recrystallization process avoiding oxalate impurities which could deteriorate the overall electrochemical performance, as seen for the cells with as-synthesized LiBOB additives (**Figure 4.4**). Here, alternative methods and materials for the high voltage cycling of $LiCoO_2$ are suggested. The promising results shown here for the high voltage $LiCoO_2$ cathodes with the recrystallized-high purity LiBOB could also open new pathways for the employment of similar strategies with other high voltage cathode applications (e.g. NMC and $LiMn_xNi_yO_4$) resulting higher current energy densities in comparison to the current state of the art and enabling future practical uses.

4.5 Conclusion

To sum up, as-synthesized LiBOB was successfully purified performing a novel recrystallization process. The removal of $LiBOB.H_2O$, HBO_2 and $Li_2C_2O_4$ impurities was verified by XRPD and FTIR analysis. According to the RIR method, above ~ 99% purity was

achieved for the recrystallized LiBOB that is essential to avoid performance decay of LIBs due to the interfacial impedance. As shown from the SEM investigations, needle-shaped crystals were occurred after the recrystallization method. The galvanostatic charge-discharge cycling tests in a potential window of 3.0 - 4.4 V with different current densities were conducted to determine electrochemical performance of high voltage LCO cathode in a cell containing purified LiBOB as an electrolyte additive. From the first charge/discharge curves, the cell with 1 wt.% LiBOB exhibited higher irreversible capacity loss compared to the reference cell due to the formation of LiBOB derived SEI layer. The cell with purified LiBOB added electrolyte delivered a first discharge capacity around 154.0 mA h g^{-1} and maintained its 100^{th} capacity of 128.0 mA h g^{-1} at a rate of 50 mA g^{-1} with a capacity retention of 89.8% showing a stable cycling with an average capacity loss approximately ~ 0.1% per cycle. In addition, enhanced energy density was achieved with a retention of 90.0% after 100 cycles related to the prevention of voltage fade in accordance with the midpoint voltage graph. Ex-situ XRPD results of cycled cathodes also revealed that the LCO cycled with the LiBOB added electrolyte preserved its hexagonal crystal structure. The rate capability tests further confirmed that LiBOB could be effectively used as an additive for improved electrochemical performance as a consequence of a stable LCO cathode at high voltages. To the best of our knowledge the obtained results are quite encouraging that the utilization of high purity LiBOB could enhance the overall performance of high voltage applications of LCO cathode for LIBs by eliminating the formation detrimental byproducts and by preserving the original structure.

Chapter 5:

Effects of Lithium Bis(oxalate) Borate (LiBOB) on the Stability of Surface Modified TiO_2 / Reduced Graphite Oxide Nanocomposite Anode

5.1 Abstract

The impacts of LiBOB on the electrochemical performance of surface modified TiO_2/RGO nanocomposite anode is thoroughly investigated by galvanostatic cycling tests in a voltage range between 1.0 - 3.0 V at different current densities. Scanning electron microscopy (SEM) is performed to evaluate the morphology changes of anodes after initial lithiation with a low rate and after cycling. Ex-situ X-ray photoelectron spectroscopy (XPS) is used to determine the surface chemistry of electrodes with the addition of LiBOB in the $LiPF_6$ electrolyte. The cell with the reference electrolyte shows high capacity and better cycling performance at a high rate, while the addition of LiBOB resulted in superior capacity retention and improved coulombic efficiency at a low rate due to the correct formation of a solid electrolyte interphase (SEI) layer. However, the high irreversible capacity loss could not be prevented which was further proven by the high LiF content on the surface of LiBOB added anode by XPS analysis. Post-mortem SEM results reveal that more homogeneous and dense surface film is able to develop during the initial discharge step preventing the direct electrical contact between the active material and electrolyte. Thus, LiBOB could be practically used to achieve long-term cycling performance with the combination of next-generation anode materials as long as

avoiding the huge irreversible capacity loss related to the decomposition products of LiBOB.

5.2 Introduction

Over the past decades, many efforts have been conducted to increase the energy density, power density, cycling performance and safety of anode materials for lithium-ion batteries [497]. TiO_2 has been regarded as a promising anode material due to its environmental friendliness, low cost, cycling stability and structural stability with a small volume change (3-4%) during cycling [498]. Commercial graphite anode may suffer from the growth of lithium dendrites at high current rates because of the low working voltage below 0.2 V, close to the Li electroplating potential [193]. Carbonate based electrolytes are susceptible to degrade at operating voltages below 0.8 V because of the reduction of the C=O group and the release of volatile products [499]. On the other hand, TiO_2 exhibits a high operating voltage above 0.8 V vs. Li^+/Li which leads to a higher safety by eliminating the decomposition of electrolyte and the formation of a thermally unstable solid electrolyte interphase (SEI) [500, 501]. Despite these features, the practical applications of TiO_2 remain a great challenge due to the low specific capacity, low electrical conductivity (10^{-12} S cm^{-1}) and low Li^+ diffusion coefficient resulting in poor rate capability [262, 502]. Therefore, various approaches like nanostructuring, carbon coating and doping with other transition metals have been proven to improve the electrochemical performance of TiO_2 anodes [503-505]. However, these strategies could not be easily adapted to large-scale applications due to the high cost of manufacturing and unsatisfactory lifetime [367].

The most used $LiPF_6$ electrolyte salt undergoes a decomposition during the first cycle with the development of a SEI on the graphite anode. The stability of SEI layer could be crucial to maintain a long lifetime and safety by eliminating the oxidation of electrolyte and side reactions. Thus, several electrolyte additives such as fluoroethylene carbonate (FEC), vinylene carbonate (VC), vinyl ethylene carbonate (VEC) and lithium bis(oxalate)borate (LiBOB) have

been incorporated to stabilize the SEI layer for high performance graphite, silicon and lithium anodes [456, 506, 507]. The uncontrollable growth of SEI increases the full cell impedance resulting in slow Li-ion diffusion and high irreversible capacity loss. Thus, electrolyte additives have been expected to develop a robust SEI on the surface of anodes at high voltages [508]. Kennedy et al. studied the impacts of VC, VEC, FEC and LiBOB as electrolyte additives on the performance of Si nanowire anode in order to buffer huge volume change (> 300%) which causes loss of electrical contact with the current collector and capacity fade. They reported that capacity retention was significantly improved through the formation of a both mechanically and chemically stable SEI that allows the transformation of a porous sponge-like network [509]. In another study, Hernandez et al. evaluated the importance of using fluorine-free salts like VC and LiBOB instead of $LiPF_6$ and FEC which act as a source of toxic and corrosive HF. They revealed that at high current rates, $LiPF_6$ electrolyte showed superior performance with the formation of a fluorine-rich SEI covering the Si particles, while at low rates LiBOB added electrolyte led to the formation of oxygen-rich SEI covering the graphite particles. Therefore, a more conductive SEI layer should be developed to eliminate the poor rate capability towards more environmentally friendly and sustainable LIBs [456]. Even though, considerable attempts have been made to enhance the cycling stability of silicon electrodes by using electrolyte additives, there is a lack of research in combination with TiO_2 based anode materials.

Herein, we aim to improve the overall electrochemical performance of as-fabricated surface modified TiO_2/reduced graphite oxide (RGO) anode with the addition of high purity LiBOB as an electrolyte additive. The surface treated TiO_2/RGO composite electrodes are investigated via galvanostatic charge-discharge cycling tests in a potential window of 1.0 - 3.0 V at different current rates. Scanning electron microscopy (SEM) and X-ray photoelectron spectroscopy (XPS) are performed as post-mortem analyses to investigate the SEI on the

surface of TiO_2/RGO-P composite anode after first discharge and 100th cycle.

5.3 Experimental Section

5.3.1 Material Characterization

X-ray photoelectron spectroscopy (XPS) was carried on in a Thermo Scientific K-Alpha spectrometer using an Aluminum anode (Al Kα= 1468.3 eV) at an electron take-off angle of 90° (between the sample surface and the axis of the analyzer lens). The spectra were recorded using an Avantage 5.9 data system. The binding energy scale was calibrated by assigning the C1 s signal at 284.5 eV. Scanning electron microscopy (SEM) analysis was performed with a Zeiss Ultra Plus field emission GeminiSEM. The cycled cells were disassembled in an Argon filled glovebox and the electrodes were washed with tetrahydrofuran (THF) to remove residual impurities after cycling.

5.3.2 Electrochemical Tests

For the fabrication of surface modified TiO_2/RGO composite electrode, (80 wt.%), (10 wt.%) conductive carbon (Super P® Timcal) and (10 wt.%) PVDF binder were mixed in an agate mortar. After that, a slurry of this powder was ultrasonicated in THF (≥99%, Merck) : toluene (≥99%, Merck) (4 : 1) solution. This slurry was cast on Titanium (Ti) current collectors and dried at 80 °C overnight. The loading of the active material on Ti current collectors was approximately ~ 4 mg / cm^2 after drying. Swagelok type cells were assembled in a argon filled glove-box using polypropylene (Celgard) and glass fiber membrane (Whatman®) separators, Li metal disks cut from Li rods serving as a counter and reference electrode, and 1 M $LiPF_6$ in ethylene carbonate (EC) and dimethyl carbonate (DMC) (1 : 1) solution as the electrolyte. For the preparation of LiBOB added electrolyte, 1 wt.% LiBOB (0.07 mol L^{-1}) was dissolved in the base electrolyte overnight in an argon-filled glove-box. First, the galvanostatic charge-discharge cycling tests were carried out using a Neware battery tester BTS3000 in a potential window of 1.0 - 3.0 V vs. Li/Li$^+$ at a current density of 100 mA g^{-1}. Secondly, for the initial

cycle, TiO_2/RGO-P anode was charged (delithiated) to 4.4 V at a rate of 10 mA g^{-1} and cycled 100 times at a rate of 100 mA g^{-1}. Finally, discharging (lithiation) was carried out from the OCV point at current density of 25 mA g^{-1} to allow correct formation of SEI and cycled subsequently with a rate of 50 mA g^{-1}. Coulombic Efficiency (CE) was calculated via the ratio of charge capacity to discharge capacity.

5.4 Results and Discussion

The electrochemical performances of TiO_2/RGO-P anode in 1M $LiPF_6$ EC:DMC electrolyte with and without LiBOB additive were investigated via galvanostatic charge-discharge tests in a voltage window of 1.0 – 3.0 V at a current density of 100 mA g^{-1}. **Figure 5.1a** compares the first charge/discharge curves between the reference electrolyte and the LiBOB added electrolyte. According to **Table 5.1**, the initial discharge/charge capacities for the reference cell were found higher at 264.6 mA h g^{-1} and 169.0 mA h g^{-1} than the one containing LiBOB with values of 221.1 mA h g^{-1} and 68.6 mA h g^{-1}. Additionally, the reversible specific capacity for the LiBOB added cell was 90.0 mA h g^{-1} with an irreversible capacity loss (C_{irr}) of 152.5 mA h g^{-1}. It is understood that during the first cycle, LiBOB is preferentially oxidized in order to passivate the TiO_2/RGO-P anode surface. Thus, the reduction of BOB^- anion to oxalate leads to the formation of SEI layer which inhibits the degradation of the $LiPF_6$ electrolyte [353, 358]. As shown in **Figure 5.1b**, upon 100 cycles the electrode with 1 wt.% LiBOB exhibits more stable cycling performance compared to the pristine electrode. The coulombic efficiency determines the irreversible reactions during cycling and reversibility that could be achieved with higher CE values above 99% [510]. However, the average CE value and the capacity retention were poorer than the reference cell after 100 cycles. These results indicate that the electron transfer and the Li^+ ion diffusion may be hindered due to the higher resistance of the electrode interphase limiting the overall electrochemical performance.

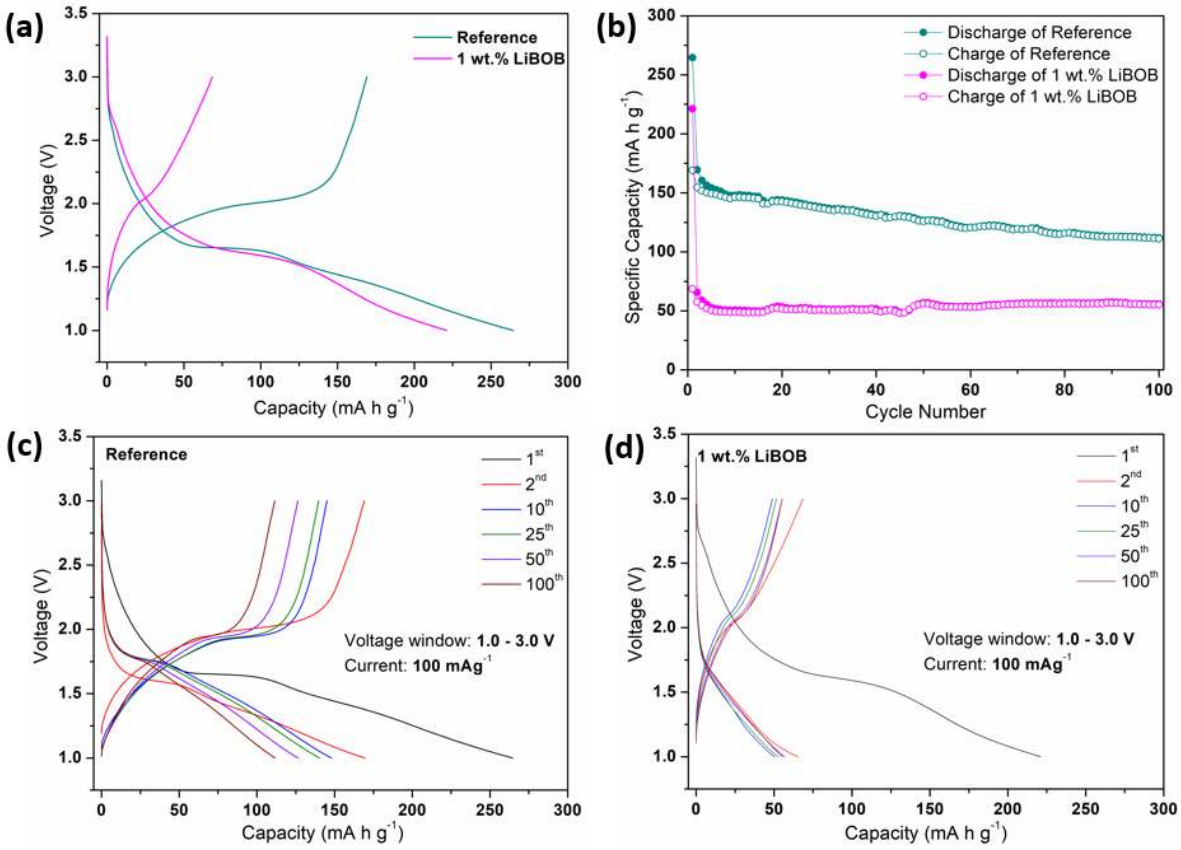

Figure 5.1: (a) The first charge/discharge curves of TiO_2/RGO-P with and without LiBOB additive at a current rate of 100 mA g^{-1}. (b) The comparison of their cycling performances. (c)The galvanostatic charge discharge curves of TiO_2/RGO-P with reference electrolyte, and (d) with LiBOB at 100 mA g^{-1}.

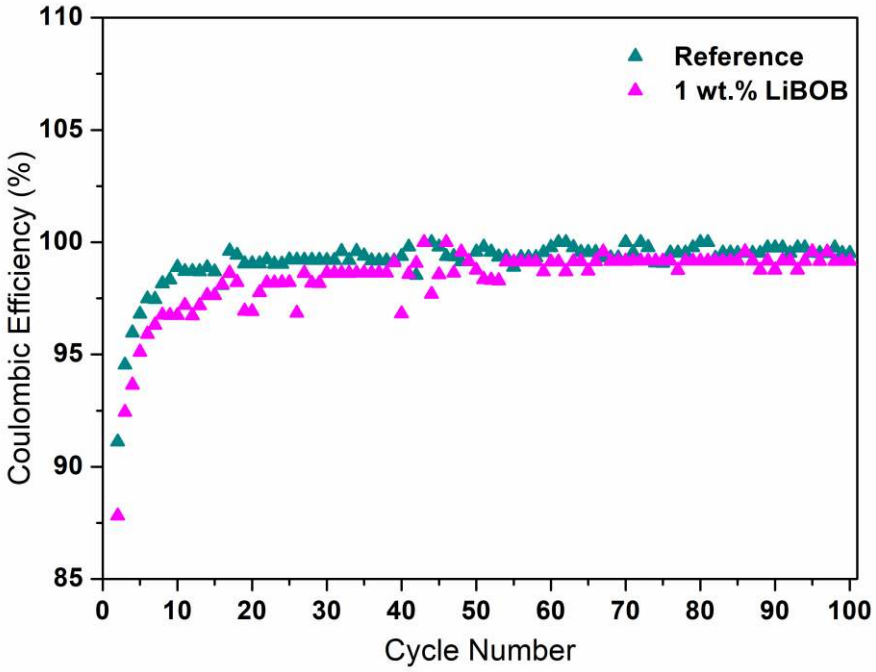

Figure 5.2: The comparison of coulombic efficiency values of reference cell vs. LiBOB added cell.

Table 5.1: The comparison of electrochemical performances between the reference electrolyte and containing purified LiBOB.

Electrolyte	1st discharge capacity ($mAhg^{-1}$)	1st charge capacity ($mAhg^{-1}$)	2nd discharge capacity ($mAhg^{-1}$)	C_{irr} ($mAhg^{-1}$)	CE (%)	100th discharge ($mAhg^{-1}$)	Capacity retention (%)
Reference	264.6	169.0	169.5	95.6	99.1	111.8	42.2
1 wt.% LiBOB	221.1	68.6	90.0	152.5	98.3	55.7	25.2

To further improve the LiBOB-originated SEI, the cells initially charged to 4.4 V at a slower rate (10 mA g^{-1}) and subsequently discharged/charged between 1.0-3.0 V with a rate of 100 mA g^{-1}. This attempt was performed owing to the formation of a LiBOB-derived SEI layer may be occurred at high potentials [509]. As given in **Figure 5.3&5.4**, the capacity retention and the CE of the cell containing reference electrolyte were slightly improved related to the

pre-charging step. In comparison with the standard procedure, after discharging from 4.4 V, the specific capacities were increased by 91% and 87% for the reference electrolyte and 1 wt.% LiBOB added electrolyte, respectively (**Table 5.1**, **Table 5.2**). Nevertheless, the reversible capacity of the anode with LiBOB additive was found even lower that may be related to the formation of a less-ion conducting SEI leading to higher capacity fade [456].

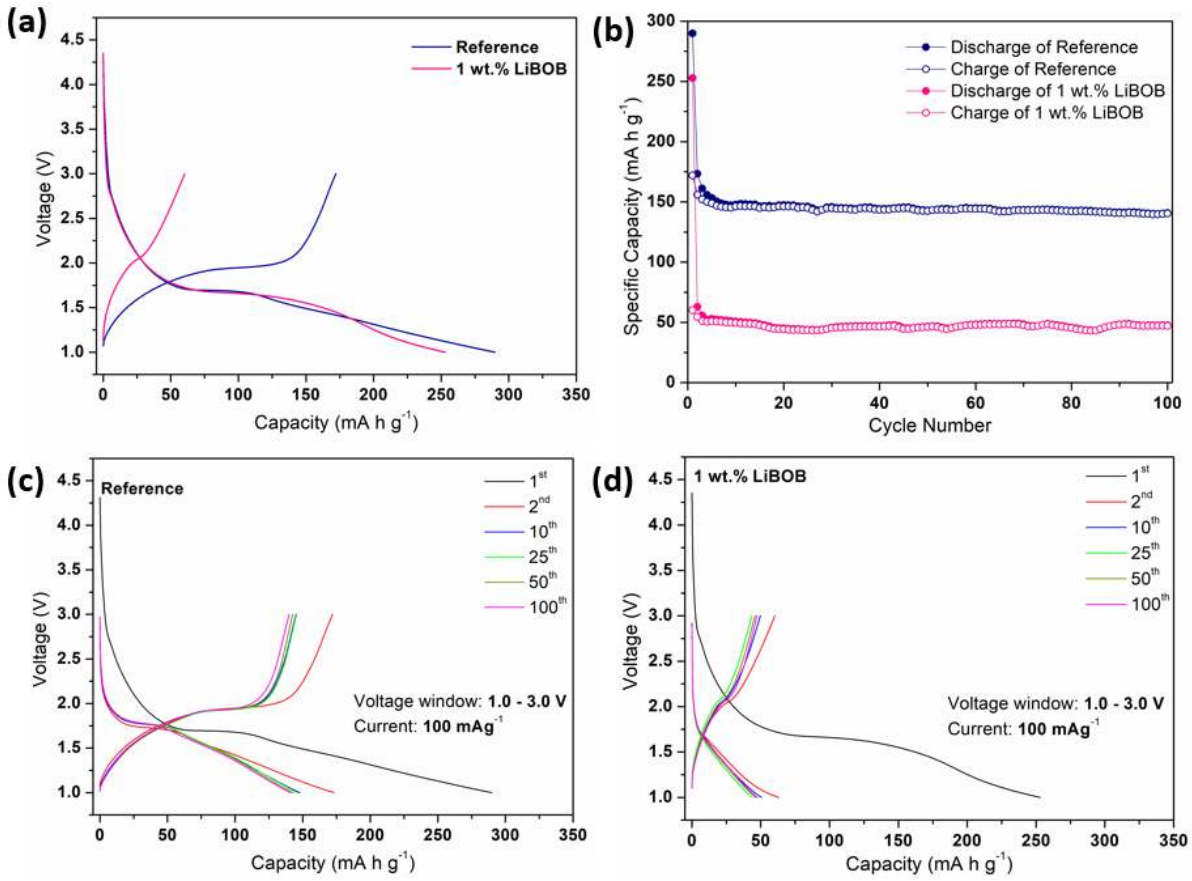

Figure 5.3: (a) The first charge/discharge curves of TiO_2/RGO-P with and without LiBOB additive at a current rate of 100 mA g^{-1} (initially charged to 4.4 V at a rate of 10 mA g^{-1}). (b) The comparison of their cycling performances. (c) The galvanostatic charge discharge curves of TiO_2/RGO-P with reference electrolyte, and (d) with LiBOB at 100 mA g^{-1}.

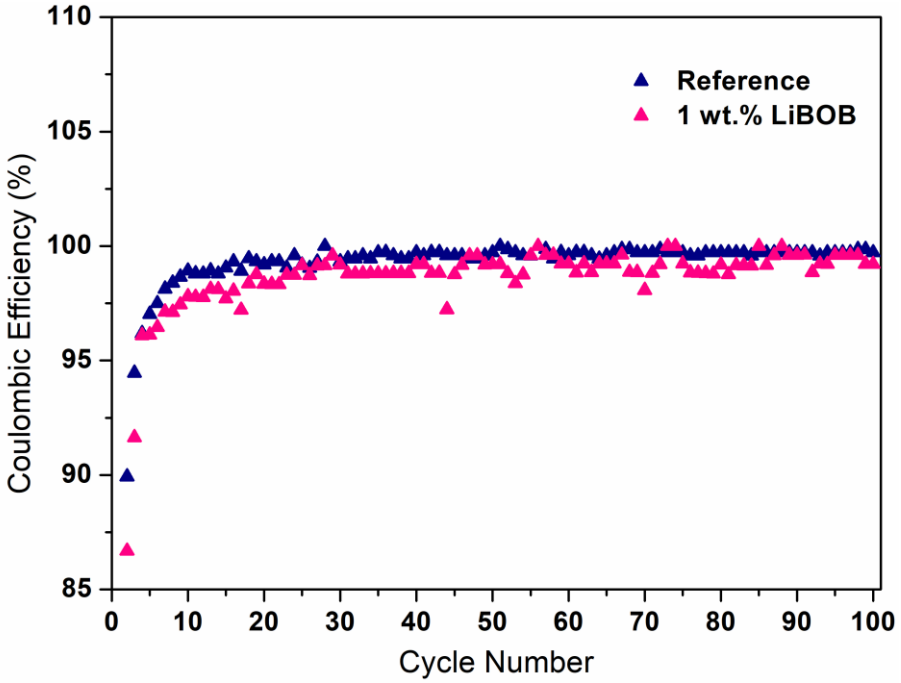

Figure 5.4: The comparison of coulombic efficiency values of reference cell vs. LiBOB added cell.

Table 5.2: The comparison of electrochemical performances between the reference electrolyte and containing purified LiBOB (first charged to 4.4 V at 10 mA g^{-1} and subsequently cycled at 100 mA g^{-1}).

Electrolyte	1st discharge capacity ($mAhg^{-1}$)	1st charge capacity ($mAhg^{-1}$)	2nd discharge ($mAhg^{-1}$)	CE (%)	100th discharge ($mAhg^{-1}$)	Capacity retention (%)	Capacity retention per cycle (medium in %)
Reference	289.8	172.0	173.3	99.3	140.8	48.6	99.2
1 wt.% LiBOB	252.8	60.2	63.0	98.6	47.5	18.8	98.2

The formation of a proper SEI layer could be occurred at slower rates during the first lithiation process [511]. Therefore, to prevent the huge initial capacity decay for the anode with the LiBOB added electrolyte, both electrodes initially discharged from their OCV point to 1.0 V at a current density of 25 mA g^{-1} and subsequently cycled 100 times at 50 mA g^{-1}. **Figure 5.5**

presents the galvanostatic charge-discharge curves of TiO_2/RGO-P anodes in a voltage window of 1.0 – 3.0 V at a current density of 50 mA g^{-1}. The capacity retention values were calculated based on the 2nd discharge capacities because of the same current rate. It can be clearly seen that the cycling performance of LiBOB added electrolyte was significantly improved with a capacity retention of 85.9%, whereas for the pristine one, the retention remained around 58.5% after 100 cycles. This phenomenon can be related to the inhibition of electrolyte oxidation upon cycling. Additionally, from **Figure 5.6**, CE could reach 99% with regard to the appropriate formation of a SEI at a low rate while this value stayed at 98.3% for a higher rate. Unfortunately, the initial charge capacity was still poorer in comparison with the pristine cell that may be related to the formation of a $B(C_2O_4)^{2-}$ originated SEI layer consuming Li^+ ions and the incomplete activation of the TiO_2/RGO anode during 1st cycle. The ex-situ SEM analysis was further performed to evaluate the capacity fading issue during the first cycle that may be related to the degradation of anode structure and unwanted side reactions.

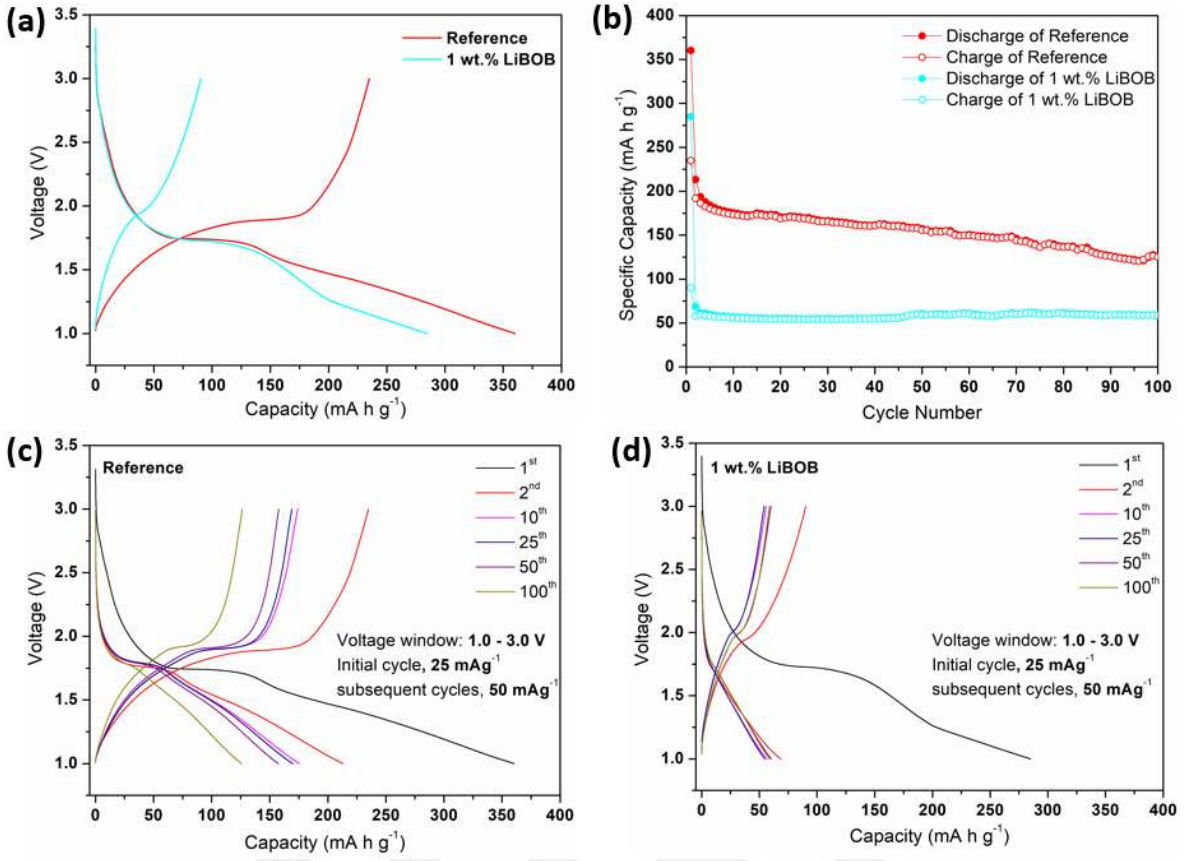

Figure 5.5: (a) The first charge/discharge curves of TiO_2/RGO-P with and without LiBOB additive at a current rate of 50 mA g^{-1} (initially discharged to 1.0 V at a rate of 25 mA g^{-1}). (b) The comparison of their cycling performances. (c) The galvanostatic charge discharge curves of TiO_2/RGO-P with reference electrolyte, and (d) with LiBOB at 50 mA g^{-1}.

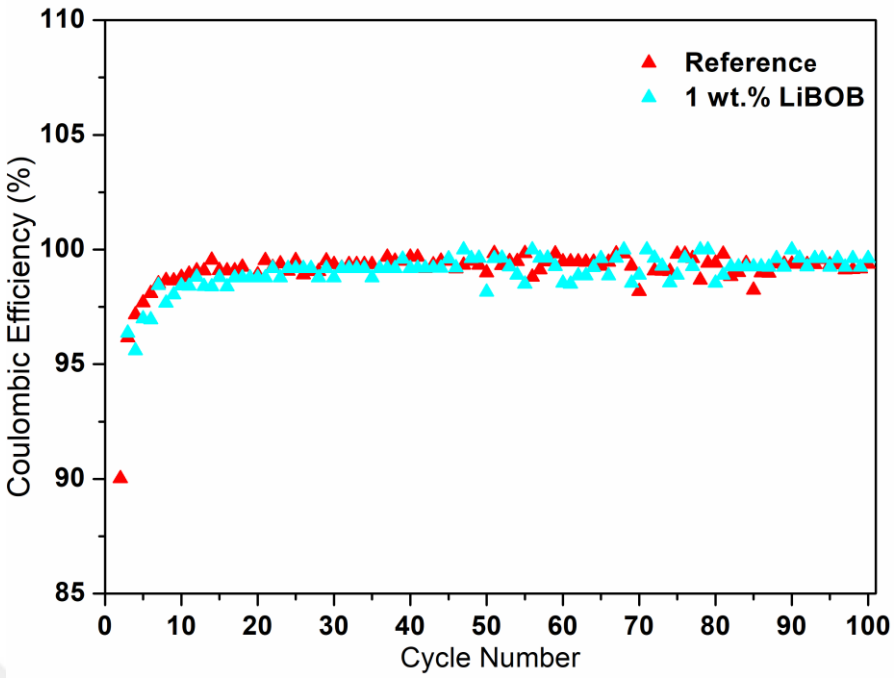

Figure 5.6: The comparison of coulombic efficiency values of reference cell vs. LiBOB added cell.

Table 5.3: The comparison of electrochemical performances between the reference electrolyte and containing purified LiBOB (first discharged at 25 mA g^{-1} and subsequently cycled at 50 mA g^{-1}).

Electrolyte	1st discharge capacity at 25 mAg^{-1} ($mAhg^{-1}$)	1st charge capacity at 50 mAg^{-1} ($mAhg^{-1}$)	2nd discharge capacity at 50 mAg^{-1} (mA h g^{-1})	CE (%)	100th discharge ($mAhg^{-1}$)	Capacity retention (%)	Capacity retention per cycle (medium in %)
Reference	360.2	234.8	213.2	99.1	124.8	58.5	99.1
1 wt.% LiBOB	285.0	90.2	68.5	98.9	58.9	85.9	99.3

Figure 5.7 shows SEM images for TiO_2/RGO-P anodes with different electrolyte compositions initially discharged at low current density. The electrode discharged with the pristine electrolyte possesses a rough surface, whilst the addition of LiBOB results in the development of a dense and smooth SEI layer covering both RGO flakes and conductive

carbon (carbon black) nanoparticles. In addition, TiO_2 nanoparticles with carbon black are homogeneously distributed within the electrode, whereas the agglomeration takes place for the reference electrode. From **Figure 5.7d&5.8b,** it can be obviously seen that for TiO_2/RGO-P anode recovered from the LiBOB-added cell, smaller sized carbon black nanoparticles were more uniformly integrated within the matrix in comparison with the reference anode. Therefore, the development of a robust SEI film results in enhanced cycling stability owing to the prevention of the direct contact of the $LiPF_6$ based electrolyte with the electrode.

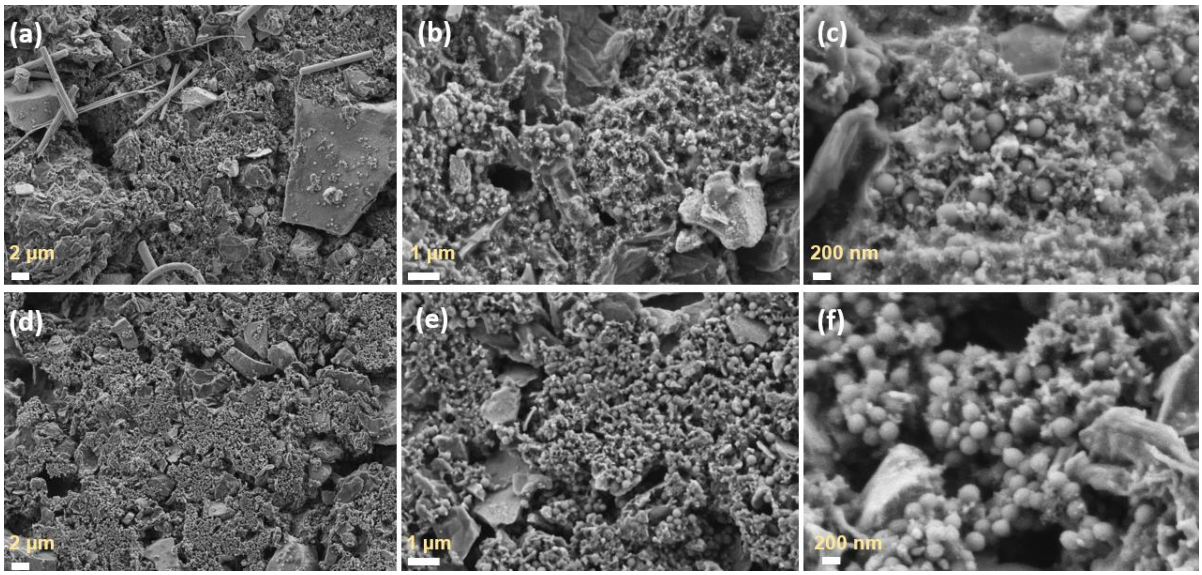

Figure 5.7: SEM images of TiO_2/RGO-P anodes after initial discharging at a rate of 25 mA g^{-1} with (a-c) reference electrolyte, (d-f) 1 wt.% LiBOB.

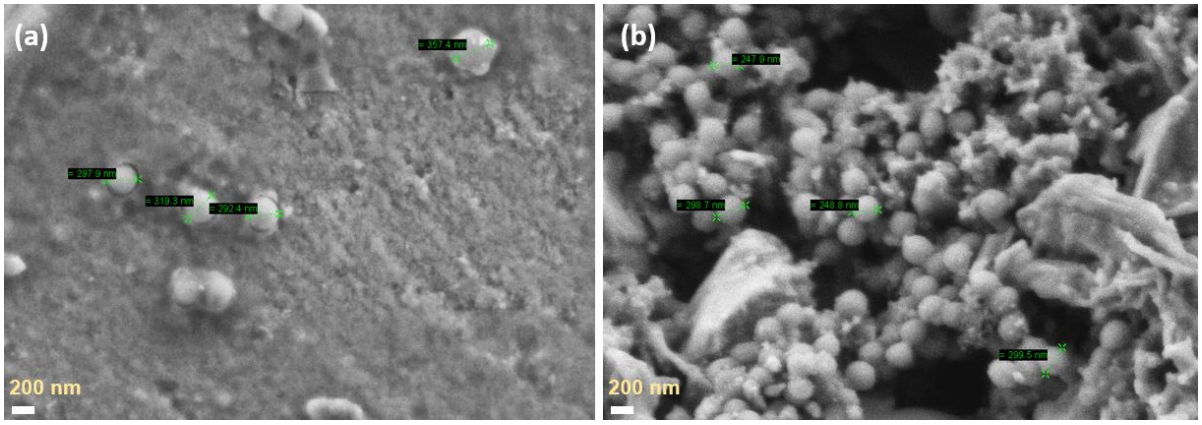

Figure 5.8: SEM images of TiO_2/RGO-P anodes after 1st discharge showing the sizes of nano carbons with (a) reference electrolyte, (b) 1 wt.% LiBOB.

The surface morphologies of TiO_2/RGO-P anodes after 100 cycles are presented in **Figure 5.9**. The anode cycled with the pristine electrolyte exhibits a bumpy surface on the RGO flakes related to the LiF species [512]. In comparison with the reference electrolyte, the white color on the electrode surface (**Figure 5.9f**) indicates the deposition of reduction products of electrolyte, which is in accordance with the obtained poor electrochemical performance at high current rates. Therefore, the uncontrollable growth of SEI film may increase cell resistance resulting in slower Li^+ ion diffusion and higher irreversible capacity loss.

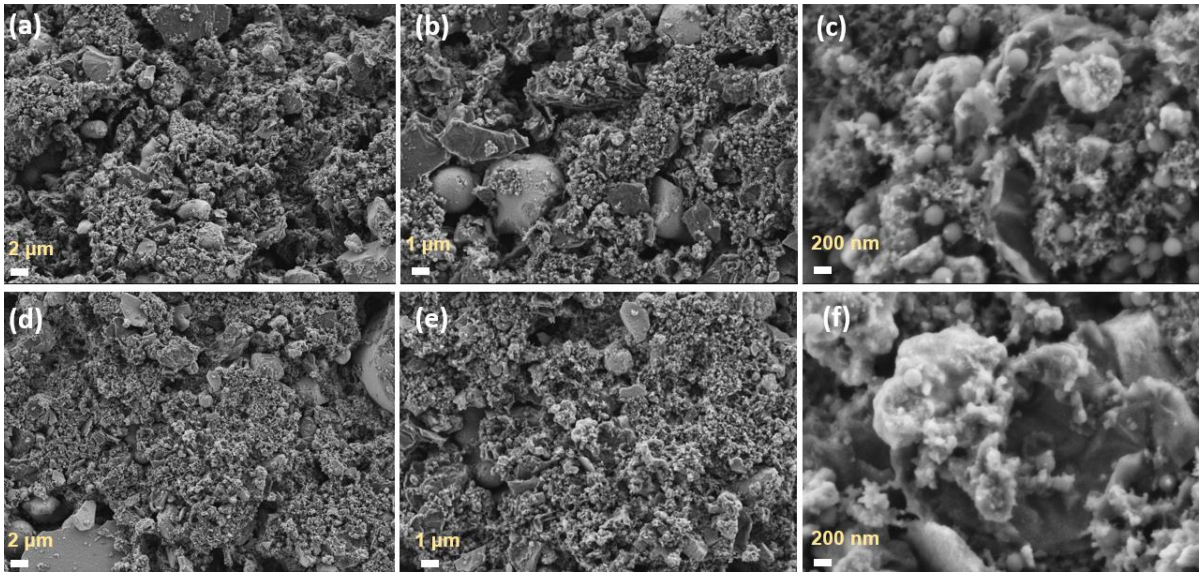

Figure 5.9: SEM images of TiO_2/RGO-P anodes at a rate of 100 mA g^{-1} after 100 cycles with (a-c) reference electrolyte, (d-f) 1 wt.% LiBOB.

To better understand the effects of LiBOB additive on the surface chemistry of TiO_2/RGO-P anodes after 1st discharging at a rate of 25 mA g^{-1} (**Figure 5.10**) and after 100th cycle at a rate of 100 mA g^{-1}, XPS spectra was performed and fitted for C 1s, O 1s, F 1s, P 2p, Ti 2p, B 1s and Li 1s (**Figure 5.11**). From the high-resolution C 1s spectrum, the peak at 284.5 eV (C-C) corresponds to the carbon black and the peak at 290.4 eV (-CF_2-) is attributed to the PVDF binder. The bands at 289.2 eV, 286.4 eV, and 285.3 eV are assigned to C=O, C-O, and C-C/C-H, respectively [513]. The intensity of C=O peak of the TiO_2/RGO-P anode cycled in the LiBOB added electrolyte is much higher than the pristine one, indicating the deposition of the decomposition products of EC solvent like Li_2CO_3 and $ROCO_2Li$ [514]. Additionally, for the reference cell, the carbon black peak is diminished which may be related to the formation of a thick SEI layer after the first discharging process [507]. The O 1s spectra includes three signals of C-O, O=C, O-Ti or Li_2O appearing at 534.3 eV, 532.3 eV and 530.4 eV. The peaks for C-O and O-Ti are relatively more intense within the reference electrode due to the thin interphase layer of TiO_2/RGO-P anode.

From the F 1s spectra, the peak at 685.4 eV (**Figure 5.10c**) and 55.6 eV of Li 1s spectra

assigning LiF (**Figure 5.13a**) increase with the addition of LiBOB in the base electrolyte due to the accelerated decomposition of $LiPF_6$ that is in line with the high irreversible capacity loss during initial lithiation step. However, after 100 cycles, the intensity of LiF in the reference electrolyte increases, whereas for the anode cycled with 1 wt.% LiBOB, its intensity decreases (**Figure 5.11c**). These findings are in agreement with the improved cycling stability through the stabilization of PF_5 and PF_6^- in the electrolyte by LiBOB [375]. According to the P 2p spectra, the two peaks at 135.0 eV ($2p_{1/2}$) and 133.5 eV ($2p_{3/2}$) can be assigned to $Li_xPO_yF_Z$ and Li_xPF_y species, respectively that are obtained in greater concentration for the LiBOB containing anode.

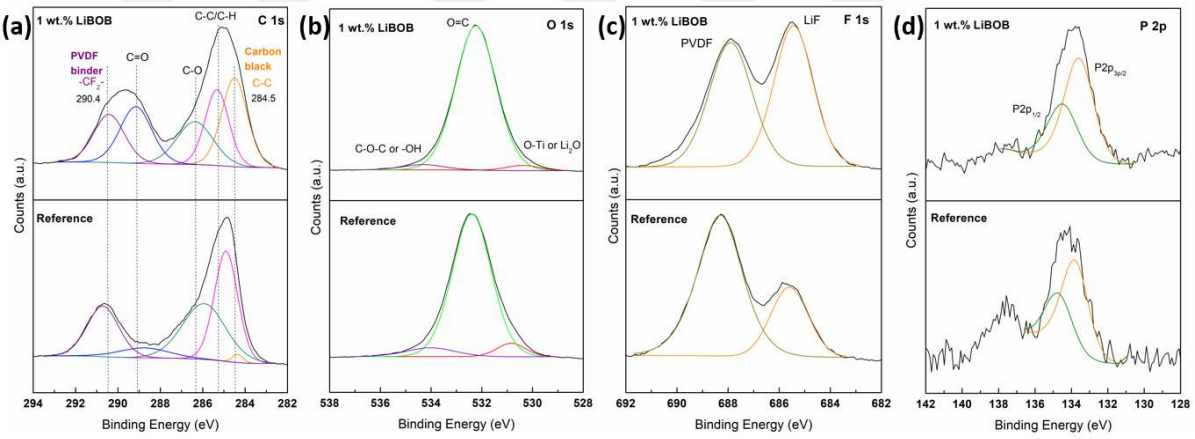

Figure 5.10: XPS spectra of TiO_2/RGO-P anodes after first discharge at a current density of 25 mA g^{-1}: (a) C 1s, (b) O 1s, (c) F 1s and (d) P 2p.

The surface elemental compositions of TiO_2/RGO-P anodes after 1st lithiation and upon cycling with and without LiBOB are given in **Table 5.4** and **Table 5.5**. For the electrode containing LiBOB after initial discharge, the amount of F, Li, O and P are slightly higher while C and Ti are lower that is in line with the results obtained from high resolution spectrums. The lower concentration of Ti suggests that the addition of LiBOB results in the growth of a thick and robust SEI layer at low current rates. Nevertheless, cycling at high current densities may lead to the occurrence of a thin and loose SEI which is in good agreement with the high content of Ti in LiBOB added electrode (**Table 5.5**).

Table 5.4: Quantitative analysis of TiO_2/RGO-P anodes after first discharge at a current density of 25 mA g^{-1} from XPS analysis.

Sample	B (%)	C (%)	F (%)	Li (%)	O (%)	P (%)	Ti (%)
Reference	-	42.78	7.29	19.11	29.53	0.24	1.06
LiBOB	1.89	35.95	8.36	22.19	31.26	0.35	0.19

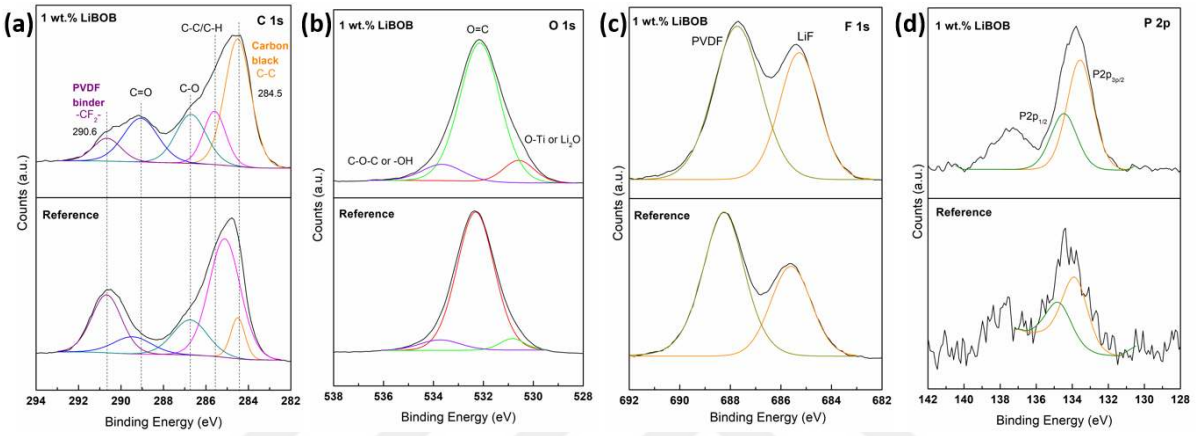

Figure 5.11: XPS spectra of TiO_2/RGO-P anodes after 100 cycles at a current density of 100 mA g^{-1}: (a) C 1s, (b) O 1s, (c) F 1s and (d) P 2p.

Upon cycling, for the LiBOB added electrolyte, the elemental composition of Li and O decrease whereas the content of Ti increases unlike to the 1st discharge.

Table 5.5: Quantitative analysis of TiO_2/RGO-P anodes after 100 cycles at a current density of 100 mA g^{-1} from XPS analysis.

Sample	B (%)	C (%)	F (%)	Li (%)	O (%)	P (%)	Ti (%)
Reference	-	41.07	8.16	19.3	30.25	0.12	1.22
LiBOB	4.42	38.45	8.59	16.18	29.89	0.99	1.46

According to the high-resolution Ti 2p spectrum (**Figure 5.12**), the characteristic signals at 464.8 eV and 459.2 eV are corresponded to the Ti $2p_{1/2}$ and Ti $2p_{3/2}$ of the Ti^{4+} ions.

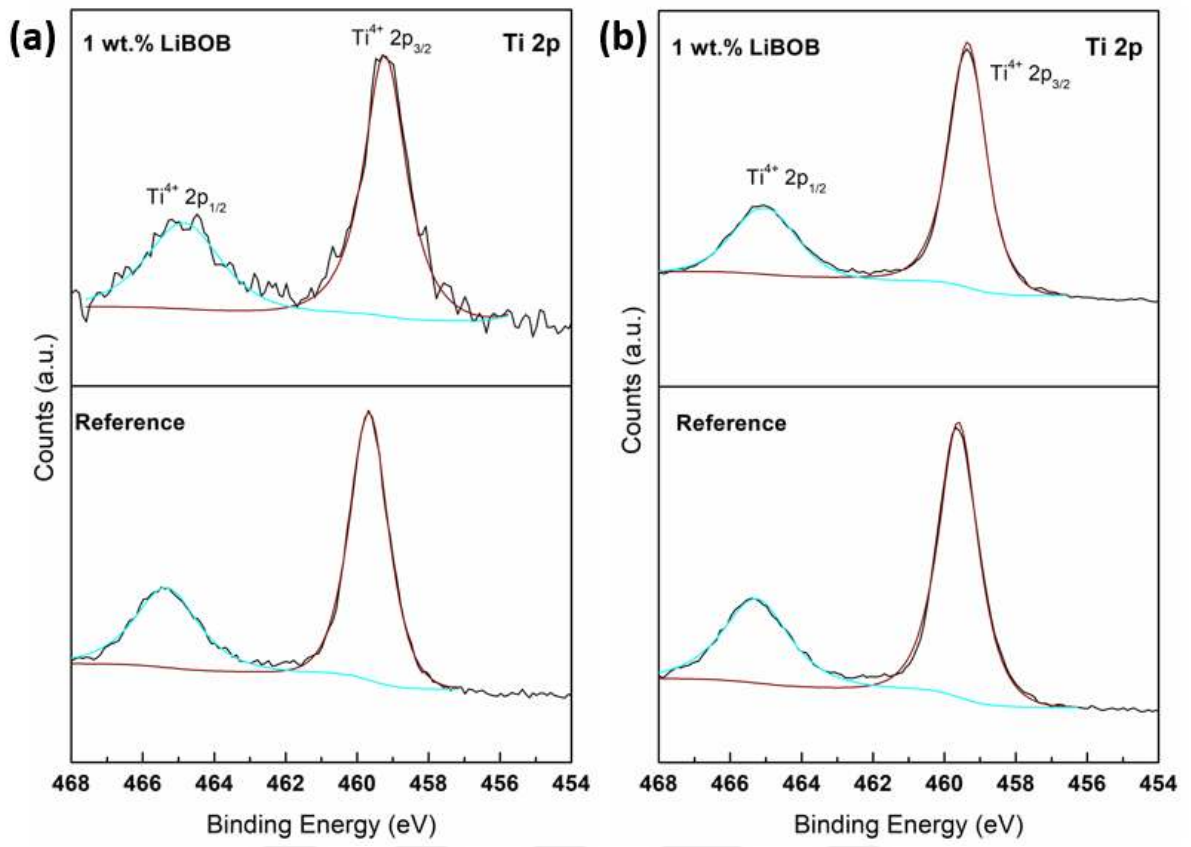

Figure 5.12: Ti 2p XPS spectra of TiO_2/RGO-P anodes after: (a) first discharge and (b) 100 cycles.

B 1s spectra of the electrodes containing LiBOB additive are shown in **Figure 5.13(a-b)**. During the initial development of a LiBOB-derived layer, the peak for B-O appears at 192.5 eV [364] while this value shifts to the lower binding energy when the cycling proceeds at high current rates that is consistent with the poor electrochemical performance related to the degradation of SEI layer.

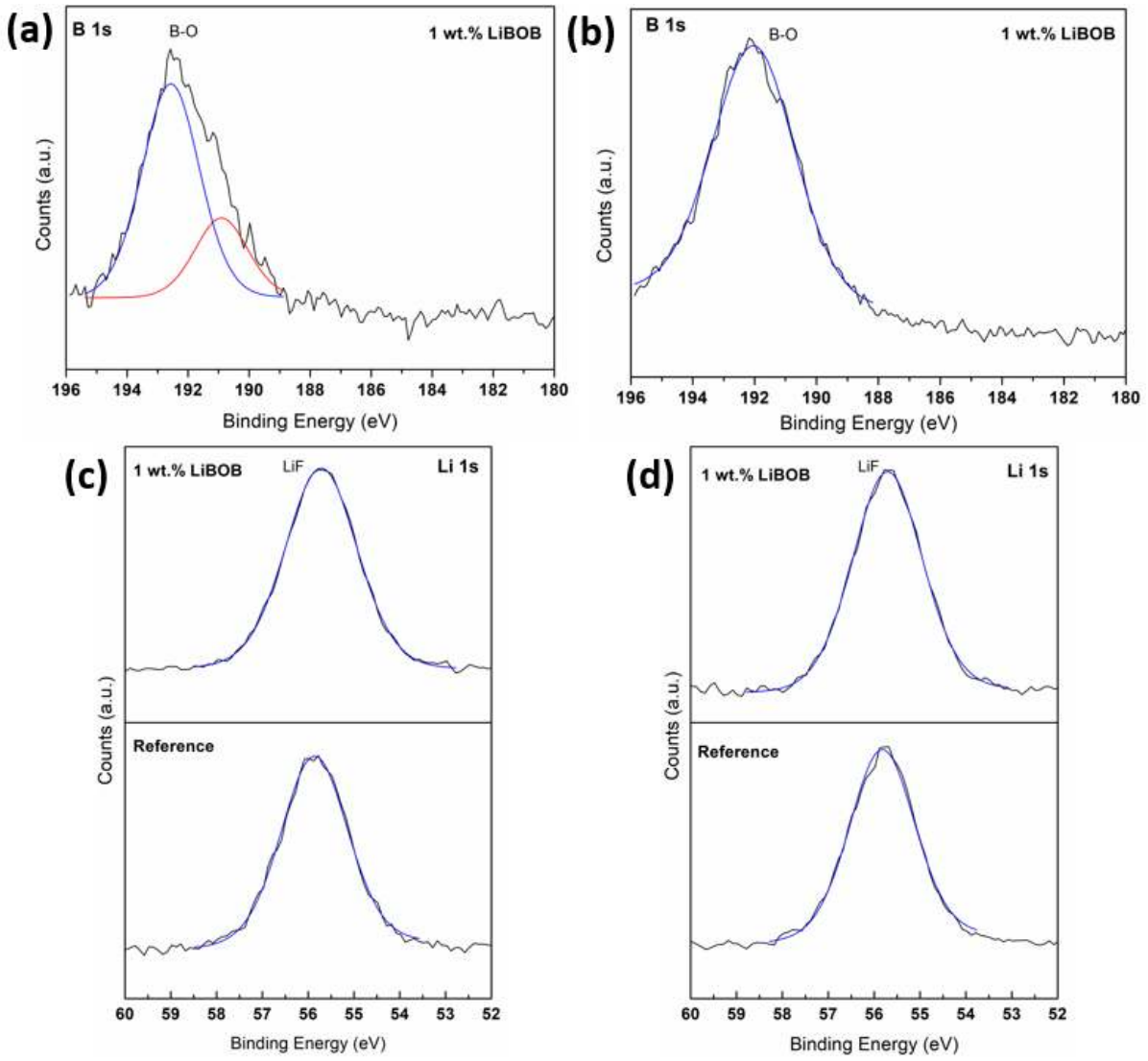

Figure 5.13: XPS spectra of TiO_2/RGO-P anodes (b-c) B 1s after 1st discharge, 100th cycle and (c-d) Li 1s after 1st discharge, 100th cycle respectively.

These results obtained from ex-situ SEM and XPS analyses proved the fact that the protective SEI develops during the first lithiation process at low rates. In the presence of LiBOB within the $LiPF_6$ electrolyte, TiO_2/RGO-P anode undergoes a high irreversible capacity loss that could not be avoided even at low current densities. However, the cycling tests revealed that the formation of a BOB^--originated layer allows more stable cycling performance decreasing the further decomposition of the base electrolyte. To the best of our knowledge, the effects of any electrolyte additives on the stability of TiO_2 anodes have not been studied before that may be attributed to the ability of TiO_2 anodes to eliminate the degradation of electrolytes owing

to its high operating voltage. Although TiO_2 anodes are not required to form a stable SEI, we have previously combined TiO_2 with reduced graphite oxide (RGO), which must need a passivating film due to the uncontrollable growth of SEI as reported in previous studies [353, 515, 516]. Therefore, it is evident that TiO_2/RGO-P anode cycled in LiBOB added electrolyte showed superior capacity retention than the one in the bare electrolyte.

5.5 Conclusion

The effect of LiBOB as a stabilizing electrolyte additive on the cycling stability, morphology, and surface chemistry of TiO_2/RGO-P anode was investigated. For LiBOB, the cycling tests at high current densities (100 mA g^{-1}) resulted in a high C_{irr}, low CE and poor cycling performance. In contrast, more chemically and mechanically SEI could be developed through the initial discharging at a low rate (25 mA g^{-1}) and subsequent cycling at two times higher of this rate. These results suggest that the long-term cycling with a capacity retention of ~86% after 100 cycles and coulombic efficiency was significantly improved owing to the formation of a dense and smooth SEI on the electrode surface depicted from SEM images. XPS spectra demonstrated that the greater amount of LiF on the surface of LiBOB added electrode gave the explanation for the high capacity loss during the first cycle that should be taken place vice versa for the reference electrode. Nevertheless, the content of LiF decreased upon cycling confirming the enhanced cycling stability of LiBOB. Additionally, the lower concentration of Ti in the LiBOB incorporated electrode confirmed the development of a mechanically robust and thick SEI during the first discharging. The results described here showed the importance of developing of an appropriate SEI for long-life LIBs. Further work should be carried out to prevent the high irreversible capacity loss arising from the formation of a passivating layer towards high energy density and safe next-generation anode materials.

Chapter 6:

CONCLUSION

With the increasing demand for high energy density, safe, sustainable, and long-life rechargeable batteries, tremendous attempts have been made to develop novel battery materials. The high capacity lithium metal could not have been used as an anode material for lithium-ion batteries due to its high reactivity resulting in dendritic growth and safety concerns. The commercially used graphite anode cannot fulfill the high energy density requirements because of its limited theoretical capacity. Therefore, TiO_2 based materials have attracted much interest owing to their safety, environmental friendliness, low cost, small volume change and cycling stability. Additionally, their low electrical conductivity problem could also be overcome by performing practical carbon coatings.

State-of-the-art lithium-ion batteries have been used $LiPF_6$ based electrolyte which is susceptible to decomposing into dangerous compounds resulting in performance decay and safety issues. Thus, various electrolyte additives have been developed to ensure overall cell stability through the formation of a protective SEI layer on electrode surfaces. At this point, LiBOB has received significant attention due to its high thermal stability, electrochemical stability in a wide potential window, low cost and environmental friendliness without the formation of toxic compounds. The effects of LiBOB as an electrolyte additive have been investigated to improve the cycling stability and safety of high voltage cathode materials as well as graphite, silicon, lithium anodes due to the enhancement in the interfacial stability.

In this thesis study, high purity LiBOB was synthesized through a low cost practical method

followed by a recrystallization step to eliminate the detrimental impacts of impurities for high performance lithium-ion batteries. The effects of LiBOB were also evaluated in detail on the high voltage $LiCoO_2$ cathodes and as-fabricated TiO_2/RGO anodes for the first time.

To summarize:

- LiBOB was synthesized using stoichiometric amounts of lithium carbonate, oxalic acid and boric acid through a ceramic processing method under a protective atmosphere. Aging experiments revealed the unfavorable effects of moisture and remaining impurities. From the DTA and XRPD analyses, it was found that LiBOB could decompose into HBO_2 and $Li_2C_2O_4$ impurities at the synthesis temperatures above 315 °C, whereas at temperatures below 200 °C the monohydrated phase obtained within the LiBOB that will cause poor electrochemical performance. SEM images also confirmed the structural deterioration of LiBOB related to exposure to air.

- The as-synthesized LiBOB was recrystallized to eliminate the lithium oxalate ($Li_2C_2O_4$) impurity, which may result in a gas pressure to vent the cell and higher cell impedance. According to the RIR method from XRPD, above 99% purity was obtained, while FTIR spectra was further confirmed the removal of oxalate peaks.

- The galvanostatic charge-discharge tests of $LiCoO_2$ cathode cycled in different electrolyte compositions were performed in a voltage range between 3.0 - 4.4 V with different current densities. For the cell containing 1 wt.% LiBOB additive, higher irreversible capacity loss was occurred because of the development of BOB^- originated SEI. The best performing electrolyte composition was the one with 1 wt.% purified LiBOB which achieved a capacity retention of 89.8% and energy density retention of 90.0% over 100 cycles. Therefore, voltage fade and energy degradation issues were significantly prevented. According to the CV measurements, the interfacial

polarization was reduced due to the stabilization of electrolyte with the addition of LiBOB at high operating voltages. In addition, the irreversible hexagonal-monoclinic-hexagonal phase transitions were also mitigated which is in line with ex-situ XRPD results and post-mortem SEM images. Thus, the high purity LiBOB lead to enhance in the cycling stability, energy density, coulombic efficiency and rate capability of high voltage $LiCoO_2$ cathodes through the formation of a chemically and mechanically stable interphase.

- Anatase TiO_2 nanoparticles with a crystallite size below 20 nm was obtained via a sol-gel process. A nanocomposite of TiO_2 with reduced graphite oxide (RGO) was fabricated to increase overall electrochemical performance by introducing a conductive network. A surface modification method with peroxide solution was performed to increase the hydrophilicity, dispersion of TiO_2 nanoparticles and mechanical stability within the RGO matrix due to the surface oxidation. These results were confirmed from SEM-EDX, FTIR and XPS analyses.

- The galvanostatic charge-discharge cycling tests were conducted in a potential window of 1.0 – 3.0 V at different current densities to compare the electrochemical performances of TiO_2, TiO_2/RGO and surface modified TiO_2/RGO-P anodes. The surface modified one exhibited the highest reversible capacity, stable cycling performance, high coulombic efficiency and superior rate capability owing to the stable formation of 3D channels of TiO_2 nanoparticles after the surface oxidation.

- LiBOB as an electrolyte additive to stabilize TiO_2/RGO-P nanocomposite anode was investigated for different current densities. From the galvanostatic cycling tests, it was found that the first lithiation step should be carried out at low rates (25 mA g^{-1}) to form a chemically and mechanically stable SEI layer on the anode surface. Thus, denser

and smoother SEI could be developed resulting in better cycling stability and coulombic efficiency. However, a huge irreversible capacity loss of the cell containing LiBOB could not be avoided in accordance with the high amount of LiF content as given in high resolution F 1s spectra. SEM images also revealed the importance of the current density towards forming a correct SEI layer to inhibit the direct contact of the electrolyte with an anode.

Thus, high purity anhydrous LiBOB could be practically used for other high voltage cathodes and new generation anodes to achieve high energy density, cycling stability and safety towards state-of-the-art lithium-ion batteries.

Publications and Conferences

- **Subaşı, Y**., Zor, C., Haciu, D., Somer, M., & Afyon, S. "Guide to Water Free Lithium Bis (oxalate) Borate (LiBOB)", *The Journal of Physical Chemistry C*, 125, 11310-11317 (2021).
- A Synthesis Set-up and Production Method for High Purity Anhydrous Lithium Bis(oxalato)Borate (LiBOB), *European Patent Application No*: 20194250.5 – 1109, 10.03.2021, EP 3789390 A1.
- **Subaşı, Y**., Somer, M., Yağcı, M.B., Afyon S. "Surface Modified TiO_2/Reduced Graphite Oxide Nanocomposite Anodes for Lithium Ion Batteries", *Journal of Solid State Electrochemistry*, 24, 1085–1093 (2020).
- **Subaşı, Y**., Haciu D., Somer, M. S., & Afyon, S., The effect of Lithium Bis(oxalate)borate, LiB(C2O4)2 (LiBOB), on the Cycling Stability of TiO_2 / Reduced Graphite Oxide Anode Materials, International Boron Symposium (BORON2019), Nevşehir, Turkey, April 2019, *Oral presentation*

BIBLIOGRAPHY

[1] Manthiram, A. (2020). A reflection on lithium-ion battery cathode chemistry. *Nature Communications, 11*(1):1550.

[2] Tarascon, J. M., & Armand, M. (2001). Issues and challenges facing rechargeable lithium batteries. *Nature, 414*(6861):359-367.

[3] Whittingham, M. S. (1979). Intercalation chemistry and energy storage. *Journal of Solid State Chemistry, 29*(3):303-310.

[4] Whittingham, M. S. (2008). Materials challenges facing electrical energy storage. *MRS Bulletin, 33*(4):411-419.

[5] Cheng, X.-B., Zhang, R., Zhao, C.-Z., & Zhang, Q. (2017). Toward Safe Lithium Metal Anode in Rechargeable Batteries: A Review. *Chemical Reviews, 117*(15):10403-10473.

[6] Mizushima, K., Jones, P. C., Wiseman, P. J., & Goodenough, J. B. (1980). LixCoO2 (0<x<-1): A new cathode material for batteries of high energy density. *Materials Research Bulletin, 15*(6):783-789.

[7] Thackeray, M., David, W., Bruce, P., & Goodenough, J. (1983). Lithium insertion into manganese spinels. *Materials Research Bulletin, 18*(4):461-472.

[8] Yoshino, A. (2012). The Birth of the Lithium-Ion Battery. *Angewandte Chemie International Edition, 51*(24):5798-5800.

[9] Nishi, Y. (2001). The development of lithium ion secondary batteries. *The Chemical Record, 1*(5):406-413.

[10] 2021). Popular information. NobelPrize.org. Nobel Prize Outreach AB 2021. Mon. 13 Sep 2021. < Retrieved from https://www.nobelprize.org/prizes/chemistry/2019/popular-information/

[11] Manthiram, A. (2017). An Outlook on Lithium Ion Battery Technology. *ACS Central Science, 3*(10):1063-1069.

[12] Armand, M., & Tarascon, J. M. (2008). Building better batteries. *Nature, 451*(7179):652-657.

[13] Goodenough, J. B., & Park, K.-S. (2013). The Li-Ion Rechargeable Battery: A Perspective. *Journal of the American Chemical Society, 135*(4):1167-1176.

[14] Bruce, P. G. (2008). Energy storage beyond the horizon: Rechargeable lithium batteries. *Solid State Ionics, 179*(21):752-760.

[15] Diouf, B., & Pode, R. (2015). Potential of lithium-ion batteries in renewable energy. *Renewable Energy, 76*:375-380.

[16] Xin, F., & Whittingham, M. S. (2020). Challenges and Development of Tin-Based Anode with High Volumetric Capacity for Li-Ion Batteries. *Electrochemical Energy Reviews, 3*(4):643-655.

[17] Wang, K., Wan, J., Xiang, Y., Zhu, J., Leng, Q., Wang, M., . . . Yang, Y. (2020). Recent advances and historical developments of high voltage lithium cobalt oxide materials for rechargeable Li-ion batteries. *Journal of Power Sources, 460*:228062.

[18] Schipper, F., Erickson, E. M., Erk, C., Shin, J.-Y., Chesneau, F. F., & Aurbach, D. (2016). Review—Recent Advances and Remaining Challenges for Lithium Ion

Battery Cathodes. *Journal of The Electrochemical Society, 164*(1):A6220-A6228.
[19] Shang, Y., Lin, X., Lu, X., Huang, T., & Yu, A. (2015). Nano-TiO2(B) coated LiMn2O4 as cathode materials for lithium-ion batteries at elevated temperatures. *Electrochimica Acta, 156*:121-126.
[20] Zhao, H., Gao, X., Li, Y., Ran, Q., Fu, C., Feng, Y., . . . Su, J. (2019). Synergistic effects of zinc-doping and nano-rod morphology on enhancing the electrochemical properties of spinel Li-Mn-O material. *Ceramics International, 45*(14):17591-17597.
[21] Xu, M., Zhou, L., Hao, L., Xing, L., Li, W., & Lucht, B. L. (2011). Investigation and application of lithium difluoro(oxalate)borate (LiDFOB) as additive to improve the thermal stability of electrolyte for lithium-ion batteries. *Journal of Power Sources, 196*(16):6794-6801.
[22] Liu, H., Cao, Q., Fu, L. J., Li, C., Wu, Y. P., & Wu, H. Q. (2006). Doping effects of zinc on LiFePO4 cathode material for lithium ion batteries. *Electrochemistry Communications, 8*(10):1553-1557.
[23] Zhang, W.-J. (2011). Structure and performance of LiFePO4 cathode materials: A review. *Journal of Power Sources, 196*(6):2962-2970.
[24] Kaskhedikar, N. A., & Maier, J. (2009). Lithium storage in carbon nanostructures. *Advanced Materials, 21*(25-26):2664-2680.
[25] Balakrishnan, P., Ramesh, R., & Kumar, T. P. (2006). Safety mechanisms in lithium-ion batteries. *Journal of Power Sources, 155*(2):401-414.
[26] Thackeray, M. M., Wolverton, C., & Isaacs, E. D. (2012). Electrical energy storage for transportation—approaching the limits of, and going beyond, lithium-ion batteries. *Energy & Environmental Science, 5*(7):7854-7863.
[27] Linden, D. (1995). *Handbook of batteries.* Paper presented at the Fuel and energy abstracts.
[28] Zhang, Y., Tang, Y., Li, W., & Chen, X. (2016). Nanostructured TiO2-Based Anode Materials for High-Performance Rechargeable Lithium-Ion Batteries. *ChemNanoMat, 2*(8):764-775.
[29] Fergus, J. W. (2010). Recent developments in cathode materials for lithium ion batteries. *Journal of Power Sources, 195*(4):939-954.
[30] Whittingham, M. S. (2004). Lithium Batteries and Cathode Materials. *Chemical Reviews, 104*(10):4271-4302.
[31] Tarascon, J. M. (2010). Key challenges in future Li-battery research. *Philos Trans A Math Phys Eng Sci, 368*(1923):3227-3241.
[32] Melot, B. C., & Tarascon, J. M. (2013). Design and Preparation of Materials for Advanced Electrochemical Storage. *Accounts of Chemical Research, 46*(5):1226-1238.
[33] Zubi, G., Dufo-López, R., Carvalho, M., & Pasaoglu, G. (2018). The lithium-ion battery: State of the art and future perspectives. *Renewable and Sustainable Energy Reviews, 89*:292-308.
[34] Rossouw, M. H., & Thackeray, M. M. (1991). Lithium manganese oxides from Li2MnO3 for rechargeable lithium battery applications. *Materials Research Bulletin, 26*(6):463-473.
[35] Antolini, E. (2004). LiCoO2: formation, structure, lithium and oxygen nonstoichiometry, electrochemical behaviour and transport properties. *Solid State Ionics, 170*(3-4):159-171.
[36] Thackeray, M. M., Kang, S.-H., Johnson, C. S., Vaughey, J. T., Benedek, R., & Hackney, S. A. (2007). Li2MnO3-stabilized LiMO2 (M = Mn, Ni, Co) electrodes for lithium-ion batteries. *Journal of Materials Chemistry, 17*(30):3112-3125.
[37] He, P., Yu, H., & Zhou, H. (2012). Layered lithium transition metal oxide cathodes towards high energy lithium-ion batteries. *Journal of Materials Chemistry,*

22(9):3680-3695.

[38] Johnston, W., Heikes, R., & Sestrich, D. (1958). The preparation, crystallography, and magnetic properties of the LixCo (1− x) O system. *Journal of Physics and Chemistry of Solids, 7*(1):1-13.

[39] Gao, S., Wei, W., Ma, M., Qi, J., Yang, J., Chu, S., . . . Guo, L. (2015). Sol–gel synthesis and electrochemical properties of c-axis oriented LiCoO 2 for lithium-ion batteries. *RSC Advances, 5*(64):51483-51488.

[40] Gummow, R. J., Thackeray, M. M., David, W. I. F., & Hull, S. (1992). Structure and electrochemistry of lithium cobalt oxide synthesised at 400°C. *Materials Research Bulletin, 27*(3):327-337.

[41] Wang, L., Chen, B., Ma, J., Cui, G., & Chen, L. (2018). Reviving lithium cobalt oxide-based lithium secondary batteries-toward a higher energy density. *Chemical Society Reviews, 47*(17):6505-6602.

[42] Cheng, H.-M., Wang, F.-M., Chu, J. P., Santhanam, R., Rick, J., & Lo, S.-C. (2012). Enhanced Cycleabity in Lithium Ion Batteries: Resulting from Atomic Layer Depostion of Al2O3 or TiO2 on LiCoO2 Electrodes. *The Journal of Physical Chemistry C, 116*(14):7629-7637.

[43] Lyu, Y., Wu, X., Wang, K., Feng, Z., Cheng, T., Liu, Y., . . . Guo, B. An Overview on the Advances of LiCoO2 Cathodes for Lithium-Ion Batteries. *Advanced Energy Materials, n/a*(n/a):2000982.

[44] Wang, Y., Zhang, Q., Xue, Z.-C., Yang, L., Wang, J., Meng, F., . . . Li, H. (2020). An In Situ Formed Surface Coating Layer Enabling LiCoO2 with Stable 4.6 V High-Voltage Cycle Performances. *Advanced Energy Materials, 10*(28):2001413.

[45] Xie, J., & Lu, Y.-C. (2020). A retrospective on lithium-ion batteries. *Nature Communications, 11*(1):2499.

[46] Winter, M., Besenhard, J. O., Spahr, M. E., & Novák, P. (1998). Insertion Electrode Materials for Rechargeable Lithium Batteries. *Advanced Materials, 10*(10):725-763.

[47] Yoshio, M., & Noguchi, H. (2009). A Review of Positive Electrode Materials for Lithium-Ion Batteries. In M. Yoshio, R. J. Brodd, & A. Kozawa (Eds.), *Lithium-Ion Batteries: Science and Technologies* (pp. 9-48). New York, NY: Springer New York.

[48] Zheng, J., Myeong, S., Cho, W., Yan, P., Xiao, J., Wang, C., . . . Zhang, J.-G. (2017). Li- and Mn-Rich Cathode Materials: Challenges to Commercialization. *Advanced Energy Materials, 7*(6):1601284.

[49] Wang, Z., Rao, M., Li, J., Ye, C., Liu, Z., Xu, Q., . . . Qiu, Y. (2019). Understanding the mechanism of cycling degradation and novel strategy to stabilize the cycling performance of graphite/LiCoO2 battery at high voltage. *Journal of Electroanalytical Chemistry, 851*:113411.

[50] Chebiam, R. V., Kannan, A. M., Prado, F., & Manthiram, A. (2001). Comparison of the chemical stability of the high energy density cathodes of lithium-ion batteries. *Electrochemistry Communications, 3*(11):624-627.

[51] Jung, Y. S., Cavanagh, A. S., Dillon, A. C., Groner, M. D., George, S. M., & Lee, S.-H. (2010). Enhanced Stability of LiCoO[sub 2] Cathodes in Lithium-Ion Batteries Using Surface Modification by Atomic Layer Deposition. *Journal of The Electrochemical Society, 157*(1):A75.

[52] Kraytsberg, A., & Ein-Eli, Y. (2012). Higher, Stronger, Better… A Review of 5 Volt Cathode Materials for Advanced Lithium-Ion Batteries. *Advanced Energy Materials, 2*(8):922-939.

[53] Ji, Y., Zhang, P., Lin, M., Zhao, W., Zhang, Z., Zhao, Y., & Yang, Y. (2017). Toward a stable electrochemical interphase with enhanced safety on high-voltage LiCoO2 cathode: A case of phosphazene additives. *Journal of Power Sources, 359*:391-399.

[54] Liao, B., Li, H., Xu, M., Xing, L., Liao, Y., Ren, X., . . . Li, W. (2018). Designing

Low Impedance Interface Films Simultaneously on Anode and Cathode for High Energy Batteries. *Advanced Energy Materials, 8*(22):1800802.

[55] Jung, Y. S., Cavanagh, A. S., Riley, L. A., Kang, S.-H., Dillon, A. C., Groner, M. D., . . . Lee, S.-H. (2010). Ultrathin Direct Atomic Layer Deposition on Composite Electrodes for Highly Durable and Safe Li-Ion Batteries. *Advanced Materials, 22*(19):2172-2176.

[56] Chang, W., Choi, J.-W., Im, J.-C., & Lee, J. K. (2010). Effects of ZnO coating on electrochemical performance and thermal stability of LiCoO2 as cathode material for lithium-ion batteries. *Journal of Power Sources, 195*(1):320-326.

[57] Hwang, B. J., Chen, C. Y., Cheng, M. Y., Santhanam, R., & Ragavendran, K. (2010) Mechanism study of enhanced electrochemical performance of ZrO2-coated LiCoO2 in high voltage region. *Journal of Power Sources, 195*(13):4255-4265.

[58] Hudaya, C., Park, J. H., Lee, J. K., & Choi, W. (2014). SnO2-coated LiCoO2 cathode material for high-voltage applications in lithium-ion batteries. *Solid State Ionics, 256*:89-92.

[59] Jung, Y. S., Lu, P., Cavanagh, A. S., Ban, C., Kim, G.-H., Lee, S.-H., . . . Dillon, A. C. (2013). Unexpected Improved Performance of ALD Coated LiCoO2/Graphite Li-Ion Batteries. *Advanced Energy Materials, 3*(2):213-219.

[60] Scott, I. D., Jung, Y. S., Cavanagh, A. S., Yan, Y., Dillon, A. C., George, S. M., & Lee, S.-H. (2011). Ultrathin Coatings on Nano-LiCoO2 for Li-Ion Vehicular Applications. *Nano Letters, 11*(2):414-418.

[61] Cho, J., Kim, Y. J., Kim, T. J., & Park, B. (2001). Zero-strain intercalation cathode for rechargeable Li-Ion cell. *Angewandte Chemie, 113*(18):3471-3473.

[62] Zhou, M., Qin, C., Liu, Z., Feng, L., Su, X., Chen, Y., . . . Liu, Z. (2017). Enhanced high voltage cyclability of LiCoO2 cathode by adopting poly[bis-(ethoxyethoxyethoxy)phosphazene] with flame-retardant property as an electrolyte additive for lithium-ion batteries. *Applied Surface Science, 403*:260-266.

[63] Kalyani, P., & Kalaiselvi, N. (2005). Various aspects of LiNiO2 chemistry: A review. *Science and Technology of Advanced Materials, 6*(6):689-703.

[64] Kalyani, P., Kalaiselvi, N., & Renganathan, N. G. (2003). Microwave-assisted synthesis of LiNiO2—a preliminary investigation. *Journal of Power Sources, 123*(1):53-60.

[65] Ohzuku, T., Ueda, A., & Nagayama, M. (1993). Electrochemistry and Structural Chemistry of LiNiO2 (R3m) for 4 Volt Secondary Lithium Cells. *Journal of The Electrochemical Society, 140*(7):1862-1870.

[66] Rougier, A., Gravereau, P., & Delmas, C. (1996). Optimization of the Composition of the $Li1-z\ Ni1+z\ O2$ Electrode Materials: Structural, Magnetic, and Electrochemical Studies. *Journal of The Electrochemical Society, 143*(4):1168-1175.

[67] Dyer, L. D., Borie, B. S., & Smith, G. P. (1954). Alkali Metal-Nickel Oxides of the Type MNiO2. *Journal of the American Chemical Society, 76*(6):1499-1503.

[68] Nitta, N., Wu, F., Lee, J. T., & Yushin, G. (2015). Li-ion battery materials: present and future. *Materials Today, 18*(5):252-264.

[69] Vitins, G., & West, K. (1997). Lithium Intercalation into Layered LiMnO2. *Journal of The Electrochemical Society, 144*(8):2587-2592.

[70] Tabuchi, M., Ado, K., Kobayashi, H., Kageyama, H., Masquelier, C., Kondo, A., & Kanno, R. (1998). Synthesis of LiMnO2 with α-NaMnO2-Type Structure by a Mixed-Alkaline Hydrothermal Reaction. *Journal of The Electrochemical Society, 145*(4):L49-L52.

[71] Armstrong, A. R., & Bruce, P. G. (1996). Synthesis of layered LiMnO2 as an electrode for rechargeable lithium batteries. *Nature, 381*(6582):499-500.

[72] Reimers, J. N., Fuller, E. W., Rossen, E., & Dahn, J. R. (1993). Synthesis and

Electrochemical Studies of LiMnO2 Prepared at Low Temperatures. *Journal of The Electrochemical Society, 140*(12):3396-3401.

[73] Gummow, R. J., Liles, D. C., & Thackeray, M. M. (1993). Lithium extraction from orthorhombic lithium manganese oxide and the phase transformation to spinel. *Materials Research Bulletin, 28*(12):1249-1256.

[74] Ceder, G. (1999). The Stability of Orthorhombic and Monoclinic-Layered LiMnO[sub 2]. *Electrochemical and solid-state letters, 2*(11):550.

[75] Tsutomu, O., & Yoshinari, M. (2001). Layered Lithium Insertion Material of LiNi1/2Mn1/2O2 : A Possible Alternative to LiCoO2 for Advanced Lithium-Ion Batteries. *Chemistry Letters, 30*(8):744-745.

[76] Schougaard, S. B., Bréger, J., Jiang, M., Grey, C. P., & Goodenough, J. B. (2006). LiNi0.5+δMn0.5–δO2—A High-Rate, High-Capacity Cathode for Lithium Rechargeable Batteries. *Advanced Materials, 18*(7):905-909.

[77] Ellis, B. L., Lee, K. T., & Nazar, L. F. (2010). Positive Electrode Materials for Li-Ion and Li-Batteries. *Chemistry of Materials, 22*(3):691-714.

[78] Hu, G., Shi, Y., Fan, J., Cao, Y., Peng, Z., Zhang, Y., . . . Du, K. (2020). Sb doping and Sb2O3 coating collaboration to improve the electrochemical performance of LiNi0.5Mn0.5O2 cathode material for lithium ion batteries. *Electrochimica Acta, 364*:137127.

[79] Liu, Y., Chen, B., Cao, F., Zhao, X., & Yuan, J. (2011). Synthesis of nanoarchitectured LiNi0.5Mn0.5O2 spheres for high-performance rechargeable lithium-ion batteries via an in situ conversion route. *Journal of Materials Chemistry, 21*(28):10437-10441.

[80] Jia, G., Liu, S., Yang, G., Li, F., Wu, K., He, Z., & Shangguan, X. (2018). The multiple effects of Al-doping on the structure and electrochemical performance of LiNi0.5Mn0.5O2 as cathode material at high voltage. *Ionics, 24*(12):3705-3715.

[81] Lee, K. S., Myung, S. T., Moon, J. S., & Sun, Y. K. (2008). Particle size effect of Li[Ni0.5Mn0.5]O2 prepared by co-precipitation. *Electrochimica Acta, 53*(20):6033-6037.

[82] Hu, G., Liu, W., Peng, Z., Du, K., & Cao, Y. (2012). Synthesis and electrochemical properties of LiNi0.8Co0.15Al0.05O2 prepared from the precursor Ni0.8Co0.15Al0.05OOH. *Journal of Power Sources, 198*:258-263.

[83] Yang, J., Zhang, Y., Zhao, P., Shang, Y., Wang, L., He, X., & Wang, J. (2015). In-situ Coating of Cathode by Electrolyte Additive for High-voltage Performance of Lithium-ion Batteries. *Electrochimica Acta, 158*:202-208.

[84] Sun, Y.-K., Myung, S.-T., Park, B.-C., & Yashiro, H. (2008). Improvement of the Electrochemical Properties of Li[Ni[sub 0.5]Mn[sub 0.5]]O[sub 2] by AlF[sub 3] Coating. *Journal of The Electrochemical Society, 155*(10):A705.

[85] Johnson, C. S., Kim, J.-S., Kropf, A. J., Kahaian, A. J., Vaughey, J. T., & Thackeray, M. M. (2003). Structural and electrochemical evaluation of (1 − x)Li2TiO3·(x)LiMn0.5Ni0.5O2 electrodes for lithium batteries. *Journal of Power Sources, 119-121*:139-144.

[86] Rossen, E., Jones, C. D. W., & Dahn, J. R. (1992). Structure and electrochemistry of LixMnyNi1−yO2. *Solid State Ionics, 57*(3):311-318.

[87] Tsutomu, O., & Yoshinari, M. (2001). Layered Lithium Insertion Material of LiCo1/3Ni1/3Mn1/3O2 for Lithium-Ion Batteries. *Chemistry Letters, 30*(7):642-643.

[88] Yabuuchi, N., & Ohzuku, T. (2003). Novel lithium insertion material of LiCo1/3Ni1/3Mn1/3O2 for advanced lithium-ion batteries. *Journal of Power Sources, 119-121*:171-174.

[89] Shao, Y., Huang, B., Lu, Z., Liu, Y., Meng, X., Du, L., . . . Liao, S. (2019). High-Performance 3D Pinecone-Like LiNi1/3Co1/3Mn1/3O2 Cathode for Lithium-Ion

Batteries. *Energy Technology, 7*(4):1800769.
[90] Liu, W., Oh, P., Liu, X., Lee, M.-J., Cho, W., Chae, S., . . . Cho, J. (2015). Nickel-Rich Layered Lithium Transition-Metal Oxide for High-Energy Lithium-Ion Batteries. *Angewandte Chemie International Edition, 54*(15):4440-4457.
[91] Chen, Z., Chao, D., Liu, J., Copley, M., Lin, J., Shen, Z., . . . Passerini, S. (2017). 1D nanobar-like LiNi0.4Co0.2Mn0.4O2 as a stable cathode material for lithium-ion batteries with superior long-term capacity retention and high rate capability. *Journal of Materials Chemistry A, 5*(30):15669-15675.
[92] Chen, Z., Kim, G.-T., Guang, Y., Bresser, D., Diemant, T., Huang, Y., . . . Shen, Z. (2018). Manganese phosphate coated Li[Ni0.6Co0.2Mn0.2]O2 cathode material: Towards superior cycling stability at elevated temperature and high voltage. *Journal of Power Sources, 402*:263-271.
[93] Chen, Z., Chao, D., Lin, J., & Shen, Z. (2017). Recent progress in surface coating of layered LiNixCoyMnzO2 for lithium-ion batteries. *Materials Research Bulletin, 96*:491-502.
[94] Mauger, A., & Julien, C. (2014). Surface modifications of electrode materials for lithium-ion batteries: status and trends. *Ionics, 20*(6):751-787.
[95] Thackeray, M. M., de Picciotto, L. A., de Kock, A., Johnson, P. J., Nicholas, V. A., & Adendorff, K. T. (1987). Spinel electrodes for lithium batteries — A review. *Journal of Power Sources, 21*(1):1-8.
[96] Thackeray, M. M., de Kock, A., & David, W. I. F. (1993). Synthesis and structural characterization of defect spinels in the lithium-manganese-oxide system. *Materials Research Bulletin, 28*(10):1041-1049.
[97] Thackeray, M. M. (1997). Manganese oxides for lithium batteries. *Progress in Solid State Chemistry, 25*(1):1-71.
[98] Thackeray, M. M., David, W. I. F., Bruce, P. G., & Goodenough, J. B. (1983). Lithium insertion into manganese spinels. *Materials Research Bulletin, 18*(4):461-472.
[99] Xu, B., Qian, D., Wang, Z., & Meng, Y. S. (2012). Recent progress in cathode materials research for advanced lithium ion batteries. *Materials Science and Engineering: R: Reports, 73*(5-6):51-65.
[100] Aurbach, D., Levi, M. D., Gamulski, K., Markovsky, B., Salitra, G., Levi, E., . . . Oesten, R. (1999). Capacity fading of LixMn2O4 spinel electrodes studied by XRD and electroanalytical techniques. *Journal of Power Sources, 81-82*:472-479.
[101] Yunjian, L., Xinhai, L., Huajun, G., Zhixing, W., Qiyang, H., Wenjie, P., & Yong, Y. (2009). Electrochemical performance and capacity fading reason of LiMn2O4/graphite batteries stored at room temperature. *Journal of Power Sources, 189*(1):721-725.
[102] Du Pasquier, A., Blyr, A., Courjal, P., Larcher, D., Amatucci, G., Gérand, B., & Tarascon, J. M. (1999). Mechanism for Limited 55°C Storage Performance of Li1.05Mn1.95 O 4 Electrodes. *Journal of The Electrochemical Society, 146*(2):428-436.
[103] Thackeray, M. M. (1999). Spinel electrodes for lithium batteries. *Journal of the American Ceramic Society, 82*(12):3347-3354.
[104] Wohlfahrt-Mehrens, M., Vogler, C., & Garche, J. (2004). Aging mechanisms of lithium cathode materials. *Journal of Power Sources, 127*(1):58-64.
[105] Hernán, L., Morales, J., Sánchez, L., & Santos, J. (1999). Use of Li–M–Mn–O [M=Co, Cr, Ti] spinels prepared by a sol-gel method as cathodes in high-voltage lithium batteries. *Solid State Ionics, 118*(3):179-185.
[106] Molenda, J., Marzec, J., Świerczek, K., Ojczyk, W., Ziemnicki, M., Molenda, M., . . . Dziembaj, R. (2004). The effect of 3d substitutions in the manganese sublattice on

the charge transport mechanism and electrochemical properties of manganese spinel. *Solid State Ionics, 171*(3):215-227.

[107] Song, J., Shin, D. W., Lu, Y., Amos, C. D., Manthiram, A., & Goodenough, J. B. (2012). Role of Oxygen Vacancies on the Performance of Li[Ni0.5–xMn1.5+x]O4 (x = 0, 0.05, and 0.08) Spinel Cathodes for Lithium-Ion Batteries. *Chemistry of Materials, 24*(15):3101-3109.

[108] Amine, K., Tukamoto, H., Yasuda, H., & Fujita, Y. (1997). Preparation and electrochemical investigation of LiMn2 − xMexO4 (Me: Ni, Fe, and x = 0.5, 1) cathode materials for secondary lithium batteries. *Journal of Power Sources, 68*(2):604-608.

[109] Santhanam, R., & Rambabu, B. (2010). Research progress in high voltage spinel LiNi0.5Mn1.5O4 material. *Journal of Power Sources, 195*(17):5442-5451.

[110] Wang, L., Li, H., Huang, X., & Baudrin, E. (2011). A comparative study of Fd-3m and P4332 "LiNi0.5Mn1.5O4". *Solid State Ionics, 193*(1):32-38.

[111] Jin, Y.-C., Lin, C.-Y., & Duh, J.-G. (2012). Improving rate capability of high potential LiNi0.5Mn1.5O4−x cathode materials via increasing oxygen non-stoichiometries. *Electrochimica Acta, 69*:45-50.

[112] Shiiba, H., Zettsu, N., Kida, S., Kim, D.-w., & Teshima, K. (2018). Impact of trace extrinsic defect formation on the local symmetry transition in spinel LiNi0.5Mn1.5O4−δ systems and their electrochemical characteristics. *Journal of Materials Chemistry A, 6*(45):22749-22757.

[113] Kim, J. H., Myung, S. T., Yoon, C. S., Kang, S. G., & Sun, Y. K. (2004). Comparative Study of LiNi0.5Mn1.5O4-δ and LiNi0.5Mn1.5O4 Cathodes Having Two Crystallographic Structures: Fd$\bar{3}$m and P4332. *Chemistry of Materials, 16*(5):906-914.

[114] Xia, H., Meng, Y. S., Lu, L., & Ceder, G. (2007). Electrochemical Properties of Nonstoichiometric LiNi[sub 0.5]Mn[sub 1.5]O[sub 4−δ] Thin-Film Electrodes Prepared by Pulsed Laser Deposition. *Journal of The Electrochemical Society, 154*(8):A737.

[115] Kim, J.-H., Pieczonka, N. P. W., Li, Z., Wu, Y., Harris, S., & Powell, B. R. (2013). Understanding the capacity fading mechanism in LiNi0.5Mn1.5O4/graphite Li-ion batteries. *Electrochimica Acta, 90*:556-562.

[116] Fang, H.-s., Wang, Z.-x., Li, X.-h., Guo, H.-j., & Peng, W.-j. (2006). Exploration of high capacity LiNi0.5Mn1.5O4 synthesized by solid-state reaction. *Journal of Power Sources, 153*(1):174-176.

[117] Cui, X.-L., Li, Y.-L., Li, S.-Y., Li, L.-X., & Liu, J.-L. (2013). Nanosized LiNi0.5Mn1.5O4 spinels synthesized by a high-oxidation-state manganese sol–gel method. *Ionics, 19*(11):1489-1494.

[118] Xu, T., Li, Y., Wang, D., Wu, M., Pan, D., Zhao, H., & Bai, Y. (2018). Enhanced Electrochemical Performance of LiNi0.5Mn1.5O4 Cathode Material by YPO4 Surface Modification. *ACS Sustainable Chemistry & Engineering, 6*(5):5818-5825.

[119] Yu, C., Dong, L., Zhang, Y., Du, K., Gao, M., Zhao, H., & Bai, Y. (2020). Promoting electrochemical performances of LiNi0.5Mn1.5O4 cathode via YF3 surface coating. *Solid State Ionics, 357*:115464.

[120] Deng, S., Mao, D., Wang, H., Wang, B., Liu, J., Ma, Y., & Yan, H. (2016). Preparation and electrochemical properties of double-shell LiNi0.5Mn1.5O4 hollow microspheres as cathode materials for Li-ion batteries. *RSC Advances, 6*(51):45369-45375.

[121] Han, C.-H., Hong, Y.-S., Park, C. M., & Kim, K. (2001). Synthesis and electrochemical properties of lithium cobalt oxides prepared by molten-salt synthesis using the eutectic mixture of LiCl–Li2CO3. *Journal of Power Sources, 92*(1):95-101.

[122] Chen, J., Huang, Z., Zeng, W., Cao, F., Ma, J., Tian, W., & Mu, S. (2021). Synthesis, Modification, and Lithium-Storage Properties of Spinel LiNi0.5Mn1.5O4. *ChemElectroChem, 8*(4):608-624.

[123] Lee, Y. S., Sun, Y. K., Ota, S., Miyashita, T., & Yoshio, M. (2002). Preparation and characterization of nano-crystalline LiNi0.5Mn1.5O4 for 5 V cathode material by composite carbonate process. *Electrochemistry Communications, 4*(12):989-994.

[124] Hwang, B. J., Wu, Y. W., Venkateswarlu, M., Cheng, M. Y., & Santhanam, R. (2009). Influence of synthesis conditions on electrochemical properties of high-voltage Li1.02Ni0.5Mn1.5O4 spinel cathode material. *Journal of Power Sources, 193*(2):828-833.

[125] Goodenough, J. B. (2014). Electrochemical energy storage in a sustainable modern society. *Energy & Environmental Science, 7*(1):14-18.

[126] Manthiram, A., Chemelewski, K., & Lee, E.-S. (2014). A perspective on the high-voltage LiMn1.5Ni0.5O4 spinel cathode for lithium-ion batteries. *Energy & Environmental Science, 7*(4):1339-1350.

[127] Yoon, T., Park, S., Mun, J., Ryu, J. H., Choi, W., Kang, Y.-S., . . . Oh, S. M. (2012). Failure mechanisms of LiNi0.5Mn1.5O4 electrode at elevated temperature. *Journal of Power Sources, 215*:312-316.

[128] Markovsky, B., Talyossef, Y., Salitra, G., Aurbach, D., Kim, H.-J., & Choi, S. (2004). Cycling and storage performance at elevated temperatures of LiNi0.5Mn1.5O4 positive electrodes for advanced 5 V Li-ion batteries. *Electrochemistry Communications, 6*(8):821-826.

[129] Ma, J., Hu, P., Cui, G., & Chen, L. (2016). Surface and Interface Issues in Spinel LiNi0.5Mn1.5O4: Insights into a Potential Cathode Material for High Energy Density Lithium Ion Batteries. *Chemistry of Materials, 28*(11):3578-3606.

[130] Kuppan, S., Xu, Y., Liu, Y., & Chen, G. (2017). Phase transformation mechanism in lithium manganese nickel oxide revealed by single-crystal hard X-ray microscopy. *Nature Communications, 8*(1):14309.

[131] Sun, Y. K., Hong, K. J., Prakash, J., & Amine, K. (2002). Electrochemical performance of nano-sized ZnO-coated LiNi0.5Mn1.5O4 spinel as 5 V materials at elevated temperatures. *Electrochemistry Communications, 4*(4):344-348.

[132] Luo, X., & Ben, L. (2019). Effect of MgO and Ta2O5 co-coatings on electrochemical performance of high-voltage spinel LiNi0. 5Mn1. 5O4 cathode material. *Journal of Alloys and Compounds, 810*:151951.

[133] Nisar, U., Amin, R., Essehli, R., Shakoor, R., Kahraman, R., Kim, D. K., . . . Belharouak, I. (2018). Extreme fast charging characteristics of zirconia modified LiNi0. 5Mn1. 5O4 cathode for lithium ion batteries. *Journal of Power Sources, 396*:774-781.

[134] Kim, J. W., Kim, D. H., Oh, D. Y., Lee, H., Kim, J. H., Lee, J. H., & Jung, Y. S. (2015). Surface chemistry of LiNi0. 5Mn1. 5O4 particles coated by Al2O3 using atomic layer deposition for lithium-ion batteries. *Journal of Power Sources, 274*:1254-1262.

[135] Mereacre, V., Bohn, N., Stüble, P., Pfaffmann, L., & Binder, J. R. (2021). Instantaneous Surface Li3PO4 Coating and Al–Ti Doping and Their Effect on the Performance of LiNi0.5Mn1.5O4 Cathode Materials. *ACS Applied Energy Materials, 4*(5):4271-4276.

[136] Zeng, H., He, J., Fang, D., Liang, Y., Zhao, R., Cai, Y., & Lu, D. (2019). Nano-Sized AlPO4 Coating Layer on Graphite Powder to Improve the Electrochemical Properties of High-Voltage Graphite/LiNi0. 5Mn1. 5O4 Li-Ion Cells. *Energy Technology, 7*(9):1801078.

[137] Xiao, B., Liu, J., Sun, Q., Wang, B., Banis, M. N., Zhao, D., . . . Sun, X. (2015).

Unravelling the Role of Electrochemically Active FePO4 Coating by Atomic Layer Deposition for Increased High-Voltage Stability of LiNi0.5Mn1.5O4 Cathode Material. *Advanced Science, 2*(5):1500022.

[138] Chu, C.-T., Mondal, A., Kosova, N. V., & Lin, J.-Y. (2020). Improved high-temperature cyclability of AlF3 modified spinel LiNi0.5Mn1.5O4 cathode for lithium-ion batteries. *Applied Surface Science, 530*:147169.

[139] Gong, Z., & Yang, Y. (2011). Recent advances in the research of polyanion-type cathode materials for Li-ion batteries. *Energy & Environmental Science, 4*(9):3223-3242.

[140] Padhi, A. K., Nanjundaswamy, K. S., & Goodenough, J. B. (1997). Phospho-olivines as Positive-Electrode Materials for Rechargeable Lithium Batteries. *Journal of The Electrochemical Society, 144*(4):1188-1194.

[141] Padhi, A. K., Nanjundaswamy, K. S., Masquelier, C., Okada, S., & Goodenough, J. B. (1997). Effect of Structure on the Fe3 + / Fe2 + Redox Couple in Iron Phosphates. *Journal of The Electrochemical Society, 144*(5):1609-1613.

[142] Guo, B., Ruan, H., Zheng, C., Fei, H., & Wei, M. (2013). Hierarchical LiFePO4 with a controllable growth of the (010) facet for lithium-ion batteries. *Scientific Reports, 3*(1):2788.

[143] Liu, S., Yan, P., Li, H., Zhang, X., & Sun, W. (2020). One-Step Microwave Synthesis of Micro/Nanoscale LiFePO4/Graphene Cathode With High Performance for Lithium-Ion Batteries. *Frontiers in Chemistry, 8*(104).

[144] Gong, C., Xue, Z., Wen, S., Ye, Y., & Xie, X. (2016). Advanced carbon materials/olivine LiFePO4 composites cathode for lithium ion batteries. *Journal of Power Sources, 318*:93-112.

[145] Yamada, A., Chung, S. C., & Hinokuma, K. (2001). Optimized LiFePO[sub 4] for Lithium Battery Cathodes. *Journal of The Electrochemical Society, 148*(3):A224.

[146] Andersson, A. S., Thomas, J. O., Kalska, B., & Häggström, L. (1999). Thermal Stability of LiFePO4-Based Cathodes. *Electrochemical and Solid State Letters, 3*(2):66.

[147] Koltypin, M., Aurbach, D., Nazar, L., & Ellis, B. (2007). More on the performance of LiFePO4 electrodes—The effect of synthesis route, solution composition, aging, and temperature. *Journal of Power Sources, 174*(2):1241-1250.

[148] Dominko, R., Bele, M., Gaberscek, M., Remskar, M., Hanzel, D., Goupil, J. M., . . . Jamnik, J. (2006). Porous olivine composites synthesized by sol–gel technique. *Journal of Power Sources, 153*(2):274-280.

[149] Lee, M.-H., Kim, J.-Y., & Song, H.-K. (2010). A hollow sphere secondary structure of LiFePO4 nanoparticles. *Chemical Communications, 46*(36):6795-6797.

[150] Yu, Z., & Jiang, L. (2018). Olivine LiFePO4 nanocrystals grown on nitrogen-doped graphene sheets as high-rate cathode for lithium-ion batteries. *Solid State Ionics, 325*:12-16.

[151] Ding, Y., Jiang, Y., Xu, F., Yin, J., Ren, H., Zhuo, Q., . . . Zhang, P. (2010). Preparation of nano-structured LiFePO4/graphene composites by co-precipitation method. *Electrochemistry Communications, 12*(1):10-13.

[152] Choi, D., & Kumta, P. N. (2007). Surfactant based sol–gel approach to nanostructured LiFePO4 for high rate Li-ion batteries. *Journal of Power Sources, 163*(2):1064-1069.

[153] Wang, G., Liu, H., Liu, J., Qiao, S., Lu, G. M., Munroe, P., & Ahn, H. (2010). Mesoporous LiFePO4/C Nanocomposite Cathode Materials for High Power Lithium Ion Batteries with Superior Performance. *Advanced Materials, 22*(44):4944-4948.

[154] Herle, P. S., Ellis, B., Coombs, N., & Nazar, L. F. (2004). Nano-network electronic conduction in iron and nickel olivine phosphates. *Nature Materials, 3*(3):147-152.

[155] Ravet, N., Chouinard, Y., Magnan, J. F., Besner, S., Gauthier, M., & Armand, M. (2001). Electroactivity of natural and synthetic triphylite. *Journal of Power Sources, 97-98*:503-507.
[156] Lu, J., Li, W., Shen, C., Tang, D., Dai, L., Diao, G., & Chen, M. (2019). Nano-scale hollow structure carbon-coated LiFePO4 as cathode material for lithium ion battery. *Ionics, 25*(9):4075-4082.
[157] Kang, B., & Ceder, G. (2009). Battery materials for ultrafast charging and discharging. *Nature, 458*(7235):190-193.
[158] Meethong, N., Kao, Y.-H., Speakman, S. A., & Chiang, Y.-M. (2009). Aliovalent Substitutions in Olivine Lithium Iron Phosphate and Impact on Structure and Properties. *Advanced Functional Materials, 19*(7):1060-1070.
[159] Mauger, A., & Julien, C. M. (2018). Olivine Positive Electrodes for Li-Ion Batteries: Status and Perspectives. *Batteries, 4*(3):39.
[160] Delacourt, C., Laffont, L., Bouchet, R., Wurm, C., Leriche, J. B., Morcrette, M., . . . Masquelier, C. (2005). Toward Understanding of Electrical Limitations (Electronic, Ionic) in LiMPO[sub 4] (M=Fe, Mn) Electrode Materials. *Journal of The Electrochemical Society, 152*(5):A913.
[161] Ling, J., Karuppiah, C., Krishnan, S. G., Reddy, M. V., Misnon, I. I., Ab Rahim, M. H., . . . Jose, R. (2021). Phosphate Polyanion Materials as High-Voltage Lithium-Ion Battery Cathode: A Review. *Energy & Fuels, 35*(13):10428-10450.
[162] Bramnik, N. N., Nikolowski, K., Trots, D. M., & Ehrenberg, H. (2008). Thermal Stability of LiCoPO[sub 4] Cathodes. *Electrochemical and solid-state letters, 11*(6):A89.
[163] Xu, W., Wang, J., Ding, F., Chen, X., Nasybulin, E., Zhang, Y., & Zhang, J.-G. (2014). Lithium metal anodes for rechargeable batteries. *Energy & Environmental Science, 7*(2):513-537.
[164] Shen, X., Liu, H., Cheng, X.-B., Yan, C., & Huang, J.-Q. (2018). Beyond lithium ion batteries: Higher energy density battery systems based on lithium metal anodes. *Energy Storage Materials, 12*:161-175.
[165] Flandrois, S., & Simon, B. (1999). Carbon materials for lithium-ion rechargeable batteries. *Carbon, 37*(2):165-180.
[166] Goodenough, J. B. (2013). Evolution of Strategies for Modern Rechargeable Batteries. *Accounts of Chemical Research, 46*(5):1053-1061.
[167] An, S. J., Li, J., Daniel, C., Mohanty, D., Nagpure, S., & Wood III, D. L. (2016). The state of understanding of the lithium-ion-battery graphite solid electrolyte interphase (SEI) and its relationship to formation cycling. *Carbon, 105*:52-76.
[168] Goriparti, S., Miele, E., De Angelis, F., Di Fabrizio, E., Proietti Zaccaria, R., & Capiglia, C. (2014). Review on recent progress of nanostructured anode materials for Li-ion batteries. *Journal of Power Sources, 257*:421-443.
[169] Qi, W., Shapter, J. G., Wu, Q., Yin, T., Gao, G., & Cui, D. (2017). Nanostructured anode materials for lithium-ion batteries: principle, recent progress and future perspectives. *Journal of Materials Chemistry A, 5*(37):19521-19540.
[170] Eftekhari, A. (2017). Lithium-ion batteries with high rate capabilities. *ACS Sustainable Chemistry & Engineering, 5*(4):2799-2816.
[171] Jin, Y., Zhu, B., Lu, Z., Liu, N., & Zhu, J. (2017). Challenges and Recent Progress in the Development of Si Anodes for Lithium-Ion Battery. *Advanced Energy Materials, 7*(23):1700715.
[172] Yue, L., Ma, J., Zhang, J., Zhao, J., Dong, S., Liu, Z., . . . Chen, L. (2016). All solid-state polymer electrolytes for high-performance lithium ion batteries. *Energy Storage Materials, 5*:139-164.
[173] Balogun, M.-S., Qiu, W., Luo, Y., Meng, H., Mai, W., Onasanya, A., . . . Tong, Y.

(2016). A review of the development of full cell lithium-ion batteries: The impact of nanostructured anode materials. *Nano research, 9*(10):2823-2851.

[174] Bai, L., Fang, F., Zhao, Y., Liu, Y., Li, J., Huang, G., & Sun, H. (2014). A sandwich structure of mesoporous anatase TiO2 sheets and reduced graphene oxide and its application as lithium-ion battery electrodes. *RSC Advances, 4*(81):43039-43046.

[175] Lu, J., Chen, Z., Pan, F., Cui, Y., & Amine, K. (2018). High-performance anode materials for rechargeable lithium-ion batteries. *Electrochemical Energy Reviews, 1*(1):35-53.

[176] Roy, P., & Srivastava, S. K. (2015). Nanostructured anode materials for lithium ion batteries. *Journal of Materials Chemistry A, 3*(6):2454-2484.

[177] Dahn, J. R., Zheng, T., Liu, Y., & Xue, J. (1995). Mechanisms for lithium insertion in carbonaceous materials. *Science*:590-593.

[178] Balogun, M.-S., Luo, Y., Qiu, W., Liu, P., & Tong, Y. (2016). A review of carbon materials and their composites with alloy metals for sodium ion battery anodes. *Carbon, 98*:162-178.

[179] Huggins, R. A. (2016). Negative Electrodes in Lithium Systems. In *Energy Storage* (pp. 361-390): Springer.

[180] Landi, B. J., Ganter, M. J., Cress, C. D., DiLeo, R. A., & Raffaelle, R. P. (2009). Carbon nanotubes for lithium ion batteries. *Energy & Environmental Science, 2*(6):638-654.

[181] Qie, L., Chen, W. M., Wang, Z. H., Shao, Q. G., Li, X., Yuan, L. X., . . . Huang, Y. H. (2012). Nitrogen-doped porous carbon nanofiber webs as anodes for lithium ion batteries with a superhigh capacity and rate capability. *Advanced materials, 24*(15):2047-2050.

[182] Wang, G., Shen, X., Yao, J., & Park, J. (2009). Graphene nanosheets for enhanced lithium storage in lithium ion batteries. *Carbon, 47*(8):2049-2053.

[183] Wang, Q., Li, H., Chen, L., & Huang, X. (2002). Novel spherical microporous carbon as anode material for Li-ion batteries. *Solid State Ionics, 152-153*:43-50.

[184] Liu, X.-M., Huang, Z. d., Oh, S. w., Zhang, B., Ma, P.-C., Yuen, M. M. F., & Kim, J.-K. (2012). Carbon nanotube (CNT)-based composites as electrode material for rechargeable Li-ion batteries: A review. *Composites Science and Technology, 72*(2):121-144.

[185] Schauerman, C. M., Ganter, M. J., Gaustad, G., Babbitt, C. W., Raffaelle, R. P., & Landi, B. J. (2012). Recycling single-wall carbon nanotube anodes from lithium ion batteries. *Journal of Materials Chemistry, 22*(24):12008-12015.

[186] Lee, D.-H., Kim, D.-W., & Park, J.-G. (2008). Enhanced Rate Capabilities of Nanobrookite with Electronically Conducting MWCNT Networks. *Crystal Growth & Design, 8*(12):4506-4510.

[187] Trevey, J. E., Rason, K. W., Stoldt, C. R., & Lee, S.-H. (2010). Improved Performance of All-Solid-State Lithium-Ion Batteries Using Nanosilicon Active Material with Multiwalled-Carbon-Nanotubes as a Conductive Additive. *Electrochemical and solid-state letters, 13*(11):A154.

[188] Fu, W., Zhao, E., Ma, R., Sun, Z., Yang, Y., Sevilla, M., . . . Yushin, G. (2020). Anatase TiO2 Confined in Carbon Nanopores for High-Energy Li-Ion Hybrid Supercapacitors Operating at High Rates and Subzero Temperatures. *Advanced Energy Materials, 10*(2):1902993.

[189] Jiang, H., Lee, P. S., & Li, C. (2013). 3D carbon based nanostructures for advanced supercapacitors. *Energy & Environmental Science, 6*(1):41-53.

[190] Yuan, W., Zhang, Y., Cheng, L., Wu, H., Zheng, L., & Zhao, D. (2016). The applications of carbon nanotubes and graphene in advanced rechargeable lithium batteries. *Journal of Materials Chemistry A, 4*(23):8932-8951.

[191] Yoo, E., Kim, J., Hosono, E., Zhou, H.-s., Kudo, T., & Honma, I. (2008). Large Reversible Li Storage of Graphene Nanosheet Families for Use in Rechargeable Lithium Ion Batteries. *Nano Letters, 8*(8):2277-2282.

[192] Mo, R., Lei, Z., Sun, K., & Rooney, D. (2014). Facile synthesis of anatase TiO2 quantum-dot/graphene-nanosheet composites with enhanced electrochemical performance for lithium-ion batteries. *Advanced materials, 26*(13):2084-2088.

[193] Li, W., Wang, F., Liu, Y., Wang, J., Yang, J., Zhang, L., . . . Zhao, D. (2015). General Strategy to Synthesize Uniform Mesoporous TiO2/Graphene/Mesoporous TiO2 Sandwich-Like Nanosheets for Highly Reversible Lithium Storage. *Nano Letters, 15*(3):2186-2193.

[194] Tao, H.-C., Fan, L.-Z., Yan, X., & Qu, X. (2012). In situ synthesis of TiO2–graphene nanosheets composites as anode materials for high-power lithium ion batteries. *Electrochimica Acta, 69*:328-333.

[195] Zhang, C., Peng, X., Guo, Z., Cai, C., Chen, Z., Wexler, D., . . . Liu, H. (2012). Carbon-coated SnO2/graphene nanosheets as highly reversible anode materials for lithium ion batteries. *Carbon, 50*(5):1897-1903.

[196] Yao, J., Shen, X., Wang, B., Liu, H., & Wang, G. (2009). In situ chemical synthesis of SnO2–graphene nanocomposite as anode materials for lithium-ion batteries. *Electrochemistry Communications, 11*(10):1849-1852.

[197] Zhang, B., Zheng, Q. B., Huang, Z. D., Oh, S. W., & Kim, J. K. (2011). SnO2–graphene–carbon nanotube mixture for anode material with improved rate capacities. *Carbon, 49*(13):4524-4534.

[198] Zhou, J., Song, H., Ma, L., & Chen, X. (2011). Magnetite/graphene nanosheet composites: interfacial interaction and its impact on the durable high-rate performance in lithium-ion batteries. *RSC Advances, 1*(5):782-791.

[199] Wang, J. Z., Zhong, C., Wexler, D., Idris, N. H., Wang, Z. X., Chen, L. Q., & Liu, H. K. (2011). Graphene-encapsulated Fe3O4 nanoparticles with 3D laminated structure as superior anode in lithium ion batteries. *Chemistry–A European Journal, 17*(2):661-667.

[200] Zhou, G., Wang, D.-W., Li, F., Zhang, L., Li, N., Wu, Z.-S., . . . Cheng, H.-M. (2010). Graphene-wrapped Fe3O4 anode material with improved reversible capacity and cyclic stability for lithium ion batteries. *Chemistry of Materials, 22*(18):5306-5313.

[201] Wang, J.-G., Jin, D., Zhou, R., Li, X., Liu, X.-r., Shen, C., . . . Wei, B. (2016). Highly flexible graphene/Mn3O4 nanocomposite membrane as advanced anodes for Li-ion batteries. *ACS Nano, 10*(6):6227-6234.

[202] Park, S.-K., Jin, A., Yu, S.-H., Ha, J., Jang, B., Bong, S., . . . Piao, Y. (2014). In situ hydrothermal synthesis of Mn3O4 nanoparticles on nitrogen-doped graphene as high-performance anode materials for lithium ion batteries. *Electrochimica Acta, 120*:452-459.

[203] Zhou, J., Ma, L., Song, H., Wu, B., & Chen, X. (2011). Durable high-rate performance of CuO hollow nanoparticles/graphene-nanosheet composite anode material for lithium-ion batteries. *Electrochemistry Communications, 13*(12):1357-1360.

[204] Zou, Y., & Wang, Y. (2011). NiO nanosheets grown on graphene nanosheets as superior anode materials for Li-ion batteries. *Nanoscale, 3*(6):2615-2620.

[205] Tao, L., Zai, J., Wang, K., Wan, Y., Zhang, H., Yu, C., . . . Qian, X. (2012). 3D-hierarchical NiO–graphene nanosheet composites as anodes for lithium ion batteries with improved reversible capacity and cycle stability. *RSC Advances, 2*(8):3410-3415.

[206] Zhou, H., Zhu, S., Hibino, M., Honma, I., & Ichihara, M. (2003). Lithium Storage in Ordered Mesoporous Carbon (CMK-3) with High Reversible Specific Energy

Capacity and Good Cycling Performance. *Advanced Materials, 15*(24):2107-2111.
[207] Zeng, L., Liu, R., Han, L., Luo, F., Chen, X., Wang, J., . . . Wei, M. (2018). Preparation of a Si/SiO2–Ordered-Mesoporous-Carbon Nanocomposite as an Anode for High-Performance Lithium-Ion and Sodium-Ion Batteries. *Chemistry – A European Journal, 24*(19):4841-4848.
[208] Zhang, H., Zhao, H., Khan, M. A., Zou, W., Xu, J., Zhang, L., & Zhang, J. (2018). Recent progress in advanced electrode materials, separators and electrolytes for lithium batteries. *Journal of Materials Chemistry A, 6*(42):20564-20620.
[209] Wu, H. B., Chen, J. S., Hng, H. H., & Lou, X. W. D. (2012). Nanostructured metal oxide-based materials as advanced anodes for lithium-ion batteries. *Nanoscale, 4*(8):2526-2542.
[210] Poizot, P., Laruelle, S., Grugeon, S., Dupont, L., & Tarascon, J. M. (2000). Nano-sized transition-metal oxides as negative-electrode materials for lithium-ion batteries. *Nature, 407*(6803):496-499.
[211] Li, Z., Liu, N., Wang, X., Wang, C., Qi, Y., & Yin, L. (2012). Three-dimensional nanohybrids of Mn3O4/ordered mesoporous carbons for high performance anode materials for lithium-ion batteries. *Journal of Materials Chemistry, 22*(32):16640-16648.
[212] Pasero, D., Reeves, N., & West, A. R. (2005). Co-doped Mn3O4: a possible anode material for lithium batteries. *Journal of Power Sources, 141*(1):156-158.
[213] Wang, J., Du, N., Wu, H., Zhang, H., Yu, J., & Yang, D. (2013). Order-aligned Mn3O4 nanostructures as super high-rate electrodes for rechargeable lithium-ion batteries. *Journal of Power Sources, 222*:32-37.
[214] Wang, H., Cui, L.-F., Yang, Y., Sanchez Casalongue, H., Robinson, J. T., Liang, Y., . . . Dai, H. (2010). Mn3O4−Graphene Hybrid as a High-Capacity Anode Material for Lithium Ion Batteries. *Journal of the American Chemical Society, 132*(40):13978-13980.
[215] Nam, I., Kim, N. D., Kim, G.-P., Park, J., & Yi, J. (2013). One step preparation of Mn3O4/graphene composites for use as an anode in Li ion batteries. *Journal of Power Sources, 244*:56-62.
[216] Li, L., Guo, Z., Du, A., & Liu, H. (2012). Rapid microwave-assisted synthesis of Mn 3 O 4–graphene nanocomposite and its lithium storage properties. *Journal of Materials Chemistry, 22*(8):3600-3605.
[217] Li, B., Cao, H., Shao, J., Li, G., Qu, M., & Yin, G. (2011). Co3O4@graphene Composites as Anode Materials for High-Performance Lithium Ion Batteries. *Inorganic Chemistry, 50*(5):1628-1632.
[218] Wang, X., Wu, X.-L., Guo, Y.-G., Zhong, Y., Cao, X., Ma, Y., & Yao, J. (2010). Synthesis and Lithium Storage Properties of Co3O4 Nanosheet-Assembled Multishelled Hollow Spheres. *Advanced Functional Materials, 20*(10):1680-1686.
[219] Kim, H., Seo, D.-H., Kim, S.-W., Kim, J., & Kang, K. (2011). Highly reversible Co3O4/graphene hybrid anode for lithium rechargeable batteries. *Carbon, 49*(1):326-332.
[220] Wang, B., Wang, Y., Park, J., Ahn, H., & Wang, G. (2011). In situ synthesis of Co3O4/graphene nanocomposite material for lithium-ion batteries and supercapacitors with high capacity and supercapacitance. *Journal of Alloys and Compounds, 509*(29):7778-7783.
[221] Wu, Z.-S., Ren, W., Wen, L., Gao, L., Zhao, J., Chen, Z., . . . Cheng, H.-M. (2010). Graphene Anchored with Co3O4 Nanoparticles as Anode of Lithium Ion Batteries with Enhanced Reversible Capacity and Cyclic Performance. *ACS Nano, 4*(6):3187-3194.
[222] Chen, J., Xu, L., Li, W., & Gou, X. (2005). α-Fe2O3 Nanotubes in Gas Sensor and

Lithium-Ion Battery Applications. *Advanced Materials, 17*(5):582-586.
[223] Chen, J. S., Zhu, T., Yang, X. H., Yang, H. G., & Lou, X. W. (2010). Top-Down Fabrication of α-Fe2O3 Single-Crystal Nanodiscs and Microparticles with Tunable Porosity for Largely Improved Lithium Storage Properties. *Journal of the American Chemical Society, 132*(38):13162-13164.
[224] Wu, C., Yin, P., Zhu, X., OuYang, C., & Xie, Y. (2006). Synthesis of Hematite (α-Fe2O3) Nanorods: Diameter-Size and Shape Effects on Their Applications in Magnetism, Lithium Ion Battery, and Gas Sensors. *The Journal of Physical Chemistry B, 110*(36):17806-17812.
[225] Pan, Q., Huang, K., Ni, S., Yang, F., Lin, S., & He, D. (2008). Synthesis of α-Fe2O3dendrites by a hydrothermal approach and their application in lithium-ion batteries. *Journal of Physics D: Applied Physics, 42*(1):015417.
[226] Zhang, L., Wu, H. B., & Lou, X. W. (2014). Iron-Oxide-Based Advanced Anode Materials for Lithium-Ion Batteries. *Advanced Energy Materials, 4*(4):1300958.
[227] Koo, B., Xiong, H., Slater, M. D., Prakapenka, V. B., Balasubramanian, M., Podsiadlo, P., . . . Shevchenko, E. V. (2012). Hollow Iron Oxide Nanoparticles for Application in Lithium Ion Batteries. *Nano Letters, 12*(5):2429-2435.
[228] Wang, Z., Luan, D., Madhavi, S., Hu, Y., & Lou, X. W. (2012). Assembling carbon-coated α-Fe2O3 hollow nanohorns on the CNT backbone for superior lithium storage capability. *Energy & Environmental Science, 5*(1):5252-5256.
[229] Kim, H. S., Piao, Y., Kang, S. H., Hyeon, T., & Sung, Y.-E. (2010). Uniform hematite nanocapsules based on an anode material for lithium ion batteries. *Electrochemistry Communications, 12*(3):382-385.
[230] Narsimulu, D., Nagaraju, G., Chandra Sekhar, S., Ramulu, B., Khaja Hussain, S., & Yu, J. S. (2020). Unveiling multi-channelled 3D porous iron oxide nanostructures with exalted capacity towards high-performance Li-ion battery applications. *Journal of Alloys and Compounds, 846*:156385.
[231] Narsimulu, D., Nagaraju, G., Sekhar, S. C., Ramulu, B., & Yu, J. S. (2019). Designed lamination of binder-free flexible iron oxide/carbon cloth as high capacity and stable anode material for lithium-ion batteries. *Applied Surface Science, 497*:143795.
[232] Zhu, X., Zhu, Y., Murali, S., Stoller, M. D., & Ruoff, R. S. (2011). Nanostructured Reduced Graphene Oxide/Fe2O3 Composite As a High-Performance Anode Material for Lithium Ion Batteries. *ACS Nano, 5*(4):3333-3338.
[233] Taberna, P. L., Mitra, S., Poizot, P., Simon, P., & Tarascon, J. M. (2006). High rate capabilities Fe3O4-based Cu nano-architectured electrodes for lithium-ion battery applications. *Nature Materials, 5*(7):567-573.
[234] Lee, S. H., Yu, S.-H., Lee, J. E., Jin, A., Lee, D. J., Lee, N., . . . Hyeon, T. (2013). Self-Assembled Fe3O4 Nanoparticle Clusters as High-Performance Anodes for Lithium Ion Batteries via Geometric Confinement. *Nano Letters, 13*(9):4249-4256.
[235] Bulut Kopuklu, B., Tasdemir, A., Alkan Gursel, S., & Yurum, A. (2021). High stability graphene oxide aerogel supported ultrafine Fe3O4 particles with superior performance as a Li-ion battery anode. *Carbon, 174*:158-172.
[236] Idota, Y., Kubota, T., Matsufuji, A., Maekawa, Y., & Miyasaka, T. (1997). Tin-based amorphous oxide: a high-capacity lithium-ion-storage material. *Science, 276*(5317):1395-1397.
[237] Wang, Z., Zhou, L., & Lou, X. W. (2012). Metal Oxide Hollow Nanostructures for Lithium-ion Batteries. *Advanced Materials, 24*(14):1903-1911.
[238] Chen, J. S., & Lou, X. W. (2013). SnO2-Based Nanomaterials: Synthesis and Application in Lithium-Ion Batteries. *Small, 9*(11):1877-1893.
[239] Chen, J. S., Archer, L. A., & Wen Lou, X. (2011). SnO2 hollow structures and TiO2 nanosheets for lithium-ion batteries. *Journal of Materials Chemistry, 21*(27):9912-

9924.
[240] Liu, L., Xie, F., Lyu, J., Zhao, T., Li, T., & Choi, B. G. (2016). Tin-based anode materials with well-designed architectures for next-generation lithium-ion batteries. *Journal of Power Sources, 321*:11-35.
[241] Li, H., Shi, L., Lu, W., Huang, X., & Chen, L. (2001). Studies on capacity loss and capacity fading of nanosized SnSb alloy anode for Li-ion batteries. *Journal of The Electrochemical Society, 148*(8):A915.
[242] Jiang, J., Li, Y., Liu, J., Huang, X., Yuan, C., & Lou, X. W. (2012). Recent Advances in Metal Oxide-based Electrode Architecture Design for Electrochemical Energy Storage. *Advanced Materials, 24*(38):5166-5180.
[243] Kamali, A. R., & Fray, D. J. (2011). Tin-based materials as advanced anode materials for lithium ion batteries: a review. *Rev. Adv. Mater. Sci, 27*(1):14-24.
[244] Zhang, M., Wang, T., & Cao, G. (2015). Promises and challenges of tin-based compounds as anode materials for lithium-ion batteries. *International Materials Reviews, 60*(6):330-352.
[245] Ding, S., Luan, D., Boey, F. Y. C., Chen, J. S., & Lou, X. W. (2011). SnO2 nanosheets grown on graphene sheets with enhanced lithium storage properties. *Chemical Communications, 47*(25):7155-7157.
[246] Yao, W., Wu, S., Zhan, L., & Wang, Y. (2019). Two-dimensional porous carbon-coated sandwich-like mesoporous SnO2/graphene/mesoporous SnO2 nanosheets towards high-rate and long cycle life lithium-ion batteries. *Chemical Engineering Journal, 361*:329-341.
[247] Lu, X., Chen, Y., Tian, Q., Zhang, W., Sui, Z., & Chen, J. (2021). Enabling improved cycling stability of hollow SnO2/C composite anode for lithium-ion battery by constructing a built-in porous carbon support. *Applied Surface Science, 537*:148052.
[248] Noerochim, L., Wang, J.-Z., Chou, S.-L., Wexler, D., & Liu, H.-K. (2012). Free-standing single-walled carbon nanotube/SnO2 anode paper for flexible lithium-ion batteries. *Carbon, 50*(3):1289-1297.
[249] Xu, G.-L., Chen, S.-R., Li, J.-T., Ke, F.-S., Huang, L., & Sun, S.-G. (2011). A composite material of SnO2/ordered mesoporous carbon for the application in Lithium-ion Battery. *Journal of Electroanalytical Chemistry, 656*(1):185-191.
[250] Tian, Q., Zhang, F., & Yang, L. (2019). Fabricating thin two-dimensional hollow tin dioxide/carbon nanocomposite for high-performance lithium-ion battery anode. *Applied Surface Science, 481*:1377-1384.
[251] Luo, B., Fang, Y., Wang, B., Zhou, J., Song, H., & Zhi, L. (2012). Two dimensional graphene–SnS2 hybrids with superior rate capability for lithium ion storage. *Energy & Environmental Science, 5*(1):5226-5230.
[252] Li, X., Sun, X., Gao, Z., Hu, X., Ling, R., Cai, S., . . . Hu, W. (2018). A Simple One-Pot Strategy for Synthesizing Ultrafine SnS2 Nanoparticle/Graphene Composites as Anodes for Lithium/Sodium-Ion Batteries. *ChemSusChem, 11*(9):1549-1557.
[253] Wang, Y., Lee, J. Y., & Deivaraj, T. C. (2004). Tin Nanoparticle Loaded Graphite Anodes for Li-Ion Battery Applications. *Journal of The Electrochemical Society, 151*(11):A1804.
[254] Xu, Y., Liu, Q., Zhu, Y., Liu, Y., Langrock, A., Zachariah, M. R., & Wang, C. (2013). Uniform Nano-Sn/C Composite Anodes for Lithium Ion Batteries. *Nano Letters, 13*(2):470-474.
[255] Qin, J., He, C., Zhao, N., Wang, Z., Shi, C., Liu, E.-Z., & Li, J. (2014). Graphene Networks Anchored with Sn@Graphene as Lithium Ion Battery Anode. *ACS Nano, 8*(2):1728-1738.
[256] Zou, Y., & Wang, Y. (2011). Sn@CNT Nanostructures Rooted in Graphene with High and Fast Li-Storage Capacities. *ACS Nano, 5*(10):8108-8114.

[257] Huang, S. Y., Kavan, L., Exnar, I., & Grätzel, M. (1995). Rocking Chair Lithium Battery Based on Nanocrystalline TiO2 (Anatase). *Journal of The Electrochemical Society, 142*(9):L142-L144.

[258] Jin, J., Huang, S.-Z., Liu, J., Li, Y., Chen, D.-S., Wang, H.-E., . . . Su, B.-L. (2014). Design of new anode materials based on hierarchical, three dimensional ordered macro-mesoporous TiO2 for high performance lithium ion batteries. *Journal of Materials Chemistry A, 2*(25):9699-9708.

[259] Chen, Z., Belharouak, I., Sun, Y.-K., & Amine, K. (2013). Titanium-Based Anode Materials for Safe Lithium-Ion Batteries. *Advanced Functional Materials, 23*(8):959-969.

[260] Zhu, G.-N., Wang, Y.-G., & Xia, Y.-Y. (2012). Ti-based compounds as anode materials for Li-ion batteries. *Energy & Environmental Science, 5*(5):6652-6667.

[261] Ren, Y., Liu, Z., Pourpoint, F., Armstrong, A. R., Grey, C. P., & Bruce, P. G. (2012). Nanoparticulate TiO2(B): An Anode for Lithium-Ion Batteries. *Angewandte Chemie International Edition, 51*(9):2164-2167.

[262] Xin, X., Zhou, X., Wu, J., Yao, X., & Liu, Z. (2012). Scalable Synthesis of TiO2/Graphene Nanostructured Composite with High-Rate Performance for Lithium Ion Batteries. *ACS Nano, 6*(12):11035-11043.

[263] Wang, W., Li, Y., Li, L., Wang, L., & Wang, K. (2020). SnO2/TiO2 nanocomposite prepared by pulsed laser deposition as anode material for flexible quasi-solid-state lithium-ion batteries. *Int. J. Electrochem. Sci, 15*(12):11709-11722.

[264] Yuan, D., Yang, W., Ni, J., & Gao, L. (2015). Sandwich structured MoO2@TiO2@CNT nanocomposites with high-rate performance for lithium ion batteries. *Electrochimica Acta, 163*:57-63.

[265] Dylla, A. G., Henkelman, G., & Stevenson, K. J. (2013). Lithium Insertion in Nanostructured TiO2(B) Architectures. *Accounts of Chemical Research, 46*(5):1104-1112.

[266] Liu, Y., Liu, M., Lan, T., Dou, J., & Wei, M. (2015). One-step hydrothermal synthesis of Nb doped brookite TiO2 nanosheets with enhanced lithium-ion intercalation properties. *Journal of Materials Chemistry A, 3*(37):18882-18888.

[267] Wei, W., Oltean, G., Tai, C.-W., Edström, K., Björefors, F., & Nyholm, L. (2013). High energy and power density TiO2 nanotube electrodes for 3D Li-ion microbatteries. *Journal of Materials Chemistry A, 1*(28):8160-8169.

[268] Zhang, Y., Jiang, Z., Huang, J., Lim, L. Y., Li, W., Deng, J., . . . Chen, Z. (2015). Titanate and titania nanostructured materials for environmental and energy applications: a review. *RSC Advances, 5*(97):79479-79510.

[269] Wang, D., Choi, D., Yang, Z., Viswanathan, V. V., Nie, Z., Wang, C., . . . Liu, J. (2008). Synthesis and Li-Ion Insertion Properties of Highly Crystalline Mesoporous Rutile TiO2. *Chemistry of Materials, 20*(10):3435-3442.

[270] Borghols, W. J. H., Wagemaker, M., Lafont, U., Kelder, E. M., & Mulder, F. M. (2008). Impact of Nanosizing on Lithiated Rutile TiO2. *Chemistry of Materials, 20*(9):2949-2955.

[271] Jiao, S., Lian, G., Jing, L., Xu, Z., Wang, Q., Cui, D., & Wong, C.-P. (2018). Sn-doped rutile TiO2 hollow nanocrystals with enhanced lithium-ion batteries performance. *ACS omega, 3*(1):1329-1337.

[272] Yang, Z., Choi, D., Kerisit, S., Rosso, K. M., Wang, D., Zhang, J., . . . Liu, J. (2009). Nanostructures and lithium electrochemical reactivity of lithium titanites and titanium oxides: A review. *Journal of Power Sources, 192*(2):588-598.

[273] Wagemaker, M., Kentgens, A. P. M., & Mulder, F. M. (2002). Equilibrium lithium transport between nanocrystalline phases in intercalated TiO2 anatase. *Nature, 418*(6896):397-399.

[274] Hanaor, D. A. H., & Sorrell, C. C. (2011). Review of the anatase to rutile phase transformation. *Journal of Materials Science, 46*(4):855-874.
[275] Chen, J. S., Tan, Y. L., Li, C. M., Cheah, Y. L., Luan, D., Madhavi, S., . . . Lou, X. W. (2010). Constructing Hierarchical Spheres from Large Ultrathin Anatase TiO2 Nanosheets with Nearly 100% Exposed (001) Facets for Fast Reversible Lithium Storage. *Journal of the American Chemical Society, 132*(17):6124-6130.
[276] Wagemaker, M., Borghols, W. J. H., & Mulder, F. M. (2007). Large Impact of Particle Size on Insertion Reactions. A Case for Anatase LixTiO2. *Journal of the American Chemical Society, 129*(14):4323-4327.
[277] Zukalová, M., Kalbáč, M., Kavan, L., Exnar, I., & Graetzel, M. (2005). Pseudocapacitive Lithium Storage in TiO2(B). *Chemistry of Materials, 17*(5):1248-1255.
[278] Cao, M., Tao, L., Lv, X., Bu, Y., Li, M., Yin, H., . . . Wang, M. (2018). Phosphorus-doped TiO2-B nanowire arrays boosting robust pseudocapacitive properties for lithium storage. *Journal of Power Sources, 396*:327-334.
[279] Armstrong, A. R., Armstrong, G., Canales, J., García, R., & Bruce, P. G. (2005). Lithium-Ion Intercalation into TiO2-B Nanowires. *Advanced Materials, 17*(7):862-865.
[280] Armstrong, A. R., Armstrong, G., Canales, J., & Bruce, P. G. (2005). TiO2–B nanowires as negative electrodes for rechargeable lithium batteries. *Journal of Power Sources, 146*(1):501-506.
[281] Armstrong, G., Armstrong, A. R., Bruce, P. G., Reale, P., & Scrosati, B. (2006). TiO2(B) Nanowires as an Improved Anode Material for Lithium-Ion Batteries Containing LiFePO4 or LiNi0.5Mn1.5O4 Cathodes and a Polymer Electrolyte. *Advanced Materials, 18*(19):2597-2600.
[282] Wang, W., Sa, Q., Chen, J., Wang, Y., Jung, H., & Yin, Y. (2013). Porous TiO2/C Nanocomposite Shells As a High-Performance Anode Material for Lithium-Ion Batteries. *ACS Applied Materials & Interfaces, 5*(14):6478-6483.
[283] Yu, K., Zhao, J., Guo, Y., Ding, X., Liu, Y., & Wang, Z. (2005). Sol–gel synthesis and hydrothermal processing of anatase nanocrystals from titanium n-butoxide. *Materials Letters, 59*(19-20):2515-2518.
[284] Liao, J.-Y., Higgins, D., Lui, G., Chabot, V., Xiao, X., & Chen, Z. (2013). Multifunctional TiO2–C/MnO2 Core–Double-Shell Nanowire Arrays as High-Performance 3D Electrodes for Lithium Ion Batteries. *Nano Letters, 13*(11):5467-5473.
[285] Wang, G. (2007). Hydrothermal synthesis and photocatalytic activity of nanocrystalline TiO2 powders in ethanol–water mixed solutions. *Journal of Molecular Catalysis A: Chemical, 274*(1):185-191.
[286] Liang, J., Wang, Z., Li, Z., Wang, X., & Yu, K. (2016). Fabrication of nanostructured TiO2 using a solvothermal reaction for lithium-ion batteries. *Nanomaterials and Nanotechnology, 6*:15.
[287] Jung, J. H., Kobayashi, H., van Bommel, K. J. C., Shinkai, S., & Shimizu, T. (2002). Creation of Novel Helical Ribbon and Double-Layered Nanotube TiO2 Structures Using an Organogel Template. *Chemistry of Materials, 14*(4):1445-1447.
[288] Gong, D., Grimes, C. A., Varghese, O. K., Hu, W., Singh, R. S., Chen, Z., & Dickey, E. C. (2001). Titanium oxide nanotube arrays prepared by anodic oxidation. *Journal of Materials Research, 16*(12):3331-3334.
[289] Macwan, D. P., Dave, P. N., & Chaturvedi, S. (2011). A review on nano-TiO2 sol–gel type syntheses and its applications. *Journal of Materials Science, 46*(11):3669-3686.
[290] Leyva-Porras, C., Toxqui-Teran, A., Vega-Becerra, O., Miki-Yoshida, M., Rojas-

Villalobos, M., García-Guaderrama, M., & Aguilar-Martínez, J. (2015). Low-temperature synthesis and characterization of anatase TiO2 nanoparticles by an acid assisted sol–gel method. *Journal of Alloys and Compounds, 647*:627-636.

[291] Armstrong, G., Armstrong, A. R., Canales, J. s., & Bruce, P. G. (2006). TiO[sub 2](B) Nanotubes as Negative Electrodes for Rechargeable Lithium Batteries. *Electrochemical and solid-state letters, 9*(3):A139.

[292] Pavasupree, S., Suzuki, Y., Yoshikawa, S., & Kawahata, R. (2005). Synthesis of titanate, TiO2 (B), and anatase TiO2 nanofibers from natural rutile sand. *Journal of Solid State Chemistry, 178*(10):3110-3116.

[293] Morgado Jr, E., Jardim, P. M., Marinkovic, B. A., Rizzo, F. C., de Abreu, M. A. S., Zotin, J. L., & Araújo, A. S. (2007). Multistep structural transition of hydrogen trititanate nanotubes into TiO2-B nanotubes: a comparison study between nanostructured and bulk materials. *Nanotechnology, 18*(49):495710.

[294] Chen, J. S., Liu, H., Qiao, S. Z., & Lou, X. W. (2011). Carbon-supported ultra-thin anatase TiO2 nanosheets for fast reversible lithium storage. *Journal of Materials Chemistry, 21*(15):5687-5692.

[295] Chen, J. S., Wang, Z., Dong, X. C., Chen, P., & Lou, X. W. (2011). Graphene-wrapped TiO2 hollow structures with enhanced lithium storage capabilities. *Nanoscale, 3*(5):2158-2161.

[296] Acevedo-Peña, P., Haro, M., Rincón, M. E., Bisquert, J., & Garcia-Belmonte, G. (2014). Facile kinetics of Li-ion intake causes superior rate capability in multiwalled carbon nanotube@TiO2 nanocomposite battery anodes. *Journal of Power Sources, 268*:397-403.

[297] Wang, B., Xin, H., Li, X., Cheng, J., Yang, G., & Nie, F. (2014). Mesoporous CNT@TiO2-C Nanocable with Extremely Durable High Rate Capability for Lithium-Ion Battery Anodes. *Scientific Reports, 4*(1):3729.

[298] Borghols, W. J. H., Lützenkirchen-Hecht, D., Haake, U., Chan, W., Lafont, U., Kelder, E. M., . . . Wagemaker, M. (2010). Lithium Storage in Amorphous TiO[sub 2] Nanoparticles. *Journal of The Electrochemical Society, 157*(5):A582.

[299] Li, S., Xue, P., Lai, C., Qiu, J., Ling, M., & Zhang, S. (2015). Pseudocapacitance of amorphous TiO2@ nitrogen doped graphene composite for high rate lithium storage. *Electrochimica Acta, 180*:112-119.

[300] Nakahara, K., Nakajima, R., Matsushima, T., & Majima, H. (2003). Preparation of particulate Li4Ti5O12 having excellent characteristics as an electrode active material for power storage cells. *Journal of Power Sources, 117*(1):131-136.

[301] Zaghib, K., Simoneau, M., Armand, M., & Gauthier, M. (1999). Electrochemical study of Li4Ti5O12 as negative electrode for Li-ion polymer rechargeable batteries. *Journal of Power Sources, 81-82*:300-305.

[302] Wagemaker, M., van Eck, E. R. H., Kentgens, A. P. M., & Mulder, F. M. (2009). Li-Ion Diffusion in the Equilibrium Nanomorphology of Spinel Li4+xTi5O12. *The Journal of Physical Chemistry B, 113*(1):224-230.

[303] Ohzuku, T., Ueda, A., & Yamamoto, N. (1995). Zero-Strain Insertion Material of $Li[Li_{1/3}Ti_{5/3}]O_4$ for Rechargeable Lithium Cells. *Journal of The Electrochemical Society, 142*(5):1431-1435.

[304] Wagemaker, M., Simon, D. R., Kelder, E. M., Schoonman, J., Ringpfeil, C., Haake, U., . . . Mulder, F. M. (2006). A Kinetic Two-Phase and Equilibrium Solid Solution in Spinel Li4+xTi5O12. *Advanced Materials, 18*(23):3169-3173.

[305] Wang, G. X., Bradhurst, D. H., Dou, S. X., & Liu, H. K. (1999). Spinel Li[Li1/3Ti5/3]O4 as an anode material for lithium ion batteries. *Journal of Power Sources, 83*(1):156-161.

[306] Sun, X., Radovanovic, P. V., & Cui, B. (2015). Advances in spinel Li4Ti5O12 anode

materials for lithium-ion batteries. *New Journal of Chemistry, 39*(1):38-63.

[307] Xu, G. B., Li, W., Yang, L. W., Wei, X. L., Ding, J. W., Zhong, J. X., & Chu, P. K. (2015). Highly-crystalline ultrathin Li4Ti5O12 nanosheets decorated with silver nanocrystals as a high-performance anode material for lithium ion batteries. *Journal of Power Sources, 276*:247-254.

[308] Chen, C. H., Vaughey, J. T., Jansen, A. N., Dees, D. W., Kahaian, A. J., Goacher, T., & Thackeray, M. M. (2001). Studies of Mg-Substituted Li[sub 4−x]Mg[sub x]Ti[sub 5]O[sub 12] Spinel Electrodes (0≤x≤1) for Lithium Batteries. *Journal of The Electrochemical Society, 148*(1):A102.

[309] Zhou, L., Zhang, X., Huang, M., & Huang, J. (2018). A facile way to prepare carbon-coated Li4Ti5O12 porous fiber with excellent rate performance as anode in lithium ion battery. *Electrochimica Acta, 283*:1418-1424.

[310] Zeng, C., Zhou, W., Chen, F., Ye, Q., Li, C., & Huang, C. (2020). Effects of different carbon coatings on the ion transport mechanism and electrochemical performance of Li4Ti5O12 anode for Lithium ion batteries. *Surface and Coatings Technology, 403*:126420.

[311] Wang, Y.-Q., Gu, L., Guo, Y.-G., Li, H., He, X.-Q., Tsukimoto, S., . . . Wan, L.-J. (2012). Rutile-TiO2 nanocoating for a high-rate Li4Ti5O12 anode of a lithium-ion battery. *Journal of the American Chemical Society, 134*(18):7874-7879.

[312] Rahman, M. M., Wang, J.-Z., Hassan, M. F., Chou, S., Wexler, D., & Liu, H.-K. (2010). Basic molten salt process—A new route for synthesis of nanocrystalline Li4Ti5O12–TiO2 anode material for Li-ion batteries using eutectic mixture of LiNO3–LiOH–Li2O2. *Journal of Power Sources, 195*(13):4297-4303.

[313] Wang, D., Liu, H., Shan, Z., Xia, D., Na, R., Liu, H., . . . Tian, J. (2020). Nitrogen, sulfur Co-doped porous graphene boosting Li4Ti5O12 anode performance for high-rate and long-life lithium ion batteries. *Energy Storage Materials, 27*:387-395.

[314] Liu, Z., Chai, J., Xu, G., Wang, Q., & Cui, G. (2015). Functional lithium borate salts and their potential application in high performance lithium batteries. *Coordination Chemistry Reviews, 292*:56-73.

[315] Li, B., Zheng, J., Zhang, H., Jin, L., Yang, D., Lv, H., . . . Zhang, C. (2018). Electrode Materials, Electrolytes, and Challenges in Nonaqueous Lithium-Ion Capacitors. *Advanced Materials, 30*(17):1705670.

[316] Xu, K. (2004). Nonaqueous Liquid Electrolytes for Lithium-Based Rechargeable Batteries. *Chemical Reviews, 104*(10):4303-4418.

[317] Tan, S., Ji, Y. J., Zhang, Z. R., & Yang, Y. (2014). Recent Progress in Research on High-Voltage Electrolytes for Lithium-Ion Batteries. *ChemPhysChem, 15*(10):1956-1969.

[318] Kalhoff, J., Eshetu, G. G., Bresser, D., & Passerini, S. (2015). Safer Electrolytes for Lithium-Ion Batteries: State of the Art and Perspectives. *ChemSusChem, 8*(13):2154-2175.

[319] Eshetu, G. G., Grugeon, S., Laruelle, S., Boyanov, S., Lecocq, A., Bertrand, J.-P., & Marlair, G. (2013). In-depth safety-focused analysis of solvents used in electrolytes for large scale lithium ion batteries. *Physical Chemistry Chemical Physics, 15*(23):9145-9155.

[320] Bushkova, O., Yaroslavtseva, T., & Dobrovolsky, Y. A. (2017). New lithium salts in electrolytes for lithium-ion batteries. *Russian Journal of Electrochemistry, 53*(7):677-699.

[321] Gnanaraj, J. S., Zinigrad, E., Levi, M. D., Aurbach, D., & Schmidt, M. (2003). A comparison among LiPF6, LiPF3(CF2CF3)3 (LiFAP), and LiN(SO2CF2CF3)2 (LiBETI) solutions: electrochemical and thermal studies. *Journal of Power Sources, 119-121*:799-804.

[322] Schipper, F., & Aurbach, D. (2016). A brief review: past, present and future of lithium ion batteries. *Russian Journal of Electrochemistry, 52*(12):1095-1121.
[323] Jow, T. R., Xu, K., Borodin, O., & Ue, M. (2014). *Electrolytes for lithium and lithium-ion batteries* (Vol. 58): Springer.
[324] Mauger, A., Julien, C. M., Paolella, A., Armand, M., & Zaghib, K. (2018). A comprehensive review of lithium salts and beyond for rechargeable batteries: Progress and perspectives. *Materials Science and Engineering: R: Reports, 134*:1-21.
[325] Nie, M., & Lucht, B. L. (2014). Role of Lithium Salt on Solid Electrolyte Interface (SEI) Formation and Structure in Lithium Ion Batteries. *Journal of The Electrochemical Society, 161*(6):A1001-A1006.
[326] Zinigrad, E., Larush-Asraf, L., Gnanaraj, J. S., Sprecher, M., & Aurbach, D. (2005). On the thermal stability of LiPF6. *Thermochimica acta, 438*(1-2):184-191.
[327] Aravindan, V., Gnanaraj, J., Madhavi, S., & Liu, H.-K. (2011). Lithium-Ion Conducting Electrolyte Salts for Lithium Batteries. *Chemistry – A European Journal, 17*(51):14326-14346.
[328] Amine, K., Liu, J., & Belharouak, I. (2005). High-temperature storage and cycling of C-LiFePO4/graphite Li-ion cells. *Electrochemistry Communications, 7*(7):669-673.
[329] Sloop, S. E., Kerr, J. B., & Kinoshita, K. (2003). The role of Li-ion battery electrolyte reactivity in performance decline and self-discharge. *Journal of Power Sources, 119-121*:330-337.
[330] Tasaki, K., Kanda, K., Nakamura, S., & Ue, M. (2003). Decomposition of LiPF[sub 6] and Stability of PF[sub 5] in Li-Ion Battery Electrolytes. *Journal of The Electrochemical Society, 150*(12):A1628.
[331] Oesten, R., Heider, U., & Schmidt, M. (2002). Advanced electrolytes. *Solid State Ionics, 148*(3):391-397.
[332] Schmidt, M., Heider, U., Kuehner, A., Oesten, R., Jungnitz, M., Ignat'ev, N., & Sartori, P. (2001). Lithium fluoroalkylphosphates: a new class of conducting salts for electrolytes for high energy lithium-ion batteries. *Journal of Power Sources, 97-98*:557-560.
[333] Gnanaraj, J. S., Zinigrad, E., Asraf, L., Gottlieb, H. E., Sprecher, M., Aurbach, D., & Schmidt, M. (2003). The use of accelerating rate calorimetry (ARC) for the study of the thermal reactions of Li-ion battery electrolyte solutions. *Journal of Power Sources, 119-121*:794-798.
[334] Gnanaraj, J. S., Zinigrad, E., Asraf, L., Sprecher, M., Gottlieb, H. E., Geissler, W., . . . Aurbach, D. (2003). On the use of LiPF3(CF2CF3)3 (LiFAP) solutions for Li-ion batteries. Electrochemical and thermal studies. *Electrochemistry Communications, 5*(11):946-951.
[335] Arbizzani, C., De Giorgio, F., Porcarelli, L., Mastragostino, M., Khomenko, V., Barsukov, V., . . . Passerini, S. (2013). Use of non-conventional electrolyte salt and additives in high-voltage graphite/LiNi0.4Mn1.6O4 batteries. *Journal of Power Sources, 238*:17-20.
[336] Zhang, S. S., Xu, K., & Jow, T. R. (2002). Study of LiBF[sub 4] as an Electrolyte Salt for a Li-Ion Battery. *Journal of The Electrochemical Society, 149*(5):A586.
[337] Zhang, S., Xu, K., & Jow, T. (2003). Low-temperature performance of Li-ion cells with a LiBF 4-based electrolyte. *Journal of Solid State Electrochemistry, 7*(3):147-151.
[338] Song, S.-W., Richardson, T. J., Zhuang, G. V., Devine, T. M., & Evans, J. W. (2004). Effect on aluminum corrosion of LiBF4 addition into lithium imide electrolyte; a study using the EQCM. *Electrochimica Acta, 49*(9):1483-1490.
[339] Ue, M., & Mori, S. (1995). Mobility and Ionic Association of Lithium Salts in a

Propylene Carbonate-Ethyl Methyl Carbonate Mixed Solvent. *Journal of The Electrochemical Society, 142*(8):2577-2581.

[340] Zhang, S. S., Xu, K., & Jow, T. R. (2006). Enhanced performance of Li-ion cell with LiBF4-PC based electrolyte by addition of small amount of LiBOB. *Journal of Power Sources, 156*(2):629-633.

[341] Zhao, Q., Zhang, Y., Tang, F., Zhao, J., & Li, S. (2017). Mixed salts of lithium difluoro (oxalate) borate and lithium tetrafluorobotate electrolyte on low-temperature performance for lithium-ion batteries. *Journal of The Electrochemical Society, 164*(9):A1873.

[342] Zhou, H., Xiao, K., & Li, J. (2016). Lithium difluoro (oxalate) borate and LiBF4 blend salts electrolyte for LiNi0. 5Mn1. 5O4 cathode material. *Journal of Power Sources, 302*:274-282.

[343] Dudley, J. T., Wilkinson, D. P., Thomas, G., LeVae, R., Woo, S., Blom, H., . . . Dahn, J. R. (1991). Conductivity of electrolytes for rechargeable lithium batteries. *Journal of Power Sources, 35*(1):59-82.

[344] Tarascon, J. M., & Guyomard, D. (1994). New electrolyte compositions stable over the 0 to 5 V voltage range and compatible with the Li1+xMn2O4/carbon Li-ion cells. *Solid State Ionics, 69*(3):293-305.

[345] Foropoulos Jr, J., & DesMarteau, D. D. (1984). Synthesis, properties, and reactions of bis ((trifluoromethyl) sulfonyl) imide,(CF3SO2) 2NH. *Inorganic Chemistry, 23*(23):3720-3723.

[346] Krause, L. J., Lamanna, W., Summerfield, J., Engle, M., Korba, G., Loch, R., & Atanasoski, R. (1997). Corrosion of aluminum at high voltages in non-aqueous electrolytes containing perfluoroalkylsulfonyl imides; new lithium salts for lithium-ion cells. *Journal of Power Sources, 68*(2):320-325.

[347] Kanamura, K. (1999). Anodic oxidation of nonaqueous electrolytes on cathode materials and current collectors for rechargeable lithium batteries. *Journal of Power Sources, 81-82*:123-129.

[348] Kanamura, K., Umegaki, T., Shiraishi, S., Ohashi, M., & Takehara, Z.-i. (2002). Electrochemical Behavior of Al Current Collector of Rechargeable Lithium Batteries in Propylene Carbonate with LiCF[sub 3]SO[sub 3], Li(CF[sub 3]SO[sub 2])[sub 2]N, or Li(C[sub 4]F[sub 9]SO[sub 2])(CF[sub 3]SO[sub 2])N. *Journal of The Electrochemical Society, 149*(2):A185.

[349] Lischka, U., Wietelmann, U., & Wegner, M. (1999). Lithium bisoxalatoborate used as conducting salt in lithium ion batteries. *DE19829030 C1*.

[350] Xu, W., & Angell, C. A. (2000). Weakly coordinating anions, and the exceptional conductivity of their nonaqueous solutions. *Electrochemical and Solid State Letters, 4*(1):E1.

[351] Xu, K., Zhang, S., Jow, T. R., Xu, W., & Angell, C. A. (2002). LiBOB as Salt for Lithium-Ion Batteries:A Possible Solution for High Temperature Operation. *Electrochemical and Solid-State Letters, 5*(1):A26-A29.

[352] Cataldo, F., Iglesias-Groth, S., & Prata, M. (2017). Neutron bombardment of lithium bis(oxalato) borate: LiBOB. *Journal of Radioanalytical and Nuclear Chemistry, 313*(1):239-247.

[353] Xu, K., Zhang, S. S., Lee, U., Allen, J. L., & Jow, T. R. (2005). LiBOB: Is it an alternative salt for lithium ion chemistry? *Journal of Power Sources, 146*(1):79-85.

[354] Aravindan, V., Gnanaraj, J., Madhavi, S., & Liu, H. K. (2011). Lithium-ion conducting electrolyte salts for lithium batteries. *Chemistry, 17*(51):14326-14346.

[355] Yu, B.-T., Qiu, W.-H., Li, F.-S., & Xu, G.-X. (2005). The electrochemical characterization of lithium bis (oxalato) borate synthesized by a novel method. *Electrochemical and Solid State Letters, 9*(1):A1.

[356] Wang, S., Qiu, W., Guan, Y., Yu, B., Zhao, H., & Liu, W. (2007). Electrochemical characteristics of LiMxFe1−xPO4 cathode with LiBOB based electrolytes. *Electrochimica Acta, 52*(15):4907-4910.

[357] Cui, X., Zhang, H., Li, S., Li, X., & Feng, H. (2014). Electrochemical performances of a novel lithium bis(oxalate)borate-based electrolyte for lithium-ion batteries with LiFePO4 cathodes. *Ionics, 20*(6):789-794.

[358] Xu, K. (2008). Tailoring Electrolyte Composition for LiBOB. *Journal of The Electrochemical Society, 155*(10):A733.

[359] Lee, S. J., Han, J.-G., Park, I., Song, J., Cho, J., Kim, J.-S., & Choi, N.-S. (2014). Effect of Lithium Bis(oxalato)borate Additive on Electrochemical Performance of Li1.17Ni0.17Mn0.5Co0.17O2Cathodes for Lithium-Ion Batteries. *Journal of The Electrochemical Society, 161*(14):A2012-A2019.

[360] Aravindan, V., Cheah, Y. L., Ling, W. C., & Madhavi, S. (2012). Effect of LiBOB additive on the electrochemical performance of LiCoPO4. *Journal of The Electrochemical Society, 159*(9):A1435-A1439.

[361] Choi, N. S., Han, J. G., Ha, S. Y., Park, I., & Back, C. K. (2015). Recent advances in the electrolytes for interfacial stability of high-voltage cathodes in lithium-ion batteries. *RSC Advances, 5*(4):2732-2748.

[362] Hofmann, A., Hoeweling, A., Bohn, N., Mueller, M., Binder, J. R., & Hanemann, T. (2019). Additives for Cycle Life Improvement of High-Voltage LNMO-Based Li-Ion Cells. *ChemElectroChem, 6*(20):5255-5263.

[363] Wu, S., Lin, Y., Xing, L., Sun, G., Zhou, H., Xu, K., . . . Li, W. (2019). Stabilizing LiCoO2/Graphite at High Voltages with an Electrolyte Additive. *ACS Appl Mater Interfaces, 11*(19):17940-17951.

[364] Xiao, Z., Liu, J., Fan, G., Yu, M., Liu, J., Gou, X., . . . Cheng, F. (2020). Lithium bis(oxalate)borate additive in the electrolyte to improve Li-rich layered oxide cathode materials. *Materials Chemistry Frontiers, 4*(6):1689-1696.

[365] Täubert, C., Fleischhammer, M., Wohlfahrt-Mehrens, M., Wietelmann, U., & Buhrmester, T. (2010). LiBOB as Electrolyte Salt or Additive for Lithium-Ion Batteries Based on LiNi0.8Co0.15Al0.05O2 / Graphite. *Journal of The Electrochemical Society, 157*(6):A721-A728.

[366] Xu, K., Zhang, S., & Jow, T. R. (2005). LiBOB as Additive in LiPF6-Based Lithium Ion Electrolytes. *Electrochemical and Solid-State Letters, 8*(7):A365-A368.

[367] Xu, K. (2014). Electrolytes and Interphases in Li-Ion Batteries and Beyond. *Chemical Reviews, 114*(23):11503-11618.

[368] Zhuang, G., Xu, K., Jow, T., & Ross Jr, P. (2004). Study of SEI layer formed on graphite anodes in PC/LiBOB electrolyte using IR spectroscopy. *Electrochemical and Solid State Letters, 7*(8):A224.

[369] Xu, M. Q., Tsiouvaras, N., Garsuch, A., Gasteiger, H. A., & Lucht, B. L. (2014). Generation of Cathode Passivation Films via Oxidation of Lithium Bis(oxalato) Borate on High Voltage Spinel (LiNi0.5Mn1.5O4). *Journal of Physical Chemistry C, 118*(14):7363-7368.

[370] Zhang, Q., Wang, K., Wang, X., Zhong, Y., Liu, M., Liu, X., . . . Li, W. (2019). Lithium Bis(oxalate)borate Reinforces the Interphase on Li-Metal Anodes. *ACS Applied Materials & Interfaces, 11*(23):20854-20863.

[371] Dong, Y., Young, B. T., Zhang, Y., Yoon, T., Heskett, D. R., Hu, Y., & Lucht, B. L. (2017). Effect of Lithium Borate Additives on Cathode Film Formation in LiNi0.5Mn1.5O4/Li Cells. *ACS Applied Materials & Interfaces, 9*(24):20467-20475.

[372] Yang, L., Wang, P., Zhao, D., Wei, Y., Han, Y., Zeng, S., . . . Li, S. (2020). Study on boron-containing electrolytes at extra-high temperatures for lithium-ion batteries. *Sustainable Energy & Fuels, 4*(8):4126-4136.

[373] Balakrishnan, P. G., Ramesh, R., & Kumar, T. P. (2006). Safety mechanisms in lithium-ion batteries. *Journal of Power Sources, 155*(2):401-414.
[374] Jiang, J., & Dahn, J. (2003). Comparison of the thermal stability of lithiated graphite in LiBOB EC/DEC and in LiPF6 EC/DEC. *Electrochemical and Solid State Letters, 6*(9):A180.
[375] Ha, S.-Y., Han, J.-G., Song, Y.-M., Chun, M.-J., Han, S.-I., Shin, W.-C., & Choi, N.-S. (2013). Using a lithium bis(oxalato) borate additive to improve electrochemical performance of high-voltage spinel LiNi0.5Mn1.5O4 cathodes at 60°C. *Electrochimica Acta, 104*:170-177.
[376] Pieczonka, N. P. W., Yang, L., Balogh, M. P., Powell, B. R., Chemelewski, K., Manthiram, A., . . . Kim, J. H. (2013). Impact of Lithium Bis(oxalate)borate Electrolyte Additive on the Performance of High-Voltage Spinel/Graphite Li-Ion Batteries. *Journal of Physical Chemistry C, 117*(44):22603-22612.
[377] Zhu, Y., Li, Y., Bettge, M., & Abraham, D. P. (2013). Electrolyte additive combinations that enhance performance of high-capacity Li1. 2Ni0. 15Mn0. 55Co0. 1O2–graphite cells. *Electrochimica Acta, 110*:191-199.
[378] An, S. J., Li, J. L., Daniel, C., Mohanty, D., Nagpure, S., & Wood, D. L. (2016). The state of understanding of the lithium-ion-battery graphite solid electrolyte interphase (SEI) and its relationship to formation cycling. *Carbon, 105*:52-76.
[379] Zhao, H., Yu, X., Li, J., Li, B., Shao, H., Li, L., & Deng, Y. (2019). Film-forming electrolyte additives for rechargeable lithium-ion batteries: progress and outlook. *Journal of Materials Chemistry A, 7*(15):8700-8722.
[380] Rauh, R. D., & Brummer, S. B. (1977). The effect of additives on lithium cycling in methyl acetate. *Electrochimica Acta, 22*(1):85-91.
[381] Abraham, K. M., Goldman, J. L., & Natwig, D. L. (1982). Characterization of Ether Electrolytes for Rechargeable Lithium Cells. *Journal of The Electrochemical Society, 129*(11):2404-2409.
[382] Choi, N.-S., Yew, K. H., Kim, H., Kim, S.-S., & Choi, W.-U. (2007). Surface layer formed on silicon thin-film electrode in lithium bis(oxalato) borate-based electrolyte. *Journal of Power Sources, 172*(1):404-409.
[383] Celik Kucuk, A., Minato, T., Yamanaka, T., & Abe, T. (2019). Effects of LiBOB on salt solubility and BiF3 electrode electrochemical properties in fluoride shuttle batteries. *Journal of Materials Chemistry A, 7*(14):8559-8567.
[384] Fan, L.-Z., Xing, T., Awan, R., & Qiu, W. (2011). Studies on lithium bis(oxalato)-borate/propylene carbonate-based electrolytes for Li-ion batteries. *Ionics, 17*(6):491-494.
[385] Barth, W. V., Peña Hueso, A., Zhou, L., Lyons, L. J., & West, R. (2014). Ionic conductivity studies of LiBOB-doped silyl solvent blend electrolytes for lithium-ion battery applications. *Journal of Power Sources, 272*:190-195.
[386] Xu, K., Lee, U., Zhang, S., Wood, M., & Jow, T. R. (2003). Chemical analysis of graphite/electrolyte interface formed in LiBOB-based electrolytes. *Electrochemical and solid-state letters, 6*(7):A144-A148.
[387] Lee, S. J., Han, J.-G., Park, I., Song, J., Cho, J., Kim, J.-S., & Choi, N.-S. (2014). Effect of lithium bis (oxalato) borate additive on electrochemical performance of Li1. 17Ni0. 17Mn0. 5Co0. 17O2 cathodes for lithium-ion batteries. *Journal of The Electrochemical Society, 161*(14):A2012.
[388] Lian, F., Li, Y., He, Y., Guan, H., Yan, K., Qiu, W., . . . Wohlfahrt-Mehrens, M. (2015). Preparation of LiBOB via rheological phase method and its application to mitigate voltage fade of Li1.16[Mn0.75Ni0.25]0.84O2 cathode. *RSC Advances, 5*(105):86763-86770.
[389] Lestariningsih, T., Wigayati, E., Ratri, C., & Sabrina, Q. (2017). Study of LiBOB

compound synthesis by vacuum process as lithium ion battery electrolytes. *Journal of Physics: Conference Series, 817*:012030.

[390] Yu, B.-T., Qiu, W.-H., Li, F.-S., & Li, L.-F. (2007). Kinetic study on solid state reaction for synthesis of LiBOB. *Journal of Power Sources, 174*(2):1012-1014.

[391] Lestariningsih, T., Wigayati, E. M., Sabrina, Q., Prihandoko, B., & Priyono, S. (2018). The effect of Li2CO3 substitution on synthesis of LiBOB compounds as salt of electrolyte battery lithium ion. *AIP Conference Proceedings, 1945*(1):020028.

[392] Holomb, R., Xu, W., Markusson, H., Johansson, P., & Jacobsson, P. (2006). Vibrational Spectroscopy and ab Initio Studies of Lithium Bis(oxalato)borate (LiBOB) in Different Solvents. *The Journal of Physical Chemistry A, 110*(40):11467-11472.

[393] Li, C., Li, Z., Wang, P., Liu, H., Zhao, D., Wang, S., & Li, S. (2019). Studies of air-exposure effects and remediation measures on lithium bis (oxalato) borate. *New Journal of Chemistry, 43*(36):14238-14245.

[394] Zavalij, P. Y., Yang, S., & Whittingham, M. S. (2003). Structures of potassium, sodium and lithium bis (oxalato) borate salts from powder diffraction data. *Acta Crystallographica Section B: Structural Science, 59*(6):753-759.

[395] Halwax, E. (1998). *The Full-Pattern Reference Intensity Ratio Method in Quantitative Phase Analysis.* Paper presented at the Materials Science Forum.

[396] Hillier, S. (2000). Accurate quantitative analysis of clay and other minerals in sandstones by XRD: comparison of a Rietveld and a reference intensity ratio (RIR) method and the importance of sample preparation. *Clay minerals, 35*(1):291-302.

[397] Hubbard, C. R., Evans, E., & Smith, D. (1976). The reference intensity ratio, I/Ic, for computer simulated powder patterns. *Journal of Applied Crystallography, 9*(2):169-174.

[398] Yang, L., Furczon, M., Xiao, A., Lucht, B., Zhang, Z., & Abraham, D. (2010). Effect of impurities and moisture on lithium bisoxalatoborate (LiBOB) electrolyte performance in lithium-ion cells. *Journal of Power Sources, 195*(6):1698-1705.

[399] Li, C., Li, Z., Wang, P., Liu, H., Zhao, D., Wang, S., & Li, S. (2019). Studies of air-exposure effects and remediation measures on lithium bis(oxalato)borate. *New Journal of Chemistry, 43*(36):14238-14245.

[400] Xu, K., Deveney, B., Nechev, K., Lam, Y., & Jow, T. R. (2008). Evaluating LiBOB/lactone electrolytes in large-format lithium-ion cells based on nickelate and iron phosphate. *Journal of The Electrochemical Society, 155*(12):A959.

[401] Xu, K., Zhang, S., Jow, T. R., Xu, W., & Angell, C. A. (2001). LiBOB as salt for lithium-ion batteries: a possible solution for high temperature operation. *Electrochemical and Solid State Letters, 5*(1):A26.

[402] Wigayati, E. M., Lestariningsih, T., Subhan, A., Ratri, C. R., & Purawiardi, I. (2016). Synthesis and characterization of LiBOB as electrolyte for lithium-ion battery. *Ionics, 22*(1):43-50.

[403] Yu, B.-T., Qiu, W.-H., Li, F.-S., & Xu, G.-X. (2006). The Electrochemical Characterization of Lithium Bis(oxalato)borate Synthesized by a Novel Method. *Electrochemical and solid-state letters, 9*(1):A1.

[404] Wang, S., Qiu, W., Li, T., Yu, B., & Zhao, H. (2006). Properties of Lithium bis (oxatlato) borate (LiBOB) as a Lithium Salt and cycle performance in LiMn2O4 Half Cell. *Int. J. Electrochem. Sci, 1*:250-257.

[405] Wachtler, M., Wohlfahrt-Mehrens, M., Ströbele, S., Panitz, J.-C., & Wietelmann, U. (2006). The behaviour of graphite, carbon black, and Li 4 Ti 5 O 12 in LiBOB-based electrolytes. *Journal of applied electrochemistry, 36*(11):1199-1206.

[406] Ha, S. Y., Han, J. G., Song, Y. M., Chun, M. J., Han, S. I., Shin, W. C., & Choi, N. S. (2013). Using a lithium bis(oxalato) borate additive to improve electrochemical

performance of high-voltage spinel LiNi0.5Mn1.5O4 cathodes at 60 degrees C. *Electrochimica Acta, 104*:170-177.

[407] Zhao, W., Zou, L., Zheng, J., Jia, H., Song, J., Engelhard, M. H., . . . Zhang, J.-G. (2018). Simultaneous Stabilization of LiNi0.76Mn0.14Co0.10O2 Cathode and Lithium Metal Anode by Lithium Bis(oxalato)borate as Additive. *ChemSusChem, 11*(13):2211-2220.

[408] Afyon, S., Kundu, D., Darbandi, A. J., Hahn, H., Krumeich, F., & Nesper, R. (2014). A low dimensional composite of hexagonal lithium manganese borate (LiMnBO3), a cathode material for Li-ion batteries. *Journal of Materials Chemistry A, 2*(44):18946-18951.

[409] Zor, C., Somer, M., & Afyon, S. (2018). LiMg0.1Co0.9BO3 as a positive electrode material for Li-ion batteries. *RSC Advances, 8*(28):15773-15779.

[410] Qiu, J., Lai, C., Wang, Y., Li, S., & Zhang, S. (2014). Resilient mesoporous TiO2/graphene nanocomposite for high rate performance lithium-ion batteries. *Chemical Engineering Journal, 256*:247-254.

[411] Liu, Z., Andreev, Y. G., Robert Armstrong, A., Brutti, S., Ren, Y., & Bruce, P. G. (2013). Nanostructured TiO2(B): the effect of size and shape on anode properties for Li-ion batteries. *Progress in Natural Science: Materials International, 23*(3):235-244.

[412] Shen, L., Zhang, X., Li, H., Yuan, C., & Cao, G. (2011). Design and Tailoring of a Three-Dimensional TiO2–Graphene–Carbon Nanotube Nanocomposite for Fast Lithium Storage. *The Journal of Physical Chemistry Letters, 2*(24):3096-3101.

[413] Lewis, C. S., Li, Y. R., Wang, L., Li, J., Stach, E. A., Takeuchi, K. J., . . . Wong, S. S. (2016). Correlating Titania Nanostructured Morphologies with Performance as Anode Materials for Lithium-Ion Batteries. *ACS Sustainable Chemistry & Engineering, 4*(12):6299-6312.

[414] Deng, D., Kim, M. G., Lee, J. Y., & Cho, J. (2009). Green energy storage materials: Nanostructured TiO2 and Sn-based anodes for lithium-ion batteries. *Energy & Environmental Science, 2*(8):818-837.

[415] Kasuga, T., Hiramatsu, M., Hoson, A., Sekino, T., & Niihara, K. (1998). Formation of Titanium Oxide Nanotube. *Langmuir, 14*(12):3160-3163.

[416] Kasuga, T., Hiramatsu, M., Hoson, A., Sekino, T., & Niihara, K. (1999). Titania Nanotubes Prepared by Chemical Processing. *Advanced Materials, 11*(15):1307-1311.

[417] Armstrong, G., Armstrong, A. R., Canales, J., & Bruce, P. G. (2006). TiO2 (B) Nanotubes as Negative Electrodes for Rechargeable Lithium Batteries. *Electrochemical and Solid-State Letters, 9*(3):A139-A143.

[418] Armstrong, G., Armstrong, A. R., Canales, J., & Bruce, P. G. (2005). Nanotubes with the TiO2-B structure. *Chemical Communications*(19):2454-2456.

[419] Afyon, S., Hagemann, M., Somer, M., & Schulze Isfort, C. (2013). Thermal and hydrothermal stability of flame hydrolytically synthesized SiO2/TiO2 mixed oxides. *Solid State Sciences, 18*:91-97.

[420] Cao, H., Li, B., Zhang, J., Lian, F., Kong, X., & Qu, M. (2012). Synthesis and superior anode performance of TiO2@reduced graphene oxide nanocomposites for lithium ion batteries. *Journal of Materials Chemistry, 22*(19):9759-9766.

[421] Mei, Y., Huang, Y., & Hu, X. (2016). Nanostructured Ti-based anode materials for Na-ion batteries. *Journal of Materials Chemistry A, 4*(31):12001-12013.

[422] Saravanan, K., Ananthanarayanan, K., & Balaya, P. (2010). Mesoporous TiO2 with high packing density for superior lithium storage. *Energy & Environmental Science, 3*(7):939-948.

[423] Guo, Y.-G., Hu, Y.-S., Sigle, W., & Maier, J. (2007). Superior Electrode Performance

of Nanostructured Mesoporous TiO2 (Anatase) through Efficient Hierarchical Mixed Conducting Networks. *Advanced Materials, 19*(16):2087-2091.

[424] Liu, Y., & Yang, Y. (2016). Recent Progress of TiO2-Based Anodes for Li Ion Batteries %J Journal of Nanomaterials. *2016*:15.

[425] Zhang, W., Xu, T., Liu, Z., Wu, N.-L., & Wei, M. (2018). Hierarchical TiO2−x imbedded with graphene quantum dots for high-performance lithium storage. *Chemical Communications, 54*(12):1413-1416.

[426] Yang, S., Feng, X., & Müllen, K. (2011). Sandwich-Like, Graphene-Based Titania Nanosheets with High Surface Area for Fast Lithium Storage. *Advanced Materials, 23*(31):3575-3579.

[427] Das, S. K., Patel, M., & Bhattacharyya, A. J. (2010). Effect of Nanostructuring and Ex situ Amorphous Carbon Coverage on the Lithium Storage and Insertion Kinetics in Anatase Titania. *ACS Applied Materials & Interfaces, 2*(7):2091-2099.

[428] Park, S.-J., Kim, H., Kim, Y.-J., & Lee, H. (2011). Preparation of carbon-coated TiO2 nanostructures for lithium-ion batteries. *Electrochimica Acta, 56*(15):5355-5362.

[429] Jin, J., Ren, X.-N., Lu, Y., Zheng, X.-F., Wang, H.-E., Chen, L.-H., . . . Su, B.-L. (2016). High lithium ion battery performance enhancement by controlled carbon coating of TiO2 hierarchically porous hollow spheres. *RSC Advances, 6*(74):70485-70492.

[430] Zhang, Z., Zhang, L., Li, W., Yu, A., & Wu, P. (2015). Carbon-Coated Mesoporous TiO2 Nanocrystals Grown on Graphene for Lithium-Ion Batteries. *ACS Applied Materials & Interfaces, 7*(19):10395-10400.

[431] Wang, J., Shen, L., Nie, P., Xu, G., Ding, B., Fang, S., . . . Zhang, X. (2014). Synthesis of hydrogenated TiO2–reduced-graphene oxide nanocomposites and their application in high rate lithium ion batteries. *Journal of Materials Chemistry A, 2*(24):9150-9155.

[432] Yu, J., Huang, H., Gan, Y., Xia, Y., Liang, C., Zhang, J., . . . Zhang, W. (2018). A new strategy for the construction of 3D TiO2 nanowires/reduced graphene oxide for high-performance lithium/sodium batteries. *Journal of Materials Chemistry A, 6*(47):24256-24266.

[433] Cai, D., Lian, P., Zhu, X., Liang, S., Yang, W., & Wang, H. (2012). High specific capacity of TiO2-graphene nanocomposite as an anode material for lithium-ion batteries in an enlarged potential window. *Electrochimica Acta, 74*:65-72.

[434] Wang, D., Choi, D., Li, J., Yang, Z., Nie, Z., Kou, R., . . . Liu, J. (2009). Self-Assembled TiO2–Graphene Hybrid Nanostructures for Enhanced Li-Ion Insertion. *ACS Nano, 3*(4):907-914.

[435] Ge, H., Hao, T., Osgood, H., Zhang, B., Chen, L., Cui, L., . . . Wu, G. (2016). Advanced Mesoporous Spinel Li4Ti5O12/rGO Composites with Increased Surface Lithium Storage Capability for High-Power Lithium-Ion Batteries. *ACS Applied Materials & Interfaces, 8*(14):9162-9169.

[436] Li, W., Wang, F., Feng, S., Wang, J., Sun, Z., Li, B., . . . Zhao, D. (2013). Sol–Gel Design Strategy for Ultradispersed TiO2 Nanoparticles on Graphene for High-Performance Lithium Ion Batteries. *Journal of the American Chemical Society, 135*(49):18300-18303.

[437] Liu, H., Cao, K., Xu, X., Jiao, L., Wang, Y., & Yuan, H. (2015). Ultrasmall TiO2 Nanoparticles in Situ Growth on Graphene Hybrid as Superior Anode Material for Sodium/Lithium Ion Batteries. *ACS Applied Materials & Interfaces, 7*(21):11239-11245.

[438] Zheng, J., Liu, L., Ji, G., Yang, Q., Zheng, L., & Zhang, J. (2016). Hydrogenated Anatase TiO2 as Lithium-Ion Battery Anode: Size–Reactivity Correlation. *ACS Applied Materials & Interfaces, 8*(31):20074-20081.

[439] Doeuff, S., Henry, M., Sanchez, C., & Livage, J. (1987). Hydrolysis of titanium

alkoxides: Modification of the molecular precursor by acetic acid. *Journal of Non-Crystalline Solids, 89*(1):206-216.

[440] Zhang, H., Lv, X., Li, Y., Wang, Y., & Li, J. (2010). P25-Graphene Composite as a High Performance Photocatalyst. *ACS Nano, 4*(1):380-386.

[441] Ding, S., Chen, J. S., Luan, D., Boey, F. Y. C., Madhavi, S., & Lou, X. W. (2011). Graphene-supported anatase TiO2 nanosheets for fast lithium storage. *Chemical Communications, 47*(20):5780-5782.

[442] Al-Tabbakh, A. A., Karatepe, N., Al-Zubaidi, A. B., Benchaabane, A., & Mahmood, N. B. (2019). Crystallite size and lattice strain of lithiated spinel material for rechargeable battery by X-ray diffraction peak-broadening analysis. *International Journal of Energy Research, 43*(5):1903-1911.

[443] Zhang, Y., & Pan, C. (2011). TiO2/graphene composite from thermal reaction of graphene oxide and its photocatalytic activity in visible light. *Journal of Materials Science, 46*(8):2622-2626.

[444] Benjwal, P., Kumar, M., Chamoli, P., & Kar, K. K. (2015). Enhanced photocatalytic degradation of methylene blue and adsorption of arsenic(iii) by reduced graphene oxide (rGO)–metal oxide (TiO2/Fe3O4) based nanocomposites. *RSC Advances, 5*(89):73249-73260.

[445] Ma, Y., Li, Y., Li, D., Liu, Y., & Zhang, J. (2019). Uniformly distributed TiO2 nanorods on reduced graphene oxide composites as anode material for high rate lithium ion batteries. *Journal of Alloys and Compounds, 771*:885-891.

[446] Afyon, S., Krumeich, F., Mensing, C., Borgschulte, A., & Nesper, R. (2014). New High Capacity Cathode Materials for Rechargeable Li-ion Batteries: Vanadate-Borate Glasses. *Scientific Reports, 4*(1):7113.

[447] Li, M., Sun, G., Yin, P., Ruan, C., & Ai, K. (2013). Controlling the Formation of Rodlike V2O5 Nanocrystals on Reduced Graphene Oxide for High-Performance Supercapacitors. *ACS Applied Materials & Interfaces, 5*(21):11462-11470.

[448] Feng, K., Ahn, W., Lui, G., Park, H. W., Kashkooli, A. G., Jiang, G., . . . Chen, Z. (2016). Implementing an in-situ carbon network in Si/reduced graphene oxide for high performance lithium-ion battery anodes. *Nano Energy, 19*:187-197.

[449] Zeng, L., Dai, C., Liu, B., & Xue, C. (2019). Oxygen-assisted stabilization of single-atom Au during photocatalytic hydrogen evolution. *Journal of Materials Chemistry A*.

[450] Zhang, K., Kemp, K. C., & Chandra, V. (2012). Homogeneous anchoring of TiO2 nanoparticles on graphene sheets for waste water treatment. *Materials Letters, 81*:127-130.

[451] Bharti, B., Kumar, S., Lee, H.-N., & Kumar, R. (2016). Formation of oxygen vacancies and Ti3+ state in TiO2 thin film and enhanced optical properties by air plasma treatment. *Scientific Reports, 6*:32355.

[452] Kim, T., Lee, H., Kim, J., & Suh, K. S. (2010). Synthesis of Phase Transferable Graphene Sheets Using Ionic Liquid Polymers. *ACS Nano, 4*(3):1612-1618.

[453] Shin, J.-Y., Samuelis, D., & Maier, J. (2011). Sustained Lithium-Storage Performance of Hierarchical, Nanoporous Anatase TiO2 at High Rates: Emphasis on Interfacial Storage Phenomena. *Advanced Functional Materials, 21*(18):3464-3472.

[454] Armstrong, A. R., Holzapfel, M., Novák, P., Johnson, C. S., Kang, S.-H., Thackeray, M. M., & Bruce, P. G. (2006). Demonstrating Oxygen Loss and Associated Structural Reorganization in the Lithium Battery Cathode Li[Ni0.2Li0.2Mn0.6]O2. *Journal of the American Chemical Society, 128*(26):8694-8698.

[455] Robertson, A. D., & Bruce, P. G. (2003). Mechanism of electrochemical activity in Li2MnO3. *Chemistry of Materials, 15*(10):1984-1992.

[456] Hernández, G., Naylor, A. J., Chien, Y.-C., Brandell, D., Mindemark, J., & Edström,

K. (2020). Elimination of Fluorination: The Influence of Fluorine-Free Electrolytes on the Performance of LiNi1/3Mn1/3Co1/3O2/Silicon–Graphite Li-Ion Battery Cells. *ACS Sustainable Chemistry & Engineering, 8*(27):10041-10052.

[457] Qian, Y., Niehoff, P., Börner, M., Grützke, M., Mönnighoff, X., Behrends, P., . . . Schappacher, F. M. (2016). Influence of electrolyte additives on the cathode electrolyte interphase (CEI) formation on LiNi1/3Mn1/3Co1/3O2 in half cells with Li metal counter electrode. *Journal of Power Sources, 329*:31-40.

[458] Liu, H., Naylor, A. J., Menon, A. S., Brant, W. R., Edström, K., & Younesi, R. (2020). Understanding the Roles of Tris(trimethylsilyl) Phosphite (TMSPi) in LiNi0.8Mn0.1Co0.1O2 (NMC811)/Silicon–Graphite (Si–Gr) Lithium-Ion Batteries. *Advanced Materials Interfaces, 7*(15):2000277.

[459] Wu, S., Lin, Y., Xing, L., Sun, G., Zhou, H., Xu, K., . . . Li, W. (2019). Stabilizing LiCoO2/Graphite at High Voltages with an Electrolyte Additive. *ACS Applied Materials & Interfaces, 11*(19):17940-17951.

[460] Wang, D. Y., Sinha, N. N., Burns, J. C., Petibon, R., & Dahn, J. R. (2014). A high precision study of the electrolyte additives vinylene carbonate, vinyl ethylene carbonate and lithium bis(oxalate)borate in LiCoO2/graphite pouch cells. *Journal of Power Sources, 270*:68-78.

[461] Ji, Y., Li, S., Zhong, G., Zhang, Z., Li, Y., McDonald, M. J., & Yang, Y. (2015). Synergistic Effects of Suberonitrile-LiBOB Binary Additives on the Electrochemical Performance of High-Voltage LiCoO2Electrodes. *Journal of The Electrochemical Society, 162*(13):A7015-A7023.

[462] Song, Y.-M., Han, J.-G., Park, S., Lee, K. T., & Choi, N.-S. (2014). A multifunctional phosphite-containing electrolyte for 5 V-class LiNi0.5Mn1.5O4 cathodes with superior electrochemical performance. *Journal of Materials Chemistry A, 2*(25):9506-9513.

[463] Pieczonka, N. P. W., Yang, L., Balogh, M. P., Powell, B. R., Chemelewski, K., Manthiram, A., . . . Kim, J.-H. J. J. O. P. C. C. (2013). Impact of Lithium Bis(oxalate)borate Electrolyte Additive on the Performance of High-Voltage Spinel/Graphite Li-Ion Batteries. *117*(44):22603-22612.

[464] Gao, H., Maglia, F., Lamp, P., Amine, K., & Chen, Z. (2017). Mechanistic Study of Electrolyte Additives to Stabilize High-Voltage Cathode–Electrolyte Interface in Lithium-Ion Batteries. *ACS Applied Materials & Interfaces, 9*(51):44542-44549.

[465] Pieczonka, N. P. W., Yang, L., Balogh, M. P., Powell, B. R., Chemelewski, K., Manthiram, A., . . . Kim, J.-H. (2013). Impact of Lithium Bis(oxalate)borate Electrolyte Additive on the Performance of High-Voltage Spinel/Graphite Li-Ion Batteries. *The Journal of Physical Chemistry C, 117*(44):22603-22612.

[466] Nie, M., & Lucht, B. L. (2014). Role of lithium salt on solid electrolyte interface (SEI) formation and structure in lithium ion batteries. *Journal of The Electrochemical Society, 161*(6):A1001.

[467] Xu, K., Zhang, S., Poese, B. A., & Jow, T. R. (2002). Lithium bis (oxalato) borate stabilizes graphite anode in propylene carbonate. *Electrochemical and Solid State Letters, 5*(11):A259.

[468] Xu, M., Tsiouvaras, N., Garsuch, A., Gasteiger, H. A., & Lucht, B. L. (2014). Generation of Cathode Passivation Films via Oxidation of Lithium Bis(oxalato) Borate on High Voltage Spinel (LiNi0.5Mn1.5O4). *The Journal of Physical Chemistry C, 118*(14):7363-7368.

[469] Zhang, S. S. (2006). A review on electrolyte additives for lithium-ion batteries. *Journal of Power Sources, 162*(2):1379-1394.

[470] Xu, K., Deveney, B., Nechev, K., Lam, Y., & Jow, T. R. (2008). Evaluating LiBOB/lactone electrolytes in large-format lithium-ion cells based on nickelate and

iron phosphate. *Journal of The Electrochemical Society, 155*(12):A959-A964.
[471] Xu, K., Zhang, S., & Jow, T. R. (2005). LiBOB as additive in LiPF6-based lithium ion electrolytes. *Electrochemical and Solid State Letters, 8*(7):A365.
[472] Dalavi, S., Xu, M., Knight, B., & Lucht, B. L. (2011). Effect of added LiBOB on high voltage (LiNi0. 5Mn1. 5O4) spinel cathodes. *Electrochemical and Solid State Letters, 15*(2):A28.
[473] Shao-Horn, Y., Levasseur, S., Weill, F., & Delmas, C. (2003). Probing lithium and vacancy ordering in O3 layered Li x CoO2 (x≈ 0.5): an electron diffraction study. *Journal of The Electrochemical Society, 150*(3):A366.
[474] Reimers, J. N., & Dahn, J. R. (1992). Electrochemical and In Situ X-Ray Diffraction Studies of Lithium Intercalation in Li x CoO2. *Journal of The Electrochemical Society, 139*(8):2091-2097.
[475] Aurbach, D., Markovsky, B., Rodkin, A., Levi, E., Cohen, Y. S., Kim, H. J., & Schmidt, M. (2002). On the capacity fading of LiCoO2 intercalation electrodes:: the effect of cycling, storage, temperature, and surface film forming additives. *Electrochimica Acta, 47*(27):4291-4306.
[476] Zor, C., Subaşı, Y., Haciu, D., Somer, M., & Afyon, S. (2021). Guide to Water Free Lithium Bis(oxalate) Borate (LiBOB). *The Journal of Physical Chemistry C, 125*(21):11310-11317.
[477] Zavalij, P. Y., Yang, S., & Whittingham, M. S. (2003). Structures of potassium, sodium and lithium bis(oxalato)borate salts from powder diffraction data. *Acta Crystallographica Section B, 59*(6):753-759.
[478] Hubbard, C. R., Evans, E. H., & Smith, D. K. (1976). The reference intensity ratio, I/Ic, for computer simulated powder patterns. *Journal of Applied Crystallography, 9*(2):169-174.
[479] Hubbard, C. (1976). EH Evans and DK Smith. *J. Appl. Crystallogr, 9*:169.
[480] Amatucci, G. G., Tarascon, J. M., & Klein, L. C. (1996). Cobalt dissolution in LiCoO2-based non-aqueous rechargeable batteries. *Solid State Ionics, 83*(1):167-173.
[481] Chen, C. H., Liu, J., Stoll, M. E., Henriksen, G., Vissers, D. R., & Amine, K. (2004). Aluminum-doped lithium nickel cobalt oxide electrodes for high-power lithium-ion batteries. *Journal of Power Sources, 128*(2):278-285.
[482] Wu, B., Ren, Y., Mu, D., Liu, X., Yang, G., & Wu, F. (2014). Effect of lithium carbonate precipitates on the electrochemical cycling stability of LiCoO2 cathodes at a high voltage. *RSC Advances, 4*(20):10196-10203.
[483] Li, X., Liu, J., Meng, X., Tang, Y., Banis, M. N., Yang, J., . . . Sun, X. (2014). Significant impact on cathode performance of lithium-ion batteries by precisely controlled metal oxide nanocoatings via atomic layer deposition. *Journal of Power Sources, 247*:57-69.
[484] Ge, J., Liang, H., Zhou, M., Zhao, C., Zheng, Z., Yan, Y., . . . Tang, K. (2019). Phosphonate-functionalized Ionic Liquid: A Novel Electrolyte Additive for Eenhanced Cyclic Stability and Rate Capability of LiCoO2 Cathode at High Voltage. *ChemistrySelect, 4*(34):9959-9965.
[485] Pang, C., Xu, G., An, W., Ding, G., Liu, X., Chai, J., . . . Cui, G. (2017). Three-Component Functional Additive in a LiPF6-Based Carbonate Electrolyte for a High-Voltage LiCoO2/Graphite Battery System. *Energy Technology, 5*(11):1979-1989.
[486] Ohzuku, T., & Ueda, A. (1994). Solid-State Redox Reactions of LiCoO2 (R3m) for 4 Volt Secondary Lithium Cells. *Journal of The Electrochemical Society, 141*(11):2972-2977.
[487] Amatucci, G. G., Tarascon, J. M., & Klein, L. C. (1996). CoO2, The End Member of the Li x CoO2 Solid Solution. *Journal of The Electrochemical Society, 143*(3):1114-

1123.
[488] Chen, Z., Lu, Z., & Dahn, J. R. (2002). Staging Phase Transitions in Li[sub x]CoO[sub 2]. *Journal of The Electrochemical Society, 149*(12):A1604.
[489] Chen, Z., & Dahn, J. R. (2004). Improving the Capacity Retention of LiCoO[sub 2] Cycled to 4.5 V by Heat-Treatment. *Electrochemical and Solid-State Letters, 7*(1):A11.
[490] Aurbach, D., Levi, M. D., Levi, E., Teller, H., Markovsky, B., Salitra, G., . . . Heider, L. (1998). Common Electroanalytical Behavior of Li Intercalation Processes into Graphite and Transition Metal Oxides. *Journal of The Electrochemical Society, 145*(9):3024-3034.
[491] Zhang, M., Zhang, J., Yang, J., Yao, J., Chen, Z., Lu, C., . . . Cui, G. (2019). Concentrated electrolyte boosting high-temperature cycling stability of LiCoO 2/graphite cell. *Chemical Communications, 55*(66):9785-9788.
[492] Hu, M., Pang, X., & Zhou, Z. (2013). Recent progress in high-voltage lithium ion batteries. *Journal of Power Sources, 237*:229-242.
[493] Zheng, X., Huang, T., Fang, G., Pan, Y., Li, Q., & Wu, M. (2019). Di(methylsulfonyl) Ethane: New Electrolyte Additive for Enhancing LiCoO2/Electrolyte Interface Stability under High Voltage. *ACS Applied Materials & Interfaces, 11*(39):36244-36251.
[494] Liu, J., Liu, N., Liu, D., Bai, Y., Shi, L., Wang, Z., . . . Schuch, A. (2007). Improving the Performances of LiCoO[sub 2] Cathode Materials by Soaking Nano-Alumina in Commercial Electrolyte. *Journal of The Electrochemical Society, 154*(1):A55.
[495] Wang, X., Xing, L., Liao, X., Chen, X., Huang, W., Yu, Q., . . . Li, W. (2015). Improving cyclic stability of lithium cobalt oxide based lithium ion battery at high voltage by using trimethylboroxine as an electrolyte additive. *Electrochimica Acta, 173*:804-811.
[496] Abraham, D., Furczon, M., Kang, S.-H., Dees, D., & Jansen, A. (2008). Effect of electrolyte composition on initial cycling and impedance characteristics of lithium-ion cells. *Journal of Power Sources, 180*(1):612-620.
[497] Ushirogata, K., Sodeyama, K., Okuno, Y., & Tateyama, Y. (2013). Additive Effect on Reductive Decomposition and Binding of Carbonate-Based Solvent toward Solid Electrolyte Interphase Formation in Lithium-Ion Battery. *Journal of the American Chemical Society, 135*(32):11967-11974.
[498] Zhu, K., Li, Q., Xue, Z., Yu, Q., Liu, X., Shan, Z., & Liu, K. (2020). Mesoporous TiO2 Spheres as Advanced Anodes for Low-Cost, Safe, and High-Areal-Capacity Lithium-Ion Full Batteries. *ACS Applied Nano Materials, 3*(2):1019-1027.
[499] Carboni, M., Manzi, J., Armstrong, A. R., Billaud, J., Brutti, S., & Younesi, R. (2019). Analysis of the Solid Electrolyte Interphase on Hard Carbon Electrodes in Sodium-Ion Batteries. *ChemElectroChem, 6*(6):1745-1753.
[500] Ren, H., Yu, R., Wang, J., Jin, Q., Yang, M., Mao, D., . . . Wang, D. (2014). Multishelled TiO2 Hollow Microspheres as Anodes with Superior Reversible Capacity for Lithium Ion Batteries. *Nano Letters, 14*(11):6679-6684.
[501] Luo, W., Wang, Y., Wang, L., Jiang, W., Chou, S.-L., Dou, S. X., . . . Yang, J. (2016). Silicon/Mesoporous Carbon/Crystalline TiO2 Nanoparticles for Highly Stable Lithium Storage. *ACS Nano, 10*(11):10524-10532.
[502] Yu, J., Huang, H., Gan, Y., Xia, Y., Liang, C., Zhang, J., . . . Zhang, W. (2018). A new strategy for the construction of 3D TiO 2 nanowires/reduced graphene oxide for high-performance lithium/sodium batteries. *Journal of Materials Chemistry A, 6*(47):24256-24266.
[503] Lu, X., Luo, F., Tian, Q., Zhang, W., Sui, Z., & Chen, J. (2021). Anatase TiO2 nanowires intertangled with CNT for conductive additive-free lithium-ion battery

anodes. *Journal of Physics and Chemistry of Solids, 153*:110037.
[504] Huang, Z., Zhao, C., Xu, R., Zhou, Y., Jia, R., Xu, X., & Shi, S. (2021). Carbon modified hierarchical hollow tubes composed of TiO2 nanoparticles for high performance lithium-ion batteries. *Journal of Alloys and Compounds, 857*:158048.
[505] Zhang, M.-M., Chen, J.-Y., Li, H., & Wang, C.-R. (2021). Recent progress in Li-ion batteries with TiO2 nanotube anodes grown by electrochemical anodization. *Rare Metals, 40*(2):249-271.
[506] Obrovac, M. N., & Chevrier, V. L. (2014). Alloy Negative Electrodes for Li-Ion Batteries. *Chemical Reviews, 114*(23):11444-11502.
[507] Xu, C., Lindgren, F., Philippe, B., Gorgoi, M., Björefors, F., Edström, K., & Gustafsson, T. r. (2015). Improved performance of the silicon anode for Li-ion batteries: understanding the surface modification mechanism of fluoroethylene carbonate as an effective electrolyte additive. *Chemistry of Materials, 27*(7):2591-2599.
[508] Rezqita, A., Sauer, M., Foelske, A., Kronberger, H., & Trifonova, A. (2017). The effect of electrolyte additives on electrochemical performance of silicon/mesoporous carbon (Si/MC) for anode materials for lithium-ion batteries. *Electrochimica Acta, 247*:600-609.
[509] Kennedy, T., Brandon, M., Laffir, F., & Ryan, K. M. (2017). Understanding the influence of electrolyte additives on the electrochemical performance and morphology evolution of silicon nanowire based lithium-ion battery anodes. *Journal of Power Sources, 359*:601-610.
[510] Jin, Y., Kneusels, N.-J. H., Marbella, L. E., Castillo-Martínez, E., Magusin, P. C. M. M., Weatherup, R. S., . . . Grey, C. P. (2018). Understanding Fluoroethylene Carbonate and Vinylene Carbonate Based Electrolytes for Si Anodes in Lithium Ion Batteries with NMR Spectroscopy. *Journal of the American Chemical Society, 140*(31):9854-9867.
[511] Li, M.-Q., Qu, M.-Z., He, X.-Y., & Yu, Z.-L. (2009). Effects of electrolytes on the electrochemical performance of Si/graphite/disordered carbon composite anode for lithium-ion batteries. *Electrochimica Acta, 54*(19):4506-4513.
[512] Andersson, A. M., & Edström, K. (2001). Chemical Composition and Morphology of the Elevated Temperature SEI on Graphite. *Journal of The Electrochemical Society, 148*(10):A1100.
[513] (1993). High Resolution XPS of Organic Polymers: The Scienta ESCA300 Database (Beamson, G.; Briggs, D.). *Journal of Chemical Education, 70*(1):A25.
[514] Dedryvère, R., Gireaud, L., Grugeon, S., Laruelle, S., Tarascon, J. M., & Gonbeau, D. (2005). Characterization of Lithium Alkyl Carbonates by X-ray Photoelectron Spectroscopy: Experimental and Theoretical Study. *The Journal of Physical Chemistry B, 109*(33):15868-15875.
[515] Xu, M., Zhou, L., Dong, Y., Chen, Y., Garsuch, A., & Lucht, B. L. (2013). Improving the Performance of Graphite/ LiNi0.5Mn1.5O4Cells at High Voltage and Elevated Temperature with Added Lithium Bis(oxalato) Borate (LiBOB). *Journal of The Electrochemical Society, 160*(11):A2005-A2013.
[516] Aurbach, D., Gamolsky, K., Markovsky, B., Gofer, Y., Schmidt, M., & Heider, U. (2002). On the use of vinylene carbonate (VC) as an additive to electrolyte solutions for Li-ion batteries. *Electrochimica Acta, 47*(9):1423-1439.